

**Agent-based modeling of active matter:
complex formation, artificial intelligence,
contagion dynamics**

Inaugural-Dissertation

zur Erlangung des Doktorgrades
der Mathematisch-Naturwissenschaftlichen Fakultät
der Heinrich-Heine-Universität Düsseldorf

vorgelegt von

Jens Christian Grauer
aus Düsseldorf

Düsseldorf, Juli 2022

aus dem Institut für Theoretische Physik II: Weiche Materie
der Heinrich-Heine-Universität Düsseldorf

Gedruckt mit der Genehmigung der
Mathematisch-Naturwissenschaftlichen Fakultät der
Heinrich-Heine-Universität Düsseldorf

Referent: Prof. Dr. Hartmut Löwen

1. Korreferent: Prof. Dr. Benno Liebchen

2. Korreferent: Prof. Dr. Sabine Klapp

Tag der mündlichen Prüfung: 21. Oktober 2022

Danksagung

An dieser Stelle nutze ich die Gelegenheit, allen Menschen zu danken, die mir das Verfassen dieser Arbeit ermöglicht haben.

Zuerst danke ich Herrn Prof. Dr. Hartmut Löwen, der mich schon während meiner Bachelor- und Masterarbeit hervorragend betreute. Seine umfassende Übersicht über die verschiedensten Forschungsthemen und meine Arbeiten, die vielen Diskussionen und Lösungsvorschläge, wenn ich Rat benötigte, sowie seine Motivation, insbesondere zu Anfangszeiten der Corona-Pandemie, haben einen maßgeblichen Anteil an den Resultaten dieser Arbeit.

In gleicher Weise danke ich Herrn Prof. Dr. Benno Liebchen, für seine stetige Unterstützung und ausgezeichnete Betreuung. Insbesondere seine Betreuung während meiner Masterarbeit hat mich zu dem Verfassen dieser Dissertation motiviert. Vielen Dank für die Inspiration und die vielen kreativen Ideen und Lösungsansätze, die meine Arbeit in dieser Form ermöglichten.

Des Weiteren danke ich Herrn Prof. Dr. Stefan Egelhaaf, der die Rolle meines Mentors übernahm.

Ohne die vielen Kollaborationspartner wäre meine Arbeit derart nicht möglich gewesen. Für die interessanten Einblicke in die experimentelle Physik der weichen Materie sowie die ergiebige Zusammenarbeit danke ich insbesondere Dr. Falko Schmidt und Prof. Dr. Giovanni Volpe, Dr. Sandra Heckel und Dr. Juliane Simmchen, sowie Prof. Dr. Liesbeth M. C. Janssen und der gesamten Forschungsgruppe um Prof. Dr. Nicolas Vogel.

Ebenso geht mein Dank an meine Kollegen mit denen ich eine sehr schöne und prägende Zeit verbracht habe: Dr. Fabian Schwarzendahl (insbesondere für die vielen Bouldersessions nach der Arbeit sowie das Korrekturlesen dieser Arbeit), Jannis Kolker (ebenso für das Korrekturlesen dieser Arbeit), Alexander Sprenger, Paul Monderkamp, Davide Breoni, Dr. Lorenzo Caprini, Dr. Rahul Gupta, Dr. René Wittmann, Claudia Stader, Joachim Wenk und all die anderen ehemaligen und derzeitigen Mitglieder aus der Theoretischen Physik II!

Ich danke meinen Freunden für die Zeit jenseits meiner wissenschaftlichen Arbeit. An dieser Stelle gilt dies insbesondere Steffen, Paulus und Florian, mit denen ich gemeinsam das Physikstudium bewältigt habe. Zusätzlicher Dank geht an Flo, der mir viele nützliche Kommentare zu dieser Arbeit gegeben hat.

Ich bedanke mich bei meinen Eltern Beate und Rainer und meinen beiden Brüdern Erik und Arne, die mich während der gesamten Zeit bedingungslos unterstützt und immer an mich geglaubt haben. Außerdem bedanke ich mich zusätzlich bei Arne,

der mit seinem mathematischen Blick auf diese Arbeit viele hilfreiche Anmerkungen gegeben hat.

Ein besonderer Dank geht an Hannah für ihre liebevolle Unterstützung und unermüdliche Geduld. Ich bedanke mich bei ihr für die Zeit, die sie sich für mich genommen hat, die Motivation, wenn ich sie dringend benötigte und nicht zuletzt ihren fachlichen Rat und das Korrekturlesen verschiedenster Versionen dieser Arbeit.

Preface

This dissertation comprises my work at the Institute for Theoretical Physics II: Soft Matter, Heinrich Heine University Düsseldorf from June 2019 to July 2022. The content of this dissertation is based on the following articles, that have been published in scientific journals or are intended for publication:

- **Paper I**
Swarm Hunting and Cluster Ejections in Chemically Communicating Active Mixtures
Jens Grauer, Hartmut Löwen, Avraham Be'er, & Benno Liebchen
Scientific Reports **10**, 5594 (2020)
- **Paper II**
Active Assembly of Spheroidal Photocatalytic BiVO_4 Microswimmers
Sandra Heckel, Jens Grauer, Maria Semmler, Thomas Gemming, Hartmut Löwen, Benno Liebchen, & Juliane Simmchen
Langmuir **36**, 12473–12480 (2020)
- **Paper III**
Active Droplids
Jens Grauer, Falko Schmidt, Jesús Pineda, Benjamin Midtvedt, Hartmut Löwen, Giovanni Volpe, & Benno Liebchen
Nature Communications **12**, 6005 (2021)
- **Paper IV**
Communicating active agents find food using machine learning
Jens Grauer, Hartmut Löwen, Benno Liebchen, & Fabian Jan Schwarzendahl
(in preparation)
- **Paper V**
Strategic spatiotemporal vaccine distribution increases the survival rate in an infectious disease like Covid-19
Jens Grauer, Hartmut Löwen, & Benno Liebchen
Scientific Reports **10**, 21594 (2020)
- **Paper VI**
Mutation induced infection waves in diseases like COVID-19
Fabian Jan Schwarzendahl, Jens Grauer, Benno Liebchen, & Hartmut Löwen
Scientific Reports **12**, 9641 (2022).

The manuscript of the following project is not part of this dissertation, but is briefly explained in Chapter 4:

- *Acoustic crystallization of two-dimensional colloidal crystals*
Johannes Menath, Reza Mohammadi, Jens Grauer, Maike Böhm, Claudius Deters, Benno Liebchen, Liesbeth M. C. Janssen, Hartmut Löwen, & Nicolas Vogel
(submitted to Advanced Materials)

Abstract

Active matter comprises self-driven units that convert energy from their environment into mechanical work and systematic motion. The study of active matter systems is of particular interest for two reasons: First, contrary to their passive counterparts, active systems are intrinsically out of equilibrium, which requires the development of new approaches to describe them. Second, such systems exist on various scales (from microswimmers, cells, and bacteria, to fish, birds, and even humans), allowing for a wide range of biological and physical applications. Meanwhile, the field of active matter extends from the development of complex self-propulsion mechanisms to the study of a wide range of observed collective phenomena in many-body systems and, more recently, to the application of machine learning methods. In this thesis, I address five topics and investigate various active matter systems using numerical simulations. It is shown how non-reciprocal interactions allow phoretic particles to form dynamic clusters, active modular swimmers, and active “droplids”. Motivated by the variety of microorganisms that use quorum sensing to communicate with each other, I start with a model of a binary mixture of chemotactic particles and demonstrate the formation of complex patterns, such as individual swarms of particles pursuing each other, as well as different cluster phases that can eject their interior once they have formed. A similar simulation model can be used to study the motion of spheroidal photocatalytic microswimmers that self-propel and self-organize into active assemblies of different geometries and speeds. Then, the interaction between light-activated particles and a phase-separating environment is modeled. Under illumination, a two-way coupling between these systems is created giving rise to a novel structure: a liquid droplet encapsulating a self-assembled colloidal engine that induces self-propulsion and drives the entire structure. By combining experiments and simulations, the speed and growth dynamics of this novel structure can be analyzed. Furthermore, colloidal assemblies are ideal model systems to study crystallization phenomena. A simple simulation method is introduced to model the annealing of two-dimensional colloidal monolayers. To take a next step towards smart particles, I then equip active particles with artificial intelligence. It is shown how they learn a strategy to consume a nutrient field as efficiently as possible. Last, I use methods from statistical physics to model the spread of infectious diseases. With an appropriate model, different vaccine distribution strategies are tested and it is shown that the question of a spatiotemporal distribution can play an important role. Similarly, in a further work, the popular susceptible-infected-recovered model is generalized to account

for recurrent mutations and their impact on the contagion dynamics is investigated. This work provides fundamental insights into novel active matter structures and collective phenomena of colloidal particles, and offers interesting links to approaches from machine learning and epidemiology.

Kurzfassung

Aktive Materie umfasst selbstangetriebene Einheiten, die Energie aus ihrer Umgebung in mechanische Arbeit und systematische Bewegung umwandeln. Die Untersuchung von Systemen aktiver Materie ist besonders aus zwei Gründen von großem Interesse: Erstens befinden sich aktive Systeme im Gegensatz zu ihren passiven Gegenständen von Natur aus außerhalb des Gleichgewichts, was die Entwicklung neuer Ansätze zu ihrer Beschreibung erfordert. Zweitens existieren solche Systeme in verschiedensten Größenordnungen (von Mikroschwimmern, Zellen und Bakterien, bis hin zu Fischen, Vögeln und auch Menschen), was eine Vielfalt an biologischen und physikalischen Anwendungen erlaubt. Mittlerweile erstreckt sich das Feld der aktiven Materie von der Entwicklung komplexer Selbstantriebsmechanismen über die Untersuchung eines breiten Spektrums von beobachteten kollektiven Phänomenen in Vielteilchensystemen bis hin zur Verwendung von Methoden des Maschinellen Lernens. In dieser Arbeit befasse ich mich mit fünf Themengebieten und untersuche verschiedene Systeme aktiver Materie mithilfe von numerischen Simulationen. Es wird gezeigt, wie sich phoretische Teilchen über nicht-reziproke Wechselwirkungen zu dynamischen Clustern, aktiven modularen Schwimmern und aktiven „Droplids“ formen. Motiviert durch die Vielzahl an Mikroorganismen, die Quorum sensing nutzen, um miteinander zu kommunizieren, beginne ich mit einem Modell einer binären Mischung von chemotaktischen Teilchen und demonstriere die Bildung komplexer Strukturen, wie einzelne Schwärme von Teilchen, die sich gegenseitig verfolgen, sowie verschiedene Clusterphasen, die ihr Inneres ausstoßen können, sobald sie sich gebildet haben. Mit einem ähnlichen Simulationsmodell lässt sich die Bewegung ellipsoider photokatalytischer Mikroschwimmer untersuchen, die sich selbst antreiben und zu aktiven Assemblierungen unterschiedlicher Geometrien und Geschwindigkeiten organisieren. Nachfolgend wird die Wechselwirkung zwischen lichtaktivierten Teilchen und einer phasentrennenden Umgebung modelliert. Unter Beleuchtung entsteht eine zwei-Wege Kopplung zwischen diesen Systemen, die zu einer neuartigen Struktur führt: ein Flüssigkeitströpfchen, das einen selbstorganisierten kolloidalen Motor einkapselt, der Selbstantrieb erzeugt und somit die gesamte Struktur antreibt. Durch eine Kombination von Experimenten und Simulationen kann die Geschwindigkeit und Wachstumsdynamik dieser neuartigen Struktur analysiert werden. Darüber hinaus eignen sich kolloidale Anordnungen auch ideal als Modellsysteme um Kristallisationsphänomene zu untersuchen. Eine einfache Simulationsmethode wird vorgestellt, mithilfe derer man das Ausheilen zweidimensionaler kolloidaler Monoschichten simulieren kann. Um einen nächsten

Schritt in Richtung intelligenter aktiver Teilchen zu gehen, statte ich als nächstes aktive Teilchen mit künstlicher Intelligenz aus. Es wird gezeigt, wie diese eine Strategie lernen, um eine Nährstoffverteilung möglichst effizient zu konsumieren. Zuletzt nutze ich Methoden aus der statistischen Physik, um die Ausbreitung von Infektionskrankheiten zu modellieren. Anhand eines geeigneten Modells werden verschiedene Strategien zur Impfstoffverteilung getestet und es zeigt sich, dass die Frage einer räumlich-zeitlichen Verteilung eine wichtige Rolle spielen kann. Ebenso wird in einer weiterführenden Arbeit das beliebte Susceptible-Infected-Removed Modell verallgemeinert, um wiederholt auftretende Mutationen zu berücksichtigen und ihre Auswirkungen auf die Infektionsdynamik zu untersuchen. Diese Arbeit liefert grundlegende Erkenntnisse über neuartige Strukturen aktiver Materie und kollektive Phänomene kolloidaler Teilchen und bietet interessante Verknüpfungen zu Ansätzen aus dem Maschinellen Lernen und der Epidemiologie.

Contents

Danksagung	iii
Preface	v
Abstract	vii
Kurzfassung	ix
1 Introduction	1
2 Self-propulsion strategies and self-assembly of chemotactic particles	5
2.1 Chemotaxis	5
2.1.1 Keller-Segel instability	8
2.2 Mixtures of chemotactic particles	9
2.3 Self-propulsion strategies of active particles	11
2.4 Spheroidal photocatalytic microswimmers	12
3 Active colloidal molecules interacting with their environment	15
3.1 Liquid-liquid phase separation	15
3.2 Ginzburg-Landau free energy	17
3.2.1 The Landau expansion: free energy of a uniform system . . .	17
3.2.2 Spatial variations: free energy of a nonuniform system . . .	18
3.3 Cahn-Hilliard equation (“Model B”)	19
3.4 Feedback driven “active droplids”	20
4 Acoustic crystallization of colloidal monolayers	23
4.1 Polycrystalline structures	23
4.2 Sound induced monolayer annealing	24
4.2.1 Simulations of the acoustic annealing of two-dimensional colloidal crystals	24
5 Machine learning for active matter	27
5.1 Artificial neural networks	27
5.2 Reinforcement learning: Q -learning	29
5.3 Communication strategies of smart active agents	32

6	Modeling contagion dynamics	33
6.1	Strategic vaccine distribution	34
6.2	Mutation induced infection waves	35
7	Computational methods	39
8	Scientific publications	43
8.1	Paper I: Swarm Hunting and Cluster Ejections in Chemically Communicating Active Mixtures	43
8.2	Paper II: Active Assembly of Spheroidal Photocatalytic BiVO ₄ Microswimmers	63
8.3	Paper III: Active Droplids	83
8.4	Paper IV: Communicating active agents find food using machine learning	101
8.5	Paper V: Strategic spatiotemporal vaccine distribution increases the survival rate in an infectious disease like Covid-19	109
8.6	Paper VI: Mutation induced infection waves in diseases like COVID-19	121
9	Summary	141
	References	143
	Eidesstattliche Versicherung	157

1 Introduction

The state of matter can usually be assigned to one of the three common categories: solid, liquid and gas. This distinction is drawn on the basis of different properties, such as whether the material is deformable in shape or confined to a fixed volume. However, for some materials this scheme is not applicable. For example, an eraser, a loaf of bread from the bakery, or the morning's toothpaste exhibit a certain intrinsic order, but they are rather "soft" than rigid because they can be easily deformed by hand. This thesis is about *soft condensed matter* [1–4], or "soft matter" for short, which is one of many intermediate states and exists in a region between solid and liquid. It includes everyday things like ink, blood or mayonnaise but also polymers [5], liquid crystals [6] and glasses [7, 8], as well as biological systems such as bacterial suspensions [9, 10]. In particular, non-deformable solid *colloidal particles* suspended in a viscous fluid are also referred to as soft matter and serve as ideal model system to study physical phenomena such as self-assembly and pattern formation [11–17].

A common feature of soft matter is the mesoscopic scale of the individual building blocks which ranges from a few nanometers to around a hundred micrometers. On the one hand, this is much larger than the length scale of individual atoms and molecules of the liquid in which the colloids are suspended. On the other hand, this is much smaller than the length scale of the characteristic patterns and hierarchical structures into which the individual building blocks may self-assemble as the system approaches equilibrium. A characteristic of soft matter are the typically weak interactions between the constituents of the system, which are on a similar energy scale as the thermal energy of the environment. Therefore, soft matter is particularly sensitive to external perturbations and its behavior is strongly affected by thermal fluctuations. For a colloidal particle, this is manifested by an irregular and erratic motion caused by random collisions of the surrounding molecules of the liquid. This motion is called *Brownian motion*, named after the Scottish botanist Robert Brown, who discovered it under the microscope in 1827 [18]. Later, an analytical description for this motion was provided by Einstein in 1905 [19] and Smoluchowski in 1906 [20].

For a bacterium, however, the question inevitably arises of how it is able to find food or to flee from toxic substances. Fortunately, nature has provided a variety of propulsion mechanisms for this purpose. For example, some bacteria have developed filamentous structures on their surface, called flagella, which provide them with motility [25]. To understand this directed motion in more detail, scientists build

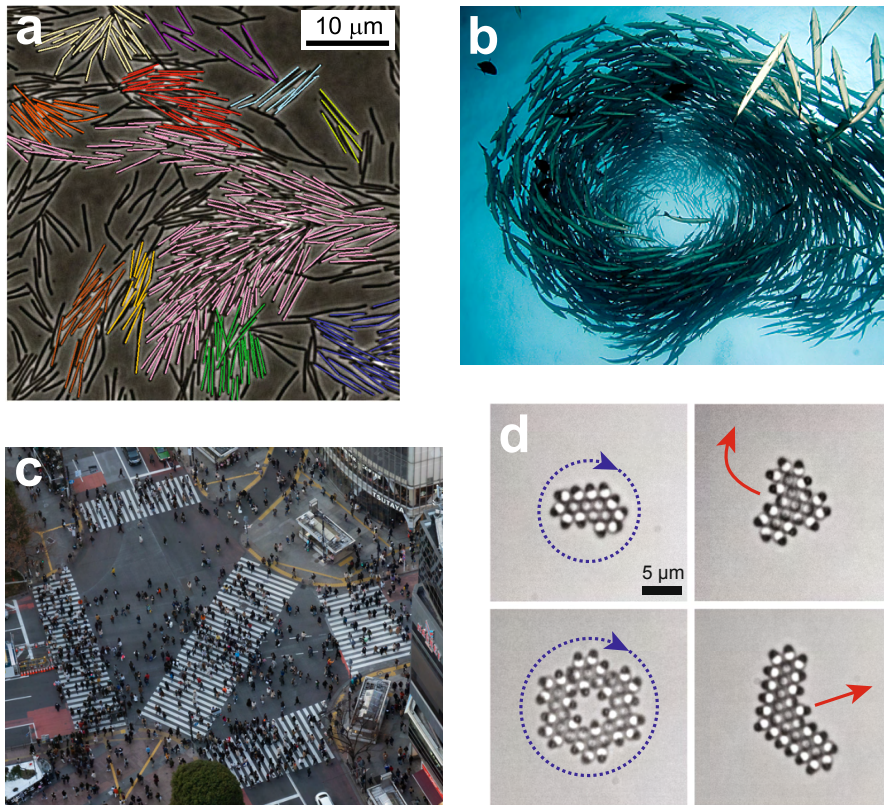


Figure 1.1: **Examples of active matter systems.** **a** Swarming bacteria move in dynamic clusters that split and merge. Colors indicate bacteria that belong to different clusters. Reproduced from [21]. CC BY 4.0. **b** A “tornado” of schooling barracudas (large, predatory fishes) [22]. **c** Pedestrian scramble at Shibuya Crossing in Tokyo [23]. **d** Programmable assemblies of colloidal metamachines with translational or rotational motion. Blue arrows indicate the direction of rotation, red arrows indicate the direction of propulsion. Identical scale for all images. Reproduced from [24]. CC BY 4.0.

artificial colloidal particles under laboratory conditions that are self-propelled by an internal drive. Here we already delve into the field of so-called *active soft matter* [26,27], whose components take energy from the environment and drive the system out of equilibrium. An important research area of active matter is constituted by biological or artificial objects that are able to self-propel. The concept of *self-propelled particles* (SPP) [28] is used to describe the motion of autonomous particles that extract energy from their environment and convert it into directed motion. For example, SPPs can be applied to model the coordinating behavior and collective motion in fish schools [29], bird flocks [30], or locust swarms [31], and on a smaller scale in swarming bacteria [21] and self-organized arrays of cells [32]. In

addition, even in computer simulations of crowd dynamics of pedestrians, models of SPPs can be used to describe their collective behavior [33,34]. See Fig. 1.1 for some examples of active matter systems.

In this thesis I use agent-based models to study various systems of (active) soft matter. In Chapter 2, the basic concepts of *chemotaxis* are explained, i.e., the movement of organisms in response to a chemical stimulus, and self-propulsion mechanisms of active particles are described, which self-propel and self-organize into active colloidal assemblies. Inspired by the variety of microorganisms that communicate by producing certain chemicals to which others respond, I explore a simple physical model beyond the commonly considered one-species limit. It is demonstrated how the species selective chemical production in an active mixture of chemotactic particles leads to collective behavior and interesting patterns.

In Chapter 3, a next step in the evolution of active matter is established by realizing a versatile feedback loop between a nonequilibrium system and its environment. Under illumination of a mixture of light-activated colloids in a near-critical bath, the colloids heat up and induce a phase separation in their local environment. This leads to the emergence of droplets, which act back on the colloids by attracting and encapsulating them. Inside the droplets, the colloids form active assemblies which work as internal engines and drive the entire structures. The resulting active structures include droplets and colloids and perform directed motion. We name them “active droploids”.

Positioning a very large number of colloidal particles on a planar surface forms an ideal model system to study crystallization phenomena. In Chapter 4, a simple but efficient method to anneal two-dimensional colloidal crystals is described. Subsequently, I present a suitable theoretical model to simulate the applied method.

Machine learning has gained tremendous attention again in recent years and has also reached the research area of active soft matter. In Chapter 5, I explain how a system of communicating active particles is able to learn collection strategies, after explaining basic principles of an *artificial neural network* and methods of *reinforcement learning*.

Although it may not be obvious at first, the field of mathematical modeling of infectious diseases is fairly close to the statistical methods used in theoretical soft matter. The Covid-19 pandemic prompted us to exploit this and create models describing the course of the pandemic in a variety of scenarios. After a brief explanation of the classical approaches to describing the spread of infectious diseases in Chapter 6, I present two theoretical models that we developed. The first one is used to test different vaccine distribution strategies, while the second one allows to study the impact of mutations on the contagion dynamics.

The computational methods are described in Chapter 7 followed by the scientific publications listed in Chapter 8. A summary and an outlook of this thesis are given in Chapter 9.

2 Self-propulsion strategies and self-assembly of chemotactic particles

2.1 Chemotaxis

Chemotaxis [35–37] describes the movement of living organisms or cells due to a chemical substance gradient [38,39] (from “chemical substance” + ancient Greek (τάξις) “orientation”). This is one of the most fundamental physiological cellular responses, because finding beneficial substances, such as food, or fleeing from toxins is of enormous importance to microorganisms. If this movement along the gradient occurs in the direction of higher concentrations of the substance, it is referred to as *positive chemotaxis* and the substance is called *attractant*. If, on the other hand, the movement is performed in the opposite direction, this is called *negative chemotaxis* and the respective substance is referred to as *repellent*. Many microorganisms and synthetic particles adapt their movement also in response to other stimuli and there exist many other forms of taxis in addition to chemotaxis, e.g., driven by a temperature field (thermotaxis) [40,41], different light intensities (phototaxis) [42–44], as well as by gravity (geotaxis or gravitaxis) [45,46] or viscosity (viscotaxis) [47] to name a few. Chemotaxis not only allows microorganisms to find locations with higher concentrations of a nutrient more quickly or to avoid areas with harmful substances, but may also serve as a communication mechanism among themselves [48]. For example, microorganisms can also be attracted to chemicals produced by others, such as cAMP in *Dictyostelium* cells [49] or autoinducers in signaling *Escherichia coli* [50,51]. However, a difficulty arises here as bacteria are not able to directly sense the direction of the chemical concentration gradient. Due to the small size of bacteria, typically a few micrometers, the local concentration gradient is obscured by their Brownian motion. In order to be able to identify the direction of the gradient, a bacterium needs to swim a distance in a random direction and uses receptors on its surface to measure whether the substance concentration changes. If, in the case of positive chemotaxis, the substance concentration increases along this path, the bacterium maintains the direction. As soon as the concentration decreases, the bacterium changes its direction of movement. Although the bacterium cannot measure the concentration gradient directly and also does not retain a sense

of orientation in memory, it moves on average in the direction of higher concentration. In certain bacteria, this results in a “run-and-tumble” motion [9, 52], in which the bacterium alternately moves in a fixed direction and then stays at a location for a short time to change orientation. So-called run-and-tumble particles are often used in the course of a mathematical description to model this motion in detail [53, 54].

Chemotaxis can be observed not only in biological systems, such as bacteria or other microorganisms, but also in synthetic systems, e.g., chemical robots or artificial enzyme molecules. Self-propelled microscopic building blocks like artificial microswimmers and active colloidal particles [55, 56], or just *active particles* [57, 58], serve as ideal model systems for active matter. The surface of such particles is typically coated with a certain material, which causes an interaction with the environment and induces an effective motion. For example, in so-called *Janus particles* (named after the Roman god with two faces) [59, 60], the surface of the particles is divided into two halves, which have different chemical or physical properties, resulting in a symmetry breaking. A reaction catalyzed on half of the surface, for example, leads to a change in the chemical concentration of a substance. This can create a gradient along the particle due to its asymmetric structure, which can induce a movement. Remarkably, the self-produced concentration field decays rather slowly and typically scales as $1/r$ in three dimensions with the distance r from the particle (if the phoretic field relaxes quasi-instantaneously and does not decay through other reactions) [61]. This allows for long-ranged interactions among the particles, for example, directing their motion towards (or away from) the producing particle. A key feature of chemical interactions between the particles is that they are in general nonreciprocal and break action-reaction symmetry. This violation of Newton’s third law (actio = reactio) results from the effective interaction between the particles via the chemical concentration field, meaning that a particle can attract others while remaining unaffected itself. The particles are able to communicate with each other and coordinate their motion. In systems with many particles, these interactions between self-propelled particles can lead to interesting collective phenomena, as also observed in the biological habitat. Therefore, artificial particles serve as a helpful synthetic analogue to microbiological systems when studying collective behavior and signaling-induced pattern formation, such as dynamic clusters [62–66], traveling waves [67–69] or collectively self-optimized patterns [48].

Within a mathematical description of a many-body system, there exists a wide range of models, which describe the behavior of a suspension of (chemotactic) particles [70–73]. While such a model itself is ideally kept minimalistic, it should cover the properties of the particles and the system as accurately as possible and represent experimental observations. This raises the question of the dominant interactions which have to be considered for active colloids [61, 74]. When modeling chemotactic particles, not only the motion of the particles must be taken into account, but also the coupling with the dynamics of the chemicals. Consequently,

the equations of motion of the particles are coupled with a diffusion equation describing the chemical field. Furthermore, besides the phoretic coupling, there are short-range steric repulsions, which are an essential part in describing agglomeration of particles and the formation of clusters. Additionally, the motility of the active particles alone can lead to a spontaneous accumulation of particles, known as *motility-induced phase separation* (MIPS) [75–79]. Hydrodynamic effects can also play a role [27, 80, 81], when active particles cause a solvent flow by their motion which in turn may affect the motion of neighboring particles. However, in the case of those active colloids discussed in this thesis, phoretic interactions are assumed to dominate [61, 63] (different from microswimmers, which change their shape to self-propel, and for which hydrodynamic effects are essential [80, 82, 83]).

Furthermore, synthetic colloids and microorganisms typically reside in fluids with low Reynolds numbers, meaning, one considers small micrometer-sized particles in very viscous fluids. The dynamics of the particles is overdamped and can be described by the well-known active Brownian particle model [58]. At this point, it should be mentioned that for larger particles or more flowable fluids, inertial effects can become relevant, which must be taken into account appropriately [84].

In the following, a basic model describing the motion of chemotactic self-propelled particles in a concentration field is explained. Considering a system of N overdamped colloids responding to a chemical field $c(\mathbf{r}, t)$ via chemotaxis, the dynamics of the particle motion are described by the Langevin equation:

$$\dot{\mathbf{r}}_i(t) = \alpha \nabla c(\mathbf{r}, t) + \sqrt{2D} \boldsymbol{\eta}_i(t) , \quad (2.1)$$

where \mathbf{r}_i is the position of particle i ($i = 1, \dots, N$), D is a translational diffusion coefficient and $\boldsymbol{\eta}_i(t)$ is a unit variance Gaussian white noise with zero mean to model the random movement of the particles due to Brownian motion. The strength of the chemotactic coupling of the particles to the concentration field is described by α , where $\alpha > 0$ leads to chemoattraction (positive chemotaxis) and $\alpha < 0$ to chemorepulsion (negative chemotaxis). It is possible to model steric repulsions among particles by using an additional force term. The dynamics of the chemical field $c(\mathbf{r}, t)$ is described by a diffusion equation $\dot{c}(\mathbf{r}, t) = D_c \Delta c$ (with diffusion coefficient D_c). If the particles interact with the field, e.g., by producing the chemical substance itself, this equation can be extended by additional point sources. Similarly, chemical reactions or other processes may decrease (or increase) the concentration in the bulk, which can also be accounted for by another appropriate sink (or source) term. One obtains the following diffusion equation for a system of N particles producing a chemical field $c(\mathbf{r}, t)$ with rate k_0 :

$$\dot{c}(\mathbf{r}, t) = D_c \Delta c + k_0 \sum_{i=1}^N \delta(\mathbf{r} - \mathbf{r}_i) - k_d c , \quad (2.2)$$

where the coefficient k_d determines a degrading of the chemical field in the bulk.

Paper I and **II** discuss the collective behavior and self-assembly of phoretically interacting particles that produce a chemical concentration field, described in a manner similar to Eqs. (2.1) and (2.2). To understand the origin of the structure formation, a linear stability analysis is performed, which is discussed below for the simplest case.

2.1.1 Keller-Segel instability

It is useful to describe the particle motion by a particle density field $\rho(\mathbf{r}, t) = \sum_{i=1}^N \delta(\mathbf{r} - \mathbf{r}_i(t))$. The corresponding Fokker-Planck equation [85], which is equivalent to the Langevin equation (Eq. (2.1)) (for point particles), gives a continuous representation of the probability distribution to find a particle at position \mathbf{r} at time t :

$$\dot{\rho}(\mathbf{r}, t) = D\Delta\rho - \nabla \cdot (\alpha\rho\nabla c) . \quad (2.3)$$

When applied to particle position distributions this equation is better known as Smoluchowski equation [86]. Accordingly, the diffusion equation for the chemical concentration field can be written as:

$$\dot{c}(\mathbf{r}, t) = D_c\Delta c + k_0\rho - k_d c . \quad (2.4)$$

In this form, Eqs. (2.3) and (2.4) are also known as Keller-Segel model [70,87]. Using these equations, a linear stability analysis can now be performed by first linearizing both equations around the steady state solution $(\rho, c) = (\rho_0, k_0\rho_0/k_d) =: (\rho_0, c_0)$, which represents the uniform phase. To study the consequences of a deviation from the homogeneous phase, small perturbations of the particle density $\rho = \rho_0 + \delta\rho$ and the chemical field $c = c_0 + \delta c$ are considered. The resulting linearized equations then read:

$$\partial_t \delta\rho = D\Delta\delta\rho - \alpha\rho_0\Delta\delta c , \quad (2.5)$$

$$\partial_t \delta c = D_c\Delta\delta c + k_0\delta\rho - k_d\delta c . \quad (2.6)$$

One can now perform a Fourier transform in space and use a separation ansatz $\hat{\rho}(\mathbf{q}, t) = e^{\lambda t}\hat{\rho}(\mathbf{q})$ and $\hat{c}(\mathbf{q}, t) = e^{\lambda t}\hat{c}(\mathbf{q})$ (with wave vector \mathbf{q}), leading to the following eigenvalue problem:

$$\lambda \begin{pmatrix} \delta\hat{\rho} \\ \delta\hat{c} \end{pmatrix} = \begin{pmatrix} -D\mathbf{q}^2 & \alpha\rho_0\mathbf{q}^2 \\ k_0 & -D_c\mathbf{q}^2 - k_d \end{pmatrix} \begin{pmatrix} \delta\hat{\rho} \\ \delta\hat{c} \end{pmatrix} . \quad (2.7)$$

The eigenvalues λ of the matrix determine the stability of the system. For eigenvalues whose real part is strictly less than zero, the steady state is stable. If, instead, there is at least one eigenvalue with a positive real part, the steady state is unstable. The determination of the eigenvalues λ followed by a Taylor expansion and the subsequent examination on a positive real part leads to the following instability criterion:

$$Dk_d < \alpha k_0\rho_0 . \quad (2.8)$$

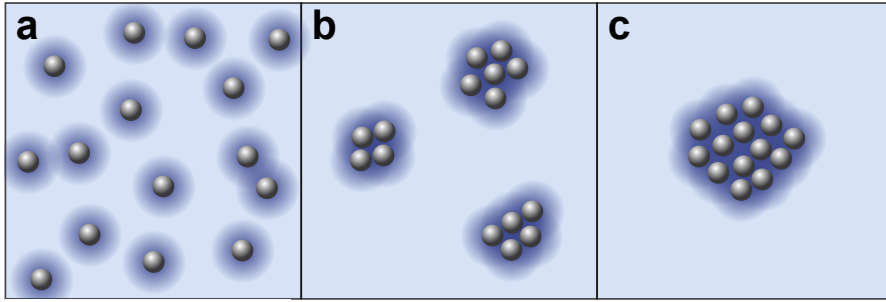


Figure 2.1: **Schematic illustration of cluster formations as a consequence of the Keller-Segel instability.** **a-c** Chemotactic particles that are initially separated (**a**), aggregate and form clusters (**b**) that merge over time (**c**).

This is also known as the *Keller-Segel instability*, which occurs due to the positive feedback between the chemical production of the particles and the attraction of the particles towards higher concentrations (for $\alpha > 0$). As can be seen in Eq. (2.8), strong chemical production and chemotactic coupling of particles leads to instability. In contrast, the homogeneous phase is approached with increasing particle diffusion and fast evaporation of the chemicals. Figure 2.1 schematically illustrates a typical formation of a cluster of passive particles due to the Keller-Segel instability, which grows over time and coalesces with surrounding clusters.

2.2 Mixtures of chemotactic particles

In many biological processes in which microorganisms or cells communicate with each other using certain (chemical) substances, there are typically several species involved that simultaneously produce different chemicals to which others respond. A simple example of a signaling loop involving different chemicals is given by the interaction between macrophages and tumor cells [88]. Macrophages are certain white blood cells and usually play an important role in human immune defense. However, the tumor cells secrete a colony-stimulating factor (CSF-1) leading to the aggregation and growth of the macrophages, which respond to this signal by moving up the chemical gradient. In turn, the macrophages release epidermal growth factors (EGF), which are actually important for the immune system, but in this context they lead to growth and increased mobility of tumor cells. While there are many models on colloidal chemotactic mixtures [89, 90], the study of such a scenario is particularly interesting because, for simplicity, most existing models describe the interaction of the mixture using only a single chemical field [91]. Motivated by the above example, in **Paper I** my coauthors and I studied a simple model in which a mixture of two different species of chemotactic particles interact

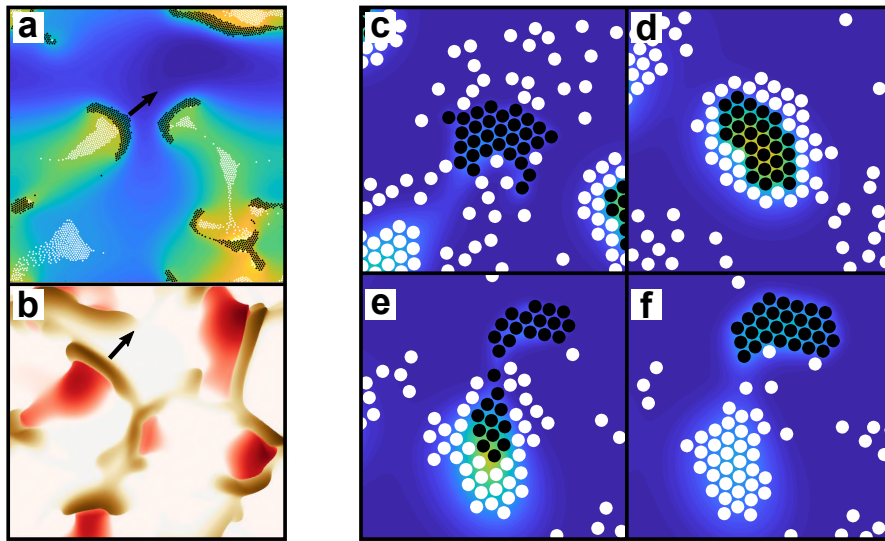


Figure 2.2: **Mixtures of chemotactic particles.** **a,b** Snapshots from particle-based (**a**) and continuum-based (**b**) simulations of a binary mixture of chemically interacting particles (black and white) which self-organize into hunting swarms. **c-f** Sequence of simulation snapshots showing a cluster ejection caused by chemical delay effects. Reproduced from [66]. CC BY 4.0.

with each other, each producing an individual chemical. Similar to the particle based description in Eqs. (2.1) and (2.2) and the continuous description in Eqs. (2.3) and (2.4), each extended by appropriate terms accounting for the coupling with the other species, we investigated and analyzed possible phases occurring in this system. Depending on the chemoattractive and chemorepulsive interactions among the species, we discovered various interesting phases, of which a “hunting-swarm phase” is particularly remarkable, in which swarms of each species form and one of them pursues the other, see Fig. 2.2a,b. Physically, this phase occurs when the particles of one species attract each other to form a cluster, but likewise attract the particles of the second species, which in turn repel the particles in the cluster. Moreover, the predicted phase diagram of this model comprises the formation of clusters composed of both types of particles, with the inner core formed by one species surrounded by a diffuse or solid shell of particles of the other species (“core-shell clusters”). In particular, a low diffusion coefficient of the chemicals can lead to delay or memory effects and, due to signaling via two chemicals, to particle clusters that exhibit complex self-dynamics. More specifically, the core-shell clusters can eject their inner particles once they have formed, whereupon the particles of both species build new clusters and the described process repeats (Fig. 2.2c-f). For more details and an explicit formulation of the equation of motion, see **Paper I** in Chapter 8 - Scientific publications.

2.3 Self-propulsion strategies of active particles

There are various ways to equip an artificial microswimmer with mobility [92], as already briefly indicated in Section 2.1. Usually, this is accomplished by symmetry breaking of the system, for example, in the case of a photocatalytic Janus particle by its asymmetric coating. The main driving mechanisms of such (light-driven) microparticles can mostly be traced back to self-diffusiophoresis [93], self-thermophoresis [94] or self-electrophoresis [95, 96], where usually the overall mechanism consists of a complex combination of several processes. Illumination of the particle then enables an asymmetric generation of substance concentrations, temperature gradients or electric fields, creating a fluid flow that drives the particle (Fig. 2.3).

As the name indicates, the mechanism of self-diffusiophoresis results from asymmetric diffusion of chemicals along the particle, e.g., when a particle converts a chemical fuel into individual reaction products. An example of this are silica (SiO_2) particles that are half coated with platinum (Pt) and catalyze the decomposition of hydrogen peroxide (H_2O_2) [97]. The surface chemical reaction $2 \text{H}_2\text{O}_2 \rightarrow \text{O}_2 + 2 \text{H}_2\text{O}$ is then catalyzed on the platinum side of the particle. A concentration gradient of the reaction products leads to an asymmetric repulsive interaction that drives the particle.

In self-thermophoresis, the surface of particles is partially coated with a photothermal material (e.g., gold) [98]. If the particle is illuminated with laser light of a certain wavelength, a temperature field is generated which causes a gradient along the particle due to the asymmetric coating. This drives the particle, where the direction of particle motion depends on the Soret coefficient $S_T = \frac{D_T}{D}$ with the diffusion coefficient D and the thermodiffusion coefficient D_T .

The self-electrophoretic drive mechanism is also often responsible for many light-driven, typically photo-semiconducting microparticles. There, electron-hole pairs are produced under illumination by a photo-semiconductor on one hemisphere of the particle. Electrons and holes then migrate to different halves of the particle where reduction and oxidation half reactions are catalyzed. In particular, this is seen when one half of a particle in water is coated with a metal (e.g., gold or platinum) along with the semiconductor photocatalyst on the other half (e.g., titanium dioxide TiO_2) [99]. This facilitates the separation of electrons and holes, with the photogenerated holes remaining in the semiconductor and carrying out the water oxidation ($2 \text{H}_2\text{O} + 4 \text{h}^+ \rightarrow \text{O}_2 + 4 \text{H}^+$), while the photogenerated electrons can easily accumulate in the metal for the reduction reaction ($4 \text{H}^+ + 4 \text{e}^- \rightarrow 2 \text{H}_2$). This asymmetric production and consumption of protons during the reaction generates an electric field that points towards the Au side. As a result, the ions migrate towards the Au side and drag the water along leading to a fluid flow and a motion of the particle in the opposite direction. In this way, the particle itself generates an electric field which drives it towards the semiconductor side.



Figure 2.3: **Schematic representation of mechanism for propulsion of synthetic catalytic particles.** **a** Self-diffusiophoresis. **b** self-thermophoresis. **c** self-electrophoresis.

2.4 Spheroidal photocatalytic microswimmers

In collaboration with Juliane Simmchen and Sandra Heckel from TU Dresden, we investigated a system of spheroidal microswimmers that individually exhibit directional motion and form into active assemblies under light illumination [100], similar to the previous section. But unlike the Janus particles in 2.3, whose characteristics are given by an asymmetric coating of the surface, the remarkable feature in our work is an isotropic construction of single-component particles. The investigated particles are coated with bismuth vanadate (BiVO_4), a semiconducting material, allowing them to self-propel in the same way under illumination without the need for an asymmetrization step [101, 102]. Here, the main characteristic is the BiVO_4 coating, which can occur in three different crystal structures, with monoclinic scheelite being the most photocatalytically active. If electron-hole pairs are generated upon illumination of the particle's surface, the monoclinic scheelite crystal structure favors spatial separation of the photogenerated electrons and holes on different crystal facets, resulting in an effective charge separation [103]. When the particles are immersed in a hydrogen peroxide (H_2O_2) solution and illuminated with UV light, the decomposition of H_2O_2 is catalyzed. In this process, the H_2O_2 reacts with the holes in the crystal producing oxygen and hydrogen ions. Then, the hydrogen ions are consumed by the other half-reaction as H_2O_2 reacts with the electrons in the crystal to form water (Fig. 2.4a). Due to the spatial separation of the electrons and holes upon illumination, the oxidation and reduction half-reaction of H_2O_2 decomposition are spatially separated. Ultimately, this creates a proton gradient around the particle that induces an intrinsic driving force, causing the particle to move. In **Paper II** we investigated those spheroidal BiVO_4 microswimmers combining an experimental approach with simulations and analytical calculations. The spheroidal swimmers are able to self-propel individually with velocities of about $4 \mu\text{ms}^{-1}$ and self-organize into different active assemblies. Due to the spheroidal shape of the particles, these assemblies appear in various

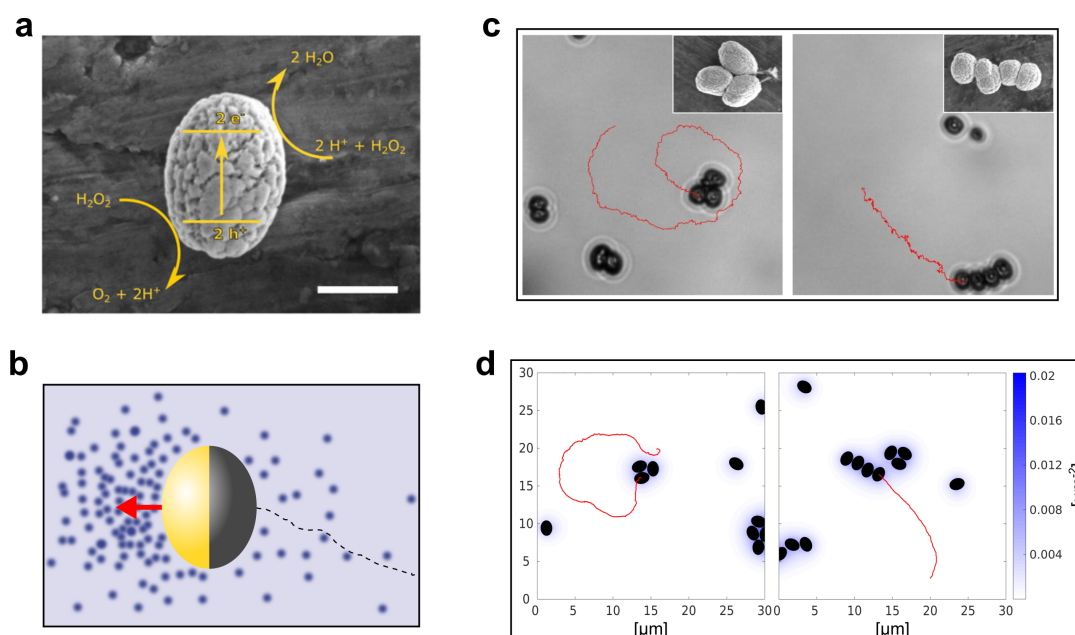


Figure 2.4: **Motion mechanism and modeling of spheroidal BiVO_4 particles.** **a** SEM image of a spheroidal BiVO_4 particle and mechanism of the H_2O_2 fuel degradation. **b** Schematic representation of a spheroidal swimmer as it is handled in a simulation, producing a chemical asymmetry on part of its surface and inducing movement in the direction of its catalytic cap. **c,d** Experimental (**c**) and simulated (**d**) tracks of three-triangle (left) and four-caterpillar (right) particle assemblies. (**a**), (**c**) and (**d**) reprinted with permission from [100]. Copyright 2020 American Chemical Society.

arrangements with different velocities, ranging from closely clustered particle assemblies to “caterpillar” structures in which the particles are lined up along their short axis, see Fig. 2.4c,d. The explicit formulation of the simulation model, particle arrangements and swimming behavior of the active assemblies are described in detail in **Paper II** in Chapter 8 - Scientific Publications.

3 Active colloidal molecules interacting with their environment

As demonstrated in the previous chapters, the individual constituents in systems of active matter are able to convert the energy from the environment into a directed motion. In contrast to systems at equilibrium, in active matter systems the environment acts as a persistent free energy source, unidirectionally feeding the system of active particles. This can induce a rich phenomenology, such as the emergence of spatiotemporal patterns in self-driven colloids [104] but also, for example, in systems of active droplets [105–110] formed through liquid-liquid phase separation [111–114].

However, in these examples, the environment can mediate effective interactions between active particles, but it does not show intrinsic dynamics that adapts to the dynamics of the active particles. In contrast, biological systems often exhibit a two-way coupling with their surrounding environment, for example, involved in homeostasis, gene-expression regulation, and structure formation [115,116].

In **Paper III**, I investigate the two-fold coupling between light-activated colloidal particles and liquid droplets formed from a critical binary mixture of water and 2,6-lutidine. The resulting feedback loop leads to novel structures that hinge on the mutual coupling between the colloids and the surrounding solvent. Before discussing this work in more detail, I will explain under which conditions phase separation of a binary liquid mixture occurs and how it can be described theoretically and modeled in a simulation.

3.1 Liquid-liquid phase separation

In thermodynamics, phase separation describes the transition of a homogeneous mixture into distinct coexisting phases [117]. A common type of phase separation system is given by binary liquid mixtures consisting of two different molecular components, e.g., a mixture of water and oil. The state of such mixtures is determined by the thermodynamically most favorable condition with the lowest energy configuration. While the water oil solution typically remains demixed, the state of a so-called critical mixture can be easily changed to be either mixed or demixed,

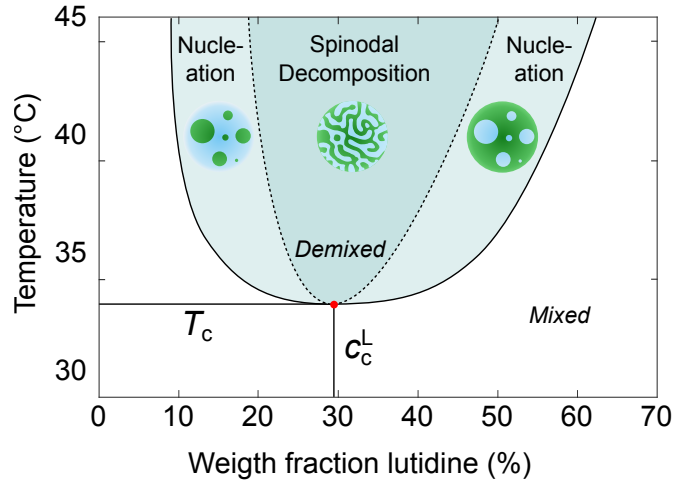


Figure 3.1: **Phase diagram of the water–2,6-lutidine mixture.** The critical point is defined by the critical lutidine mass fraction at $c_c^L = 0.286$ and the critical temperature at $T_c = 34.1^\circ\text{C}$ [118]. Depending on the temperature and composition, the system is found in the mixed phase (white background) or demixed phase (green background). The dashed line indicates the region of spinodal decomposition, where both phases separate from each other resulting in characteristic worm-like structures (dark green background). Between the spinodal and binodal (light green background), nucleation occurs in one of the two phases as individual droplets of the minority phase form (i.e., at supercritical 2,6-lutidine concentration, water-rich droplets form in a lutidine-rich background). Reproduced from [119]. CC BY 4.0.

depending on the composition ratio of the components and the temperature of the solution. The critical mixture of water and 2,6-lutidine is a common choice in experiments because the system can be easily prepared near its critical temperature close to room temperature. The phase diagram of the water–2,6-lutidine mixture is shown in Fig. 3.1. Below the critical temperature, the equilibrium state is given by the phase in which the fluid is homogeneously mixed. The solid line in Fig. 3.1 is called the “binodal”, above which both phases can coexist in separated regions (sometimes also called coexistence line). If a mixed fluid is then heated to a temperature above the binodal line, the fluid phase separates by forming domains of A-rich (2,6-lutidine) and B-rich (water) phases that grow over time. Above the dashed line, the fluid separates by spinodal decomposition, which is why this line is called “spinodal” [120]. Here, the fluid phase separates into a characteristic worm-like structure, as it is illustrated in the inset in the dark green area of Fig. 3.1. The spinodal curve is defined by the condition that the second derivative of the free energy with respect to the composition is zero. At the critical

point (defined by the fluid's critical concentration c_c^L and critical temperature T_c), the binodal and spinodal line coincide and no thermodynamic barrier impedes the system to demix. This is characteristic for a second order (continuous) phase transition, where the free energy's first derivative with respect to some thermodynamic variable, e.g., temperature, is continuous, while a discontinuity occurs in the second derivatives. As a result, a fluid with critical concentration c_c^L becomes thermodynamically unstable and its free energy is at a local maximum, when it is heated above the critical temperature T_c (see Fig. 3.2). At this point, single fluctuations in the fluid are sufficient to induce a phase separation. A different situation, i.e., a first order phase transition, occurs when the fluid is prepared in an off-critical state, for example due to a higher 2,6-lutidine concentration. With increasing temperature, the homogeneous phase becomes metastable and remains resistant to small fluctuations, as opposed to the scenario described above. The system initially requires time to overcome a nucleation barrier, after which droplets of the lower concentrated phase form. This regime of *nucleation and growth* is in between the binodal and the spinodal (light green area in Fig. 3.1) [121]. At later times, these separated regions grow with a power law, where the domain size increases with $L \sim t^{\frac{1}{3}}$ according to the Lifshitz-Slyozov law [122–124].

3.2 Ginzburg-Landau free energy

3.2.1 The Landau expansion: free energy of a uniform system

The Landau theory is a phenomenological mean-field theory for the description of continuous phase transitions [125]. Although this theory was originally established as an attempt to describe second-order (continuous) phase transitions, it can also be used as a quantitative model for first-order (discontinuous) transitions. The central idea of the Landau theory is the introduction of an order parameter ϕ specifying the free energy $\mathcal{F}(\phi)$ of the system. In general, the order parameter is the mean value of some observables which indicate the state of the system. In **Paper III**, the order parameter is introduced as the relative concentration difference of the two species A (2,6-lutidine) and B (water) of the mixture. In regions where A and B are homogeneously mixed, ϕ equals zero, whereas $\phi = \pm 1$ in pure regions of A and B, respectively. The phase of the system, at given temperature T , is then determined by minimizing the free energy $\mathcal{F}(\phi)$. According to the Landau theory, the order parameter ϕ is assumed to be small near the transition temperature between the two phases, allowing an expansion of $\mathcal{F}(\phi)$ in powers of ϕ . The phase separation is described in sufficiently good approximation if the free energy is expanded up to the 4th order in ϕ (sometimes also called ϕ^4 -theory [126]). The free energy density of a uniform system is then:

$$f_0(\phi) = u_0 + u_1\phi + \frac{u_2}{2}\phi^2 + \frac{u_3}{3}\phi^3 + \frac{u_4}{4}\phi^4 + \dots, \quad (3.1)$$

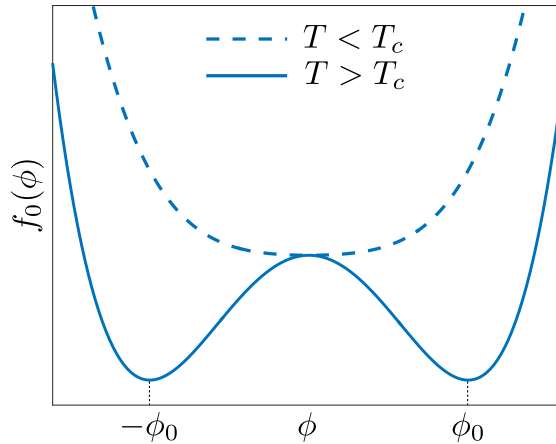


Figure 3.2: **Schematic illustration of the homogeneous free energy profile.**

The free energy density $f_0(\phi)$ features a single minimum for $T < T_c$, retaining the mixture in the homogeneous phase. For $T > T_c$, two minima at $\phi = \pm\phi_0$ arise and the fluid demixes.

with the free energy $\mathcal{F}_0 = V f_0$, where V is the volume of the system. Assuming the symmetric case of a binary mixture, where the free energy is invariant to reflection operations so that the relation $f_0(\phi) = f_0(-\phi)$ holds, allows us to eliminate the odd terms in Eq. (3.1). The Landau coefficients are experimentally determined parameters, where a change of sign in $u_2 = u_2(T)$ due to a temperature change decides the occurrence of a phase transition. The order parameter of the system is assumed to remain finite when minimizing the energy, i.e., $u_4(T) > 0$. The critical temperature of the system is determined by $u_2(T_c) = 0$, which allows to approximate $u_2(T) \approx a_0(T - T_c)$ for temperatures close to T_c , with $a_0 < 0$ for a lower critical solution temperature. Similarly, for small deviations around T_c , $u_4(T) = b = \text{const.}$ can be approximated. Figure 3.2 shows a schematic plot of the free energy $f_0(\phi) \sim \frac{a_0}{2}(T - T_c)\phi^2 + \frac{b}{4}\phi^4$ for the cases $T > T_c$ and $T < T_c$, respectively. The minima $\pm\phi_0$ are given by the equilibrium condition when minimizing the Landau free energy with respect to ϕ : $\frac{df_0}{d\phi} = 0 \Rightarrow a_0(T - T_c)\phi + b\phi^3 = 0$. The solution is given by

$$\phi_0(T) = \begin{cases} 0, & \text{if } T \leq T_c \\ \pm\left(\frac{-a_0(T - T_c)}{b}\right)^{1/2}, & \text{if } T > T_c \end{cases} \quad (3.2)$$

meaning the mixed phase is stable for $T \leq T_c$, whereas, by contrast, the demixed phase is stable for $T > T_c$.

3.2.2 Spatial variations: free energy of a nonuniform system

Now we consider a spatially nonuniform system, like a phase-separating fluid. Per definition, the order parameter must be spatially dependent, $\phi = \phi(\mathbf{r})$. In a region

with a nonuniform composition, the local free energy depends not only on the local composition, but may also depend on the composition of the local environment. Thereby, the free energy is a function that depends on the order parameter as well as its derivatives [127]:

$$f(\phi, \nabla\phi, \nabla^2\phi, \dots) = f_0(\phi) + \sum_i \frac{\partial f}{\partial \frac{\partial\phi}{\partial r_i}} \frac{\partial\phi}{\partial r_i} + \sum_{ij} \frac{\partial f}{\partial \frac{\partial^2\phi}{\partial r_i \partial r_j}} \frac{\partial^2\phi}{\partial r_i \partial r_j} + \frac{1}{2} \sum_{ij} \frac{\partial^2 f}{\partial \frac{\partial\phi}{\partial r_i} \partial \frac{\partial\phi}{\partial r_j}} \frac{\partial\phi}{\partial r_i} \frac{\partial\phi}{\partial r_j} + \dots \quad (3.3)$$

Using the same argument as in Eq. (3.1), the odd terms in r_i vanish for an isotropic medium, truncating Eq. (3.3) to:

$$f(\phi, \nabla\phi, \nabla^2\phi, \dots) = f_0(\phi) + \kappa_1 \nabla^2\phi + \kappa_2 (\nabla\phi)^2 + \dots, \quad (3.4)$$

with $\kappa_1 = \frac{\partial f}{\partial \nabla^2\phi}$ and $\kappa_2 = \frac{\partial^2 f}{\partial |\nabla\phi|^2}$. Integrating Eq. (3.4) over a volume V and applying the divergence theorem, the total free energy functional is obtained:

$$\mathcal{F}[\phi(\mathbf{r}, t)] = \int_V f(\phi, \nabla\phi, \nabla^2\phi, \dots) dV = \int_V f_0(\phi) + \frac{\kappa}{2} (\nabla\phi)^2 + \dots dV, \quad (3.5)$$

where $\frac{\kappa}{2} = -\frac{d\kappa_1}{d\phi} + \kappa_2$. Equation (3.5) is also called Ginzburg-Landau free energy, tracing back to the 1950 Ginzburg-Landau paper [128]. The gradient term $\kappa(\nabla\phi)^2$ in Eq. (3.5) models the surface energy of the interfaces separating the phases and, thus, prevents discontinuities. It can also be interpreted as an additional energetic cost due to a variation of the order parameter.

3.3 Cahn-Hilliard equation (“Model B”)

As the total concentration of the two substances remains unchanged during the phase separation, the order parameter must be conserved. The dynamics of such a system is described by the so-called *Model B* [129], which implies the convergence of the conserved order parameter towards equilibrium with a rate proportional to the divergence of its current:

$$\frac{\partial\phi(\mathbf{r}, t)}{\partial t} = -\nabla \cdot \mathbf{j}(\mathbf{r}, t). \quad (3.6)$$

The current $\mathbf{j}(\mathbf{r}, t)$ is proportional to the gradient of the chemical potential μ

$$\mathbf{j}(\mathbf{r}, t) = -M \nabla \mu(\mathbf{r}, t), \quad (3.7)$$

where M is the inter-diffusion constant of the mixture and μ can be obtained from

$$\mu(\mathbf{r}, t) = \frac{\delta \mathcal{F}}{\delta \phi}, \quad (3.8)$$

with the functional derivative $\frac{\delta \mathcal{F}}{\delta \phi(\mathbf{r})} = \frac{\partial f}{\partial \phi} - \nabla \cdot \frac{\partial f}{\partial \nabla \phi}$. Combining Eqs. (3.6), (3.7), and (3.8) and inserting the Ginzburg-Landau free energy (Eq. (3.5)) yields

$$\frac{\partial \phi(\mathbf{r}, t)}{\partial t} = M \Delta (a(T - T_c)\phi + b\phi^3 - \kappa \nabla^2 \phi), \quad (3.9)$$

which is known as *Cahn-Hilliard equation* [127, 130] (or Model B). The Cahn-Hilliard equation, derived by John W. Cahn and John E. Hilliard, is a mathematical equation capable of describing the process of phase separation of a binary mixture, where the two components of the fluid, which are described by the order parameter ϕ , can spontaneously separate and form distinct domains of each component.

3.4 Feedback driven “active droplids”

In **Paper III**, we demonstrate a possibility to implement a simple and controllable system of colloids and a “responsive environment”, creating a versatile feedback loop. In collaboration with Giovanni Volpe and Falko Schmidt from University of Gothenburg, we experimentally realized and theoretically modeled a system of colloidal particles, exposed in a critical mixture. More specifically, we used two types of hydrophilic particles: light-absorbing and non-absorbing particles. The non-absorbing particles are less hydrophilic than the absorbing ones. These particles are immersed in a near-critical water–2,6-lutidine mixture, which has a critical lutidine composition $c_c^L = 0.286$ and a critical temperature at $T_c = 34.1^\circ\text{C}$. The temperature of the mixture is maintained near-critical at $T_0 = 32.5^\circ\text{C}$ using a heatbath. Under illumination (wavelength $\Lambda = 1070\text{ nm}$, intensity $I = 142\ \mu\text{W}\mu\text{m}^{-2}$), the light-absorbing particles then absorb the light and convert it into heat. As a result, the particles raise the temperature of the surrounding liquid just above T_c and induce local phase separation of water and lutidine. Due to the phase segregation and the hydrophilicity of the particles, water accumulates in the vicinity of the light-absorbing particles. From the point of view of neighboring non-absorbing particles, the symmetry of the environment is broken, since the water concentration increases in the direction of a light-absorbing particle. Due to the generated local gradient in the composition, the hydrophilic non-absorbing particles experience a phoretic force pointing in the direction of the light-absorbing particles. Notably, this attractive force is non-reciprocal and causes the non-absorbing particles to move towards the light-absorbing particles and to push them forward. “Active molecules” are formed, which move ballistically through the environment and coalesce into active

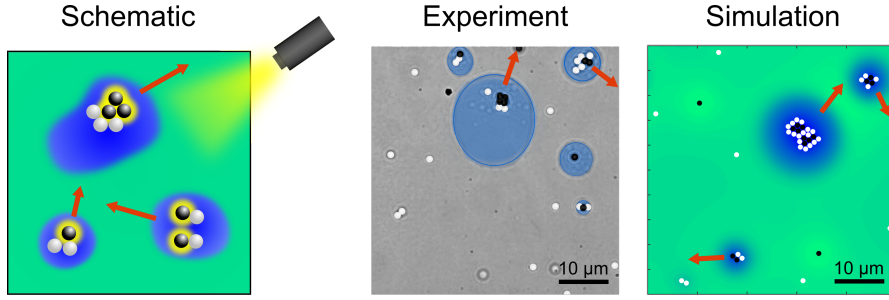


Figure 3.3: **Formation of active droplids.** Schematic and snapshots from the experiment and the simulation. Reproduced from [119]. CC BY 4.0.

clusters with multiple particles [131]. As the number of light-absorbing particles increases locally over time, the temperature significantly exceeds T_c and a water droplet forms, enclosing the entire particle cluster. Remarkably, the active cluster of particles transfers its motility to the droplet and acts like an internal motor. This happens because the light-absorbing particles inside the droplet continuously phase separate their environment, causing the droplet to follow the particle motion. In this way, not only do the particles influence their environment by inducing phase separation, but the environment also acts back on the particles by enabling their motion and encapsulating the particles inside a droplet. We name these novel structures of droplets with a colloidal motor “active droplids” [119]. Once formed, the active droplids move, collide and merge with each other, growing in size over time (see Fig. 3.3). Remarkably, size and speed of the active droplids can be controlled by the laser intensity.

In the simulation model we consider N overdamped colloidal particles at position \mathbf{r}_i , where $i = 1, \dots, N$. To model the phase separation dynamics of this specific system, we extend the Cahn-Hilliard equation taking into account an inhomogeneous temperature distribution $T(\mathbf{r})$. The temperature field produced by the light-absorbing particles results from the heat equation

$$\dot{T}(\mathbf{r}, t) = D_T \Delta T + k_0 \sum_{\text{absorb.}} \delta(\mathbf{r} - \mathbf{r}_i) - k_d (T - T_0), \quad (3.10)$$

where D_T is the diffusion constant of the temperature field, k_0 is the strength of the heat production and k_d is the heat dissipation due to the coupling of the sample to an external water heatbath. Subsequently, the inhomogeneous temperature field is coupled to the Cahn-Hilliard equation:

$$\begin{aligned} \dot{\phi}(\mathbf{r}, t) = & M \Delta \left(a(T - T_c) \phi + b \phi^3 - \kappa \nabla^2 \phi \right. \\ & \left. + A_a \sum_{\text{absorb.}} \delta(\mathbf{r} - \mathbf{r}_i) + A_{na} \sum_{\text{non-abs.}} \delta(\mathbf{r} - \mathbf{r}_i) \right). \end{aligned} \quad (3.11)$$

Here, we describe the effective accumulation of water near the hydrophilic particles by an additional source term for the solvent-composition at the position of each particle. Since the non-absorbing particles are less hydrophilic than the absorbing particles, the coefficients A_a (absorbing) and A_{na} (non-absorbing) can be chosen to account for the different hydrophilicities of the two types of particles. Similar as in Chapter 2, we model the dynamics of the colloids as Brownian particles using Langevin equations

$$\gamma \dot{\mathbf{r}}_i^s(t) = \beta_s \nabla \phi + \alpha_s \nabla (\nabla \phi)^2 - \nabla_{\mathbf{r}_i} V + \sqrt{2D} \gamma \boldsymbol{\eta}_i^s, \quad (3.12)$$

where D is the translational diffusion coefficient, γ is the Stokes drag coefficient, $\boldsymbol{\eta}_i^s(t)$ represents Gaussian white noise with zero mean and unit variance, and V accounts for steric repulsions among the colloids (see Chapter 7 for details on the implementation). The first two terms on the right side of Eq. (3.12) describe the coupling of the particles to the composition field. On the one hand, this is the attraction of the hydrophilic particles towards water-rich regions, described by the first term with $\beta < 0$ (because $\phi < 0$ corresponds to a higher water concentration, as described above). On the other hand, the second term describes a movement towards the water-lutidine interface, which mainly affects the weakly hydrophilic non-absorbing particles. At high temperatures, the active cluster inside the droplet dissolves and the non-absorbing particles move towards the water-lutidine interface to reduce the interfacial area of the system and hence the total interfacial free energy. See **Paper III** for further information on the simulation model, a detailed explanation of the experimental setup, and a quantitative analysis of the active droplid dynamics.

4 Acoustic crystallization of colloidal monolayers

4.1 Polycrystalline structures

Colloidal assemblies also serve as ideal model systems to study crystallization phenomena [132–137]. In a further collaboration, a simple and generic method was investigated to efficiently anneal two-dimensional (2D) colloidal crystals at liquid interfaces.

A small microscopic crystal within a polycrystalline structure is called *grain* (or *crystallite*). Each grain is a region with a periodic arrangement of building blocks and a certain crystallographic orientation. Polycrystalline materials, or polycrystals, consist of many crystallites of different sizes and orientations, each separated by so-called *grain boundaries*, 2D defects in the crystal structure. Most inorganic materials have a polycrystalline structure, like rocks, common metals or ice. For example, when water begins to freeze, small ice crystals form and grow until they fuse together. The separated highly ordered small crystals with random orientations then form a polycrystalline structure, which macroscopically does not show a periodic pattern. An important property of a material is the average size of the grains, as this can determine the properties of the material. A small grain size, for example, is accompanied by a higher ductility of the material. In contrast, a large grainsize with high order layers leads to increased electrical and thermal conductivity and is necessary for functional surfaces, such as photonic [138], phononic [139, 140] or plasmonic materials [141, 142]. Consequently, methods to control the grain size as well as an understanding of the underlying growth processes are of enormous interest.

By external stimuli, such as vibrations [143, 144], increase in temperature [145], movement of active particles [146] or electric fields [147], the so-called *grain coarsening*, i.e., the growth and fusion of grains in a polycrystalline material, can be enhanced. Upon stimulation, dislocations and vacancies at the disordered grain boundaries can rearrange more rapidly, allowing to efficiently anneal defects and generate grain boundary movement. Overall, this leads to enhanced grain growth and a higher ordered crystal structure.

4.2 Sound induced monolayer annealing

In collaboration with Nicolas Vogel's group from Friedrich-Alexander University Erlangen-Nuremberg and Liesbeth Janssen from Eindhoven University of Technology, we investigated a simple monolayer annealing setup in which it is possible to efficiently anneal two-dimensional colloidal crystals at liquid interfaces using a conventional loudspeaker. The acoustic stimuli from the loudspeaker generate standing waves at the interface, which generates additional surface area. This allows local reorganization of the colloidal particles into a structure of higher order. Remarkably, the grain size can be controlled by the amplitude and frequency of the loudspeaker, as well as the particle density.

Using a simple generic simulation model, we can accurately unveil the dependence of the grain size on amplitude, frequency, and particle density. In addition, the simulations allow us to track the particle trajectories, giving us a better understanding of the exact annealing process. We found that the main mechanism is given by collective rotations of particle groups around fixed centers (see Fig. 4.1). The exact process of rotation depends on the orientation angle mismatch between the grains.

During the completion of this thesis, the manuscript about this work is still in preparation. Nevertheless, since the simulation model introduces a new method to model the additional surface area available to particles during acoustic stimuli and allows to unveil the mechanism underlying the annealing process, I will briefly explain the simulation details in the following section.

4.2.1 Simulations of the acoustic annealing of two-dimensional colloidal crystals

In our simulation model, we consider an ensemble of N overdamped colloidal particles at positions \mathbf{r}_i in two spatial dimensions, where $i = 1, \dots, N$ is the particle index. The particle coordinates are considered in the domain from $-L/2$ to $L/2$ in both directions with box length L and periodic boundary conditions. The dynamics of the particle motion is described by the following Langevin equations

$$\dot{\mathbf{r}}_i(t) = \sqrt{2D}\boldsymbol{\eta}_i(t) - \nabla_{\mathbf{r}_i}V(\mathbf{r}_1, \dots, \mathbf{r}_N)/\gamma, \quad (4.1)$$

where γ the Stokes friction coefficient, D is the translational diffusion coefficient (both assumed to be equal for all particles) and $\boldsymbol{\eta}_i$ represents unit variance Gaussian white noise with zero mean. The strong repulsions among particle pairs are modeled using a repulsive Yukawa pair potential $V(\mathbf{r}_1, \dots, \mathbf{r}_N) = \frac{1}{2} \sum_{i,j \neq i} V_{ij}(\mathbf{r}_i, \mathbf{r}_j)$, where $V_{ij}(\mathbf{r}_i, \mathbf{r}_j) = V_0 \frac{\exp(-r_{ij}/\lambda)}{r_{ij}}$. Here, $r_{ij} = \|\mathbf{r}_i - \mathbf{r}_j\|$ is the distance between particles i and j , V_0 is the amplitude of the potential and λ is a screening length. To model the generated additional surface area upon acoustic stimulation, the simulation box

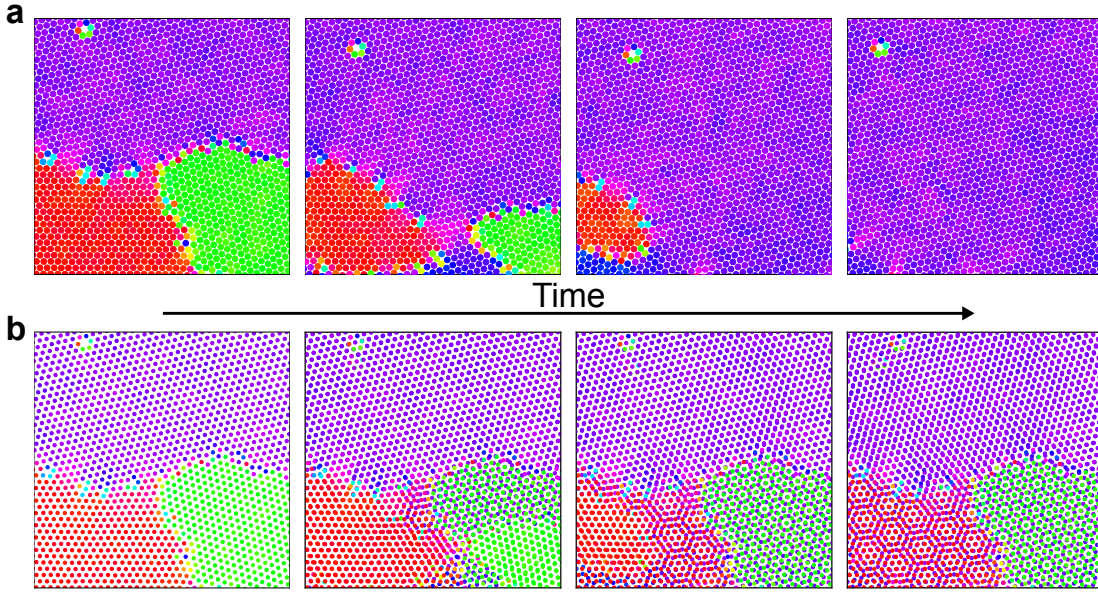


Figure 4.1: **Exemplary snapshots from the simulations.** **a** Evolution of grain sizes during the annealing process over time. The coloration of the individual particles indicates the orientation, i.e., their arrangement to neighboring particles, and allows detection of different grains. **b** Superposition of the particle positions, in each case of the initial configuration (left panel from (a)) and the particle positions at later times. In the lower part of the simulation box, a typical moiré pattern can be observed, resulting from the characteristic particle motion during the annealing process, i.e., the rotation of particle groups around a center particle.

length $L(t)$ is periodically expanded and shrunk with the frequency f associated with the loudspeaker. The time-dependent box length reads

$$L(t) = L_0(1 + A(1 - \cos(2\pi ft)) , \quad (4.2)$$

ranging between the minimum value of the initial box length L_0 and the maximal possible box length $L_0(1 + 2A)$ determined by the amplitude A .

In each simulation step of time Δt , two subsequent moves are applied for given particle positions $\mathbf{r}_i(t)$. First, the particle positions are updated to $\mathbf{r}_i^{(1)}$, by numerically solving Eq. (4.1) using an Euler integration scheme [148]. Second, the particle positions $\mathbf{r}_i^{(1)}$ are scaled with the simulation box length at time $t + \Delta t$ as:

$$\mathbf{r}_i(t + \Delta t) = \frac{L(t + \Delta t)}{L(t)} \mathbf{r}_i^{(1)} . \quad (4.3)$$

These two steps are performed repeatedly to generate particle trajectories.

Figure 4.1 shows typical simulation snapshots at different times during the annealing process. The coloration indicates which particles belong to the same grain. A point defect, or more precisely a vacancy, can be detected in the upper part of the panels. Such defects are annealed by movement and repositioning of neighboring particles until the defect reaches a grain boundary. In the lower part of the panels, merging of entire grains to remove grain boundaries can be observed. Such merging results from the transfer of particles from one grain to another. This process occurs in several steps as individual groups of particles sequentially rotate around a fixed center particle. The time sequence of these realignments as well as the rotating shift of particles can be seen in Fig. 4.1b.

5 Machine learning for active matter

In recent years, machine learning methods have become increasingly important. On the one hand, this results from the availability of vast amounts of data and, on the other hand, from a permanent increase in computer resources and possibilities to store and analyze these data. The application of machine learning has also gained popularity in the natural sciences, specifically in the field of active matter [149, 150]. For example, machine learning techniques are applied in digital microscopy to characterize and track different types of matter such as active particles or droplets [119, 151]. Using convolutional neural networks, complex pattern formations can be investigated and classified [152]. Furthermore, active particles can be equipped with artificial intelligence and used as microrobots, e.g., for learning collective behavior [153, 154], exploring and navigating in complex environments [155–159], delivering drugs [160, 161] or environmental remediation [162].

In **Paper IV**, a system of particles in a complex environment is studied that use machine learning to develop a strategy for adapting their collective behavior. First, I will present some basic concepts of neural networks in Section 5.1 and explain the used machine learning algorithm in Section 5.2 to finally come back to its application in the paper in Section 5.3.

5.1 Artificial neural networks

When talking about a neural network, one might initially think of a network of neurons in the nervous system of a living being. Although the name is biologically inspired, in the context of artificial neural networks it refers to a model for processing information [163]. Basically, a neural network is a large universal function approximator or, more precisely, a general function $F_{\theta}(x)$ with parameters $\theta = (\theta_1, \theta_2, \dots)$, which is supposed to approximate a certain (often unknown) function F using many training examples. The artificial neural network consists of individual units called *neurons* that hold a scalar value y and are located on *layers* that are connected to each other. Signals can be transmitted between neurons via these connections, allowing to pass information through the neural network. This signal is nothing else than a real number, which is received by a neuron, evaluated by a non-linear function and transferred to the next neuron. Hence, the value of a

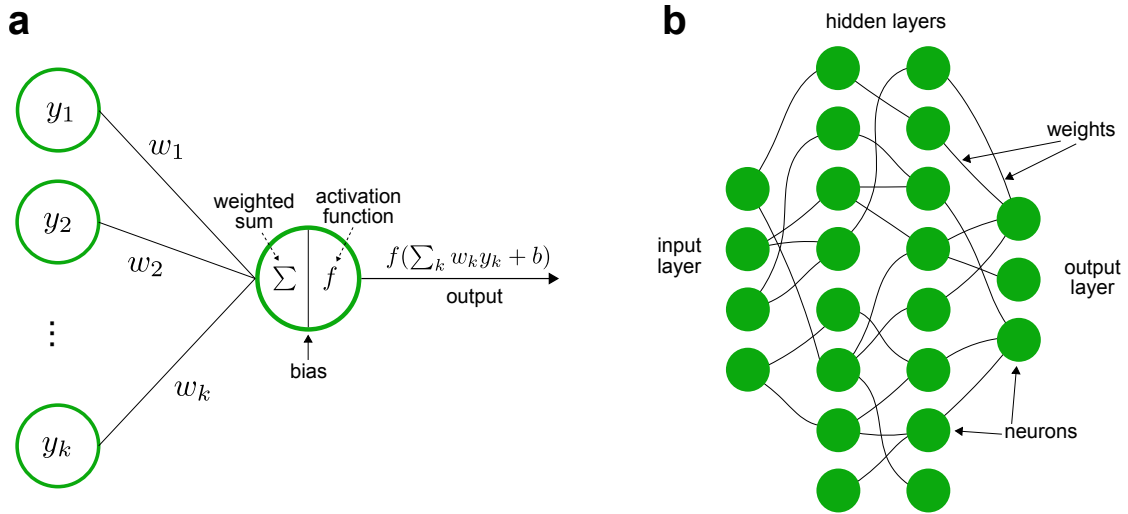


Figure 5.1: **Schematic of a dense neural network.** **a** Illustration of a typical artificial neuron operation. **b** Structure of an artificial dense neural network with two hidden layers.

neuron is computed by the previous layer’s values of the network. In addition, an offset b , called *bias*, is added to each value of a neuron and the connections between neurons are weighted with so-called *weights* w (see Fig. 5.1). To approximate an arbitrary function sufficiently well, a large number of neurons (and layers) may be required. The value of a neuron l in layer $n + 1$ is given by:

$$y_j^{(n+1)} = f\left(\sum_k w_{jk}^{(n+1,n)} y_k^{(n)} + b_j^{(n+1)}\right), \quad (5.1)$$

where the biases $b_j^{(n+1)}$ determine the offset of neuron j in layer $n + 1$ and the weights $w_{jk}^{(n+1,n)}$ specify the strength of the connection between neuron j in layer $n + 1$ and neuron k in layer n . The function f is a non-linear *activation function* that is equally applied to all neurons of the same layer. A commonly used activation function is the so-called Rectified Linear Unit (“ReLU”) function, which is piecewise linear with $f(x) = 0$ for $x < 0$ and $f(x) = x$ for $x \geq 0$. Other used activation functions are for example the smoothed step-function “sigmoid” or the tangent hyperbolic function. All values of the network are obtained by starting from the values in the input layer and computing Eq. (5.1) for all subsequent layers. If a network consists of many hidden layers, i.e., many layers between the input and the output layer, it is called a *deep neural network*. The use of several layers form a more extensive inner structure and increase the efficiency of the network. In order to measure the accuracy of the network and to be able to adjust the network parameters (weights and biases) during training, a *cost function* is introduced, which identifies the deviation of the network output $F_\theta(x)$ to the approximated

function $F(x)$. The cost function describes how well the neural network predicts the expected output. In the simplest case, the square of the deviation is used, allowing to write a cost function depending on the weights and biases as:

$$C(\theta) = \frac{1}{2}(F_\theta - F)^2 . \quad (5.2)$$

Then, the idea is to use gradient decent to find the parameters θ for which the cost function becomes minimal. For this purpose, the parameters are shifted along the negative gradient of the cost function:

$$\delta\theta_l = -\eta \frac{\partial C(\theta)}{\partial \theta_l} , \quad (5.3)$$

where η is called the *learning rate*. Applying the chain rule, we obtain:

$$\frac{\partial C(\theta)}{\partial \theta_l} = \sum_j ([F_\theta]_j - [F]_j) \frac{\partial [F_\theta]_j}{\partial \theta_l} , \quad (5.4)$$

where $[F_\theta]_j$ corresponds to the value $y_j^{(N)}$ of the respective neuron in the output layer N . Using Eq. (5.1) and applying the chain rule again yields:

$$\frac{\partial y_j^{(n)}}{\partial \theta_l} = f'(z_j^{(n)}) \frac{\partial z_j^{(n)}}{\partial \theta_l} , \quad (5.5)$$

where $z_j^{(n)} = \sum_k w_{jk}^{(n,n-1)} y_k^{(n-1)} + b_j^{(n)}$. If θ_l is not in layer n this leads to:

$$\frac{\partial y_j^{(n)}}{\partial \theta_l} = f'(z_j^{(n)}) \sum_k w_{jk}^{(n,n-1)} \frac{\partial y_k^{(n-1)}}{\partial \theta_l} . \quad (5.6)$$

As can be seen in Eq. (5.6), the layered structure of the artificial neural network results in a recursivity that allows to determine all necessary derivatives starting from the output layer N up to the layer with the respective θ_l . Once reaching layer \hat{n} , where the θ_l is located, one obtains $\frac{\partial z_j^{(\hat{n})}}{\partial \theta_l} = y_l^{(\hat{n}-1)}$ (if $\theta_l = w_{jl}^{(\hat{n},\hat{n}-1)}$) or $\frac{\partial z_j^{(\hat{n})}}{\partial \theta_l} = 1$ (if $\theta_l = b_j^{(\hat{n})}$), respectively. This is called the *backpropagation algorithm* and is the essential step when using neural networks [164].

5.2 Reinforcement learning: Q-learning

As previously described, knowledge about the function F to be approximated is a crucial point in the learning process of the neural network. In the case explained so far, F was always known, allowing the cost function in Eq. (5.2) to be computed.

Because of this knowledge of the “correct answer” that the network should reproduce, this scenario is called *supervised learning*. However, a further field of machine learning includes scenarios with unknown functions F . One imagines a robot (called an *agent* in this context) in an environment in which it moves and with which it interacts. At each time step of a sequence $t = 1, 2, 3, \dots$ the agent observes a *state* s_t and takes an *action* a_t . By giving the agent a reward (or punishment) for an action it performs, it learns a strategy predicting the most profitable action based on the state it is in. The mapping from state to action is called *policy*. This method of independent learning of a strategy through feedback from the environment belongs to the field of *reinforcement learning* (RL) [165–167].

Basically, there are two main types of RL methods, value-based and policy-based methods. All other methods can either be traced back to one of them or are a combination of them (e.g., like *actor-critic* RL methods) [168, 169]. Value-based methods approximate a so-called *value function*, which maps a state-action pair to a value. The better the action, the larger the value. With value-based methods no explicit policy is learned, the policy depends on the value-function itself. Accordingly, value-based methods create a deterministic policy that can be implicitly derived from the value function. Policy-based algorithms try to create an explicit representation of a (stochastic) policy $\pi_\theta(a|s)$, which provides a probability for an action $a_t = a$ in a state $s_t = s$.

In the following, I will elaborate on a value-based RL approach called *Q-learning* [170], since I used this method in **Paper IV**. The approach of this method is to introduce a so-called *quality-function* $Q(s, a)$, which indicates the expected future return when performing some action a in some state s . Here, a “discounted” future reward is calculated as $R_t = r_t + \gamma r_{t+1} + \dots + \gamma^{T-t} r_T = r_t + \gamma R_{t+1}$, where r_t is the reward at time step $t = 0, 1, 2, \dots, T$ and the discount factor $0 \leq \gamma < 1$ allows to value short-time rewards more than long-term ones. More precisely, the *Q-value* of a state-action pair is then given as the expectation value of the return over all trajectories that start in (s, a) and follow the policy π :

$$Q^\pi(s, a) = \mathbb{E}_\pi[R_t | s_t = s, a_t = a] . \quad (5.7)$$

In the same way, a value for a state s can be given as the expected discounted return received by an agent in state s following policy π :

$$V^\pi(s) = \mathbb{E}_\pi[R_t | s_t = s] . \quad (5.8)$$

Naturally, the *Q*- and *V*-values are related, meaning that the value of a state depends on the possible actions in that state. The value of a state s is therefore given by the value $Q^\pi(s, a)$ weighted by the probability that action a is chosen: $V^\pi(s) = \sum_{a \in \mathcal{A}} \pi(a|s) Q^\pi(s, a)$. For a deterministic policy (as in *Q-learning*), the value of a state is equal to the *Q*-value of the action selected by the policy.

Inserting R_t in Eq. (5.7) and using the law of iterated expectation yields the *Bellmann equation* for Q^π :

$$\begin{aligned} Q^\pi(s, a) &= \mathbb{E}_\pi[R_t | s_t = s, a_t = a] \\ &= \mathbb{E}_\pi[r_t + \gamma R_{t+1} | s_t = s, a_t = a] \\ &= \sum_{s'} P(s' | s, a) \sum_{a'} \pi(a' | s') [r(s, a, s') + \gamma \mathbb{E}_\pi[R_{t+1} | s_{t+1} = s', a_{t+1} = a']] \\ &= \sum_{s'} P(s' | s, a) [r(s, a, s') + \gamma \sum_{a'} \pi(a' | s') Q^\pi(s', a')], \end{aligned}$$

where $P(s' | s, a)$ is given by the dynamics of the environment and denotes the probability of the transition into state s' with expected reward $r(s, a, s')$ when performing action a in state s . For the optimal policy π^* , the expected return is maximal for each possible state-action pair (s, a) : $Q^{\pi^*}(s, a) = \max_{\pi} Q^\pi(s, a)$. In Q-learning, the optimal policy is deterministic and *greedy*, which means that always the action with the highest Q-value is taken. Substituting the optimal Q-function into the Bellmann equation results in:

$$Q^{\pi^*}(s, a) = \sum_{s'} P(s' | s, a) [r(s, a, s') + \gamma \max_{a'} Q^{\pi^*}(s', a')]. \quad (5.9)$$

In practice, one can use sample-based methods such as temporal difference methods and use the following update rule:

$$Q^\pi(s, a) \leftarrow Q^\pi(s, a) + \alpha (r(s, a, s') + \gamma \max_{a'} Q^\pi(s', a') - Q^\pi(s, a)). \quad (5.10)$$

Here, α is the learning rate, a small positive number, which relates to the speed of improvement. At the beginning of the learning process, exactly those Q-values in state s are high which provide an immediate reward. During learning with many training trajectories, the update rule causes the high Q-values in state s to affect neighboring states s' , which can be reached quickly from state s . From there, this in turn affects neighboring states of s' and the Q-values propagate through the state space.

Depending on the specific problem, the number of state-action pairs can quickly become very large. When coming back to the example of the robot in an environment, the state is defined as the current position of the robot, possibly along with additional information describing the environment locally. In each state, the robot has a variety of possible actions, such as changing the position, altering the environment, etc. Evaluating all state-action pairs sufficiently often during training is far too expensive in this situation. However, in such cases, the Q-table $Q(s, a)$ can be approximated by a neural network, which is called *Deep Q-Learning*. During training, the update rule in Eq. (5.10) is then applied by fitting the output of

the neural network to $r(s, a, s') + \gamma \max_{a'} Q^\pi(s', a')$. For certain situations, the *deep Q-Network* (DQN) algorithm can be an efficient method, especially by using further techniques to improve the approximating network, such as *double DQNs* [171], *dueling DQNs* [172], or *prioritized experience replay* [173].

5.3 Communication strategies of smart active agents

A variety of microorganisms communicate with each other by producing signaling molecules to which others respond (quorum sensing). Motivated by this, in a further work we modeled communicating active agents equipped with artificial intelligence. We studied a system of active agents whose goal is to consume a nutrient field as efficiently as possible. By using a reinforcement learning algorithm the agents learn an optimal strategy to cooperatively consume a nutrient field. Depending on the particle density and the rate of consuming nutrients, the particles apply different strategies that determine their orientation along the nutrient field and the self-produced quorum sensing field. These can be classified into three strategies: a “uniting strategy”, where all agents cooperatively accumulate together; a “spreading strategy”, where agents stay separated from each other; and an “adaptive strategy”, where the agents adaptively decide whether to follow or stay away from others. These results demonstrate the potential of active systems equipped with artificial intelligence for future applications and could be applied, e.g., to help microrobots in finding efficient strategies to decontaminate polluted water.

For a detailed explanation of the RL algorithm and the learned strategies see **Paper IV**.

6 Modeling contagion dynamics

Due to the worldwide outbreak of the disease COVID-19 caused by the coronavirus SARS-CoV-2 [174–176], there has been an immense increase in the research of infectious diseases and pandemics worldwide. This research involves not only experts in virology, biology, medicine or pharmacy, but also physicists who develop and study mathematical models to understand the spread of a pandemic. In particular, the field of statistical physics, where systems of very large numbers of particles are studied, provides well-tested theories and methods, and is therefore closely related to the modeling of large crowds of people and the transmission of infectious diseases.

For example, ordinary diffusion equations combined with the *SIR model* were used to study the spread of plague in medieval Europe [177]. The SIR model is a classic compartmental model in epidemiology that divides the population into certain groups and models the total number of individuals in each group [178–181]. The name originates from the classification of the population into **S**usceptibles, **I**nfected and **R**ecovered. Other physical modeling approaches use more sophisticated “agent-based” models that describe the behavior of individuals and provide a more accurate picture of contagion dynamics [182–185]. Prompted by the question of effective measures that help against the pandemic, the effects of social distancing and lockdowns have also recently been studied [186, 187]. Another newly presented model uses dynamical density functional theory (DDFT) [188, 189] to describe a society of social distancing individuals as a system of particles with repulsive interactions that can infect each other in the form of a “SIR-DDFT model” [190].

In **Paper V** and **Paper VI**, we similarly use concepts from statistical physics and study the spread of a pandemic in different scenarios. In **Paper V**, we introduce an individual-based model, which we use to develop a strategy for optimal vaccination distribution in space and time. In **Paper VI**, we use the classical SIR model and generalize it to account for mutations that lead to repeatedly occurring new strains. Before discussing this work in more detail, I give a brief introduction to mathematical modeling of pandemics and the well-known SIR model.

The SIR model is a classical approach to describe the spread of infectious diseases. In addition to the SIR model, there are a number of variations and extensions that, for example, include exposed persons, i.e., those who are infected but not yet infectious (SEIR model) [191], consider the number of deaths (D) separately (SIRD model) [192], or describe the spread of diseases without the development of immunity (SIS model) [193]. Typically, the different variables describe the total

number of individuals in each group, and the model consists of a combination of ordinary differential equations. Assuming that each person can be infected only once and then either becomes immune or dies, and that infected persons are immediately infectious (unlike in the SEIR model), the SIR model reads as:

$$\begin{aligned}\dot{S}(t) &= -\beta \frac{SI}{N}, \\ \dot{I}(t) &= \beta \frac{SI}{N} - \gamma I, \\ \dot{R}(t) &= \gamma I.\end{aligned}\tag{6.1}$$

Here $S(t)$ denotes the number of healthy individuals not yet infected, $I(t)$ the number of infected and $R(t)$ the number of removed or resistant individuals. The total number of individuals remains constant : $N = S + I + R$. β is the number of new infections per time unit caused by an infected individual, where βSI is the so-called *bilinear incidence rate* [194]. $1/\beta$ thus describes the mean time between two contagious contacts. The rate at which infected persons recover or die is given by γ . The *basic reproduction number*, which is a epidemiological measure of the spread of an infectious disease, is here $R_0 = \frac{\beta}{\gamma}$. More precisely, R_0 describes the expected number of further contagions caused by one infected person within its disease duration (in a fully susceptible population). At the beginning of a pandemic, one can approximate $N \approx S$ (all individuals are healthy and not immune) where the change in infections in Eq. (6.1) is given by: $\dot{I} = (\beta - \gamma)I$. If the number of infections increases, i.e., if $\dot{I} > 0$, then $\beta > \gamma$ and $R_0 = \frac{\beta}{\gamma} > 1$. Note, that this then predicts an exponential growth in infection numbers. If the number of susceptibles decreases in the further course of the pandemic, the number of infected individuals continues to increase when $R_0 \frac{S}{N} > 1$ and finally saturates once S reaches $\frac{N}{R_0}$. For the SARS-CoV-2 coronavirus, for example, the reproduction number is estimated to be between three and four, meaning that two-thirds to three-quarters of the population must be infected or resistant before so-called ‘‘herd immunity’’ is achieved [195].

6.1 Strategic vaccine distribution

In mid-June 2020, the available measures to contain the pandemic were contact-tracing [196], social-distancing [197–199], and testing [200], and the hope was for rapid development of an effective vaccine to achieve herd immunity more quickly. However, even after development and admission, it takes a long time before a sufficient supply is available to offer a vaccination to the entire population. Therefore, an important question is what strategy to use to efficiently distribute a vaccine that is initially available in limited quantities. Existing vaccination guidelines mainly focus on a demographic distribution practice and the question

to whom vaccine should be provided first (e.g., prioritizing individuals of certain age or risk groups). Encouraged by this, we raised the question of an optimal distribution strategy of vaccines in space and time [201].

Our simulation model is based on Brownian agents whose random motion is described via Langevin equations. We assume that infected agents can infect others within a radius R_c . Furthermore, from the Brownian agents we derive a (nonuniform) statistical mean-field model that allows a continuous description of the contagion dynamics. This model can be seen as an generalization of the SIR or SEIR model to inhomogeneous situations with the consideration of possible immunization by vaccination. We divide the whole population into six categories: susceptible $S(\mathbf{r}, t)$, exposed $E(\mathbf{r}, t)$ (infected but not yet diseased), infected but free of symptoms (or having mild symptoms) $F(\mathbf{r}, t)$, infected with symptoms $I(\mathbf{r}, t)$, removed (vaccinated or recovered) $R(\mathbf{r}, t)$, and victims $V(\mathbf{r}, t)$.

For several parameters, such as the initial reproductive number or the vaccination rate, we examined the evolution of the number of infections and deaths over time and compared different distribution strategies. We found that the optimal distribution does not only depend on individual-based factors but also on a spatiotemporal distribution (i.e., where and when to provide vaccines). In these strategies, the vaccine distribution is controlled by the bilinear incidence rate βSI , rather than by population density. For all considered parameters, an “infection-weighted” strategy, in which the available vaccine is distributed proportionally to the locations with the highest bilinear incidence rate, generally results in a lower number of deaths than a demographic distribution practice, in which vaccine doses are distributed proportionally to population density [202]. This is particularly efficient if the regions with the highest bilinear incidence rates are sequentially prioritized, i.e., only those regions (e.g., cities) with the highest number of new infections in a certain time frame receive all available vaccine doses (“focusing strategy”).

See **Paper V** for a detailed evaluation of the different strategies, especially for different initial reproduction numbers and vaccine production rates, as well as taking into account additional social-distancing rules and delays in registration of new cases.

6.2 Mutation induced infection waves

During a pandemic and the ongoing vaccination of the population, which can take several months or years until herd immunity is achieved, the occurrence of a mutation can have an important influence on the course of the pandemic [203–207]. This can lead to a competition between vaccination and the emergence of new, potentially more contagious mutations. Not only regarding the coronavirus, but also for future pandemics, the development of powerful models that can simulate such scenarios is essential. In another work, we therefore generalized the popular

SIR model to account for mutations which lead to repeatedly occurring new strains and investigate their consequences on the pandemic, e.g., also in combination with nonpharmaceutical interventions and vaccinations [208].

In our model, we allow for the continuous occurrence of new strains depending on a certain mutation rate. The fraction of susceptible and recovered individuals is denoted by S and R , respectively, and the fraction of individuals infected with strain n is given by I_n :

$$\begin{aligned}\dot{S} &= - \sum_n \beta_n S I_n, \\ \dot{I}_n &= \beta_n S I_n - \gamma I_n, \\ \dot{R} &= \sum_n \gamma I_n.\end{aligned}\tag{6.2}$$

Here β_n is the infection rate of strain n , which is randomly chosen from a certain characteristic distribution, and $1/\gamma$ is the average disease duration. By averaging over many strains, the model described by Eqs. (6.2) can be coarse grained, yielding the following effective model:

$$\begin{aligned}\dot{S} &= -\beta(t, I) S I, \\ \dot{I} &= \beta(t, I) S I - \gamma I, \\ \dot{R} &= \gamma I.\end{aligned}\tag{6.3}$$

Here, I describes the total number of infections of all strains and $\beta(t, I)$ is the averaged infection rate (the specific dependence on infection numbers depends on the underlying mutational dynamics). This model allows the prediction of the averaged or most likely outcome of the infection numbers. Using a numerical evaluation of the multi-strain model (Eqs. (6.2)) and an analytical prediction based on the mean-field model (Eqs. (6.3)), we investigated the impact of mutations on the course of the pandemic.

First, we studied the direct effect of mutations by assuming that mutations and new strains emerge at a constant rate μ . Second, we tried to estimate indirect effects through a self-amplification of mutations, assuming that (i) new mutations can serve as seeds for further, possibly more contagious, mutations and (ii) mutation rates are higher when infection numbers are high. To model this, we used a mutation rate that depends on current infection numbers $\mu(I)$.

A general finding from the models is that mutations can lead to an explosive increase in infection numbers, which, in contrast to the common SIR model, is characterized by a super-exponential growth. If herd immunity is achieved during the course of the pandemic, i. e., if $R < 1$, new mutations can induce a rebound in the reproduction number, leading to a new wave of infections. This process can even repeat several times over the course of the pandemic, leading to a pattern of multiple

infection waves. If the mutation rate also increases with the number of infections, an even stronger effect occurs. New mutations emerge at a self-accelerating rate and infection numbers grow extremely rapidly, making it increasingly difficult for the population to achieve herd immunity.

For more details and a full description of the studied scenarios as well as the infection wave patterns, see **Paper VI**.

7 Computational methods

In this chapter I will explain the computational methods I used to model the equations of motion described in the previous chapters. The overdamped Langevin equation that describes the Brownian dynamics of a many-body system of N particles at position $\mathbf{r}_i(t)$ at time t reads:

$$\dot{\mathbf{r}}_i(t) = \frac{1}{\gamma} \mathbf{F}_i + \sqrt{2D} \boldsymbol{\eta}_i, \quad (7.1)$$

where \mathbf{F}_i is the total force acting on particle i , e.g., due to a chemical concentration gradient or interactions with neighboring particles, and, as described in the previous chapters, γ is the friction coefficient and D the diffusion coefficient. To account for the excluded volume effects in the simulations, I used both a Yukawa potential [209] and a Weeks-Chandler-Anderson potential [210] as approximations. For the latter, one would obtain in Eq. (7.1) $\mathbf{F}_i = -\nabla_{\mathbf{r}_i} V$ with $V = \frac{1}{2} \sum_{i,j \neq i} V_{ij}$, where the sum includes all particles and $V_{ij} = 4\epsilon \left[\left(\frac{\sigma}{r_{ij}} \right)^{12} - \left(\frac{\sigma}{r_{ij}} \right)^6 \right] + \epsilon$ if $r_{ij} \leq 2^{1/6} \sigma$ and zero otherwise. Here r_{ij} describes the distance between particles i and j , ϵ gives the strength of the potential, $\sigma = 2R$ is the particle diameter (with radius R for all particles), and $r_c = 2^{1/6} \sigma$ specifies a cutoff radius beyond which the potential is zero.

Instead of iterating over all particle pairs when calculating the interactions among the particles, which is computationally very expensive and scales with $\mathcal{O}(N^2)$, there are more efficient methods to calculate the forces between neighboring particles. I used the so-called neighbor list, where the simulation box is divided into cells of size $r_c \times r_c$, with r_c being the cutoff radius of the potential that is used to model the steric repulsions between the particles. Then, the interaction of a particle in cell $\{c_x, c_y\}$ is restricted to particles from neighboring cells indexed by $\{c_x - 1, c_x, c_x + 1\}$ and $\{c_y - 1, c_y, c_y + 1\}$. This allows for a much faster calculation as the computational cost is reduced to $\mathcal{O}(N)$.

The right-hand side of Eq. (7.1) contains a stochastic contribution (second term) in order to account for the translational fluctuations of the particle. These random forces are described using Gaussian white noise with zero mean $\langle \boldsymbol{\eta}_i(t) \rangle = 0$ and unit variance $\langle \boldsymbol{\eta}_i(t) \boldsymbol{\eta}_j(t') \rangle = \delta_{ij} \delta(t - t') \mathbf{I}$, where $\langle \cdot \rangle$ denotes an average over different realizations, δ_{ij} is the Kronecker delta, $\delta(\cdot)$ denotes the Dirac delta function and \mathbf{I} the (dimension dependent) unit matrix.

In computer simulations, the particle trajectories are obtained by numerical integration of Eq. (7.1) [148]. Due to the Gaussian process, Eq. (7.1) has the

typical form of a stochastic differential equation (SDE). It is considerably more complicated to solve this equation compared to deterministic differential equations (DDE) and there is only a sparse number of methods to analytically solve it [211,212]. Likewise, the well established numerical schemes for solving DDEs cannot be easily extended to SDEs, which is why equations of the type like Eq. (7.1) are also often just integrated using the simple Euler-Maruyama method [213]. This first simple method was developed by Maruyama in 1955 and is a generalization of Euler's method for DDE. Here, the simulation time is partitioned into small intervals of the size Δt and a simple Taylor expansion is used to obtain the positions of the particles at the next time step:

$$\mathbf{r}_i(t + \Delta t) = \mathbf{r}_i(t) + \frac{1}{\gamma} \mathbf{F}_i(\mathbf{r}_i(t)) \Delta t + \sqrt{2D} \mathbf{R}_i \sqrt{\Delta t}. \quad (7.2)$$

Note that the increments in a Brownian motion are normally distributed with mean 0 and variance Δt . This can be modeled by drawing a set of independent Gaussian random variables \mathbf{R}_i of zero mean and unit variance multiplied by the factor $\sqrt{\Delta t}$ [214]. For each time step, the forces at time t are calculated, which are used to determine the new positions at time $t + \Delta t$.

However, there are a variety of more efficient numerical methods for SDEs of the type of Eq. (7.1), such as the stochastic Runge-Kutta methods [214,215]. Due to the simple noise term (the prefactor $\sqrt{2D}$ is constant), higher order schemes can be easily constructed. Higher accuracy can be obtained by a second-order Runge-Kutta algorithm by calculating the forces on the particles at two stages. The positions of the particles can then be obtained as:

$$\tilde{\mathbf{r}}_i(t + \Delta t) = \mathbf{r}_i(t) + \frac{1}{\gamma} \mathbf{F}_i(\mathbf{r}_i(t)) \Delta t + \sqrt{2D} \mathbf{R}_i \sqrt{\Delta t} \quad (7.3)$$

$$\mathbf{r}_i(t + \Delta t) = \mathbf{r}_i(t) + \frac{1}{2\gamma} (\mathbf{F}_i(\mathbf{r}_i(t)) + \mathbf{F}_i(\tilde{\mathbf{r}}_i(t + \Delta t))) \Delta t + \sqrt{2D} \mathbf{R}_i \sqrt{\Delta t}. \quad (7.4)$$

Equation (7.3) is the simple Euler-Maruyama step, which allows a first estimate of the next particle position. Equation (7.4) then determines the average of the forces $\mathbf{F}_i(\mathbf{r}_i(t))$ and $\mathbf{F}_i(\tilde{\mathbf{r}}_i(t + \Delta t))$ at the two stages. This method offers a higher accuracy than the simple Euler-Maruyama method and allows larger time steps Δt .

In Chapters 2, 3 and 5 the dynamics of the particles is coupled to a phoretic field (e.g., chemical concentration, temperature). The phoretic field is sampled on a uniform grid, while the particles can move freely without any restrictions. Finite difference methods are used to solve the dynamics of the phoretic field, where the particle positions (described above) and the phoretic field are iterated alternately by one step. The dynamics of the phoretic fields are solved with central difference in space and the forward Euler method in time. The temporal and spatial discretizations are chosen small enough to satisfy the Courant-Friedrich-Lewy

condition [216]. Particles that produce the phoretic field are simulated as point sources. The interaction between particles and the phoretic field is approximated by bilinear interpolation. That means, that each particle contributes to the values at the four nearest grid points proportionally to the relative distances from the particle to the grid point.

Furthermore, boundary conditions must be taken into account. Usually a small sample of the configuration is considered in computer simulations and particles in a box of size L are simulated with periodic boundary conditions. That means the box is periodically repeated in all directions, such that each particle has an image in each direction at distance L .

8 Scientific publications

8.1 Paper I: Swarm Hunting and Cluster Ejections in Chemically Communicating Active Mixtures

Reproduced from

J. Grauer, H. Löwen, A. Be'er & B. Liebchen
Swarm Hunting and Cluster Ejections in Chemically Communicating Active Mixtures
Sci. Rep. **10**, 5594 (2020)

Digital Object Identifier (DOI): <https://doi.org/10.1038/s41598-020-62324-0>

Statement of contribution

H.L. and B.L. planned the research project. My contribution to this work partially overlaps with earlier results from my master thesis. The numerical simulation and investigation of the dynamical ejections of particle clusters belongs to this dissertation. I performed the computer simulations including the analysis of numerical results and prepared the figures. All authors discussed the results. B.L. and I wrote the manuscript. H.L. and A.B. edited the manuscript.

Copyright and license notice

This article is licensed under a Creative Commons Attribution 4.0 International License, which permits use, sharing, adaptation, distribution and reproduction in any medium or format, as long as you give appropriate credit to the original author(s) and the source, provide a link to the Creative Commons license, and indicate if changes were made. To view a copy of this license, visit <http://creativecommons.org/licenses/by/4.0/>

OPEN

Swarm Hunting and Cluster Ejections in Chemically Communicating Active Mixtures

Jens Grauer¹, Hartmut Löwen¹, Avraham Be'er^{2,3} & Benno Liebchen^{1,4*}

A large variety of microorganisms produce molecules to communicate via complex signaling mechanisms such as quorum sensing and chemotaxis. The biological diversity is enormous, but synthetic inanimate colloidal microswimmers mimic microbiological communication (synthetic chemotaxis) and may be used to explore collective behaviour beyond the one-species limit in simpler setups. In this work we combine particle based and continuum simulations as well as linear stability analyses, and study a physical minimal model of two chemotactic species. We observed a rich phase diagram comprising a "hunting swarm phase", where both species self-segregate and form swarms, pursuing, or hunting each other, and a "core-shell-cluster phase", where one species forms a dense cluster, which is surrounded by a (fluctuating) corona of particles from the other species. Once formed, these clusters can dynamically eject their core such that the clusters almost turn inside out. These results exemplify a physical route to collective behaviours in microorganisms and active colloids, which are so-far known to occur only for comparatively large and complex animals like insects or crustaceans.

Chemotaxis - the movement of organisms in response to a chemical stimulus - allows them to navigate in complex environments, find food and avoid repellants. It is involved in many biological processes where microorganisms (or cells) coordinate their motion; these include wound healing, fertilization, pathogenic invasion of a host, and bacterial colonization^{1,2}. In such cases, microorganisms are attracted (or repelled) by certain substances (chemoattractants/ chemorepellents), but they are also attracted to chemicals produced by other microorganisms (or cells), such as cAMP in the case of Dictyostelium cells³ or autoinducers in signaling Escherichia coli⁴, which leads to chemical interactions (communication) among the microorganisms.

While many existing models studying microbiological chemotaxis (or chemical interactions) focus on a single species⁵⁻¹², the typical situation in the microbiological habitat is that various different species simultaneously produce certain chemicals to which others respond via chemotaxis or based on quorum sensing mechanisms. One simple example involving chemical signaling across species is provided by macrophage-facilitated breast cancer cell invasion which has recently been modeled¹³. There, tumor cells attract macrophages, which are certain white blood cells normally playing a key role in the human immune system. They then control the physiological function of the macrophages and exploit their abilities. More specifically, the tumor cells produce the colony-stimulating factor (CSF-1) leading to the attraction and growth of macrophages which in turn release epidermal growth factors (EGF) resulting in the growth and mobility increase of the tumor cells (see Fig. 1).

Similarly to microorganisms, synthetic inanimate colloids, coated with a material which catalyzes a certain reaction on (a part of) their surface, show chemical interactions as well¹⁴⁻¹⁶. There, the colloids act as sources of the chemical field, which shows a $1/r$ -steady-state far-field profile in 3D (if the chemical does not 'decay' e.g. through bulk reactions), leading to long-ranged chemical interactions between the colloids. For active colloids¹⁷⁻²¹, these interactions have been explored in single-species systems²²⁻²⁷, and more recently also in mixtures²⁸⁻³⁴, where chemical interactions can be non-reciprocal and break action-reaction symmetry^{28,35,36}. This allows for the formation of active molecules²⁸⁻³⁰, where self-propulsion spontaneously emerges when the underlying nonmotile 'colloidal atoms' bind together. Similarly as for their microbiological counterparts, in all these studies on mixtures of synthetic colloids it has been assumed that the different species interact via a single chemical substance.

¹Institute for Theoretical Physics II: Soft Matter, Heinrich-Heine University Düsseldorf, Universitätsstraße 1, 40225, Düsseldorf, Germany. ²Zuckerberg Institute for Water Research, The Jacob Blaustein Institutes for Desert Research, Ben-Gurion University of the Negev, Sede Boqer Campus, 84990, Midreshet Ben-Gurion, Israel. ³Department of Physics, Ben-Gurion University of the Negev, Beer Sheva, 84105, Israel. ⁴Institut für Festkörperphysik, Technische Universität Darmstadt, 64289, Darmstadt, Germany. *email: liebchen@fkp.tu-darmstadt.de

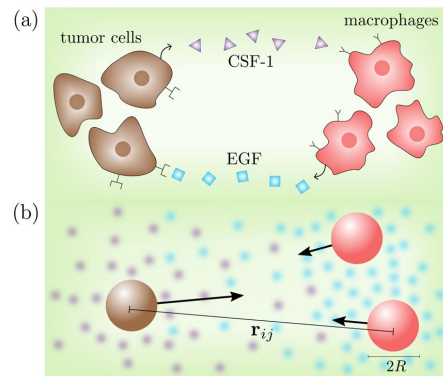


Figure 1. Schematic: (a) Interaction between tumor cells and macrophages (b) physical minimal model used in the simulation: two species realized as different particles (brown and red) with radius R and distance r_{ij} . The movement of the particles depends both on their self-produced chemicals (blue and purple) and on the concentration produced by the other species. Arrows represent effective chemical interactions among the particles, which in general are non-reciprocal.

In the present work, we propose and explore a physical minimal model for two species of chemically interacting particles, both of which produce an individual chemical substance. Such a situation occurs for example in tumor-macrophage systems involving the EGF/CSF-1 paracrine signalling loop between two cell types mentioned above¹³. By comparing numerical simulations of Langevin equations describing the particle dynamics (Fig. 2(a–d)) with numerical solutions of deterministic continuum equations describing the dynamics of their density fields (Fig. 2(e–h)) and a linear stability analysis, we systematically explore and analyze the phase diagram of this system. As our key result, we discover a “hunting-swarm phase” (see Fig. 2(a,e)), where both species segregate and form individual swarms, one of them closely pursuing the other one. This phase resembles a group of hunters chasing a group of prey trying to stay together, not allowing the hunters to split up the group. It is interesting to note that a phenomenologically similar form of swarm hunting also occurs in much larger systems, e.g. in insects and systems of larvae hunting crustaceans (*Daphnia*)^{37–39}, where collective predation phenomena and escape strategies have already been analyzed⁴⁰, but not for microorganisms or synthetic colloids. Physically this phase occurs, if one species (“the hunters”) is attracted by the chemicals produced by the other species (“the prey”) and the prey is in turn repelled by the chemicals produced by the hunters. Note that a different form of moving clusters has recently been observed also in simulations involving only one chemical species³³. Unlike the hunting swarms which we present here, the moving clusters in³³ do not involve a species segregation into two individual swarms, but rather consist of a single aggregate of asymmetrically distributed predator and prey particles. By systematically exploring the parameter space underlying our model, we find that hunting swarms in fact occur generically if the chemical interactions are strong enough and have opposite sign. However, if the response of hunters and prey to the chemicals produced by the respective other species is strongly asymmetric, we instead find dense clusters of one species surrounded by a diffusive or rigid corona of particles from the other species (see Fig. 2(b,d,f,h)). These core-shell clusters can show a complex dynamics, ejecting their interior once they have formed. This behaviour hinges on model-ingredients which have not been considered in previous models of chemically interacting particle mixtures^{31,33,41}. These are (i) a finite relaxation time of the chemicals leading to delay or memory effects in the absence of which the cluster ejections do not occur and (ii) the presence of two chemicals, which can lead e.g. to a coexistence of instantaneous and non-instantaneous interactions and in general also to coexisting attractions and repulsions with different ranges. The setup considered in the present work allows us to exemplify that a phenomenologically similar ejection may in principle originate from a remarkably simple mechanism hinging on a systematic invasion of the hunters into a cluster of prey particles, as we will later discuss in detail.

Model

We consider an ensemble of two species of overdamped colloids (synthetic or biological), which we call prey and hunters, $s \in \{p, h\}$, each of which contains N particles which produce a chemical field $c^s(\mathbf{r}, t)$ with a rate k_0 . We assume that each particle responds to the chemical fields either via synthetic chemotaxis, which leads to a coupling $\propto \nabla c^s$ in far-field^{22,27}, similar as for apolar colloids, or via biological chemotaxis which is sometimes modeled using an analogous form of the coupling⁶. To model the particle dynamics we use Langevin equations ($i = 1, \dots, N, s \in \{p, h\}$):

$$\gamma \partial_t \mathbf{r}_i^s(t) = \sum_{s' \in \{p, h\}} \alpha_{ss'} \nabla c^{s'} - \nabla_{\mathbf{r}_i} V + \sqrt{2D} \boldsymbol{\eta}_i^s \quad (1)$$

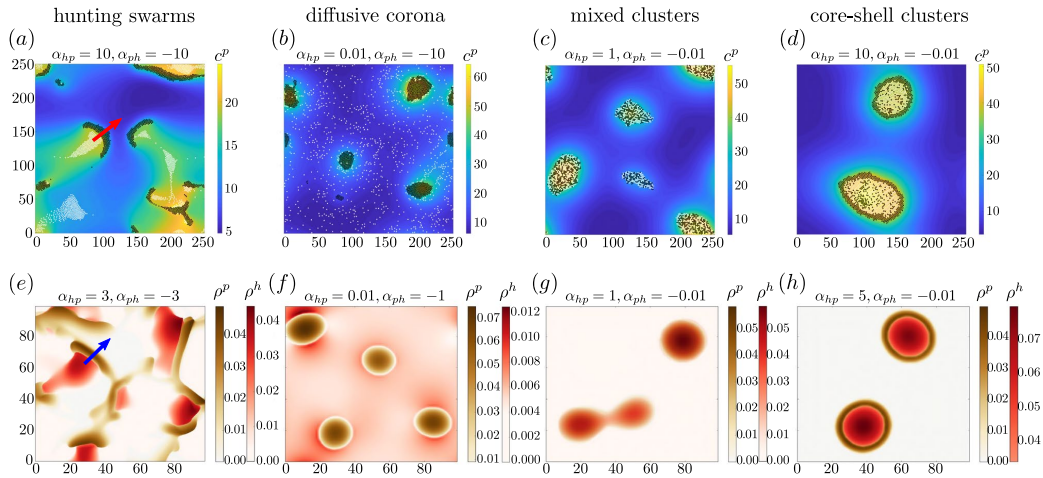


Figure 2. *Hunting swarms and core-shell clusters:* Simulation snapshots of Eqs. (3), (4) for $2N = 2000$ chemically interacting particles (white dots represent hunter-particles; black dots show prey-particles) coupled to self-produced chemical fields at time $t = 1500$ (a), 5000 (b-d). Panels (a-d) show particle based simulations, where colours show the chemical field produced by the prey c^p , panels (e-h) show simulations of the associated continuum equations at time $t = 5000$ (e), 10000 (f-h), where colours show the density of hunters ρ^h and prey ρ^p . (a,e) show *hunting swarm* patterns, (c,g) show *mixed clusters*, (b,f) show *core-shell clusters* with diffusive and (d,h) with rigid corona. Dimensionless parameters (tildes omitted): $\alpha_{pp} = 1, \alpha_{hh} = 0, \mu = 0.001, D_c = 1, D = 0.001$ (a-d), $D = 0.01$ (e-h) for reasons of stability, $\epsilon = 1$ and box length $L_{\text{box}} = 250$ (a-d), $L_{\text{box}} = 100$ (e-h). See supplementary material for simulation details and the stabilization method used for the field equations underlying panels (e-h).

where D is the translational diffusion coefficient of the particles, γ is the Stokes drag coefficient (assumed to be the same for both species) and $\eta_i^s(t)$ represents unit-variance Gaussian white noise with zero mean. The chemotactic coupling coefficient of species s to the chemical of species s' is denoted as $\alpha_{ss'}$, where $\alpha_{ss'} > 0$ leads to chemoattraction and $\alpha_{ss'} < 0$ results in chemorepulsion (negative chemotaxis). In addition, V accounts for excluded volume interactions among the particles which all have the same radius R and which we model using the Weeks-Chandler-Anderson potential $V = \frac{1}{2} \sum_{i,j \neq i} V_{ij}$ where the sums run over all particles and where $V_{ij} = 4\epsilon \left[\left(\frac{\sigma}{r_{ij}} \right)^{12} - \left(\frac{\sigma}{r_{ij}} \right)^6 \right] + \epsilon$ if $r_{ij} \leq 2^{1/6} \sigma$ and zero else. Here ϵ determines the strength of the potential, r_{ij} denotes the distance between particles i and j , $r_c = 2^{1/6} \sigma$ indicates a cutoff radius beyond which the potential energy is zero and $\sigma = 2R$ is the particle diameter.

The chemical fields $c^h(\mathbf{r}, t)$, $c^p(\mathbf{r}, t)$ are produced by particles of hunters and prey, respectively. The dynamics of these fields, follows a diffusion equation (diffusion coefficient D_c), with additional (point) sources. We also use a sink term whose coefficient may be zero or nonzero if chemical reactions or other processes degrading the chemical occur in bulk. For simplicity we focus on the case where D_c, k_0, k_d are identical for both species.

$$\partial_t c^s(\mathbf{r}, t) = D_c \Delta c^s - k_d c^s + k_0 \sum_{i=1}^N \delta(\mathbf{r} - \mathbf{r}_i^s) \tag{2}$$

To reduce the parameter space, we choose $x_0 = R$ and $t_0 = \frac{1}{k_0}$ as the units of length and time. The resulting dimensionless parameters are $\tilde{\alpha}_{kl} = \frac{\alpha_{kl}}{\gamma k_0 R^{d+2}}$, $\tilde{\epsilon} = \frac{\epsilon}{\gamma k_0 R^2}$, $\tilde{D}_c = \frac{D_c}{k_0 R^2}$, $\tilde{D} = \frac{D}{k_0 R^2}$ and $\mu = \frac{k_d}{k_0}$ (see the Supplementary Material (SI) for details) and Eqs. (1), (2) reduce to (omitting tildes)

$$\partial_t \mathbf{r}_i^s(t) = \sum_{s' \in \{p,h\}} \alpha_{ss'} \nabla c^{s'} - \nabla_{\mathbf{r}_i} V + \sqrt{2\tilde{D}} \boldsymbol{\eta}_i^s \tag{3}$$

$$\partial_t c^s(\mathbf{r}, t) = (D_c \Delta - \mu) c^s + \sum_{i=1}^N \delta(\mathbf{r} - \mathbf{r}_i^s) \tag{4}$$

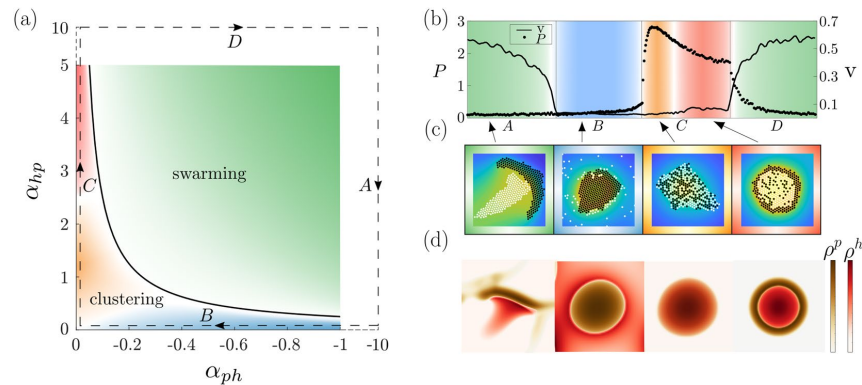


Figure 3. (a) State diagram in the plane spanned by the chemotactic cross coupling coefficients α_{ph} and α_{hp} for fixed $\alpha_{pp} = 1$; $\alpha_{hh} = 0$. The green domain represents hunting swarms, which are characterized by their ballistic motion and their emergence from an oscillatory instability (the black line shows the analytical prediction of the transition line), whereas colours for the remaining cluster phases are defined via the value of the mixing parameter shown in panel (b) (see text). The state diagram was created with more than 200 evaluated state points. (b) Mixing parameter P , counting the average number of black next neighbors per white particle and mean particle velocity v at late times discriminating between the individual states: Each point corresponds to a parameter set on the dashed line in the parameter plane of panel a. The labels A, B, C, D correspond to those shown on the dashed line in panel a. (c,d) Extracts from the simulations underlying Fig. 2 (see movies 1–8).

Hunting Swarms and Core-Shell Clusters

To explore the collective behaviour of many chemotactic agents, we now solve Eqs. (3) and (4) using Brownian dynamics simulations for the particle dynamics coupled to a finite difference scheme to calculate the dynamics of the self-produced chemical fields. We solve the diffusion equation in 2D for numerical efficiency and do not expect that our results would change qualitatively when solving the 3D diffusion equation (see the exemplar simulation snapshot Fig. 2 in the SI and notice that the linear stability analysis which does not depend on the dimensionality of the diffusion equation is also in very good agreement with the particle based simulations). We use a quadratic simulation box with periodic boundary conditions (see SI for details) and observe the following patterns or nonequilibrium phases:

- (i) A hunting swarm phase (see Fig. 2(a,e) and movies 1, 5), where both species segregate and form moving swarms which hunt each other.
- (ii) A clustering phase (see Fig. 2(c,g) and movies 3, 7), where both species form a cluster and the different species are mixed.
- (iii,iv) Two phases showing core-shell clustering, where one species forms the inner core and the other one forms a corona which may be diffusive (b,f) or rigid and which is strongly localized around the core (d,h).

Let us now characterize these phases and the dynamics leading to their emergence in detail.

To see in which parameter regimes each of these patterns prevails, in Fig. 3 we show a slice through the state diagram in the plane of the chemotactic cross-species coupling coefficients $\alpha_{ph} < 0$ and $\alpha_{hp} > 0$. Here we fix $\alpha_{pp} = 1$ and $\alpha_{hh} = 0$ so that prey-particles chemo-attract each other whereas the hunter-particles do not, but note that the specific values chosen here do not have much impact on the emerging patterns.

Hunting swarms. The green area in Fig. 3(a,b,c) (movies 1, 5) represents the hunting-swarm phase which generically occurs if $|\alpha_{hp}\alpha_{ph}|$ is large enough, as we will later show using a linear stability analysis. Here the chemicals produced by the black-coloured particles in Fig. 2(a) (“prey”) attract the white coloured particles (“hunters”), whereas the hunter-produced chemicals repel the prey. This results in a swarm of “prey” pursued by a swarm of “hunters”. When two or more prey-swarms collide, the pursuing hunters produce a “cage” of high chemical density repelling the prey and trapping it temporarily in a small spatial domain. The prey then ‘evades’ sideways to escape from the hunter-fronts, forming new swarms moving perpendicular to the original ones (see movies 1, 5).

Core-shell clusters. When decreasing α_{hp} (blue domain in Fig. 3(a,b) and movies 2, 6), so that the prey chemo-attracts the hunters only weakly, we observe that the prey aggregates and forms dense clusters, surrounded by a diffusive corona of hunters. Surprisingly, when staying with a large α_{hp} but decreasing α_{ph} instead (red domain in Fig. 3(a–c)), so that the hunters are strongly chemo-attracted by the prey, but the prey has only a weak tendency to avoid the hunter-produced chemicals, we see the opposite case: Although not attracting each other, the hunter-particles form a dense core, surrounded by the prey-particles (red domain in Fig. 3(c) and right panel of Fig. 3(d) and movies 4, 8). To see how these remarkable clusters emerge, let us explore the dynamics underlying

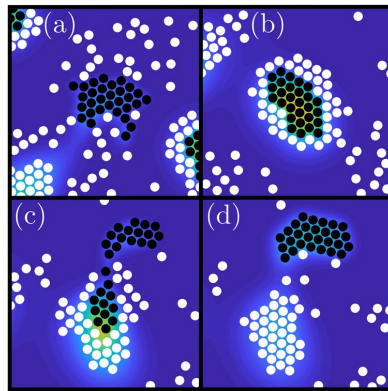


Figure 4. Sequence of simulation snapshots showing a cluster ejection which occurs due to chemical delay effects. Dimensionless parameters: $\alpha_{pp} = 100$, $\alpha_{hh} = 0$, $\alpha_{ph} = -1000$, $\alpha_{hp} = 10$, $\mu^p = 0.1$, $\mu^h = 0.01$, $D_c^p = 0.5$, $D_c^h = 10$, $D = 0.001$, $\epsilon = 10$ with 500 prey-particles and 2000 hunter-particles.

their formation. Initially, the prey-particles, which chemo-attract each other aggregate and form very small clusters. While these clusters are forming, the aggregation of prey-particles locally increases the concentration of c^p resulting in an attraction of hunter-particles, which directly invade the cluster, because $|\alpha_{hp}| > |\alpha_{pp}|$. Consequently, as more and more hunters enter the cluster, the density of c^h increases in the cluster center, repelling the prey. Since the prey-particles, in turn, couple stronger to their self-produced chemicals than to those produced by the hunters $|\alpha_{pp}| > |\alpha_{ph}|$, they do not flee from the cluster but try to stay together. While in the simulations underlying Fig. 2, the hunters invade even small prey-clusters, for appropriate initial conditions, we can see a proper inside out reversal of comparatively large clusters (movie 9) (species reversal). In each case, the result is a counterintuitive pattern consisting of a dense cluster containing mostly hunters surrounded by ring of prey-particles.

Dynamical ejections of particle clusters. We have investigated the dynamics of these core-shell clusters more precisely. Assuming the diffusion of c^p is considerably lower than that of c^h and c^h is produced very slowly, this results in a certain delay effect. A typical course of this process is shown in Fig. 4 (see also movie 10). The prey-particles that attract each other initially accumulate and form clusters (Fig. 4(a)). Due to a resulting higher concentration of c^p , the hunters are also attracted. These hunter-particles then form a surrounding shell, but cannot immediately invade the prey-cluster as $\alpha_{pp} > \alpha_{hp}$ (Fig. 4(b)). Although slowly, the concentration of c^h increases with time as more hunter-particles join. At some point a significant concentration of c^h is exceeded and since $|\alpha_{ph}| > |\alpha_{pp}|$, the prey-particles are ejected outwards from the center of the cluster (Fig. 4(c)). Since the chemicals c^p produced by the prey diffuses on a much smaller timescale, the hunter-particles still move towards each other, form a dense cluster which persists for a while (Fig. 4(d)), before the hunter-cluster dissolves slowly and the whole process starts all over again.

Irregular aggregation. Finally, when α_{ph} , α_{hp} are both small, with $|\alpha_{ph}| < |\alpha_{hp}|$ (orange regime in Fig. 3(a,b) and movies 3, 7), prey and hunter particles form clusters containing a seemingly irregular mixture of hunter and prey particles (Fig. 3(c), orange). These clusters emerge because we have a chemically mediated prey-prey attraction and a hunter-by-prey attraction which exceeds the prey-by-hunter-repulsion, so that effectively prey particles similarly strongly attract all other particles, leading to a rather irregular aggregation.

Classification. In contrast to the static clusters, structures in the green region of Fig. 3(a) move ballistically and hence show a non-vanishing velocity. Figure 3(b) depicts the mean particle velocity $v(t)$ (see SI for details) at late times for parameters chosen along the dashed line in Fig. 3(a), where one can easily see how the velocity in regions of hunting swarms exceeds that in other regimes. While the hunting swarm phase, which emerges from an oscillatory instability, as discussed further below, can be clearly distinguished from the stationary cluster phases, let us define an “order parameter” P to distinguish the remaining cluster phases. We define P as the average number of black next neighbors (prey) per white particle (hunter), where we denote a neighbor as a particle within a distance $r_{ij} < 2 + 0.1$. Figure 3(b) shows P for parameters chosen along the dashed line in Fig. 3(a). This parameter would have a value of 3 for completely irregular and infinitely large dense clusters. For the orange region, where particles aggregate almost irregularly, it has a value $P > 2.5$, whereas red means $(1.5 < P < 2.3)$ and blue means $P < 0.5$. Crossover regions between the individual patterns are marked by white domains in Fig. 3(a).

Linear Stability Analysis – Emergence and Dynamics of Patterns at Early Times

To understand the structure of the state diagram we now introduce a continuum description for the particle dynamics and perform a linear stability analysis.

Continuum model. The Smoluchowski equation, describing the dynamics of the (non-normalized) probability $\rho^s(\mathbf{r}, t)$ to find a particle of species s at position \mathbf{r} at time t reads as follows ($s \in \{p, h\}$):

$$\partial_t \rho^s = D\Delta \rho^s - \sum_{s' \in \{p, h\}} \alpha_{ss'} \nabla \cdot (\rho^{s'} \nabla c^{s'}). \quad (5)$$

These deterministic equations are equivalent to the Langevin Equation (1) for point particles ($V = 0$). We can now also rewrite the evolution equation for the chemical fields as follows:

$$\partial_t c^s = (D_c \Delta - \mu) c^s + \rho^s. \quad (6)$$

Before carrying out a linear stability analysis, let us solve these equations numerically to test them: Integrating Eqs. (5), (6) for a uniform initial state (plus small fluctuations) on a square box of size $L_{\text{box}} = 100$, we indeed find the same patterns as in our particle based simulations (Figs. 2(c–h) and 3) (see SI for details regarding these simulations and the used method to stabilize them).

Linear stability analysis. We now linearize these four coupled equations around the stationary solution $(\rho, c) = (\rho_0, \rho_0/\mu)$, which represents the uniform disordered phase, and solve them in Fourier Space, to understand the dynamics of a small plane wave perturbation with wavenumber q around the uniform phase. We denote the dispersion relation of these fluctuations as $\lambda(q)$. If λ has a positive real part for some q value, the uniform phase is unstable. Calculating λ (see Supplementary Material for details), we find that the uniform phase loses stability if

$$2D\mu < \rho_0 \text{Re} \left[\alpha_{pp} + \sqrt{4\alpha_{ph}\alpha_{hp} + \alpha_{pp}^2} \right], \quad (7)$$

where we have chosen $\alpha_{hh} = 0$ as in our simulations. While Fig. 3 shows only parameter regimes where the uniform phase is unstable, we have performed additional simulations (see SI) which are in close quantitative agreement with the prediction of the onset of the instability due to Eq. (7). This holds true both in the regime where the instability is stationary and where it is oscillatory. The instability criterion shows that chemo-attractants among the prey particles support the emergence of a pattern in competition with diffusion and the potential decay of the chemical, whereas cross interactions only support the emergence of a pattern if they, α_{ph} and α_{hp} , have the same sign.

To understand the transition between static clusters and hunting swarms, we also derive a criterion discriminating between stationary instability (static clusters, λ is real) and oscillatory instabilities (moving structures, complex λ) which reads as follows (see SI):

$$2\sqrt{-\alpha_{ph}\alpha_{hp}} > \alpha_{pp}. \quad (8)$$

This criterion defines the solid black line in Fig. 3(a), which quantitatively agrees with our simulations. It shows that an oscillatory instability and hence moving patterns can appear only if $\alpha_{ph}\alpha_{hp}$ have opposite sign, i.e. if one species effectively hunts the other one, whereas the other one tries to escape. In this parameter regime where it is oscillatory, we have numerically tested the instability criterion (Eq. (7)) to see if it is shifted due to “perturbation convection”, see⁴². We did not find any shift, suggesting that the advective and absolute instability are very close to each other in the present case.

In Fig. 5 we show the complete dispersion relation $\lambda(q)$ (real and imaginary part) of small plane wave fluctuations around the uniform phase. Here the location of the maxima in $\text{Re}[\lambda(q)] > 0$ define the fastest growing mode, typically determining the length scale of the pattern at early times.

Having understood the transition line between the cluster phases and the hunting swarms, let us also explore if we can understand how fast the swarms move. To do this, in Fig. 6, we compare the imaginary part of λ (the expected speed of the hunting swarm is $v(q) = \frac{\text{Im}(\lambda)}{q} \rightarrow \langle v \rangle \approx \frac{\text{Im}(\lambda_{q_{\text{max}}})}{q_{\text{max}}}$) with the velocity of the hunting swarms in our particle based simulations at early times and find close agreement.

Structure and Growth at Late Times

Having explored how the patterns emerge and behave at early times, we now want to explore their structure and dynamics also at late times. To do this, we introduce the instantaneous pair-correlation function $g(\mathbf{r})$ defined as

$$g(\mathbf{r}) = \frac{1}{\rho_{\text{id}}} \left\langle \sum_{i \neq 0} \delta(\mathbf{r} - \mathbf{r}_i) \right\rangle, \quad (9)$$

for an average number density $\rho_{\text{id}} = \frac{2N}{L_{\text{box}}^2}$ with box length $L_{\text{box}} = 250$, total number of particles $2N$ and $\langle \cdot \rangle$ denoting the ensemble average. The radially averaged and time averaged pair-correlation function $g(r)$, where $r = |\mathbf{r}|$, shown in Fig. 7 describes how the density varies as a function of distance from a reference particle at which we averaged over all particles of hunters and prey.

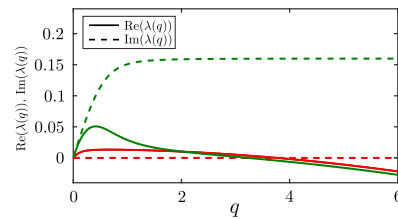


Figure 5. Real and imaginary part of the dispersion relation λ , for hunting swarms (green) and static clusters (red). Parameters as in Fig. 2(a,d).

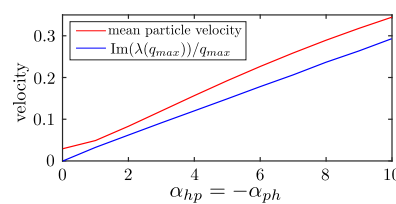


Figure 6. Mean particle velocity in the hunting swarm phase, extracted from the simulations underlying Fig. 3(a) at early times (red) and reduced imaginary part of λ at the wavenumber corresponding to the fastest growing mode, i.e. $\text{Im}(\lambda(q_{\text{max}}))/q_{\text{max}}$ (blue) as a function of $-a_{\text{ph}} = a_{\text{hp}}$.

As one can see in the inset of Fig. 7, there is a large peak around $r = 2$, which is the typical distance between two particles ($R = 1$ in dimensionless units). We can also find peaks around $r = 2\sqrt{3}$ and $r = 4$ caused by the next two neighbors. This reflects the fact that the static clusters (blue, orange, red) show a hexagonal packing.

Late-stage dynamics. Once the patterns have emerged, they reach a state where their morphology changes only slowly. However, even at late stages the size of the individual structures still increases in time. The swarms move ballistically and frequently collide with each other often leading to their break up. They still grow on average, ultimately leading to a single swarm at late times. This is because after each collision a new swarm forms rapidly, i.e. on timescales before the individual particles which were part of the ‘old’ swarm significantly diffuse away. The newly forming swarm rapidly reaches a size exceeding that of its ‘ancestors’, because it involves particles from both swarms which were involved in the collision. To quantify this growth, we consider the time evolution of the radial distribution function $g(r, t)$ and define the length scale $L_1(t)$ of clusters as the smallest value where $g(r, t) \leq 1$, for all $r > L_1$. Thus, the $g(r)$ shown in Fig. 7 corresponds to a length scale of $L_1 \approx 20$ (dimensionless units). At late-times, we find that $L_1(t) \propto t^\beta$ follows a power law with an exponent of $\beta \approx 0.35$ (Fig. 8) for the (nonmoving) cluster phases, which is close to the value of $\beta = \frac{1}{3}$ as expected for diffusive growth (in the absence of hydrodynamic interactions)^{43–47}. We find a much larger exponent, of $\beta \approx 0.56$ (Fig. 8), for the patterns in the green region, which is close to $\beta = 0.5$ as expected for ballistic aggregation. This is a consequence of the fact that the individual structures move ballistically, collide and merge with each other much faster (but also break up).

As a second measure for the growth of the clusters, we measure the distance between them. To do this, we consider the structure factor of the system:

$$S(\mathbf{k}) = 1 + \rho_{\text{id}} \int_V d\mathbf{r} e^{-i\mathbf{k}\cdot\mathbf{r}} [g(\mathbf{r}) - 1] \quad (10)$$

and calculate the distance between clusters as the inverse of the first moment of the structure factor⁴⁸, i.e. as:

$$L_2(t) = 2\pi \left[\frac{\int_{2\pi/L}^{k_{\text{cut}}} k S(k, t) dk}{\int_{2\pi/L}^{k_{\text{cut}}} S(k, t) dk} \right]^{-1}, \quad (11)$$

where we choose the cutoff wavelength k_{cut} as the first local minimum of $S(k)$ ⁴⁸. Figure 9 shows the structure factor for a cluster in the red region of Fig. 3(a) at time $t = 250$ for small values of k . The peaks that can be seen in the inset of Fig. 9 correspond to the distance of two possible lattice planes of the hexagonal structure. The peak at $k = 3.3$ results from the minimum distance between two particles ($\frac{2\pi}{3.3} \approx 2$). One finds a huge peak around $k = 0.11$ with which we can estimate a typical length, $l \approx \frac{2\pi}{k} = 57.1$; the enormous size of the peak hinges on the fact that each of the contributing clusters contains a large number of particles. The k -value where this peak occurs

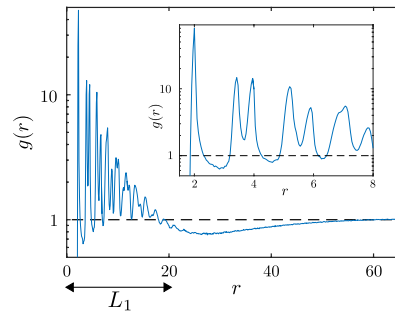


Figure 7. Pair-correlation function $g(r)$ (radial average of $g(\mathbf{r})$) of a system of $2N = 2000$ particles at time $t = 250$. The data are averaged over 100 independent ensembles. The dashed line shows a threshold to extract a characteristic length scale. Parameters as in Fig. 2(d).

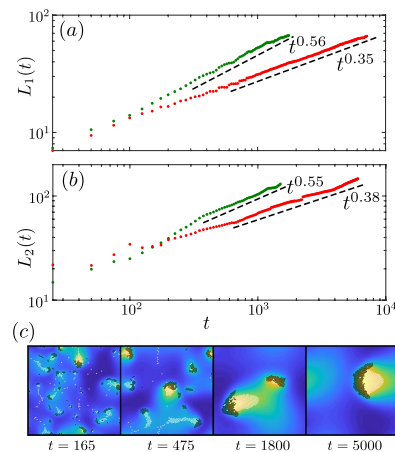


Figure 8. Time-dependent characteristic length scale (a) obtained from the pair-correlation function and (b) from the structure factor for structures in the red region (red dotted line) and in the green region (green dotted line of Fig. 3(a)). The dashed lines indicate the fitted exponents. Parameters as in Fig. 2(a,d). Panel (c) shows a sequence of snapshots from a representative simulation of the hunting swarms which continuously collide, split up and grow to a larger size.

corresponds to the mean cluster distance, which corresponds to the value of r where $g(r)$ approaches 1 from below (see Fig. 7). This distance grows basically with the same power law as the cluster sizes, as shown in Fig. 8, i.e. calculating cluster sizes via $L_1(t)$ and calculating cluster-distances $L_2(t)$ basically leads to the same growth law (Fig. 8)⁴⁹. Thus, there is only one independent macroscopic length scale in the system.

Conclusions

Inspired by the generic presence of multi-species chemotaxis in microbiological communities, e.g. in macrophage-tumor cell systems, we have proposed and explored a physical minimal model to study the collective behaviour beyond the commonly considered one-species limit. We have found that the novel key ingredient of our model - the species selective chemical production - leads to interesting behavior: patterns that comprise a "hunting swarm" phase consisting of a crowd of particles of one species pursuing the other species, and a phase where the two-species self-aggregate in a core-shell structure, which then dissolves abruptly in a dynamic process by ejecting the inner particles.

All these patterns could be observed both on the level of a particle-based description (Eqs. (3), (4)) and in a continuum model (Eqs. (5), (6)), allowing to analytically understand the transition line between cluster phases, which originate from a stationary instability of the uniform phase, and hunting swarms, emerging from an oscillatory instability. As a further characteristic difference between these phases, we find that clusters (and the

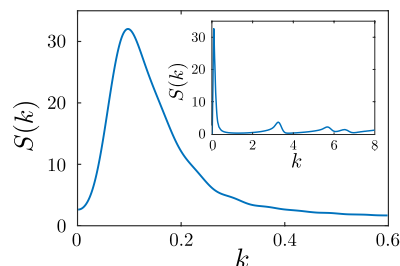


Figure 9. Small wavenumber regime of the structure factor $S(k)$ for a system of $2N = 2000$ particles at time $t = 250$. Inset shows $S(k)$ for a larger wavenumber regime. The wavenumber k is given in dimensionless units ($k_0 = \frac{2\pi}{R}$). Parameters as in Fig. 2(d).

distance between them) grow diffusively ($L(t) \propto t^{0.35}$)^{43–47,49}, whereas hunting swarms grow significantly faster ($L(t) \propto t^{0.56}$)⁵⁰.

While the key aim of the present work was to explore a minimal framework illustrating how chemical cross-interactions may lead to complex behavior, it should in principle be possible to realize the present model also with (autophoretic) colloidal mixtures, e.g. based on a combination of nonreciprocal repulsive thermo-phoretic and attractive chemo-phoretic interactions, which have been confirmed to be non-reciprocal in recent experiments²⁹.

Future work might include more specific biological details and could address the effect of confining boundaries or obstacles^{51–54}. Other topics concern additional aligning interactions and their impact on the cluster structure^{55–57} and ternary systems describing species of a longer biological food chain.

Data availability

All relevant data are available from the authors upon reasonable request.

Received: 27 February 2020; Accepted: 9 March 2020;

Published online: 27 March 2020

References

- Cejková, J., Holler, S., Nguyenová, T. Q., Kerrigan, C., Štěpánek, F. & Hanczyc, M. M. In *Advances in Unconventional Computing* (Springer, 2017)
- Wadhams, G. H. & Armitage, J. P. Making sense of it all: bacterial chemotaxis. *Nat. Rev. Mol. Cell Biol.* **5**, 1024 (2005).
- Eidi, Z., Mohammad-Rafiee, F., Khorrami, M. & Gholami, A. Modelling of Dictyostelium discoideum movement in a linear gradient of chemoattractant. *Soft Matter* **13**, 8209 (2017).
- Laganenka, L., Colin, R. & Sourjik, V. Chemotaxis towards autoinducer 2 mediates autoaggregation in Escherichia coli *Nat. Commun.* **7**, 12984 EP (2016).article
- Tindall, M. J., Maini, P. K., Porter, S. L. & Armitage, J. P. Overview of mathematical approaches used to model bacterial chemotaxis II: bacterial populations. *Bull. Math. Biol.* **70**, 1570 (2008).
- Murray, J. D. Bacterial Patterns and Chemotaxis, In *Mathematical Biology: II: Spatial Models and Biomedical Applications*, edited by Murray, J. D. (Springer New York, New York, NY, 2003)
- Hillen, T. & Painter, K. J. A user's guide to PDE models for chemotaxis. *J. Math. Biol.* **58**, 183 (2008).
- Painter, K. J. Mathematical models for chemotaxis and their applications in self-organisation phenomena. *J. Theor. Biol.* (2018).
- Painter, K. J. & Hillen, T. Spatio-temporal chaos in a chemotaxis model. *Phys. D* **240**, 363 (2011).
- Dolak, Y. & Schmeiser, C. Kinetic models for chemotaxis: Hydrodynamic limits and spatio-temporal mechanisms. *J. Math. Biol.* **51**, 595 (2005).
- Mukherjee, M. & Ghosh, P. Growth-mediated autochemotactic pattern formation in self-propelling bacteria. *Phys. Rev. E* **97**, 012413 (2018).
- Bergmann, F., Rapp, L. & Zimmermann, W. Active phase separation: A universal approach. *Phys. Rev. E* **98**, 020603 (2018).
- Knútsdóttir, H., Palsson, E. & Edelman-Keshet, L. Mathematical model of macrophage-facilitated breast cancer cells invasion. *J. Theor. Biol.* **357**, 184199 (2014).
- Stark, H. Artificial Chemotaxis of Self-Phoretic Active Colloids: Collective Behavior. *Acc. Chem. Res.* **51**, 2681 (2018).
- Robertson, B., Huang, M.-J., Chen, J.-X. & Kapral, R. Synthetic Nanomotors: Working Together through Chemistry. *Acc. Chem. Res.* **51**, 2355 (2018).
- Liebchen, B. & Löwen, H. Synthetic Chemotaxis and Collective Behavior in Active Matter. *Acc. Chem. Res.* **51**, 2982 (2018).
- Marchetti, M. C. *et al.* Hydrodynamics of soft active matter. *Rev. Mod. Phys.* **85**, 1143 (2013).
- Romanczuk, P., Bär, M., Ebeling, W., Lindner, B. & Schimansky-Geier, L. Active Brownian particles. *Eur. Phys. J.-Spec. Top.* **202**, 1 (2012).
- Kurzthaler, C. *et al.* Probing the Spatiotemporal Dynamics of Catalytic Janus Particles with Single-Particle Tracking and Differential Dynamic Microscopy. *Phys. Rev. Lett.* **121**, 078001 (2018).
- Bechinger, C. *et al.* Active particles in complex and crowded environments. *Rev. Mod. Phys.* **88**, 045006 (2016).
- Aranson, I. S. Active colloids. *Phys.-Usp* **56**, 79 (2013).
- Saha, S., Golestanian, R. & Ramaswamy, S. Clusters, asters, and collective oscillations in chemotactic colloids. *Phys. Rev. E* **89**, 062316 (2014).
- Pohl, O. & Stark, H. Dynamic Clustering and Chemotactic Collapse of Self-Phoretic Active Particles. *Phys. Rev. Lett.* **112**, 238303 (2014).

24. Liebchen, B., Marenduzzo, D., Pagonabarraga, I. & Cates, M. Clustering and Pattern Formation in Chemorepulsive Active Colloids. *Phys. Rev. Lett.* **115**, 258301 (2015).
25. Liebchen, B., Marenduzzo, D. & Cates, M. Phoretic Interactions Generically Induce Dynamic Clusters and Wave Patterns in Active Colloids. *Phys. Rev. Lett.* **118**, 268001 (2017).
26. Huang, M.-J., Schofield, J. & Kapral, R. Chemotactic and hydrodynamic effects on collective dynamics of self-diffusiophoretic Janus motors. *New J. Phys.* **19**, 125003 (2017a).
27. Liebchen, B. & Löwen, H. Which interactions dominate in active colloids? *J. Chem. Phys.* **150**, 061102 (2019).
28. Soto, R. & Golestanian, R. Self-Assembly of Catalytically Active Colloidal Molecules: Tailoring Activity Through Surface Chemistry. *Phys. Rev. Lett.* **112**, 068301 (2014).
29. Schmidt, F., Liebchen, B., Löwen, H. & Volpe, G. Light-controlled assembly of active colloidal molecules. *J. Chem. Phys.* **150**, 094905 (2019).
30. Niu, R., Palberg, T. & Speck, T. Self-Assembly of Colloidal Molecules due to Self-Generated Flow. *Phys. Rev. Lett.* **119**, 028001 (2017).
31. Stürmer, J., Seyrich, M. & Stark, H. Chemotaxis in a binary mixture of active and passive particles. *J. Chem. Phys.* **150**, 214901 (2019).
32. Singh, D. P., Choudhury, U., Fischer, P. & Mark, A. G. Non-Equilibrium Assembly of Light-Activated Colloidal Mixtures. *Advanced Materials* **29**, 1701328 (2017).
33. Agudo-Canalejo, J. & Golestanian, R. Active Phase Separation in Mixtures of Chemically Interacting Particles. *Phys. Rev. Lett.* **123**, 018101 (2019).
34. Wang, L., Popescu, M. N., Stavale, F., Ali, A., Gemming, T. & Simmchen, J. Cu@TiO₂ Janus microswimmers with a versatile motion mechanism. *Soft Matter* **14**, 6969 (2018).
35. Ivlev, A., Bartnick, J., Heinen, M., Du, C.-R., Nosenko, V. & Löwen, H. Statistical mechanics where Newton's third law is broken. *Phys. Rev. X* **5**, 011035 (2015).
36. Sengupta, A., Kruppa, T. & Löwen, H. Chemotactic predator-prey dynamics. *Phys. Rev. E* **83**, 031914 (2011).
37. Boonman, A., Yovel, Y. & Fenton, B. The benefits of insect-swarm hunting in echolocating bats, and its influence on the evolution of bat echolocation signals, bioRxiv, 554055 (2019).
38. Jeschke, J. M. & Tollrian, R. Prey swarming: which predators become confused and why? *Animal Behaviour* **74**, 387 (2007).
39. Zhdankin, V. & Sprott, J. C. Simple predator-prey swarming model. *Phys. Rev. E* **82**, 056209 (2010).
40. Angelani, L. Collective Predation and Escape Strategies. *Phys. Rev. Lett.* **109**, 118104 (2012).
41. Hauke, F., Löwen, H. & Liebchen, B. Clustering-induced velocity-reversals of active colloids mixed with passive particles. *J. Chem. Phys.* **152**, 014903 (2020).
42. Aranson, I. S. & Kramer, L. The world of the complex Ginzburg-Landau equation. *Rev. Mod. Phys.* **74**, 99 (2002).
43. Lifshitz, I. & Slyozov, V. The kinetics of precipitation from supersaturated solid solutions. *J. Phys. Chem. Solids* **19**, 35 (1961).
44. Bray, A. J. Theory of phase-ordering kinetics. *Adv. Phys.* **51**, 481 (2002).
45. Gonnella, G., Marenduzzo, D., Suma, A. & Tiribocchi, A. Motility-induced phase separation and coarsening in active matter. *C. R. Phys.* **16**, 316 (2015).
46. Laradji, M. & Kumar, P. B. Sunil Domain growth, budding, and fission in phase-separating self-assembled fluid bilayers. *J. Chem. Phys.* **123**, 224902 (2005).
47. Camley, B. A. & Brown, F. L. H. Dynamic scaling in phase separation kinetics for quasi-two-dimensional membranes. *J. Chem. Phys.* **135**, 225106 (2011).
48. Stenhammar, J., Tiribocchi, A., Allen, R. J., Marenduzzo, D. & Cates, M. E. Continuum Theory of Phase Separation Kinetics for Active Brownian Particles. *Phys. Rev. Lett.* **111**, 145702 (2013).
49. Stanich, C. *et al.* Coarsening Dynamics of Domains in Lipid Membranes. *Biophys. J.* **105**, 444 (2013).
50. Cremer, P. & Löwen, H. Scaling of cluster growth for coagulating active particles. *Phys. Rev. E* **89**, 022307 (2014).
51. Morin, A., Desreumaux, N., Caussin, J.-B. & Bartolo, D. Distortion and destruction of colloidal flocks in disordered environments. *Nat. Phys.* **13**, 63 EP (2016).
52. Toner, J., Guttenberg, N. & Tu, Y. Hydrodynamic theory of flocking in the presence of quenched disorder. *Phys. Rev. E* **98**, 062604 (2018).
53. Huang, M.-J., Schofield, J. & Kapral, R. Transport in active systems crowded by obstacles. *J. Phys. A: Math. Theor.* **50**, 074001 (2017b).
54. Rahmani, P., Peruan, F. & Romanczuk, P. Flocking in complex environments – attention trade-offs in collective information processing. arXiv:1907.11691 [physics.bio-ph] (2019).
55. Das, S. K. Pattern, growth, and aging in aggregation kinetics of a Vicsek-like active matter model. *J. Chem. Phys.* **146**, 044902 (2017).
56. Mones, E., Czirák, A. & Vicsek, A. Anomalous, T. segregation dynamics of self-propelled particles. *New J. Phys.* **17**, 063013 (2015).
57. Nilsson, S. & Volpe, G. Metastable clusters and channels formed by active particles with aligning interactions. *New J. Phys.* **19**, 115008 (2017).

Acknowledgements

H.L. was supported by the German Research Foundation (DFG) within the SPP 1726 (project LO 418/17-2). A.B. thanks partial support from The Israel Science Foundation Grant 373/16.

Author contributions

H.L. and B.L. have planned and designed the research project; J.G. has performed most of the research; all authors have discussed the results; J.G. and B.L. have written the manuscript; H.L. and A.B. have edited it.

Competing interests

The authors declare no competing interests.

Additional information

Supplementary information is available for this paper at <https://doi.org/10.1038/s41598-020-62324-0>.

Correspondence and requests for materials should be addressed to B.L.

Reprints and permissions information is available at www.nature.com/reprints.

Publisher's note Springer Nature remains neutral with regard to jurisdictional claims in published maps and institutional affiliations.

www.nature.com/scientificreports/



Open Access This article is licensed under a Creative Commons Attribution 4.0 International License, which permits use, sharing, adaptation, distribution and reproduction in any medium or format, as long as you give appropriate credit to the original author(s) and the source, provide a link to the Creative Commons license, and indicate if changes were made. The images or other third party material in this article are included in the article's Creative Commons license, unless indicated otherwise in a credit line to the material. If material is not included in the article's Creative Commons license and your intended use is not permitted by statutory regulation or exceeds the permitted use, you will need to obtain permission directly from the copyright holder. To view a copy of this license, visit <http://creativecommons.org/licenses/by/4.0/>.

© The Author(s) 2020

Supplemental Material - Swarm Hunting and Cluster Ejections in Chemically Communicating Active Mixtures

I. DIMENSIONLESS EQUATIONS

In order to extract the essential parameters controlling the behaviour of the considered model, we non-dimensionalize it and introduce *characteristic units*.

A. PDEs for chemotaxis

Every physical quantity is written as a product of a non-dimensional quantity times a normalization constant containing the units, e.g.

$$\mathbf{x} = \tilde{\mathbf{x}} x_u, \quad t = \tilde{t} t_u \quad (1)$$

Here, all the quantities with a tilde are dimensionless while those with a subscript "u" contain the units. We also introduce the dimensionless chemical field, $\tilde{c}^{p,h} = c^{p,h} x_u^d$, where d denotes the spatial dimension ($d = 2$ in our case). Eq. (2) in the main text then reads in dimensionless form as

$$\partial_t \frac{\tilde{c}^s}{x_u^d} = \frac{D_c t_u}{x_u^2} \tilde{\Delta} \frac{\tilde{c}^s}{x_u^d} - k_d t_u \frac{\tilde{c}^s}{x_u^d} + \frac{k_0 t_u}{x_u^d} \sum_{i=1}^N \delta(\tilde{\mathbf{r}} - \tilde{\mathbf{r}}_i^s), \quad s \in \{p, h\}, \quad (2)$$

where we have used that $\delta(\alpha \mathbf{r}) = \frac{1}{\alpha^d} \delta(\mathbf{r})$. Next, we choose $x_0 = R$, where R denotes the (soft) radius of a particle and $t_u = \frac{1}{k_0}$ yielding:

$$\partial_t \tilde{c}^s = \tilde{D}_c \tilde{\Delta} \tilde{c}^s - \mu \tilde{c}^s + \sum_{i=1}^N \delta(\tilde{\mathbf{r}} - \tilde{\mathbf{r}}_i^s), \quad (3)$$

where the normalised coefficients \tilde{D}_c and μ are then given by: $\tilde{D}_c = \frac{D_c}{k_0 R^2}$ and $\mu = \frac{k_d}{k_0}$.

B. Particle ODEs

The same normalization is applied to Eq. (1) in the main text which leads to:

$$\partial_t \tilde{\mathbf{r}}_i^p = \frac{t_u}{\gamma x_u^{d+2}} \left(\alpha_{pp} \tilde{\nabla} \tilde{c}^p(\tilde{\mathbf{r}}_i^p, t) + \alpha_{ph} \tilde{\nabla} \tilde{c}^h(\tilde{\mathbf{r}}_i^p, t) \right) - \tilde{\nabla} \tilde{V} + \sqrt{\frac{2D t_u}{x_u^2}} \tilde{\boldsymbol{\eta}}_i^p \quad (4)$$

$$\partial_t \tilde{\mathbf{r}}_i^h = \frac{t_u}{\gamma x_u^{d+2}} \left(\alpha_{hh} \tilde{\nabla} \tilde{c}^h(\tilde{\mathbf{r}}_i^h, t) + \alpha_{hp} \tilde{\nabla} \tilde{c}^p(\tilde{\mathbf{r}}_i^h, t) \right) - \tilde{\nabla} \tilde{V} + \sqrt{\frac{2D t_u}{x_u^2}} \tilde{\boldsymbol{\eta}}_i^h, \quad (5)$$

where $\boldsymbol{\eta}_i^s(t)$ represents unit-variance Gaussian white noise with zero mean. With the additional definitions of $\tilde{\alpha}_{kl} = \frac{\alpha_{kl}}{\gamma k_0 R^{d+2}}$ and $\tilde{D} = \frac{D}{k_0 R^2}$ we obtain:

$$\partial_t \tilde{\mathbf{r}}_i^p = \tilde{\alpha}_{pp} \tilde{\nabla} \tilde{c}^p(\tilde{\mathbf{r}}_i^p, t) + \tilde{\alpha}_{ph} \tilde{\nabla} \tilde{c}^h(\tilde{\mathbf{r}}_i^p, t) - \tilde{\nabla} \tilde{V} + \sqrt{2\tilde{D}} \tilde{\boldsymbol{\eta}}_i^p \quad (6)$$

$$\partial_t \tilde{\mathbf{r}}_i^h = \tilde{\alpha}_{hh} \tilde{\nabla} \tilde{c}^h(\tilde{\mathbf{r}}_i^h, t) + \tilde{\alpha}_{hp} \tilde{\nabla} \tilde{c}^p(\tilde{\mathbf{r}}_i^h, t) - \tilde{\nabla} \tilde{V} + \sqrt{2\tilde{D}} \tilde{\boldsymbol{\eta}}_i^h. \quad (7)$$

2

We model V using the Weeks-Chandler-Anderson potential, with $\tilde{V} = \frac{1}{2} \sum_{i,j \neq i} \tilde{V}_{ij}$, where the sums run over all particles and where

$$\tilde{V}_{ij} = \begin{cases} 4\tilde{\epsilon} \left[\left(\frac{\tilde{\sigma}}{\tilde{r}_{ij}} \right)^{12} - \left(\frac{\tilde{\sigma}}{\tilde{r}_{ij}} \right)^6 \right] + \tilde{\epsilon} & \text{if } \tilde{r}_{ij} \leq 2^{1/6} \tilde{\sigma} \\ 0 & \text{if } \tilde{r}_{ij} > 2^{1/6} \tilde{\sigma} \end{cases} \quad (8)$$

Here r_{ij} denotes the distance between particle i and j , $\tilde{r}_{ij} = r_{ij}/x_u$, $\tilde{\sigma} = \sigma/x_u$ and $\tilde{\epsilon} = \frac{\epsilon}{\gamma k_0 R^2}$.

In the following, we omit tildes. The specific value of ϵ hardly affects our results, so the following independent and relevant dimensionless parameters remain:

- 1) effective diffusion constants D_c and D ,
- 2) reduced coupling constants α_{kl} ,
- 3) ratio of decay and production of the chemical μ
- 4) density of species p, h (which is conserved throughout the dynamics)

II. DESCRIPTION OF NUMERICAL METHODS

A. Numerical methods for solving the equations of the particle-based chemotaxis model

We solve our model Eqs. (3,6,7) by discretizing space and time. We perform simulations in two spatial dimensions (2D) with periodic boundary conditions. Interactions between the particles are described using the Weeks-Chandler-Anderson potential. The PDEs (3) for the dynamics of the chemical fields are solved in time with a forward Euler method. This does not impose any restriction on the timestep dt due to the Courant-Friedrich-Lewy (CFL) condition [1] of the heat equation ($D_c \left(\frac{dt}{dx^2} + \frac{dt}{dy^2} \right) < \frac{1}{4}$, where dt and dx, dy denote the temporal and spatial discretisations), since the necessary timestep dt for the particle dynamics is small enough to not violate the above CFL condition. The Laplace operator of the heat term is approximated with central differences. The particle dynamics of the colloids (Eqs. 6,7) is solved in time with the Euler-Maruyama scheme [2] for incorporation the noise term. The interactions of the colloids is effectively treated by applying a cell-list summation [3].

In order to speed up the calculations, we make use of cell lists [3], with a minimal image convention. This is motivated by the fact that the repulsive force caused by the potential V is short ranged and hence we can introduce a cutoff radius $r_c = 2^{1/6} \sigma$. More explicitly, we consider only interactions within a cutoff radius r_c such that the pair interaction $V_{ij} = 0$ for $r_{ij} > r_c$.

Different simulations are performed by varying the diffusion constants D and D_c , the coupling constants α_{kl} and the ratio of decay and production of the chemical μ .

Typical parameters used in the simulation of the dimensionless Eqs. (3,6,7):

# of particles N	$2 * 10^3$
WCA-potential amplitude ϵ	1
coupling constants	$-10 < \alpha_{kl} < 10$
diffusion constant D_c	1
diffusion constant D	$0.001 - 1$
decay/production of c	$0.001 < \mu < 1$
time step	$\Delta t = 0.001 t_0$
simulation time	$\sim 10^4 t_0$
grid for chemical	250×250 grid cells

B. Numerical methods for solving the equations of the continuum chemotaxis model

In addition to the particle-based simulations, we have also numerically solved the system of the four coupled dimensionless PDEs of the continuum model, Eqs. (5,6) of the main text as before in two spatial dimensions with periodic boundary conditions. We use a forward Euler method to propagate the densities ρ^s and the chemical fields c^s in time. The Laplace operator is approximated with central differences.

1. Repulsion between cells

We must be careful when implementing the chemotactic continuum model, which unlike our particle based equations, neglect the steric repulsions among the particles, preventing sharp density peaks, destabilizing the simulation. In view of this effect, we add an additional nonlinear term to the continuum model to effectively describe local repulsions among the particles [4]:

$$\partial_t \rho^s = D \Delta \rho^s - \sum_{s' \in \{p, h\}} \alpha_{ss'} \nabla \cdot (\rho^s \nabla c^{s'}) + D_{\text{rep}}^s \nabla \cdot (\rho^s \nabla (\rho^p + \rho^h)). \quad (9)$$

Here, D_{rep}^s with $s \in \{p, h\}$ are dimensionless repulsion coefficients and we assume that the strength of the repulsion is the same between the two different species, $D_{\text{rep}}^p = D_{\text{rep}}^h$.

2. Regularization of the density

As a second adjustment of the continuum model, avoiding a blow up [5] we use:

$$\partial_t \rho^s = D \Delta \rho^s - \sum_{s' \in \{p, h\}} \alpha_{ss'} \nabla \cdot \left(\frac{\rho^s}{1 + \kappa \rho^s} \nabla c^{s'} \right) + D_{\text{rep}}^s \nabla \cdot (\rho^s \nabla (\rho^p + \rho^h)), \quad (10)$$

where κ is a small regularization parameter and $\kappa \rightarrow 0$ leads to the original system. In [5] it was shown that the solutions of equations of the kind of Eq. (5) of the main text typically have a spiky structure and Eq. (10) can be used to model the aggregation phenomena.

III. LINEAR STABILITY ANALYSIS

To understand the origin of the observed pattern formation, we perform a linear stability analysis of Eqs. (5,6) of the main text around the homogeneous solution $(\rho^s, c^s) = (\rho_0^s, \rho_0^s / \mu) =: (\rho_0^s, c_0^s)$, $s \in \{p, h\}$. The PDEs of the density in the continuous model for two different sorts of particles $\rho^s = \rho^s(\mathbf{r}, t)$, $s \in \{p, h\}$ read (in dimensionless units)

$$\partial_t \rho^p = D \Delta \rho^p - \alpha_{pp} \nabla \cdot (\rho^p \nabla c^p) - \alpha_{ph} \nabla \cdot (\rho^p \nabla c^h) \quad (11)$$

$$\partial_t \rho^h = D \Delta \rho^h - \alpha_{hh} \nabla \cdot (\rho^h \nabla c^h) - \alpha_{hp} \nabla \cdot (\rho^h \nabla c^p), \quad (12)$$

where the corresponding PDEs for the phoretic field $c^s = c^s(\mathbf{r}, t)$, $s \in \{p, h\}$ are given by:

$$\partial_t c^s = D_c \Delta c^s + \rho^s - \mu c^s. \quad (13)$$

For the linear stability analysis, we consider small perturbations from the homogeneous steady state of the particle density $\rho^s = \rho_0^s + \delta \rho^s$ and the phoretic field $c^s = c_0^s + \delta c^s$.

The resulting linearised system of four equations describes the time-evolution of the deviations of the particle density and the chemical field from the homogeneous state $\rho^s = \rho_0^s$ and $c^s = \rho_0^s / \mu$.

4

$$\partial_t \delta \rho^p = D \Delta \delta \rho^p - \alpha_{pp} \rho_0^p \Delta \delta c^p - \alpha_{ph} \rho_0^p \Delta \delta c^h \quad (14)$$

$$\partial_t \delta \rho^h = D \Delta \delta \rho^h - \alpha_{hh} \rho_0^h \Delta \delta c^h - \alpha_{hp} \rho_0^h \Delta \delta c^p, \quad (15)$$

$$\partial_t \delta c^s = D_c \Delta \delta c^s + \delta \rho^s - \mu \delta c^s. \quad (16)$$

Since the linearised equations Eqs. (14-16) do not depend explicitly on time, we perform a Fourier transformation in space and make a separation Ansatz $\hat{\rho}^s(\mathbf{q}, t) = e^{\lambda t} \hat{\rho}^s(\mathbf{q})$, $\hat{c}^s(\mathbf{q}, t) = e^{\lambda t} \hat{c}^s(\mathbf{q})$, leading immediately to the following eigenvalue problem (we set $\alpha_{hh} = 0$ as in the main text):

$$\lambda \begin{pmatrix} \delta \hat{\rho}^p \\ \delta \hat{c}^p \\ \delta \hat{\rho}^h \\ \delta \hat{c}^h \end{pmatrix} = \begin{pmatrix} -D\mathbf{q}^2 & \alpha_{pp}\rho_0^p\mathbf{q}^2 & 0 & \alpha_{ph}\rho_0^p\mathbf{q}^2 \\ 1 & -D_c\mathbf{q}^2 - \mu & 0 & 0 \\ 0 & \alpha_{hp}\rho_0^h\mathbf{q}^2 & -D\mathbf{q}^2 & 0 \\ 0 & 0 & 1 & -D_c\mathbf{q}^2 - \mu \end{pmatrix} \begin{pmatrix} \delta \hat{\rho}^p \\ \delta \hat{c}^p \\ \delta \hat{\rho}^h \\ \delta \hat{c}^h \end{pmatrix}, \quad (17)$$

where the stability of the system is determined by the eigenvalues λ of the matrix, as follows:

- (a) The steady state is stable, if the eigenvalues of the matrix all have real parts strictly less than zero.
- (b) The steady state is unstable, if at least one of the eigenvalues of the matrix has a positive real part.
- (c) Otherwise in the marginal case higher order terms determine the stability of the problem.

The four eigenvalues λ of the linearised system are explicitly given by ($\alpha_{hh} = 0$, $\rho_0^p = \rho_0^h = \rho_0$):

$$\lambda = -\frac{q^2}{2} \left(D_c + D + \frac{\mu}{q^2} \right) \pm \frac{1}{2} \sqrt{[q^2(D_c + D + \frac{\mu}{q^2})]^2 - 4(D_c + \frac{\mu}{q^2})Dq^4 + 2\alpha_{pp}\rho_0q^2 \pm 2q^2\rho_0\sqrt{4\alpha_{ph}\alpha_{hp} + \alpha_{pp}^2}} \quad (18)$$

For the parameter range under consideration, eigenvalues with non-vanishing imaginary part exist ($\text{Im}(\lambda) \neq 0$), if the condition $-4\alpha_{ph}\alpha_{hp} > \alpha_{pp}^2$ is fulfilled. In order to develop an instability for long wavelengths ($|q| \rightarrow 0$), a Taylor series extension of (18) and an examination where $\text{Re}(\lambda) > 0$ provides us with the criterion

$$2D\mu < \alpha_{pp}\rho_0. \quad (19)$$

If the eigenvalues are real (here, $\text{Im}(\lambda) = 0 \iff -4\alpha_{ph}\alpha_{hp} < \alpha_{pp}^2$), then we obtain the following criterion for instability from calculating $\text{Re}(\lambda) > 0$:

$$2D\mu < \rho_0 \left(\alpha_{pp} + \sqrt{4\alpha_{ph}\alpha_{hp} + \alpha_{pp}^2} \right) \quad (20)$$

Altogether, an instability is given, when the following criterion is fulfilled:

$$2D\mu < \rho_0 \text{Re} \left[\alpha_{pp} + \sqrt{4\alpha_{ph}\alpha_{hp} + \alpha_{pp}^2} \right] \quad (21)$$

and this instability is also oscillatory if

$$-4\alpha_{ph}\alpha_{hp} > \alpha_{pp}^2. \quad (22)$$

If the local repulsions among the particles is taken into account and the linear stability analysis is performed with Eq. (9) instead of Eq.(5) of the main text, the uniform phase is unstable, when the following criterion is fulfilled:

$$2\mu(D + \rho_0 D_{rep}) < \rho_0 \text{Re} \left[\alpha_{pp} + \sqrt{4\alpha_{ph}\alpha_{hp} + \alpha_{pp}^2 - 4\mu D_{rep}(\alpha_{ph} + \alpha_{hp} - \mu D_{rep})} \right] \quad (23)$$

which is then also oscillatory if

$$-4\alpha_{ph}\alpha_{hp} > \alpha_{pp}^2 - 4\mu D_{rep}(\alpha_{ph} + \alpha_{hp} - \mu D_{rep}) . \quad (24)$$

Since the term μD_{rep} is very small for the considered parameters in Fig. 2 (of the main text), the instability criterion is barely influenced by this additional D_{rep} -term approximately leading to Eqs. (21,22) again.

Note that the instability criterion, Eq. (21), does not depend on the chemical diffusion constant D_c . Therefore, a faster alternative to obtain Eq. (21), would be to assume that the dynamics of the chemical is fully enslaved by the motion of the colloids and relaxes quasi-instantaneously to its steady state, i.e. to assume $\partial_t c^s = 0$. Note however, that only the instability criterion itself is independently of D_c and not the instability band. In addition, once the instability has emerged, the fact that $\partial_t c^s \neq 0$ is of crucial importance for the phenomenology of the resulting patterns, which can be seen best for the clusters ejecting their inner particles, which hinge on chemical delay (or memory) effects.

We have numerically tested the instability criterion in the parameter regime where it is oscillatory (i.e. non-vanishing imaginary part) to see if it is shifted due to perturbation convection, see [6]. Snapshots of the additional performed simulations are shown below in Fig. 1. The snapshots are arranged in a row with increasing decay-rate of the chemical μ . Above a certain value, this rate is too large, such that the concentration of the chemical substances is insufficient and the homogeneous phase is stable. The dashed line indicates for which μ the instability criterion (Eq. (7)) is fulfilled. As can be seen, this transition line fits well to the simulations and we did not find any shift, suggesting that the advective and absolute instability are very close to each other in the present case.

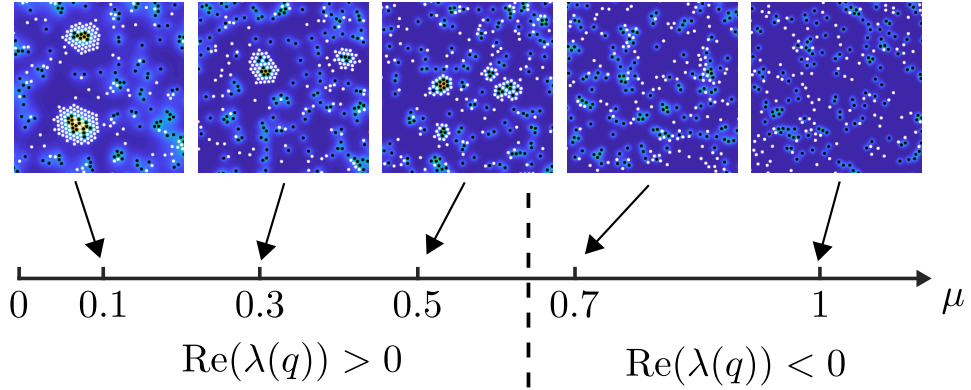


FIG. 1: Snapshots of simulations with different decay-rate μ . The dashed line indicates for which μ the instability criterion is fulfilled. Parameters used in these simulations: $\alpha_{pp} = 1$, $\alpha_{hh} = 0$, $\alpha_{ph} = -10$, $\alpha_{hp} = 10$, $D = 0.01$, $N = 2000$, $L = 250$

IV. MEAN PARTICLE VELOCITY

In order to distinguish between the different phases, in particular between the clusters and the hunting swarm phase, we calculate the mean particle velocity, which is defined as

$$v(t) = \left\langle \frac{1}{2N} \sum_{\substack{i=1,N \\ s=p,h}} \left| \frac{\mathbf{r}_i^s(t+dt) - \mathbf{r}_i^s(t)}{dt} \right| \right\rangle \quad (25)$$

where we average over all particles of species $s \in \{p, h\}$ and $\langle \cdot \rangle$ denotes the ensemble average.

V. DIFFUSION EQUATION IN 3D

To verify that our results do not change qualitatively when solving the diffusion equation in 3D, we have performed additional simulations for verification. Figure 2 shows an exemplaric simulation snapshot of the particle based model in three dimensions for a cluster in the blue domain ($\alpha_{hp} = 0.01, \alpha_{ph} = -10$).

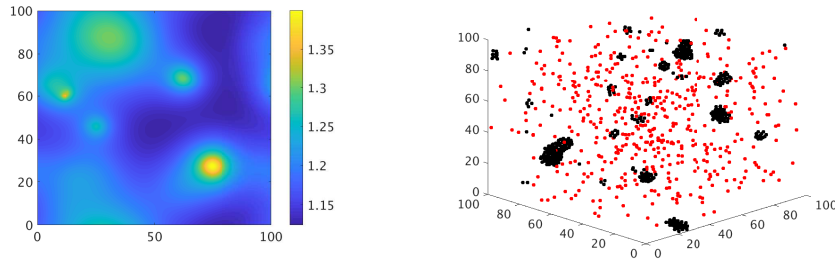


FIG. 2: Simulation snapshot of the particle based model in 3D. Left panel shows the diffusion of c^p by looking at the cross section of the chemical field in a plane perpendicular to the z -axis. Right panel shows the prey and the hunters, colored in black and red, respectively. Parameters as in Fig. 2(b) of the main text.

VI. DESCRIPTION OF THE MOVIES

The movies 1-8 show the time-evolution of the different patterns, hunting swarms, mixed clusters and core-shell clusters, for the particle-based and the continuum model for the same parameters as used in Fig. 2 of the main text (panels (a-h) corresponding to the files mov1-mov8). Movie 9 shows a dynamical inside out reversal for an appropriate initial condition, starting with a dense and comparatively large cluster of prey particles, which is then invaded by the hunter particles. Parameters used for movie 9: $\alpha_{pp} = 1, \alpha_{hh} = 0, \alpha_{hp} = 10, \alpha_{ph} = -0.01, \mu = 0.001, D_c = 0.1, D = 0.003, \epsilon = 1, 2N = 300$ particles and $L_{\text{box}} = 80$. Movie 10 shows clusters ejecting their inner particles that occur starting from a uniform initial state. Parameters used for movie 10: $\alpha_{pp} = 100, \alpha_{hh} = 0, \alpha_{hp} = 10, \alpha_{ph} = -1000, \mu^p = 0.1, \mu^h = 0.01, D_c^p = 0.5, D_c^h = 10, D = 0.001, \epsilon = 10, L_{\text{box}} = 200$ with 500 prey-particles and 2000 hunter-particles.

REFERENCES

-
- [1] R. Courant, K. Friedrichs, and H. Lewy, Über die partiellen Differenzgleichungen der mathematischen Physik, *Math. Ann.* **100**, 32 (1928).
 - [2] D. J. Higham., An Algorithmic Introduction to Numerical Simulation of Stochastic Differential Equations, *SIAM Rev.* **43**, 525 (2001).
 - [3] M. P. Allen and D. J. Tildesley, *Computer Simulation of Liquids* (Clarendon Press, New York, NY, USA, 1989).
 - [4] H. Knútsdóttir, E. Palsson, and L. Edelstein-Keshet, Mathematical model of macrophage-facilitated breast cancer cells invasion, *J. Theor. Biol.* **357**, 184199 (2014).
 - [5] A. Kurganov and M. Lukacova-Medvidova, Numerical study of two-species chemotaxis models, *Discrete and Continuous Dynamical Systems. Series B* **1** (2014).
 - [6] I. S. Aranson and L. Kramer, The world of the complex Ginzburg-Landau equation, *Rev. Mod. Phys.* **74**, 99 (2002).

8.2 Paper II: Active Assembly of Spheroidal Photocatalytic BiVO₄ Microswimmers

Reproduced from

S. Heckel, J. Grauer, M. Semmler, T. Gemming, H. Löwen, B. Liebchen, & J. Simmchen

Active Assembly of Spheroidal Photocatalytic BiVO₄ Microswimmers
Langmuir **36**, 12473–12480 (2020)

Digital Object Identifier (DOI): <https://doi.org/10.1021/acs.langmuir.0c01568>

Statement of contribution

I contributed to this publication by implementing the theoretical model, analyzing the numerical results and writing the simulation methods section. S.H. performed most of the experimental research. All authors discussed the results, and wrote or edited the manuscript.

Copyright and license notice

Reprinted with permission from Langmuir 2020, 36, 42, 12473–12480. Copyright 2020 American Chemical Society.

LANGMUIR

pubs.acs.org/Langmuir

Article

Active Assembly of Spheroidal Photocatalytic BiVO₄ Microswimmers

Sandra Heckel, Jens Grauer, Maria Semmler, Thomas Gemming, Hartmut Löwen, Benno Liebchen, and Juliane Simmchen*

 Cite This: *Langmuir* 2020, 36, 12473–12480

 Read Online

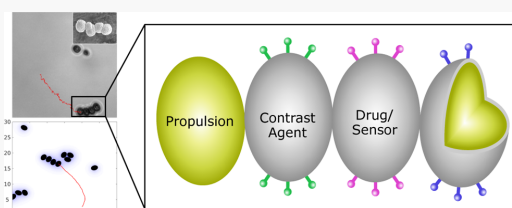
ACCESS |

 Metrics & More

 Article Recommendations

 Supporting Information

ABSTRACT: We create single-component photocatalytic bismuth vanadate (BiVO₄) microswimmers with a spheroidal shape that move individually upon irradiation without any asymmetrization step. These particles form active assemblies which we investigate combining an experimental approach with numerical simulations and analytical calculations. We systematically explore the speed and assembly of the swimmers into clusters of up to four particles and find excellent agreement between experiment and theory, which helps us to understand motion patterns and speed trends. Moreover, different batches of particles can be functionalized separately, making them ideal candidates to fulfill a multitude of tasks, such as sensing or environmental remediation. To exemplify this, we coat our swimmers with silica (SiO₂) and selectively couple some of their modules to fluorophores in a way which does not inhibit self-propulsion. The present work establishes spheroidal BiVO₄ microswimmers as a versatile platform to design multifunctional microswimmers.



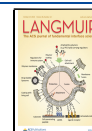
INTRODUCTION

Numerous applications have been proposed for catalytic microswimmers in the recent past. Researchers are currently probing their potential for sensing,¹ drug delivery,² and environmental remediation.³ To create an asymmetry in fuel degradation which is essential for swimming, hemispherical metal coating is the method of choice in most examples.⁴ Even though it is not limited to spheres,⁵ this process requires perfect monolayers of particles and therefore limits the throughput of microswimmer production. Moreover, it excludes half of the swimmer surface from additional functionalization. Mostly, potential applications then depend on further modification with sensing/contrast agents or a drug to add functionality. This makes complicated and costly multistep fabrication not suitable for upscaling, which is highly desired because collective interactions are often a prerequisite to successfully fulfill a task.

As an alternative approach to create self-propulsion, researchers have recently developed a modular concept to microswimming, opening up the possibility of reconfigurable swimmers that can fulfill multiple tasks because of differently modified building blocks. One advantage of this approach is that different and possibly competing functionalities of the swimmers no longer have to be implemented in a single particle but can be distributed among their modules. Thus, the number of fabrication steps on one swimmer particle as well as the risk of reactions impeding each other decreases. To overcome these limitations, some material-specific binary assemblies have already been proposed in the past,^{6,7} but mostly, laborious synthetic strategies are required.⁸

Modular microswimmers can generally be divided into rigidly bound and dynamic structures, where dynamic structures bear the clear advantage of reconfigurability.⁹ After several examples of the assembly observed in classical Janus particles^{10,11} and droplets,¹² Niu et al. have constructed ion-exchange-driven modular microswimmers.¹³ Here, passive cargo particles assemble around cationic exchange particles.^{14,15} Kei Cheang et al. have assembled magnetic microspheres into modular swimmers in a Helmholtz coil setup,¹⁶ and also, electric fields have been explored extensively.^{17,18} Schmidt et al. in turn have combined absorbing (active) and nonabsorbing (passive) particles in a subcritical liquid mixture. Illumination with laser light then leads to a temperature increase around absorbing particles and therefore to attraction among different colloids. The so-formed “colloidal molecules” show directed motion caused by the response of the nonabsorbing particles to the temperature and concentration gradient surrounding the absorbing particles.¹⁹ All of the mentioned examples consist of spherical particles, which only become active upon assembly. More examples have recently been described theoretically^{20,21} and discussed in reviews.^{9,22} A different approach was followed by the Tierno group, who relied on dominating magnetic interactions.^{23,24}

Received: May 27, 2020
 Revised: August 21, 2020
 Published: August 21, 2020



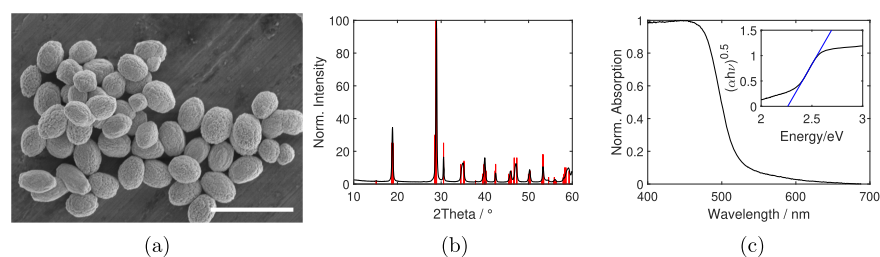


Figure 1. Material properties of BiVO_4 microparticles. (a) SEM image. The spheroidal particles have an average length of $2.09 \mu\text{m}$ and an average width of $1.54 \mu\text{m}$, which results in an aspect ratio of 1.37. The scale bar is $5 \mu\text{m}$. (b) XRD pattern of the particles (black) agrees with the monoclinic scheelite crystal structure (red) (JCPD 14-688) of BiVO_4 . (c) Normalized DRS spectrum and Tauc plot show an indirect band gap of 2.26 eV .

In this work, we present microswimmers based on spheroidal bismuth vanadate building blocks, which self-propel and self-organize into a variety of active assemblies of different geometries and speeds. We call them modular swimmers, although in contrast to the aforementioned examples, single particles (modules) also show activity and an assembly is not required for active motion. As a particularly interesting property, BiVO_4 swimmers, which we²⁵ and others²⁶ have recently introduced, can self-propel without any asymmetrization of their surface. Instead, these photocatalytic swimmers show an internal asymmetric distribution of electrons and holes upon excitation which results in a net propulsion. This further reduces the number of required preparation steps, and, accordingly, active swimmers can be obtained without the throughput-limiting process of hemispherical metal deposition. In the present work using a combined approach based on experiments and numerical simulations, we systematically explore the interactions between single swimmers and how the resulting aggregates move depending on their conformation. We modified the particles with a silica shell, which enables easy functionalization with a variety of entities, such as fluorophores or positively charged amino groups, and demonstrate combined swimmers of pristine and functionalized BiVO_4 modules.

RESULTS AND DISCUSSION

Characterization of Single BiVO_4 Swimmers. BiVO_4 microparticles were synthesized via a solvothermal approach. Figure 1a shows the obtained spheroidal particles, with an average length of $2.09 \pm 0.22 \mu\text{m}$, a width of $1.54 \pm 0.15 \mu\text{m}$, and an aspect ratio of 1.37 ± 0.13 . A histogram with particle size distribution can be found in Figure S1a. A closer look on the particles reveals a rough, highly structured surface, indicating their formation from smaller nano- and micro-sized crystals during the synthesis process (see also Figure S1b). As BiVO_4 is an oxidic material, the surface charge in neutral pH regimes is generally negative for this material. This is proven by a negative zeta potential of -26.3 mV .

Naturally, BiVO_4 appears in three different crystal structures, of which monoclinic scheelite is the photocatalytically most active one.²⁷ As can be seen in Figure 1b, the particles synthesized here are in good agreement with the powder X-ray diffraction (XRD) pattern of monoclinic scheelite, which is an important prerequisite for photochemical microswimmers. Additionally, the absorption spectrum derived by diffuse reflectance spectroscopy (DRS) in Figure 1c proves absorption up into the visible range for these particles with a band gap of

2.26 eV , implying that propulsion with ultraviolet (UV) as well as blue light can be achieved. To prove this, we determined the speed of single particles under UV and blue excitation. However, for the following experiments with active assemblies and functionalized particles, only UV excitation was applied.

Locomotion Mechanism. To induce directed motion, it is sufficient to immerse these particles in a 0.3% hydrogen peroxide (H_2O_2) aqueous solution and excite them with 385 nm UV or 469 nm blue light. Figure 2a shows the reaction

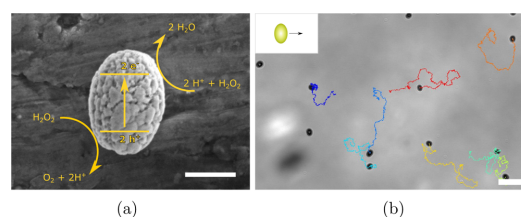


Figure 2. Motion mechanism and pattern of single particles. (a) Mechanism of H_2O_2 fuel degradation, integrated in a SEM image. The choice of reduction and oxidation spots in this image is for illustrative purposes only and does not necessarily represent the actual reaction distribution. The scale bar is $1 \mu\text{m}$. (b) Tracks of single pristine BiVO_4 swimmers under UV illumination for 30 s. The scale bar is $5 \mu\text{m}$.

mechanism of H_2O_2 fuel degradation. Upon excitation, H_2O_2 reacts with holes in the crystal to produce oxygen and hydrogen ions. These cations are consumed by the other half-reaction, where H_2O_2 reacts with electrons in the crystal to water. A proton gradient is thus created around the particle that induces directed motion, which, if compared to pure Brownian motion, can be distinguished by the faster growth of its mean-square displacement (MSD) (see Figure S2). It should be highlighted that these particles do not require any additional asymmetrization to perform active motion but can directly be used as single-component swimmers. The reason for this unique behavior can be twofold: the monoclinic scheelite crystal structure favors electron–hole separation onto different facets,^{28,29} thus spatially separating the oxidation and reduction half-reactions of H_2O_2 degradation when excited with light. Therefore, an intrinsic driving force for a fuel gradient around the particle is provided.³⁰ Figure 2b shows trajectories of single spheroidal swimmers at low concentration and emphasizes that the particles move mainly perpendicular to their long axis (see also Videos S1 and S2). This strengthens

the assumption that the crystal has a certain orientation within these particles so that the oxidation and reduction sites are intrinsically separated. We additionally assume the effect to be enhanced by the nano- and microstructured appearance of the particle surface as irregularities on the surface can enhance the development of a fuel gradient around the particle.

In general, it is also possible to consider environmental fluctuations or the vicinity of other particles as a potential drive for directed motion. However, in our previous work about square-shaped BiVO₄ microswimmers, we excluded these because of the rather large size that minimizes the influence of random fluctuations and observed particle swimming behavior upon repeated excitation cycles.²⁵ Here, we have shown that the particles always move in the same direction in consecutive excitation cycles, independent of their surroundings. Similar particle dimensions and behavior in this work suggest again a dominant importance of the catalytic properties.

The speed of these single spheroidal swimmers spreads between 3 and 6 $\mu\text{m s}^{-1}$, with an average of $4.20 \pm 0.71 \mu\text{m s}^{-1}$ for UV light and $4.47 \pm 0.57 \mu\text{m s}^{-1}$ for blue light (the values are also summarized in Table 1).

Table 1. Mean Speeds and Standard Deviations for Different Modular Conformations, Retrieved from Experiments (under UV Excitation) and Simulations^a

number of modules	mean speed/ $\mu\text{m s}^{-1}$ (experiment)	mean speed/ $\mu\text{m s}^{-1}$ (simulation)	percentage of swimmers/%
1	4.20 ± 0.71	4.23 ± 0.59	46
2	3.83 ± 0.73	3.92 ± 0.63	23
3-caterpillar	3.70 ± 0.49	3.76 ± 0.85	7
3-triangle	3.32 ± 0.21	3.07 ± 0.59	9
others			15

^aWe observe a trend for a decreased speed with an increasing amount of particles in one swimmer. Also, the percentage of swimmers after 15 s was obtained from simulations. The simulation parameters are as in Figure 3.

Active Assemblies. If the swimmers are at higher concentration so that random particle–particle encounters are more likely, we observe that they attract each other over a distance of more than two particle radii, leading to self-propelled assemblies. While these attractions can originate from different effects, as discussed previously by Wang et al.,³ photochemical swimmers such as ours are mostly subject to hydrodynamic and chemical-field-induced interactions. As shown in Figure 2, the overall product of the reaction is oxygen, while the produced protons are directly consumed in the oxidation reaction. We speculate that this interplay contributes to favorable attraction between individual modules. Additionally, the hydrodynamic flows created by the oxygen gradient as well as the migrating protons also seem to favorably influence the attraction.

We observe recurring geometries of swimmers consisting of up to four modules, which can be seen in Figure 3 (see also Video S3). In contrast to the work of Perry et al.,³¹ these active assemblies do not reconfigure or fluctuate between different geometries but rather keep on growing over time. The longer the swimmers are illuminated with UV light, the larger the modular swimmers get, leading to actively moving agglomerates of many more than four modules. The motility then

decreases strongly, and these active clusters require a separate consideration which is beyond the scope of this article.

In general, it can be noted that contingent on their spheroidal shape, the particles mainly attract each other perpendicularly to their long axis. Although these are single-component swimmers, their shape introduces favorable modular conformations without the need to induce them externally. This represents a strong difference from previous works where individual modules usually consist of isotropic, spherical particles.^{14,16,19}

Examples for experimental swimmer trajectories with reproducible geometries of two, three, and four modules are displayed in Figure 3a. In the simulation model, these swimmers produce a chemical field to which they respond themselves. This results in self-propulsion as well as in an attraction of other swimmers. The resulting assemblies then show the same geometries as those in the experiment and move on similar trajectories (Figure 3b). More experimental and simulated trajectories can be found in Figure S3.

For swimmers consisting of two modules, only one stable conformation exists. If three modules are combined into a swimmer, two different stable conformations are found. First, we observe a “caterpillar” structure, where all three spheroids are lined up along their short axis. Second, a “triangle” assembly is observed, with the third module not being aligned along the short axis but interacting with the short ends of the other two modules. This leads to a more compact structure. Finally, two different conformations with four modules are observed as well. Analogous to the three modular swimmers, a caterpillar is formed. A more compact assembly is called the “rectangle” conformation. It should be noted that especially the caterpillar structures can only be formed because of the spheroidal shape of the particles and have only been possible to be achieved through magnetic interactions earlier.²⁴

Once the particles assemble into modular swimmers, their motion patterns change compared to those of single swimmers. As can be seen in all trajectories in Figure 3, we observe a tendency for curved trajectories of modular swimmer conformations in both the experiment and simulation. Moreover, for swimmers consisting of three and four modules, the trajectory radii of the more compact conformations (triangle and rectangle) appear to be smaller as compared to those of elongated caterpillar conformations. An explanation for this can be found in the forces affecting the swimmer, which result from the gradient field around it. In addition to a longitudinal propulsion force, a triangular swimmer also experiences a torque, which results in a more curved trajectory, as will be discussed in more detail in the framework of our theoretical model below (see also Figure S4).

Let us now systematically examine how often the different modular swimmers occur in our simulations, that is, we assess the frequency at which certain conformations appear and evaluate their occurrence after 15 s. The results can be found in Table 1. As expected, single particles are observed most frequently, followed by assemblies consisting of two and then three modules. Swimmers consisting of four modules appear too rarely to give statistically validated information on the speed or the ratio between the caterpillar and rectangle swimmers. As a general trend, we find that larger swimmers move slower. This is observed in experiments as well as in simulations, which are in excellent qualitative agreement (see Figure 4). An explanation can be found in the overall concentration gradient surrounding a cluster, which is less

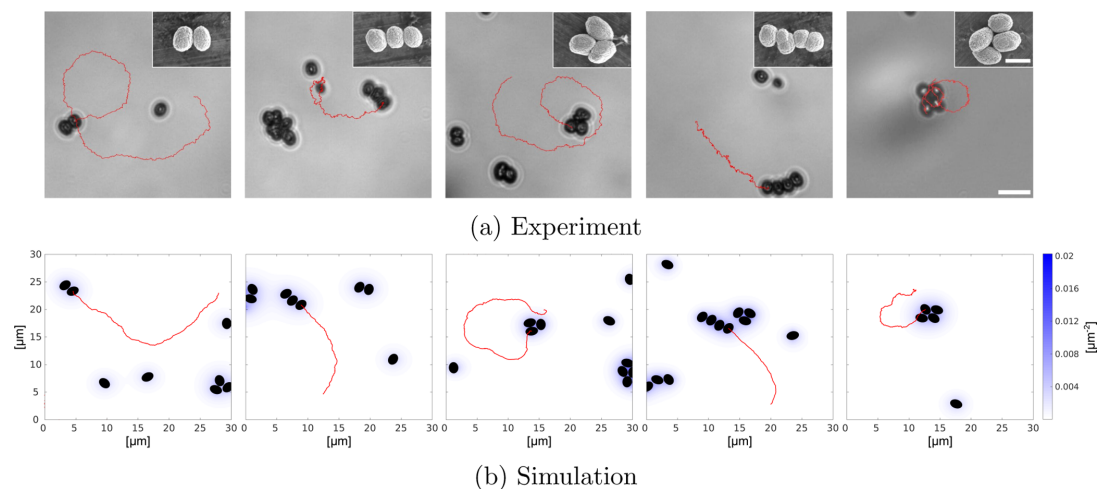


Figure 3. Exemplary tracks of modular swimmers after 20 s consisting of two to four particles in experiments and simulations. (a) Experimental tracks of two, three-caterpillar, three-triangle, four-caterpillar, and four-rectangle particle assembly. The scale bar is 5 μm . Insets represent SEM images of exemplary assembled particles with the corresponding structure. The inset scale bar is 2 μm . (b) Simulated tracks. The shown box length is $L = 30 \mu\text{m}$, and the color shows the concentration of the solute. Simulation parameters: $N = 60$, $L_{\text{box}} = 100 \mu\text{m}$, $k_0 = 70 \text{ s}^{-1}$, $k_d = 0.7 \times 10^3 \text{ s}^{-1}$, $\alpha/\gamma = \alpha_r/\gamma = 80 \times 10^3 \mu\text{m}^4 \text{ s}^{-1}$, $D_c = 1.4 \times 10^3 \mu\text{m}^2 \text{ s}^{-1}$, $D = 0.1 \mu\text{m}^2 \text{ s}^{-1}$, $D_r = 0.1 \text{ s}^{-1}$, and $\epsilon/\gamma = 100 \mu\text{m}^2 \text{ s}^{-1}$.

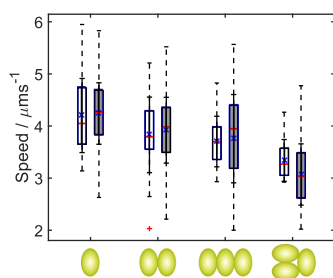


Figure 4. Mean speeds of swimmers consisting of one, two, and three particles under UV excitation. White boxes represent experimental data, whereas gray boxes show simulated data. Boxes indicate the interquartile range, the red line is the respective median, and dotted lines show the maximum and minimum values. For comparison, the mean values are marked with a blue cross (“ \times ”) and the standard deviation is displayed in solid black lines. The red cross represents an outlier data point. The simulation parameters are as in Figure 3.

pronounced for larger clusters. In the caterpillar configuration, for example, the chemical field produced by the central colloid attracts both of its neighbors and therefore hardly contributes to the motion of the cluster. However, it still provides drag and therefore effectively slows down the assembled swimmer. Note that in our simulations, we have chosen the same particle density as in our experiments. When choosing a higher particle density instead, larger aggregations form faster and are therefore more frequently present at a given time than for a low density. At late times, the clusters merge and form larger and larger clusters, finally resulting in one macrocluster containing most of the particles in our simulations.

Functionalized Particles and Active Assemblies. A strong advantage of modular microswimmers in terms of possible applications is the absence of the need to fit all desired functionalities into one single particle. Here, we demonstrate a

very versatile functionalization approach for our BiVO_4 swimmers. By coating the as-synthesized particles with a thin shell of silicon dioxide (SiO_2), we introduce a coupling possibility to a variety of different entities. Because of facile and universal coupling protocols, nontoxic SiO_2 has been used for decades as a carrier material, for example, fluorophores,³² drugs,³³ and enzymes.³⁴ Figure 5a shows an exemplary

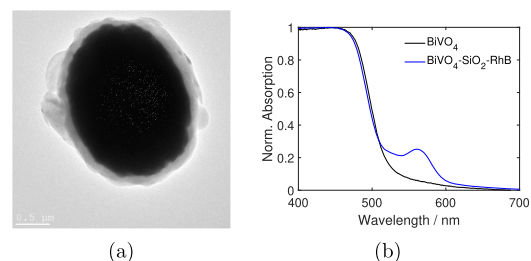


Figure 5. Material properties of SiO_2 -coated particles. (a) TEM image of a SiO_2 shell-coated BiVO_4 particle. (b) DRS spectra of pristine and RhB-functionalized swimmers. The band gap remains unaffected by the functionalization, and the absorption peak of the dye appears.

transmission electron microscopy (TEM) image of a successfully coated BiVO_4 particle. Scanning TEM in combination with energy-dispersive X-ray spectroscopy (STEM-EDX) confirms the SiO_2 identity of the shell (see Figure S5), which is around 150 nm thick.

We now modify the silica shell with different functional groups to demonstrate the functionality of this process. First, we bind the fluorescent dye rhodamine B (RhB) to distinguish shelled and pristine swimmers by fluorescence. Figure 5b confirms the successful coupling to the dye by an additional peak appearing in the DRS spectrum, which can be identified as the absorption peak of RhB. The speed of these

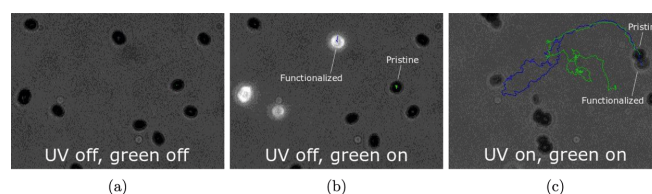


Figure 6. Microscope snapshots of mixed pristine and RhB-functionalized particles. (a) Particles without green or UV illumination. (b) Particles under green illumination. The functionalized particles absorb the light and can be detected via fluorescence of the dye. (c) Particles under green and UV illumination after 45 s. A combined swimmer consisting of a pristine (green trajectory) and a functionalized (blue trajectory) module is formed. For better recognizability, the concerned fluorescent particle has been marked in (b,c). As the dye bleaches over time, detection becomes more challenging.

functionalized swimmers remains almost unchanged compared to that of single pristine swimmers at $4.19 \pm 0.48 \mu\text{m s}^{-1}$, suggesting a certain porosity of the SiO_2 shell. Also, the surface charge of these swimmers remains negative (zeta potential: -22.4 mV) as SiO_2 commonly has a negative zeta potential at neutral pH values. Figure 6 shows a mixture of functionalized and pristine swimmers under the microscope. Whereas in Figure 6a, all particles optically appear to be the same, illumination with green light (555 nm) excites RhB and reveals three fluorescent particles in Figure 6b. If additionally UV light is turned on, the particles start to move actively and form assemblies consisting of fluorescent and pristine units, as can be seen in Figure 6c. See also Video S4 for more examples of mixed assemblies.

Second, we also modified our silica shell with (3-aminopropyl)triethoxysilane (APTES) to invert the surface charge to positive, caused by positively charged amino groups which lead to a zeta potential of $+41.0 \text{ mV}$ at neutral pH. By this, we overcome the limitation to negatively charged substrates as swimmer environments and broaden the possible field of application to more complex environments. We demonstrate successful active motion on positively charged surfaces (see Figure S6), which would otherwise lead to attractive forces between particles and the surface and therefore inhibit active motion.

The formation of combined assemblies with and without functionality demonstrated here opens up numerous functionalization opportunities for photochemical microswimmers, without concerns about numerous fabrication steps that inhibit upscaling. We envision that these results pave the way for the development and application of multifunctional modular swimmers and their theoretical understanding.

CONCLUSIONS

To summarize, in this article, we develop modular microswimmers made from BiVO_4 that are able to undergo self-propelled motion without any asymmetrization step in the manufacturing process, overcoming the throughput limits of hemispherical metal coating and enabling large-scale microswimmer synthesis. After irradiation with UV light, individual modules start moving and eventually meet their peers to form assemblies. We explore their motion experimentally as well as in numerical simulations, finding excellent agreement between both. We furthermore apply analytical calculations to understand speed distributions as well as motion patterns of these active assemblies. The present work broadens the variety of active components available for modular microswimming, adding the options of photocatalytic propulsion as well as new shapes.

In a second part, we demonstrate that the developed modular microswimmers serve as a useful platform for implementing functionalities. In particular, we show that neither the motility nor the formation of assemblies is inhibited by covering the individual spheroids by a thin silica layer. This coverage allows multiple functionalizations to increase the range of capabilities beyond simple self-propulsion. To exemplify this, we add a fluorescent dye to improve detection and facilitate discrimination between the pristine and functionalized modules. We also demonstrate an inversion of the surface charge from negative to positive by functionalizing the silica shell with APTES. This enables the swimmers to move on positively charged surfaces. In the future, it would be interesting to explore the large-scale collective behavior of BiVO_4 microswimmers, possibly leading to dynamic clustering,³⁵ and to examine BiVO_4 microswimmers with magnetic interactions. Different batches of modules can then be functionalized with different agents, paving the way for combining different tasks such as guidance, drug transport, sensing, or imaging in the final assembly.

EXPERIMENTAL SECTION

Synthesis of Bismuth Vanadate Microparticles. The synthesis is based on a protocol reported previously by Jiang et al. with some modifications.³⁶ Briefly, 2.5 mL of concentrated nitric acid and 2.78 g (15 mmol) of dodecylamine were added to 12.5 mL of a 1:1 ethanol/ethylene glycol mixture under stirring. Then, 2.425 g (5 mmol) of bismuth nitrate pentahydrate and 0.585 g (5 mmol) of ammonium metavanadate were added and dissolved. With 2 M NaOH in a 1:1 ethanol/ethylene glycol mixture, the pH was adjusted to 2. Next, the solution was transferred to a Teflon-lined stainless steel autoclave and left to ripen for 3 h. Subsequently, it was treated hydrothermally at $100 \text{ }^\circ\text{C}$ for 12 h. After centrifugation and repeated washing with ethanol and water, the sample was dried at $60 \text{ }^\circ\text{C}$ for 12 h and stored under air.

Silica Coating of Microparticles and Functionalization. To increase surface reactivity, 100 mg of bismuth vanadate microparticles was dispersed in 10 mL of 1 M nitric acid and sonicated for 15 min. After centrifugation, the supernatant was discarded and particles were redispersed in 10 mL of 0.01 M citric acid. After sonication for 15 min and centrifugation, 4 mL of deionized water and 4 μL of concentrated ammonia were added to the particles. In a glass vial, a mixture of 15 mL of ethanol, 4.7 mL of deionized water, and 0.3 mL of concentrated ammonia were prepared. After adding the particle dispersion to this vial, 100 μL of tetraethyl orthosilicate (TEOS) was added under vigorous stirring. After 20 min, another 100 μL of TEOS was added. After being stirred at room temperature overnight, the dispersion was centrifuged and washed with ethanol and deionized water before storing the sample in 1 mL of deionized water.

For functionalizing with rhodamine, 10 mg of RhB isothiocyanate was dissolved in 10 mL of dimethyl sulfoxide. After adding 8.6 μL of APTES under stirring, the solution labeled as RITC-APTES was

stirred overnight at room temperature and stored in the dark afterward. In a glass vial, 0.3 mL of the silica-coated bismuth vanadate particles was dispersed in 15 mL of isopropanol. After addition of 1.5 mL of concentrated ammonia, 100 μL of TEOS was added dropwise, followed by 150 μL of RITC–APTES. After being stirred overnight in the dark, particles were washed with ethanol and water extensively. To remove excess silica, the sample was centrifuged at 1000 rpm repeatedly and the supernatant was discarded. The particles were dispersed in deionized water and stored in the dark at 8 °C.

For functionalizing with APTES, 10 mg of SiO_2 -shelled BiVO_4 particles was dispersed in 10 mL of isopropanol. After addition of 1.5 mL of concentrated ammonia, particles were sonicated for 10 min. APTES (20 μL) was added under stirring at room temperature, and the solution was stirred overnight. After washing with ethanol and deionized water four times, the particles were dispersed in deionized water and stored under ambient conditions.

Microscopy Experiments. Experiments were conducted on an inverted Zeiss microscope with a Colibri 7 light source. Spheroidal BiVO_4 particles of a few milligrams were dispersed in deionized water and sonicated for 3 min. Then, samples were prepared on a 24 \times 24 mm glass slide by mixing 6.5 μL of deionized water with 3 μL of 1% H_2O_2 and 0.5 μL of BiVO_4 dispersion.

For experiments with functionalized/nonfunctionalized particle mixtures, 6 μL of deionized water, 3 μL of 1% H_2O_2 , and 0.5 μL of the functionalized and nonfunctionalized particle solutions each were combined on a 24 \times 24 mm glass slide. Samples were illuminated with a green (555 nm, 50 mW) light-emitting diode (LED) for RhB excitation and a UV (385 nm, 315 mW) or blue (469 nm, 230 mW) LED for propulsion.

For experiments with positively charged swimmers, substrates (cover glasses) were modified with APTES through a gas-phase reaction to induce a positive charge. Deionized water (6 μL), 3 μL of 1% H_2O_2 , and 1 μL of the particle solution were combined on the modified glass slide and illuminated with a UV LED for propulsion.

Scanning Electron Microscopy. For scanning electron microscopy (SEM) imaging, diluted solutions of BiVO_4 microparticles were drop-cast on aluminum tape-coated sample holders and dried overnight. The images were obtained using a Zeiss DSM 982 GEMINI electron microscope.

TEM. For TEM imaging, diluted solutions of microparticles were drop-cast on carbon-coated copper TEM grids and dried under vacuum overnight. Images were taken on an FEI Tecnai F30 microscope (300 kV). The same device was used for STEM.

Powder X-ray Crystallography. XRD patterns were acquired using a Bruker 2D phaser in a 2θ range of 10–100°, where symmetrical scans were performed. The microparticles were dispersed in ethanol and drop-cast on a Si wafer.

DRS. DRS measurements were recorded in diluted aqueous particle solutions using a Cary 60 spectrophotometer (Agilent Technologies).

Video Evaluation. Videos were tracked with the Fiji plugin TrackMate,³⁷ and the resulting trajectory files were processed with a MATLAB script and with the help of the msdalyzer function package.³⁸ For single particles as well as each assembly configuration, the averaged instantaneous speeds over at least 400 frames (10 s) were calculated for at least 20 independent trajectories from different sessions. The average of these speeds was calculated to determine the mean speed of a specific assembly conformation. The MSD curves were calculated with the msdalyzer function as well, and the weighted average of several curves was determined for the MSD.

Model. To model our experimental findings, we consider an ensemble of N overdamped spheroidal colloids at position \mathbf{r}_i and with orientation $\hat{\mathbf{u}}_i$ in two spatial dimensions, where i is the particle index. The photochemical reaction on the particles causes an asymmetric internal distribution of electrons and holes, and hence, a chemical concentration field (or “solute”) $c(\mathbf{r}, t)$ is asymmetrically produced (catalyzed) with a rate k_0 (see Figure 7) to which all colloids in the system respond. Effectively, the production occurs predominantly along one of the long sides of the spheroids which causes both self-propulsion and cross-interactions among the particles such that no explicit self-propulsion term is required in our equations of motion

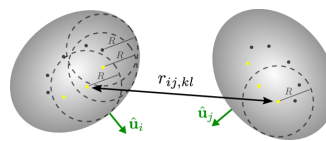


Figure 7. Schematic of the implementation of the model: two spheroidal colloids constructed by an arrangement of partly overlapping spheres with radius R and segment–segment distance $r_{ij,kl}$. The solute is produced on one long side of the colloids (yellow marked segments).

(similar to that in ref 39). To describe the dynamics of the particle motion, we use Langevin equations ($i = 1, \dots, N$) coupled to the self-produced chemical field $c(\mathbf{r}, t)$ ^{40–43}

$$\begin{aligned} \mathbf{f}_T \partial_t \mathbf{r}_i(t) &= \alpha \nabla_{\mathbf{r}_i} c - \nabla_{\mathbf{r}_i} V + \sqrt{2D} \mathbf{f}_T \boldsymbol{\eta}_i \\ \mathbf{f}_R \partial_t \hat{\mathbf{u}}_i(t) &= \alpha \nabla_{\hat{\mathbf{u}}_i} c - \nabla_{\hat{\mathbf{u}}_i} V + \sqrt{2D} \mathbf{f}_R \boldsymbol{\xi}_i \end{aligned} \quad (1)$$

Here, D is the diffusion coefficient of the particles, D_r is the effective rotational diffusion rate around the short axis of the particles, $\boldsymbol{\eta}_i(t)$ and $\boldsymbol{\xi}_i(t)$ represent unit-variance Gaussian white noise with zero mean, and $\nabla_{\hat{\mathbf{u}}_i}$ is the gradient on the unit circle (see refs 44 and 45). The matrices \mathbf{f}_T and \mathbf{f}_R represent the translational and rotational friction tensors determined by the Perrin coefficients for a spheroid⁴⁶ and the Stokes friction coefficient γ of a sphere of an equivalent volume, respectively. The coupling coefficient of the particles to the solute is denoted as α , where $\alpha > 0$ leads to phoretic attraction and $\alpha < 0$ results in phoretic repulsion among the colloids. In addition, V accounts for steric repulsions among the spheroids, represented by Weeks–Chandler–Anderson (WCA) repulsions here.

Details on the Implementation. For simplicity, we approximate each spheroidal colloid as a rigid body of m partly overlapping spheres, called “segments” in the following (see Figure 7). To describe the steric repulsions, we let all segment–segment pairs belonging to different particles interact through a repulsive WCA potential $V = \frac{1}{2} \sum_{i,j \neq i} V_{ij}$, where the sums run over all particles and where $V_{ij} = \frac{4\epsilon}{m^2} \sum_{k=1}^m \sum_{l=1}^m \left[\left(\frac{\sigma}{r_{ij,kl}} \right)^{12} - \left(\frac{\sigma}{r_{ij,kl}} \right)^6 \right] + \epsilon$ if $r_{ij,kl} \leq 2^{1/6} \sigma$ and 0 otherwise. Here, ϵ determines the strength of the potential, $r_{ij,kl}$ denotes the Euclidean distance between segment k of particle i and segment l of particle j , $r_c = 2^{1/6} \sigma$ indicates a cutoff radius beyond which the potential energy is 0, and $\sigma = 2R$ is the segment diameter.

The solute $c(\mathbf{r}, t)$ is produced on one long side of the particles (yellow marked segments at position $\mathbf{r}_{i,k}$ in Figure 7). The dynamics of c follows a diffusion equation (diffusion coefficient D_c), with additional (point) sources. In addition, we also use a sink term to describe a possible decay (e.g., due to bulk reactions) of the solute.

$$\partial_t c(\mathbf{r}, t) = D_c \Delta c - k_d c + k_0 \sum_{i=1}^N \sum_{k=k'}^N \delta(\mathbf{r} - \mathbf{r}_{i,k}) \quad (2)$$

The system of equations (eqs 1, 2) is numerically solved in two spatial dimensions (2D) with periodic boundary conditions.

Mean Velocity. The averaged velocities of the “molecular swimmers” consisting of one to three particles were calculated by averaging over at least 30 independent trajectories with a minimum time of 10 s and a sampling rate of 40/s (see Table 1). The relatively large standard deviation is due to the rather short trajectory length which has been used, in analogy to our experiments, to calculate the mean speed.

■ ASSOCIATED CONTENT

Supporting Information

The Supporting Information is available free of charge at <https://pubs.acs.org/doi/10.1021/acs.langmuir.0c01568>.

Additional characterization, size distribution histogram, zoomed-in SEM image, MSD data, additional assembly trajectories, analytic prediction of swimming velocities, STEM–EDX analysis, and snapshots of positively functionalized swimmers (PDF)

Motion pattern of single ellipsoid particles (0.3% H₂O₂, 100% UV illumination) (AVI)

Simulated motion pattern of single ellipsoid particles and assembly (activation after 3 s) (AVI)

Motion of different active assemblies (0.3% H₂O₂, 100% UV illumination) (AVI)

Formation and motion of functionalized active assemblies (0.3% H₂O₂, 100% green illumination, 100% UV illumination) (AVI)

AUTHOR INFORMATION

Corresponding Author

Juliane Simmchen – Physical Chemistry, TU Dresden, 01069 Dresden, Germany; orcid.org/0000-0001-9073-9770; Phone: +49 351 463-37433; Email: juliane.simmchen@tu-dresden.de

Authors

Sandra Heckel – Physical Chemistry, TU Dresden, 01069 Dresden, Germany

Jens Grauer – Theoretical Physics II: Soft Matter, Heinrich Heine University Düsseldorf, 40225 Düsseldorf, Germany

Maria Semmler – Physical Chemistry, TU Dresden, 01069 Dresden, Germany

Thomas Gemming – Institute of Complex Materials, Leibniz IFW Dresden, 01069 Dresden, Germany

Hartmut Löwen – Theoretical Physics II: Soft Matter, Heinrich Heine University Düsseldorf, 40225 Düsseldorf, Germany

Benno Liebchen – Institute of Condensed Matter Physics, TU Darmstadt, 64289, Germany

Complete contact information is available at:

<https://pubs.acs.org/10.1021/acs.langmuir.0c01568>

Notes

The authors declare no competing financial interest.

ACKNOWLEDGMENTS

The authors thank Helena Decker for TEM images. This work was supported by a Freigeist fellowship from the Volkswagen foundation (grant number 91619) and by the DFG within the project LO 418/17-2.

REFERENCES

- Jurado-Sánchez, B.; Pacheco, M.; Rojo, J.; Escarpa, A. Magnetocatalytic Graphene Quantum Dots Janus Micromotors for Bacterial Endotoxin Detection. *Angew. Chem., Int. Ed.* **2017**, *56*, 6957–6961.
- Sonntag, L.; Simmchen, J.; Magdanz, V. Nano- and Micromotors Designed for Cancer Therapy. *Molecules* **2019**, *24*, 3410.
- Wang, L.; Kaeppler, A.; Fischer, D.; Simmchen, J. Photocatalytic TiO₂ Micromotors for Removal of Microplastics and Suspended Matter. *ACS Appl. Mater. Interfaces* **2019**, *11*, 32937–32944.
- Wang, W.; Lv, X.; Moran, J. L.; Duan, S.; Zhou, C. A practical guide to active colloids: choosing synthetic model systems for soft matter physics research. *Soft Matter* **2020**, *16*, 3846.
- Shemi, O.; Solomon, M. J. Self-Propulsion and Active Motion of Janus Ellipsoids. *J. Phys. Chem. B* **2018**, *122*, 10247–10255.
- Yu, T.; Chuphal, P.; Thakur, S.; Reigh, S. Y.; Singh, D. P.; Fischer, P. Chemical micromotors self-assemble and self-propel by spontaneous symmetry breaking. *Chem. Commun.* **2018**, *54*, 11933–11936.
- Wang, Z.; Wang, Z.; Li, J.; Tian, C.; Wang, Y. Active colloidal molecules assembled via selective and directional bonds. *Nat. Commun.* **2020**, *11*, 2670.
- Simmchen, J.; Baeza, A.; Ruiz, D.; Esplandiu, M. J.; Vallet-Regí, M. Asymmetric hybrid silica nanomotors for capture and cargo transport: Towards a novel motion-based DNA sensor. *Small* **2012**, *8*, 2053–2059.
- Niu, R.; Palberg, T. Modular approach to microswimming. *Soft Matter* **2018**, *14*, 7554–7568.
- Ebbens, S.; Jones, R. A.; Ryan, A. J.; Golestanian, R.; Howse, J. R. Self-assembled autonomous runners and tumblers. *Phys. Rev. E: Stat., Nonlinear, Soft Matter Phys.* **2010**, *82*, No. 015304(R).
- Nourhani, A.; Brown, D.; Pletzer, N.; Gibbs, J. G. Engineering Contactless Particle-Particle Interactions in Active Microswimmers. *Adv. Mater.* **2017**, *29*, 1703910.
- Krüger, C.; Bahr, C.; Herminghaus, S.; Maass, C. C. Dimensionality matters in the collective behaviour of active emulsions. *Eur. Phys. J. E* **2016**, *39*, 64.
- Niu, R.; Fischer, A.; Palberg, T.; Speck, T. Dynamics of Binary Active Clusters Driven by Ion-Exchange Particles. *ACS Nano* **2018**, *12*, 10932–10938.
- Niu, R.; Botin, D.; Weber, J.; Reinmüller, A.; Palberg, T. Assembly and Speed in Ion-Exchange-Based Modular Phoretic Microswimmers. *Langmuir* **2017**, *33*, 3450–3457.
- Liebchen, B.; Niu, R.; Palberg, T.; Löwen, H. Unraveling modular microswimmers: From self-assembly to ion-exchange-driven motors. *Phys. Rev. E* **2018**, *98*, 052610.
- Kei Cheang, U.; Meshkati, F.; Kim, H.; Lee, K.; Fu, H. C.; Kim, M. J. Versatile microrobotics using simple modular subunits. *Sci. Rep.* **2016**, *6*, 30472.
- Yan, J.; Han, M.; Zhang, J.; Xu, C.; Luijten, E.; Granick, S. Reconfiguring active particles by electrostatic imbalance. *Nat. Mater.* **2016**, *15*, 1095–1099.
- Ma, F.; Wang, S.; Wu, D. T.; Wu, N. Electric-field-induced assembly and propulsion of chiral colloidal clusters. *Proc. Natl. Acad. Sci. U.S.A.* **2015**, *112*, 6307–6312.
- Schmidt, F.; Liebchen, B.; Löwen, H.; Volpe, G. Light-controlled assembly of active colloidal molecules. *J. Chem. Phys.* **2019**, *150*, 094905.
- Mallory, S. A.; Cacciuto, A. Activity-assisted self-assembly of colloidal particles. *Phys. Rev. E* **2016**, *94*, 022607.
- Bär, M.; Großmann, R.; Heidenreich, S.; Peruani, F. Self-Propelled Rods: Insights and Perspectives for Active Matter. *Annu. Rev. Condens. Matter Phys.* **2020**, *11*, 441–466.
- Löwen, H. Active colloidal molecules. *Europhys. Lett.* **2018**, *121*, 58001.
- Martinez-Pedrero, F.; Massana-Cid, H.; Tierno, P. Assembly and Transport of Microscopic Cargos via Reconfigurable Photoactivated Magnetic Microdockers. *Small* **2017**, *13*, 1603449.
- Martinez-Pedrero, F.; Navarro-Argemí, E.; Ortiz-Ambríz, A.; Pagonabarraga, I.; Tierno, P. Emergent hydrodynamic bound states between magnetically powered micropropellers. *Sci. Adv.* **2018**, *4*, No. eaap9379.
- Heckel, S.; Simmchen, J. Photocatalytic BiVO₄ Microswimmers with Bimodal Swimming Strategies. *Adv. Intell. Syst.* **2019**, *1*, 1900093.
- Villa, K.; Novotný, F.; Zelenka, J.; Browne, M. P.; Ruml, T.; Pumera, M. Visible-Light-Driven Single-Component BiVO₄ Micromotors with the Autonomous Ability for Capturing Microorganisms. *ACS Nano* **2019**, *13*, 8135–8145.
- Tokunaga, S.; Kato, H.; Kudo, A. Selective preparation of monoclinic and tetragonal BiVO₄ with scheelite structure and their photocatalytic properties. *Chem. Mater.* **2001**, *13*, 4624–4628.
- Li, R.; Zhang, F.; Wang, D.; Yang, J.; Li, M.; Zhu, J.; Zhou, X.; Han, H.; Li, C. Spatial separation of photogenerated electrons and holes among {010} and {110} crystal facets of BiVO₄. *Nat. Commun.* **2013**, *4*, 1432–1437.

- (29) Li, R.; Han, H.; Zhang, F.; Wang, D.; Li, C. Highly efficient photocatalysts constructed by rational assembly of dual-cocatalysts separately on different facets of BiVO₄. *Energy Environ. Sci.* **2014**, *7*, 1369–1376.
- (30) Lardhi, S.; Cavallo, L.; Harb, M. Significant Impact of Exposed Facets on the BiVO₄ Material Performance for Photocatalytic Water Splitting Reactions. *J. Phys. Chem. Lett.* **2020**, *11*, 5497–5503.
- (31) Perry, R. W.; Holmes-Cerfon, M. C.; Brenner, M. P.; Manoharan, V. N. Two-Dimensional Clusters of Colloidal Spheres: Ground States, Excited States, and Structural Rearrangements. *Phys. Rev. Lett.* **2015**, *114*, 228301.
- (32) van Schooneveld, M. M.; Cormode, D. P.; Koole, R.; Van Wijngaarden, J. T.; Calcagno, C.; Skajaa, T.; Hilhorst, J.; 't Hart, D. C.; Fayad, Z. A.; Mulder, W. J. M.; Meijerink, A. A fluorescent, paramagnetic and PEGylated gold/silica nanoparticle for MRI, CT and fluorescence imaging. *Contrast Media Mol. Imaging* **2010**, *5*, 231–236.
- (33) Liong, M.; Angelos, S.; Choi, E.; Patel, K.; Stoddart, J. F.; Zink, J. I. Mesostuctured multifunctional nanoparticles for imaging and drug delivery. *J. Mater. Chem.* **2009**, *19*, 6251–6257.
- (34) Sun, J.; Zhang, H.; Tian, R.; Ma, D.; Bao, X.; Su, D. S.; Zou, H. Ultrafast enzyme immobilization over large-pore nanoscale mesoporous silica particles. *Chem. Commun.* **2006**, *1*, 1322–1324.
- (35) Palacci, J.; Sacanna, S.; Steinberg, A. P.; Pine, D. J.; Chaikin, P. M. Living crystals of light-activated colloidal surfers. *Science* **2013**, *339*, 936–940.
- (36) Jiang, H.; Dai, H.; Meng, X.; Ji, K.; Zhang, L.; Deng, J. Porous olive-like BiVO₄: Alchohydrothermal preparation and excellent visible-light-driven photocatalytic performance for the degradation of phenol. *Appl. Catal., B* **2011**, *105*, 326–334.
- (37) Tinevez, J.-Y.; Perry, N.; Schindelin, J.; Hoopes, G. M.; Reynolds, G. D.; Laplantine, E.; Bednarek, S. Y.; Shorte, S. L.; Eliceiri, K. W. TrackMate: An open and extensible platform for single-particle tracking. *Methods* **2017**, *115*, 80–90.
- (38) Tarantino, N.; Tinevez, J.-Y.; Crowell, E. F.; Boisson, B.; Henriques, R.; Mhlanga, M.; Agou, F.; Israël, A.; Laplantine, E. Tnf and il-1 exhibit distinct ubiquitin requirements for inducing NEMO-IKK supramolecular structures. *J. Cell Biol.* **2014**, *204*, 231–245.
- (39) Hauke, F.; Löwen, H.; Liebchen, B. Clustering-induced velocity-reversals of active colloids mixed with passive particles. *J. Chem. Phys.* **2020**, *152*, 014903.
- (40) Saha, S.; Golestanian, R.; Ramaswamy, S. Clusters, asters, and collective oscillations in chemotactic colloids. *Phys. Rev. E: Stat., Nonlinear, Soft Matter Phys.* **2014**, *89*, 062316.
- (41) Pohl, O.; Stark, H. Dynamic clustering and chemotactic collapse of self-phoretic active particles. *Phys. Rev. Lett.* **2014**, *112*, 238303.
- (42) Scagliarini, A.; Pagonabarraga, I. Non-equilibrium phases in suspensions of self-propelled colloidal particles controlled by phoretic mobility and hydrodynamics. *arXiv* **2016**, *2*, 1–8.
- (43) Liebchen, B.; Marenduzzo, D.; Pagonabarraga, I.; Cates, M. E. Clustering and Pattern Formation in Chemorepulsive Active Colloids. *Phys. Rev. Lett.* **2015**, *115*, 258301.
- (44) Baskaran, A.; Cristina Marchetti, M. Hydrodynamics of self-propelled hard rods. *Phys. Rev. E: Stat., Nonlinear, Soft Matter Phys.* **2008**, *77*, 011920.
- (45) Janssen, L. M. C.; Kaiser, A.; Löwen, H. Aging and rejuvenation of active matter under topological constraints. *Sci. Rep.* **2017**, *7*, 5667.
- (46) Perrin, F. Mouvement brownien d'un ellipsoïde—I. Dispersion diélectrique pour des molécules ellipsoïdales. *J. Phys. Radium* **1934**, *5*, 497–511.

Supporting Information

Active Assembly of Spheroidal Photocatalytic BiVO_4 Microswimmers

Sandra Heckel,[†] Jens Grauer,[‡] Maria Semmler,[†] Thomas Gemming,[¶] Hartmut
Löwen,[‡] Benno Liebchen,[§] and Juliane Simmchen^{*,†}

[†]*Physical Chemistry, TU Dresden, Zellescher Weg 19, 01069 Dresden, Germany*

[‡]*Theoretical Physics II: Soft Matter, Heinrich Heine University Düsseldorf, 40225
Düsseldorf, Germany*

[¶]*Institute of Complex Materials, Leibniz Institute for Solid State and Materials Research
Dresden, Helmholtzstrasse 3 20, 01069 Dresden*

[§]*Institute of Condensed Matter Physics, TU Darmstadt, 64289 Darmstadt, Germany*

E-mail: juliane.simmchen@tu-dresden.de

Phone: +49 351 463-37433

Supporting Videos

Table S1: Content of supporting videos.

No.	Title
1	Motion pattern of single ellipsoid particles
2	Simulated motion pattern of single ellipsoid particles and assembly
3	Motion of different active assemblies
4	Formation and motion of functionalized active assemblies

Size Distribution

Size distributions of particle length and width as well as a zoomed-in SEM image are displayed here to further illustrate the particle dimensions and the topology of their surface.

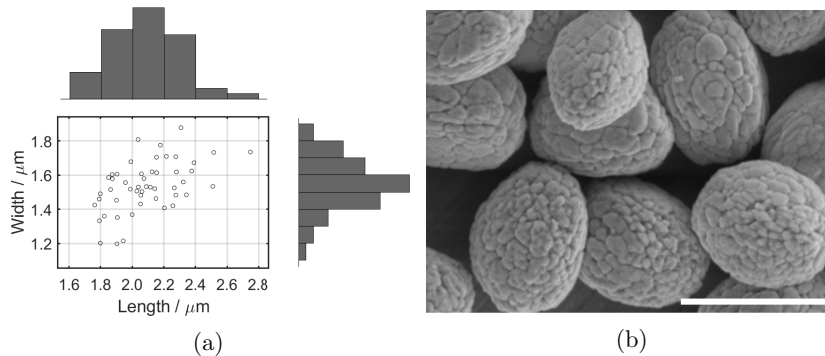


Figure S1: a) Size distribution of as-synthesized BiVO_4 spheroids in length and width. b) Zoom-in SEM image of BiVO_4 spheroids. The structured surface is a sign for the assembly of these spheroids out of smaller crystallites during the synthesis process. Scale bar is $2 \mu\text{m}$.

Comparison to Brownian Motion

For comparison, the average speed and mean-squared displacement (MSD) was calculated for the single spheroidal particles immersed in deionized water when no excitation by UV or blue light is present. The mean speed for these settings was calculated to be $3.49 \pm 0.54 \mu\text{m/s}$. Figure S2 shows the mean MSD curves of the particles in Brownian (blue) and directed (red) motion under UV light. The active component of the particle motion when excited with UV light is clearly shown by the non-linear shape of the red curve in Figure S2a. For better visualisation, Figure S2b shows the same data in a log-log plot. On very short timescales, both plots can be described as $MSD \propto \tau$. For slightly longer timescales, the ballistic red curve follows $MSD \propto \tau^2$ whereas the slope of the Brownian blue curve remains unchanged.

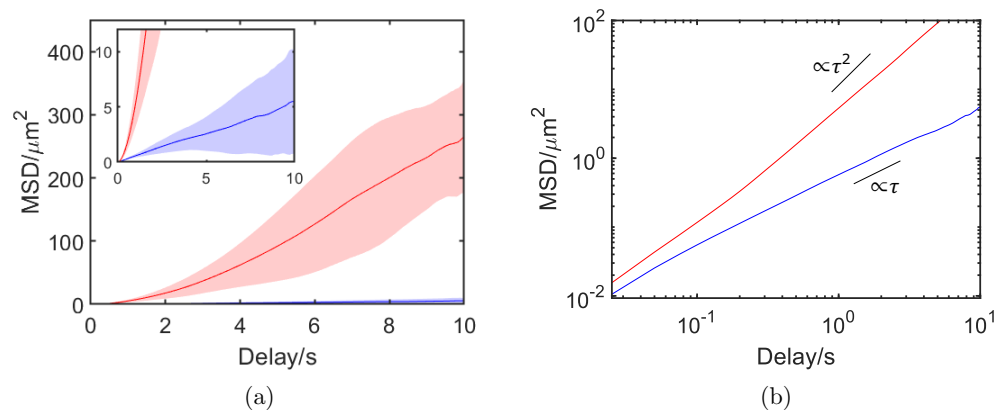


Figure S2: Mean MSD curves of particles in Brownian (blue) and directed motion under UV light (red). a) With standard deviations as error area. b) As log-log plot with $\propto \tau$ and $\propto \tau^2$ guides.

Trajectories of Assemblies

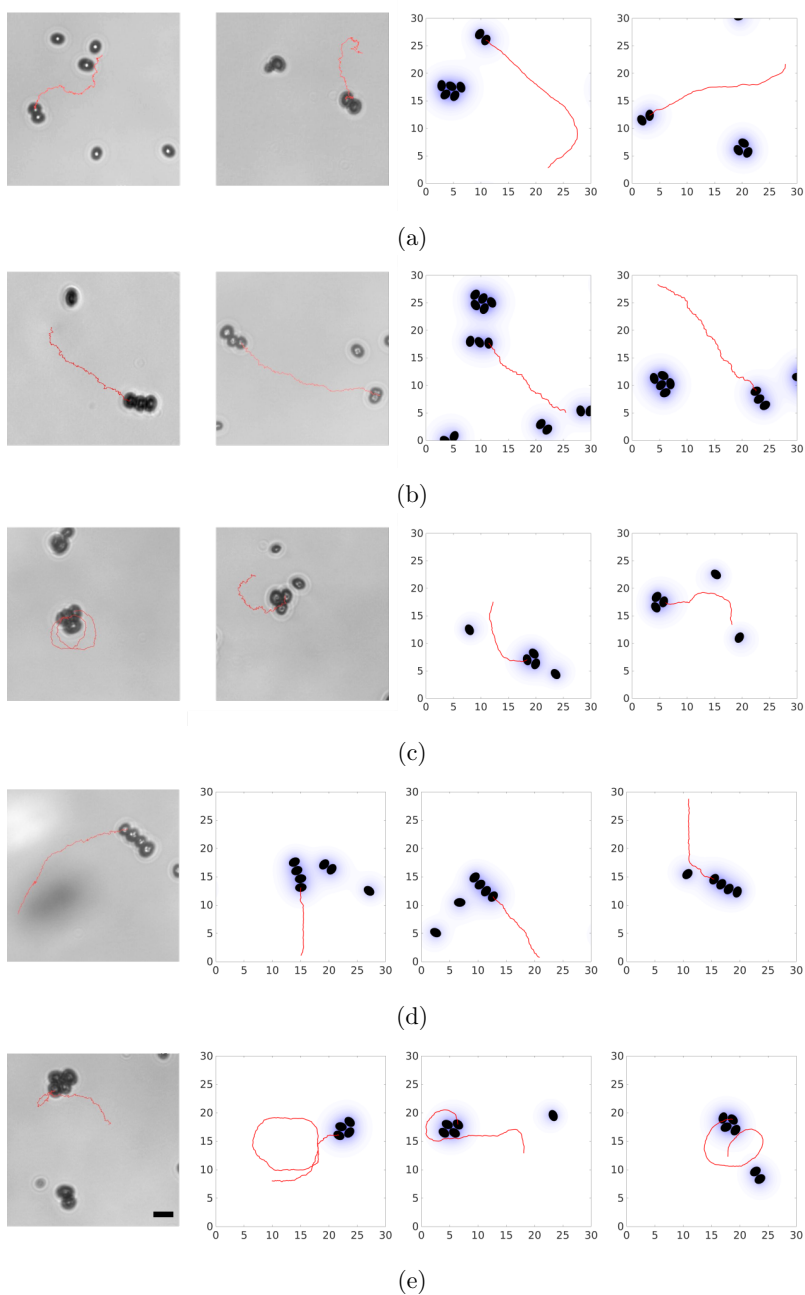


Figure S3: Additional trajectory examples of assemblies with 2-4 building blocks from experiments and simulations ($30 \times 30 \mu\text{m}$ area). Scale bar is $2 \mu\text{m}$.

Analytic prediction of swimming velocities

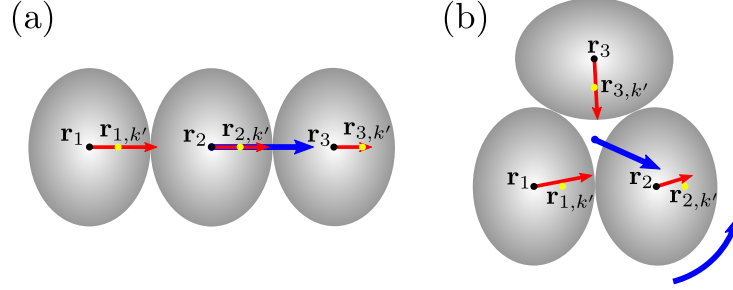


Figure S4: Model for the forces. The forces acting on the individual particles are indicated by red arrows for the caterpillar (a) and the triangle (b) assembly.

Each particle produces a chemical concentration field $c(r) = \frac{k_0}{D_c} K_0(\sqrt{\frac{k_d}{D_c}} r)$ (in two dimensions), where $K_0(x)$ is a Macdonald function, r describes the radial distance from the production source, diffusion coefficient D_c , production rate k_0 and decay rate k_d . This concentration field results in a force $F(r) = \alpha \partial_r c$ acting on the particles, such that the force on particle i reads (indicated by red arrows in Fig. S4)

$$\mathbf{F}_i = \sum_{j=1}^N \frac{\mathbf{r}_{j,k'} - \mathbf{r}_i}{|\mathbf{r}_{j,k'} - \mathbf{r}_i|} F(|\mathbf{r}_{j,k'} - \mathbf{r}_i|), \quad (\text{S1})$$

where \mathbf{r}_i is the position of particle i and $\mathbf{r}_{j,k'}$ is the position of the production source of particle j (for simplicity we assume that the solute is produced only at the location of a single segment $\mathbf{r}_{j,k'}$ which is shifted by a distance $w/4$ from the particle center, as shown in Fig. S4). The sum of these forces $\mathbf{F}_{COM} = \sum_{i=1}^{N_m} \mathbf{F}_i$ is decisive for its velocity, where the sum runs over all N_m modules of the assembly. We now demonstrate an approximation for the analytical calculation of the swimming speeds for the modular swimmer shown in Fig. S4. In particular we approximate the overall Stokes drag for an aggregate by the sum of bulk Stokes drag contributions of the individual spheroids. In the coordinate system of the center of mass of the assembly in panel (a), the coordinate vectors of the three spheroidal particles

with width $w = 1.5\mu\text{m}$ and length $l = 2\mu\text{m}$ read:

$$\begin{aligned}\mathbf{r}_1 &= (-w, 0, 0), \\ \mathbf{r}_2 &= (0, 0, 0), \\ \mathbf{r}_3 &= (w, 0, 0), \\ \mathbf{r}_{1,k'} &= \mathbf{r}_1 + (w/4, 0, 0), \\ \mathbf{r}_{2,k'} &= \mathbf{r}_2 + (w/4, 0, 0), \\ \mathbf{r}_{3,k'} &= \mathbf{r}_3 + (w/4, 0, 0).\end{aligned}$$

From that we can estimate the force F_{COM} acting on the modular swimmer (blue arrows in Fig. S4) whose velocity can then be calculated as:

$$|\mathbf{v}| = \frac{|\mathbf{F}_{COM}|}{N_m \gamma} = \frac{2.71 F_s}{3\gamma} = \frac{2.71 v_s}{3} = 3.79 \frac{\mu\text{m}}{\text{s}}. \quad (\text{S2})$$

Here we have used the relation $v_s = \frac{F_s}{\gamma}$, where F_s is the strength of the self-propulsion of a single particle with the mean velocity $v_s = 4.2 \frac{\mu\text{m}}{\text{s}}$ obtained from the experiment and γ is the Stokes friction coefficient.

For the structure in panel (b) of Fig. S4 we have

$$\begin{aligned}\mathbf{r}_1 &= (-w/2, -(l+w)/6, 0), \\ \mathbf{r}_2 &= (w/2, -(l+w)/6, 0), \\ \mathbf{r}_3 &= (0, (l+w)/3, 0), \\ \mathbf{r}_{1,k'} &= \mathbf{r}_1 + (w/4, 0, 0), \\ \mathbf{r}_{2,k'} &= \mathbf{r}_2 + (w/4, 0, 0), \\ \mathbf{r}_{3,k'} &= \mathbf{r}_3 + (0, -w/4, 0)\end{aligned}$$

and can thus determine the velocity of the ‘‘triangle’’ assembly to

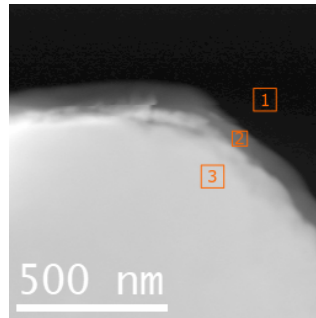
$$|\mathbf{v}| = \frac{|\mathbf{F}_{COM}|}{N_m \gamma} = \frac{2.09 F_s}{3 \gamma} = \frac{2.09 v_s}{3} = 2.93 \frac{\mu\text{m}}{\text{s}}. \quad (\text{S3})$$

Here the forces additionally lead to a torque, which is determined by

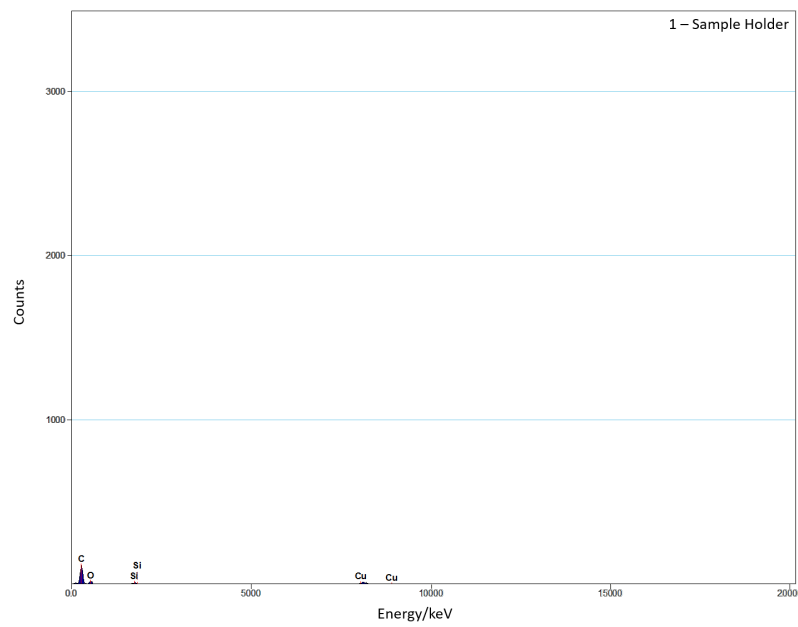
$$\mathbf{M} = \sum_{i=1}^{N_m} \mathbf{r}_i \times \mathbf{F}_i = (0, 0, 1.07 F_s \mu\text{m}). \quad (\text{S4})$$

and which leads to the rather curved trajectory of the triangle conformation.

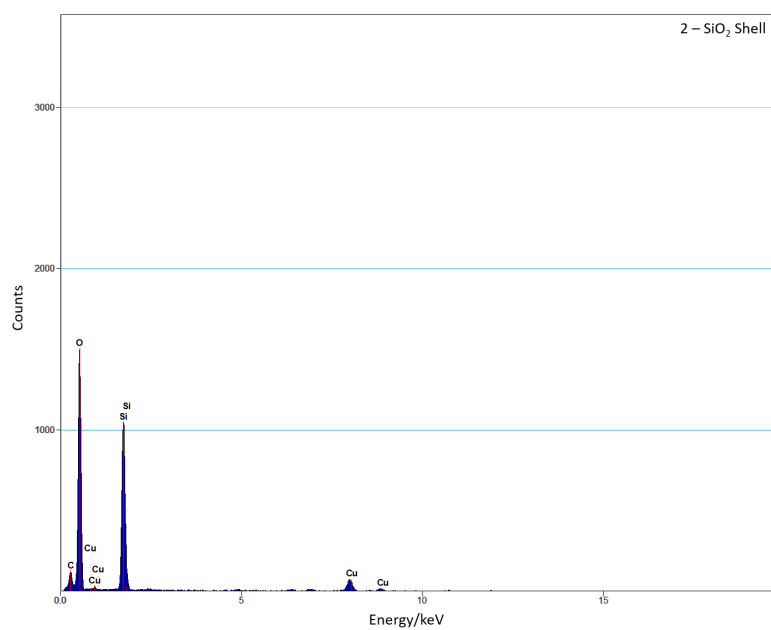
STEM-EDX Analysis



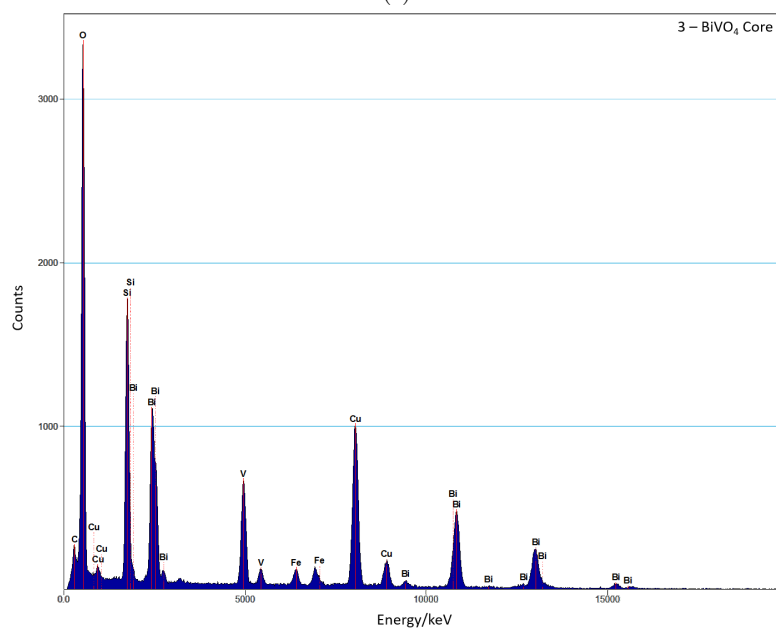
(a)



(b)



(c)



(d)

Figure S5: EDX data of SiO₂-coated BiVO₄ particles. a) STEM image with designated areas 1-3 for EDX measurements. b) EDX spectrum of specimen support, c) EDX spectrum of particle shell, d) EDX spectrum of the particle core and shell.

Positively functionalized swimmers

By functionalizing the silica shell of our BiVO_4 particles with (3-aminopropyl)triethoxysilane (APTES), we enable motion on positively charged substrates, which would otherwise lead to attraction between the swimmer and the surface. The surfaces (cover glasses) were positively functionalized by coating them with APTES as well. When immersed in a solution containing hydrogen peroxide and irradiating them with UV light, the particles move actively and do not stick to the surface, as can be seen in Figure S6.

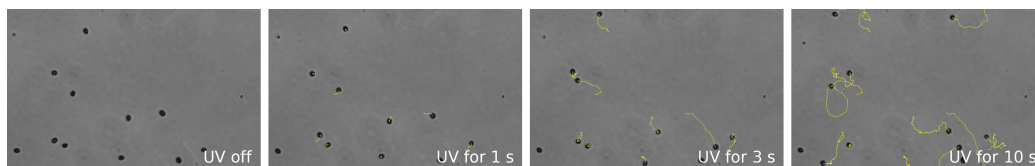


Figure S6: Snapshots of APTES-functionalized swimmers actively moving on a positive substrate under UV illumination after 1, 3 and 10 seconds. Normally, oxidic particles like BiVO_4 and SiO_2 have a negative zeta potential and therefore show no motion on positive substrates.

8.3 Paper III: Active Droploids

Reproduced from

J. Grauer, F. Schmidt, J. Pineda, B. Midtvedt, H. Löwen, G. Volpe & B. Liebchen
Active Droploids
Nat. Commun. **12**, 6005 (2021)

Digital Object Identifier (DOI): <https://doi.org/10.1038/s41467-021-26319-3>

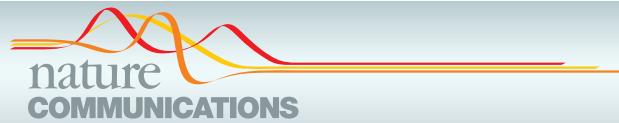
See also the related article *Motorisierte Tröpfchen* in Physik in unserer Zeit 53(1), pages: 9-10 (2022)

Statement of contribution

H.L., B.L. and I developed the theoretical model. I performed the simulations, analyzed the numerical and experimental data, and prepared the figures and manuscript for publication. F.S. and G.V. planned the experiments. F.S. performed the experiments and analyzed the experimental data. J.P. and B.M. quantitatively tracked the colloids. All authors discussed the results, and wrote or edited the manuscript.

Copyright and license notice

This article is licensed under a Creative Commons Attribution 4.0 International License, which permits use, sharing, adaptation, distribution and reproduction in any medium or format, as long as you give appropriate credit to the original author(s) and the source, provide a link to the Creative Commons license, and indicate if changes were made. To view a copy of this license, visit <http://creativecommons.org/licenses/by/4.0/>



ARTICLE

<https://doi.org/10.1038/s41467-021-26319-3>

OPEN

Active droplids

Jens Grauer^{1,4}, Falko Schmidt^{1,2,4}, Jesús Pineda^{1,2}, Benjamin Midtvedt², Hartmut Löwen¹, Giovanni Volpe^{1,2} & Benno Liebchen^{3✉}

Active matter comprises self-driven units, such as bacteria and synthetic microswimmers, that can spontaneously form complex patterns and assemble into functional microdevices. These processes are possible thanks to the out-of-equilibrium nature of active-matter systems, fueled by a one-way free-energy flow from the environment into the system. Here, we take the next step in the evolution of active matter by realizing a two-way coupling between active particles and their environment, where active particles act back on the environment giving rise to the formation of superstructures. In experiments and simulations we observe that, under light-illumination, colloidal particles and their near-critical environment create mutually-coupled co-evolving structures. These structures unify in the form of active superstructures featuring a droplet shape and a colloidal engine inducing self-propulsion. We call them active droplids—a portmanteau of droplet and colloids. Our results provide a pathway to create active superstructures through environmental feedback.

¹Institut für Theoretische Physik II: Weiche Materie, Heinrich-Heine-Universität Düsseldorf, D-40225 Düsseldorf, Germany. ²Department of Physics, University of Gothenburg, SE-41296 Gothenburg, Sweden. ³Institut für Physik der kondensierten Materie, Technische Universität Darmstadt, D-64289 Darmstadt, Germany. ⁴These authors contributed equally: Jens Grauer, Falko Schmidt. ✉email: benno.liebchen@pkm.tu-darmstadt.de

ARTICLE

NATURE COMMUNICATIONS | <https://doi.org/10.1038/s41467-021-26319-3>

Active matter consists of microscopic objects which are capable of self-propulsion, such as motile microorganisms, like *Escherichia coli* bacteria¹, and synthetic colloidal microswimmers, like autophoretic Janus colloids^{2,3}. In contrast to equilibrium systems, active-matter systems evade the rules of equilibrium thermodynamics by continuously dissipating the energy obtained from their environment and converting part of it into a persistent motion at the level of individual constituents. Thus, the environment acts as a persistent free-energy source that emancipates active systems from the fundamental constraint of entropy maximization (or free-energy minimization) and induces a rich phenomenology, which is fundamentally beyond equilibrium physics. This includes, in particular, the spontaneous emergence of spatiotemporal patterns^{3,4}, e.g., through liquid–liquid phase separation^{5–7}, which illustrates the remarkable fact that driving systems far away from equilibrium often creates structures, not chaos.

Two key examples of self-driven agents are active colloids⁸ and active droplets^{9,10}. These are ideal model systems providing fundamental insights into the principles that govern the dynamical behavior of self-organized structures^{11,12}. Active colloids catalyze reactions on part of their surface resulting in self-propulsion and collective self-organization as, e.g., living clusters^{2,13–18}, swarms^{19,20} and phase-separating macrostructures²¹. Active droplets exhibit complex dynamical behavior down to the level of individual droplets, where, e.g., chemical reactions drive them out of equilibrium and can influence the droplet formation process through growth suppression²² or spontaneous droplet division²³. Recent studies have also demonstrated internally propelled droplets, where a dense suspension of motile bacteria encapsulated in an emulsion droplet is able to transfer activity to the droplet, making it active^{24,25}.

In all these examples, and other typical active-matter systems, the environment serves as a continuous free-energy source which can also mediate effective interactions between active agents, such as hydrodynamic interactions synchronizing filaments²⁶ or interactions based on visual perception²⁷, acoustic signals²⁸, or chemical fields²⁹—but it does not typically show intrinsic dynamics that adapts to the dynamics of the active agents. In contrast, biological systems often feature a two-way coupling with their environment, which is involved, e.g., in homeostasis, gene-expression regulation, and structure formation^{30,31}, calling for synthetic realizations to enable a controllable exploration of two-way feedback coupled systems.

Here, we experimentally realize and theoretically model a versatile feedback loop between light-activated colloids and their near-critical environment. This leads to structure formation both on the level of the colloids and their environment and results in the formation of a new type of self-propelling superstructures.

As these active superstructures combine droplets and colloids, we name them active droplids. To realize this feedback loop and the corresponding structure formation processes in the environment, we suspend a mixture of colloids in a near-critical solvent. When illuminated by laser light, these colloids absorb the light, locally heat up their surrounding environment and induce a local phase separation, which leads to the emergence of droplets around the colloids (see Fig. 1a). In turn, these droplets encapsulate the colloids, which under confinement interact non-reciprocally and form self-assembled colloidal engines, which finally drive the droplid superstructures, making them active (see Fig. 1a). Note that, crucially, both the colloids and the droplets continuously evolve in time, rather than adiabatically following the respective other component, which is fundamental to the droplids' structure formation and self-propulsion ability. Our findings offer a novel route to create superstructured soft active materials whose size and motility is controllable by laser light. Since it is based on the two-way interaction between

colloidal particles and a near-critical environment, the involved mechanism of colloidal self-encapsulation and activation might also serve as a useful framework to recreate and explore aspects of fundamental biological processes in a well-controllable synthetic colloidal minimal system. Examples might comprise, e.g., processes which are involved in the compartmentalization of the cytoplasm and the formation of membrane-free organelles, which share various features with liquid droplets and do not need a stabilizing lipid bilayer to maintain themselves.

Results

Experimental observations of active droplids. We study a system of hydrophilic colloidal particles (radius $R = 0.49 \mu\text{m}$) quasi-two-dimensionally confined between two glass slides separated by a distance smaller than two particle diameters. These particles are immersed in a near-critical water–2,6-lutidine mixture, which has a critical lutidine composition $c_c^L = 28.4\%$ and a lower critical temperature $T_c = 34.1^\circ\text{C}$ ³². In this work, we use a slightly off-critical composition (29.4–32.4%) to ensure the formation of water-rich droplets around the hydrophilic particles when the mixture's temperature locally exceeds T_c . We fix the temperature of the sample at $T_0 = 32.5^\circ\text{C} < T_c$ using a water heatbath and a feedback temperature controller (see experimental setup in Supplementary Fig. 2).

We use two species of hydrophilic particles: light-absorbing and non-absorbing particles. In the absence of an external light source, both species perform passive Brownian motion with a diffusion coefficient of $D = 0.012 \pm 0.002 \mu\text{m}^2 \text{s}^{-1}$ and are homogeneously distributed in the sample chamber (Fig. 1b). The non-absorbing particles are less hydrophilic than the absorbing ones.

Under illumination with a defocused laser beam ($\lambda = 1070 \text{ nm}$, $I = 142 \mu\text{W} \mu\text{m}^{-2}$, beam waist $w = 100 \mu\text{m}$), light-absorbing particles raise the temperature of the surrounding liquid slightly above T_c , thus altering their local environment by inducing a local demixing of the liquid. This leads to the creation of local gradients of the mixture's temperature and composition, which phoretically attract other particles present nearby^{33–36}. In particular, this generates a non-reciprocal effective attraction of the non-absorbing particles by the absorbing ones leading to ballistically moving active molecules (Fig. 1c), Janus-dimers being the simplest example³⁶.

At comparatively large light intensities, where the system of active colloids induces local temperatures exceeding the critical temperature (i.e., $T \gg T_c$, Fig. 1d), we observe a stronger feedback between the particles and the environment: the absorbing colloids induce phase separation in their vicinity, which leads to the confinement of the active colloidal molecules within water-rich droplets immersed in a lutidine-rich background. Remarkably, we observe that these droplets can adopt the mobility of the active molecules which they comprise. This occurs because the colloidal molecules contained within a droplet constantly alter their local environment causing the droplet to follow the molecules' motion. Moreover, we find that the molecules' direction inside the droplet is reversed leading now with absorbing particles in front due to the local changes in composition³⁷. In this state, we observe the emergence of active droplids. Once formed, these active droplids move, collide, and merge with each other and consequently grow over time (Fig. 1e), until they eventually all coalesce into a large active droplid (Fig. 1f).

Model and simulations. Let us now build a minimalist theoretical model to identify the key ingredients and mechanisms determining the experimental observations described in the previous section. This model describes the combined dynamics and

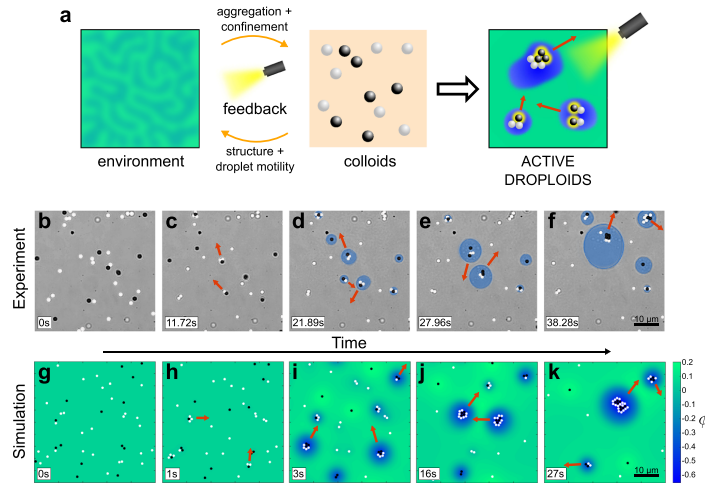


Fig. 1 Active droplet formation and growth. **a** Schematic of the light-induced two-way coupling (feedback loop) between the colloids and their environment which results in active droplets. **b–f** Experiment and **g–k** simulation of the formation and growth of active droplets. **b, g** Single particles of two species, light-absorbing (black) and non-absorbing (white), are immersed in a near-critical mixture and, at low temperature, behave as passive particles in a standard liquid. **c, h** Upon illumination, absorbing particles heat up the surrounding liquid, providing phoretic forces that bring and hold particles together to form small colloidal molecules that move in the direction of the red arrows. **d, i** Eventually, local phase separation leads to water-rich droplets (blue shading) surrounding absorbing particles and colloidal molecules. **e, j** Over time, the active droplets move together with their active molecules (direction indicated by the red arrows), grow in size, and **f, k** eventually coalesce together to form even larger active droplets. The light irradiation is $I = 150 \mu\text{W} \mu\text{m}^{-2}$, composition $\phi_0 = 0.05$ and initial temperature $T_0 = 32.5 \text{ }^\circ\text{C}$ (and $\lambda = 0.025$ in simulations, see 'Methods' for other parameter values). Videos of experiment (Supplementary Movie 1) and simulation (Supplementary Movie 2) are provided in SI.

feedback between the near-critical mixture and the colloidal particles.

The state of the mixture is defined by the order parameter field $\phi(\mathbf{r}, t)$, which represents the relative concentration difference between the two phases of the mixture: phase A (2,6-lutidine) and phase B (water). Thus, we have $\phi = 0$ in regions where A and B are homogeneously mixed, and $\phi = \pm 1$ in pure A and B regions, respectively.

The dynamics of the colloids is modeled as overdamped Brownian particles at positions $\mathbf{r}_i^s(t)$ following Langevin dynamics ($i = 1, \dots, N$, where N is the number of particles and $s \in \{a, \text{na}\}$ for absorbing and non-absorbing particles, respectively)

$$\gamma \partial_t \mathbf{r}_i^s(t) = \beta_s \nabla \phi + \alpha_s \nabla (\nabla \phi)^2 - \nabla_{\mathbf{r}_i} V + \sqrt{2D} \boldsymbol{\eta}_i^s, \quad (1)$$

where D is the translational diffusion coefficient of the particles, γ is the Stokes drag coefficient (assumed to be the same for both equally sized species), $\boldsymbol{\eta}_i^s(t)$ represents Gaussian white noise with zero mean and unit variance, and V accounts for steric repulsions between the colloids, represented by Weeks-Chandler-Anderson (WCA) interactions³⁸. The coupling to the composition field $\phi(\mathbf{r}, t)$ (environment) is described by the first two terms on the RHS of Eq. (1). The first term describes the net effect of wetting, i.e., the fact that hydrophilic particles ($\beta_s < 0$) are attracted by water-rich droplets, whereas hydrophobic particles ($\beta_s > 0$) tend to remain outside of these regions (see Supplementary Fig. 3). The second term, which is proportional to $\nabla(\nabla \phi)^2$, induces motion towards interfaces (where $(\nabla \phi)^2$ is large) essentially for the non-absorbing particles. This term describes the tendency of the weakly hydrophilic particles to move towards the water–lutidine interface in order to reduce the interfacial area of the water–lutidine interface and hence the total interfacial free energy of the system.

To model the phase separation dynamics induced by the light-absorbing particles, we use the Cahn-Hilliard equation³⁹ taking

into account an inhomogeneous temperature distribution $T(\mathbf{r}, t)$ as induced by the light-absorbing particles

$$\partial_t \phi(\mathbf{r}, t) = M \nabla^2 \left(a(T - T_c) \phi + b \phi^3 - \kappa \nabla^2 \phi + A_s \sum_{s \in \{a, \text{na}\}} \delta(\mathbf{r} - \mathbf{r}_i) \right), \quad (2)$$

where M is the inter-diffusion constant of the mixture, and T_c is the critical temperature, with constants $a < 0$ and $b, \kappa > 0$ such that the fluid demixes at locations where $T > T_c$. To describe the net effect of the accumulation of water at the hydrophilic surfaces of the colloids, we include a (point-like) source term for the solvent-composition at the position of each particle. The coefficients A_a and A_{na} are chosen such that they account for the strong and weak hydrophilicity of the absorbing and non-absorbing particles, respectively. As a result, the water concentration slightly increases at the location of each particle. Note that this increase alone cannot initiate phase separation, but it biases the location where water-rich droplets occur once phase separation takes place.

The two-way coupling between the nonequilibrium system of particles and its environment is controlled by the mixture concentration and the energy supply. The former is given by the order parameter field $\phi(\mathbf{r}, t)$, described above. The latter depends on the density of absorbing particles ρ_a and the light intensity $I(\mathbf{r})$, and involves a suitable source term for the absorbed power per unit volume $\frac{\alpha'}{\rho c_p} I(\mathbf{r}) \equiv k_0 \delta(\mathbf{r} - \mathbf{r}_i)$, where α' is the optical absorption coefficient, ρ is the density of the mixture, c_p is the specific heat at constant pressure, and k_0 is the strength of the light source at the particle position \mathbf{r}_i ⁴⁰. The inhomogeneous temperature field is then to be calculated from the heat equation as

$$\partial_t T(\mathbf{r}, t) = D_T \Delta T + k_0 \sum_{\text{absorb.}} \delta(\mathbf{r} - \mathbf{r}_i) - k_d (T - T_0) \quad (3)$$

with diffusion constant D_T . Here, the decay rate k_d describes the

ARTICLE

NATURE COMMUNICATIONS | <https://doi.org/10.1038/s41467-021-26319-3>

coupling of the sample to an external water heatbath stabilizing the temperature (see SI for a detailed description of the experimental setup and methods for the equations of motion). Overall, this permits us to introduce a concise measure of the energy input under the approximation that the adsorbed energy scales linearly with the density of the absorbing particles and the irradiated light intensity as $\lambda = \frac{\rho_a k_0}{T_0 k_d}$.

Using the model we have described, we can investigate the complex dynamics involved in the formation of droplets and molecules including the involved feedback loop between the colloids and their near-critical environment. In particular, we are able to replicate in simulations all experimentally observed states, i.e., from passive disperse particles to ballistically moving active droplets (Fig. 1g–k).

Phase diagram. By continuously altering their local environment, absorbing particles create feedback loops that, depending on the criticality of the environment and the energy input to the system, induce assembly and disassembly of colloidal molecules and determine the dynamics of the colloid–droplet superstructure. To gain a systematic overview of the possible states achievable by this system, we now determine the full nonequilibrium state-diagram as a function of the composition order parameter ϕ_0 (see also phase diagram in Supplementary Fig. 1) and of the measure of the energy input into the system λ (see previous section). The resulting phase diagram after 30 s of light illumination is shown in Fig. 2 for $\phi_0 > 0$ (i.e., at supercritical 2,6-lutidine concentrations, $c^l > c_c^l$, leading to water-rich droplets in a lutidine-rich background). Similar and symmetric results can be observed for $\phi_0 < 0$ (i.e., $c^l < c_c^l$, where lutidine-rich droplets emerge in a water-rich background). Note that the different structures can dynamically move, coalesce, and grow over time (see also Fig. 3), but determining the different phases at much later times qualitatively produces the same phase diagram (see Supplementary Fig. 5).

As can be seen in Fig. 2a, we identify four distinct states differing in their level of activity and in the presence of droplets. At low energy input and at concentrations far away from the critical composition, we observe a disordered phase (purple region in Fig. 2a), which is characterized by randomly dispersed Brownian particles essentially behaving as passive particles at thermodynamic equilibrium (Fig. 2b, purple frame). Increasing the energy input, we observe an active molecules' phase (yellow region in Fig. 2a), where active and passive colloids come together to form active colloidal molecules (Fig. 2b, yellow frame).

The remaining two phases of the phase diagram are located at even higher energy inputs. In these cases, the temperature around absorbing particles and active colloidal molecules significantly exceeds the critical temperature ($T > T_c$), which induces a local phase separation of the mixture and results in the formation of water-rich droplets surrounding the absorbing particles and colloidal molecules. Subsequently, nearby colloids are absorbed into the droplet due to their own hydrophilicity, so that the colloidal molecules inside the droplets grow in size over time. This procedure permits a good observation of the influence of colloids on their environment, which deform the interface when entering the droplet or while moving alongside it (see Fig. 4a, b), which has also been observed for vesicles⁴¹. At a moderate energy input, we observe the active droplets' phase in our phase diagram (green region in Fig. 2a): the active colloidal molecules contained within a droplet manage to propel the droplet (Fig. 2b, green frame); thus, the droplets become active by themselves. Thus, active colloidal molecules contained inside a droplet act as internal motors that propel the droplet. Over time, these active droplets can collect other molecules and droplets, thereby growing in size and possibly altering their speed and direction of movement (see Supplementary Movies 1 and 2). The speed and growth process of the droplets can be controlled by light intensity as discussed in the following section.

At even higher energy inputs (achievable either by increasing the light intensity or by a higher density of absorbing particles), the

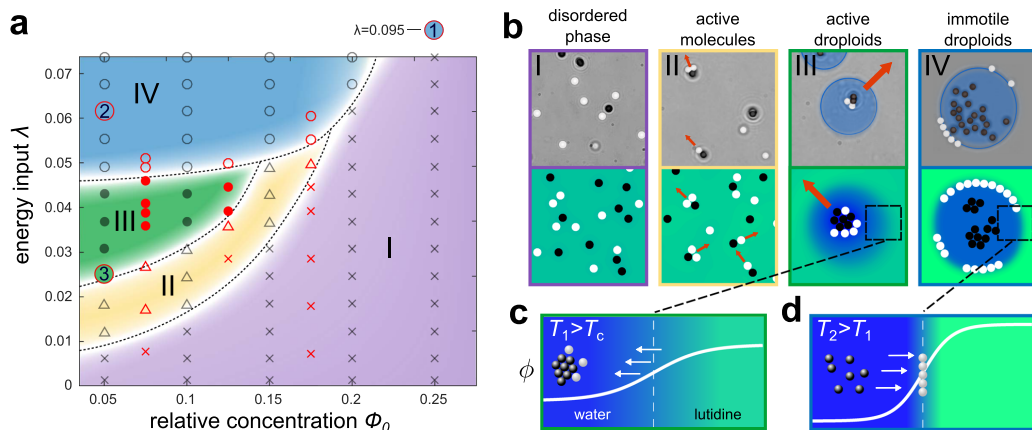


Fig. 2 Nonequilibrium phase diagram. **a** Phase diagram as a function of the net energy input λ and the averaged relative concentration difference from the critical point ϕ_0 . The evaluated state points from the experiment (red) fitted with $\lambda = C\lambda_a$ and $C = 1 \times 10^{-4} \mu\text{m}^4 \mu\text{W}^{-1}$, and the simulations (black) are indicated by crosses (purple region - disordered phase), triangles (yellow region - active molecules), filled circles (green region - active droplets), and empty circles (blue region - droplets with particles at the interface). Dashed lines indicate approximate boundaries between phases and serve as a guide to the eye. The quantitative criteria for the phases and the corresponding colors are given in the SI. The red-bordered numbers mark reference points that relate to different scenarios discussed in the main text. **b** Typical snapshots from experiments (top) and simulations (bottom) of the phases I–IV as indicated in the state diagram. Magnified concentration profiles of the composition in phases III (**c**) and IV (**d**) show that the gradient at the interface steepens as temperature locally increases from $T_1 > T_c$ (active droplets, phase III) to $T_2 > T_1$ (immotile droplets, phase IV). Simulation parameters can be found in ‘Methods’.

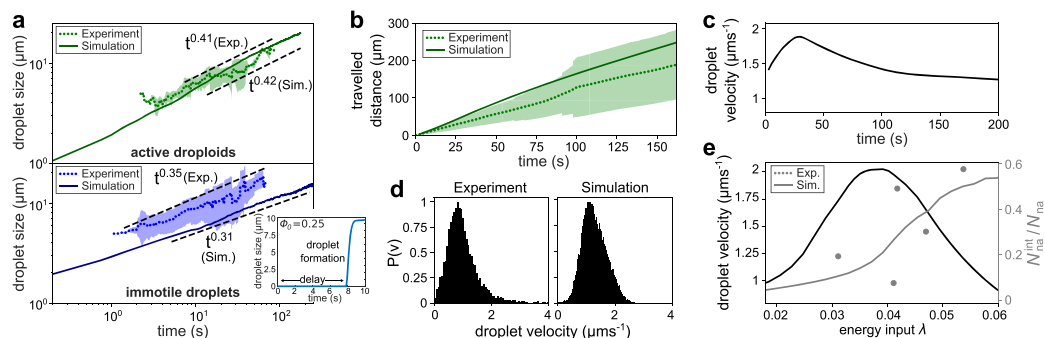


Fig. 3 Droplet velocity and growth over time. **a** Average size of active droplets (green) and immotile droplets (blue) over time calculated from experiments (dotted) and simulations (solid) for $\phi_0 = 0.05$. The shaded area represents the standard deviation. The inset shows the delay in the formation of an immotile droplet at early times for an off-critical composition of $\phi_0 = 0.25$. **b** Mean (and shaded standard deviation) of the total travelled distance of an active droplet over time measured from experiments (dotted) and simulations (solid). **c** Simulated active droplet velocity over time. **d** Velocity distribution of active droplets in experiments (left) and simulations (right). **e** Simulated mean velocity of active droplets after 30 s of light illumination (black curve) and fraction of non-absorbing particles located at the interface of the droplets N_{na}^{int}/N_{na} (gray curve simulations, gray dots experimental data) fitted with $\lambda = C/\rho_a$ and $C = 3 \times 10^{-4} \mu\text{m}^4 \mu\text{W}^{-1}$) as a function of the energy input λ for $\phi_0 = 0.05$. Note that the fitting factor C is different here than in Fig. 2 because the present measurements are based on a fixed concentration of $\phi_0 = 0.05$, whereas those in Fig. 2 have been taken at various concentrations up to $\phi_0 = 0.2$. The full list of simulation parameters is provided in the 'Methods' section.

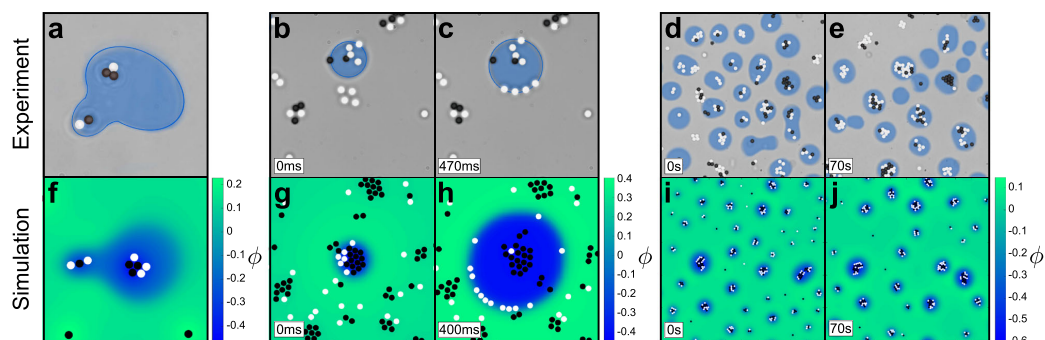


Fig. 4 Examples of droplet behavior. **a–e** Experimental snapshots (highlighting the segmentation of the droplets), and **f–j** simulated snapshots (background displays the relative concentration ϕ) of various behaviors: **a, f** Clusters of colloids deforming the boundary of the droplet at $\lambda = 0.03$. **b, c** and **g, h** Accumulation of absorbing particles in an off-critical supersaturated background phase ($\phi_0 = 0.2$ in experiments, $\phi_0 = 0.25$ in simulations) leading to an explosive formation of droplets within a very short time at $\lambda = 0.095$ (Supplementary Movies 3 and 4). **d, e** and **i, j** Formation of size-stabilized droplets around absorbing particles with periodic light illumination (on and off for 10 s each, Supplementary Movies 5 and 6) at $\lambda = 0.025$. Other simulation parameters can be found under 'Methods'.

induced temperatures greatly exceed the critical temperature ($T \gg T_c$) and result into a large phoretic gradient close to the interface of the droplet (Fig. 2d) compared to active droplets where the gradient is more moderate (Fig. 2c). Because the dynamics of the particles is mainly controlled by the interaction of their surface with the local composition of the mixture, non-absorbing particles, which are less hydrophilic than their absorbing counterpart, move towards the droplet's interface to reduce the total interfacial area of the system (Fig. 2b, blue frame). Consequently, the existing colloidal molecules break up with absorbing particles remaining at the center of the droplet and non-absorbing particles decorating its interface. The ensuing loss of motility characterizes this phase as the immotile droplets' phase (blue region in Fig. 2a).

Overall, the dynamics shown by this phase diagram shows that absorbing particles continuously alter their local environment, and, in turn, their behavior is affected by the environment. This feedback induces both assembly and disassembly of active

colloidal molecules and, therefore, determines the ensuing activity of the whole system of colloids and droplets.

Characterization and control of droplet dynamics and growth.

By tuning the external energy input and the mixture's criticality, we can control the degree of interaction between active colloids and their local environment, which determines the overall state of the system (Fig. 2) as well as its evolution over time.

We start by characterizing the overall growth of our system (Fig. 3a). At early times, the system is characterized by nucleation and formation of droplets initiated by light-absorbing particles. In this initial process, the droplets slowly grow over time as additional colloidal molecules diffuse from the bulk phase and contribute to the local heating that creates the droplet. The dominant growth process is therefore diffusion-limited and a droplet diameter $L \sim t^{1/2}$ is expected⁷.

ARTICLE

NATURE COMMUNICATIONS | <https://doi.org/10.1038/s41467-021-26319-3>

Using a composition of $\phi_0 = 0.25$ (marked with a red-bordered 1 in Fig. 2) which is far away from the critical composition, we observe that droplets form only after a significant initial delay. For off-critical compositions, the bulk phase is already supersaturated and a considerable (free-energy) barrier emerges, separating the mixed phase from complete phase separation (see Supplementary Fig. 1b). Consequently, a large accumulation of absorbing particles is required to provide sufficient local energy to overcome this barrier and cause nucleation, resulting in a ballistic formation of a droplet. This means that droplets do not form immediately, but with a slight time delay, and then grow rapidly in size. The size of such a droplet is shown in the inset of Fig. 3a, where it takes 8 s after the critical temperature has already been exceeded to allow the formation of a droplet. We observe such an explosive droplet formation both in experiments (Fig. 4b, c and Supplementary Movie 3) and in simulations (Fig. 4g, h and Supplementary Movie 4). Droplet nucleation can be further delayed if other nearby absorbing particles also form clusters or even droplets, which then compete with each other as the concentration of the droplet's phase (here water) is locally decreased inside the bulk mixture.

For concentrations around $\phi_0 = 0.05$ (marked with a red-bordered 2 in Fig. 2a), after the droplets have formed, we observe a transition from nucleation and growth to coarsening. Such a late-time coarsening regime is expected, determined by Brownian coalescence of droplets and diffusion-limited coarsening. For Brownian coalescence, small droplets collide with each other and fuse to form larger droplets, reducing the overall interface. For diffusion-limited coarsening, the dominant growth process is given by the transport of droplet-forming molecules from small droplets into large droplets growing by diffusion from the bulk phase. For both coalescence and coarsening, $L \sim t^{\frac{1}{2}}$ is expected^{7,42–47}, which we can also find in our experiments ($L \sim t^{0.35}$) and simulations ($L \sim t^{0.31}$) by measuring the average size of non-moving droplets over time (blue curves in Fig. 3a), and that are passive because, either the number of non-absorbing particles is small, or these particles are concentrated at the droplet's interface.

The picture is different if the droplets feature ballistic movement driven by the presence of active colloidal molecules within the droplets themselves. In fact, the self-propulsion of active droplets accelerates the growth process described above. We observe that the size of active droplets grows as $L \sim t^{0.42}$ (marked with a red-bordered 3 in Fig. 2a and shown in Fig. 3a), which is significantly faster than the observed $L \sim t^{0.31}$ growth law for passive droplets. The accelerated growth is a direct consequence of the ballistic motion of the active droplets which allows them to recruit additional colloids faster than the passive droplets. This can be easily seen by measuring the total distance traveled in time by an active droplet (shown in Fig. 3b for experiment and simulation), revealing that the ballistically moving active droplets are able to cover a comparatively large area allowing them to efficiently collide and fuse. The enhanced growth process is depicted by the average size of the droplet domain in the experiments and the simulations in Fig. 3a (green curves), which is close to the expected $L \sim t^{\frac{1}{2}}$ growth law for ballistic aggregation^{48,49}. As shown in Fig. 3c, the active droplets slow down at later times. Ultimately, they would reach a state where light-absorbing and non-absorbing particles form a major cluster of almost randomly arranged particles within the droplet shell, resulting, for statistical reasons, in a reduced self-propulsion³⁶. The growth of the colloidal clusters within the droplet shells also enhances the temperature locally, which increases the degree of demixing and provides a further reason for the slow-down of the droplets.

Since the self-propulsion of a droplet is determined by the number and composition of the contained colloidal molecules, we

have explored the velocity distribution of the active droplets in our experiments and simulations (Fig. 3d), revealing, in particular, a small positive skewness of the distribution in both cases, indicating a tail towards large velocities.

Furthermore, we can additionally control the droplet velocity by light intensity. In the parameter regime in which active droplets can be found (Fig. 2, phase III, $0.023 < \lambda < 0.048$), an increase in light intensity leads to an increase in droplet speed (Fig. 3e). For increasing intensities, however, the velocity reduces as the resulting temperature in the sample increases and non-absorbing particles accumulate at the water–2,6-lutidine interface (transition from green to blue in the state diagram in Fig. 2a). Consequently, molecules inside the droplet slowly dissolve. We can characterize this transition counting the number of non-absorbing particles located at the interface N_{na}^{int} as a fraction of the total number of non-absorbing particles N_{na} (see gray line in Fig. 3e). Between $\lambda = 0.037$ and 0.045 , the fraction of non-absorbing particles at the interface significantly increases from $N_{na}^{int}/N_{na} = 0.15$ to 0.35 , whereas the growth in the droplet's velocity has slowly decreased with reaching its maximum velocity of $v = 2 \mu\text{m s}^{-1}$ at $\lambda = 0.038$. For larger values of λ , the number of non-absorbing particles at the interface is sufficiently large to rapidly decrease the droplet's velocity and finally reach a value similar to that of immotile droplets ($v < 0.8 \mu\text{m s}^{-1}$).

While droplet speed and the growth of droplets can be accelerated by increasing the laser intensity, the growth process can also be arrested by periodic light illumination. Employing periodic illumination, where the light is alternately switched on and off for a duration of 10 s (0.1 Hz), we show that the further growth of droplets can be slowed down and even arrested (Fig. 4d, e and Supplementary Movie 5), which is in good agreement with simulations (Fig. 4i, j and Supplementary Movie 6). During times of no illumination, temperatures quickly drop below T_c , droplets dissolve and colloidal molecules disassemble as their constituent particles diffuse apart. Upon illumination, this process is reversed and colloid–droplet superstructures reappear. This shows that by adjusting light illumination, we achieve temporal and spatial control over the system of colloids and droplets.

Discussion

Our results show that a two-way coupling between the motion of colloidal particles and the dynamics of their environment creates a route towards a novel class of active superstructures. These structures hinge on mutually coupled structure formation processes of the colloids, which form an engine, and the surrounding solvent, which phase separates in regions of high colloidal density and encapsulates the engine within a droplet shell. Our results create a bridge between the physics of active colloids and droplets and provide fundamental insights into the role of feedback for the emergence of ordered active superstructures, which opens up new possibilities for active-matter research to investigate two-way feedback loops in other systems and to create light-activated biomimetic materials.

Methods

Experimental setup. We consider a suspension of colloidal particles in a critical mixture of water and 2,6-lutidine at the critical lutidine mass fraction $c_c^l = 0.286$ with a critical temperature at $T_c = 34.1 \text{ }^\circ\text{C}$ ⁵⁰ (see Supplementary Fig. 1a). The light-absorbing particles consist of silica microspheres with light-absorbing iron-oxide inclusions (microParticles GmbH), while the non-absorbing particles consist of equally sized plain silica microspheres (microParticles GmbH). Both particle species possess the same radius ($R = 0.49 \pm 0.03 \mu\text{m}$) and have similar density ($\rho = 2 \text{ g cm}^{-3}$). The suspension is confined in a sample chamber quasi-two-dimensionally between a microscope slide and a cover slip, where the particles are sedimenting due to gravity. We use spacer particles (silica microspheres, microParticles GmbH) with a radius $R = 0.85 \pm 0.02 \mu\text{m}$ for constant separation but with a concentration $c \ll 5\%$, in order to not interfere with the observed

phenomena. We have treated our glass surface prior with NaOH solution ($c = 1$ mol) creating a smooth hydrophilic layer on top. Surprisingly, we found that a particle solution prepared at c_c^* in such a sample chamber behaved off-critical (i.e., nucleation of droplets). By adding about 2% more water to the mixture critical behavior returned (i.e., spinodal demixing). We expect that the hydrophilic surfaces of the sample chamber reduced the bulk concentration of water for which we have compensated.

A schematic of the setup is shown in Supplementary Fig. 2. The particle motion is captured by digital video microscopy at 12 fps. Using a two-stage feedback temperature controller^{50,51}, the sample's temperature is kept near-critical at $T_0 = 32.5^\circ\text{C}$, where water and 2,6-lutidine are homogeneously mixed. Under these conditions, the microspheres of both species are passive immotile Brownian particles performing standard diffusion (Fig. 1b, g). The sample is illuminated from above using a defocused laser of wavelength $\lambda = 1070$ nm at varying intensities. The increase of temperature surrounding the light-absorbing particles is rather small ($\Delta T \approx 2^\circ\text{C}$) such that they still behave as non-active Brownian particles.

The segmentation of the droplets is made using a deep neural network implemented and trained using DeepTrack 2.0⁵² (see details in SI and also Supplementary Movie 7).

Details on the simulation model. To model our experimental findings, we consider an ensemble of N overdamped spheroidal colloids at position \mathbf{r}_i immersed in a near-critical water–lutidine mixture, described by the Cahn–Hilliard equation, which can be derived from the total free-energy functional

$$\mathcal{F}[\phi] = \int d\mathbf{r} \left(\frac{a}{2} (T - T_c) \phi^2 + \frac{b}{4} \phi^4 + \frac{\kappa}{2} (\nabla \phi)^2 + \sum_{i=1}^N \phi V_{co}^i \right) \quad (4)$$

where T_c is the critical temperature of the composition, with constant $a < 0$ and $b, \kappa > 0$ such that the fluid demixes, where $T > T_c$. Here we describe the coupling of the hydrophilic particles to the concentration of the mixture with an external potential which we approximate with $V_{co}^i(\mathbf{r} - \mathbf{r}_i) \approx A_s \delta(\mathbf{r} - \mathbf{r}_i)$, where $s \in \{a, na\}$ for absorbing and non-absorbing particles, respectively. The evolution of the conserved order parameter ϕ (composition of the two components) is then given by the Cahn–Hilliard equation

$$\partial_t \phi = M \Delta \frac{\delta \mathcal{F}[\phi]}{\delta \phi} \quad (5)$$

$$\partial_t \phi = M \nabla^2 \left(a(T - T_c) \phi + b \phi^3 - \kappa \nabla^2 \phi + A_s \sum_{\text{absorb.}} \delta(\mathbf{r} - \mathbf{r}_i) + A_{na} \sum_{\text{non-abs.}} \delta(\mathbf{r} - \mathbf{r}_i) \right) \quad (6)$$

where M is the inter-diffusion constant of the mixture. We describe the impact of the hydrophilicity of the light-absorbing and non-absorbing particles on the dynamics of the fluid with an additional term including a δ -function at the particle positions, whose strength is given by A_s and A_{na} , respectively. The inhomogeneous temperature field produced by the light-absorbing particles with rate k_0 is to be calculated from the heat equation

$$\partial_t T(\mathbf{r}, t) = D_T \Delta T + k_0 \sum_{\text{absorb.}} \delta(\mathbf{r} - \mathbf{r}_i) - k_d (T - T_0) \quad (7)$$

with decay rate k_d and diffusion constant D_T . We can then phenomenologically describe the motion of the light-absorbing and non-absorbing particles $\mathbf{r}_i^s(t)$ ($i = 1, \dots, N, s \in \{a, na\}$)

$$\gamma \partial_t \mathbf{r}_i^s(t) = \beta_s \nabla \phi + \alpha_s \nabla (\nabla \phi)^2 - \nabla_{\mathbf{r}_i} V + \sqrt{2D} \boldsymbol{\eta}_i^s \quad (8)$$

where D is the translational diffusion coefficient of the particles, γ is the Stokes drag coefficient (assumed to be the same for both species) and $\boldsymbol{\eta}_i^s(t)$ represents unit-variance Gaussian white noise with zero mean. Here, the first term describes the attraction into water-rich regions, caused by the particles' hydrophilicity, where the second term describes the tendency of the particles to attach themselves to the interface of the two components. In addition, V accounts for excluded volume interactions among the particles which all have the same radius R and which we model using the Weeks–Chandler–Anderson potential $V = \frac{1}{2} \sum_{i \neq j} V_{ij}$ where the sums run over all particles and where $V_{ij} = 4\epsilon \left[\left(\frac{\sigma}{r_{ij}} \right)^{12} - \left(\frac{\sigma}{r_{ij}} \right)^6 \right] + \epsilon$ if $r_{ij} \leq 2^{1/6} \sigma$ and zero else. Here ϵ determines the strength of the potential, r_{ij} denotes the distance between particles i and j , $r_c = 2^{1/6} \sigma$ indicates a cutoff radius beyond which the potential energy is zero and $\sigma = 2R$ is the particle diameter.

Simulation parameters. In the simulation model we measure the distance in units of $1 \mu\text{m}$ and the time in units of 1 s and match the parameters such as diffusion constants, particle radius and typical velocity of the particles with the experiment. In all our simulations we use for the Cahn–Hilliard equation $M = 10^2 \mu\text{m}^2 \text{s}^{-1}$, $a = -2.5 \text{K}^{-1}$, $b = 50$, $\kappa = -5 \mu\text{m}^2$, $A_s = 2.5 \mu\text{m}^2$, $A_{na} = 1.5 \mu\text{m}^2$, for the dynamics of the heat equation $k_0 = 60 \times 10^3 \text{K} \mu\text{m}^2 \text{s}^{-1}$, $k_d = 0.5 \times 10^3 \text{s}^{-1}$, $D_T = 10^4 \mu\text{m}^2 \text{s}^{-1}$, $T_0 = 32.5^\circ\text{C}$, and for the Langevin equation of the particles $\beta_s/\gamma = -0.5 \times 10^3 \mu\text{m}^2 \text{s}^{-1}$, $\beta_{na}/\gamma = -0.2 \times 10^3 \mu\text{m}^2 \text{s}^{-1}$, $\alpha_a/\gamma = 0$, $\alpha_{na}/\gamma = 1.5 \times 10^3 \mu\text{m}^4 \text{s}^{-1}$, $D = 0.1 \mu\text{m}^2 \text{s}^{-1}$, and $\epsilon/\gamma = 100 \mu\text{m}^2 \text{s}^{-1}$.

Additionally we used in Fig. 1 $L_{\text{box}} = 50 \mu\text{m}$, $N_a = 15$, $N_{na} = 25$, $\phi_0 = 0.05$, and in Fig. 3 $L_{\text{box}} = 200 \mu\text{m}$, $N_{na} = 160$, $\phi_0 = 0.05$, and $k_0 = 80 \times 10^3 \text{K} \mu\text{m}^2 \text{s}^{-1}$,

$N_a = 200$ (active droplets) and $k_0 = 50 \times 10^3 \text{K} \mu\text{m}^2 \text{s}^{-1}$, $N_a = 800$ (immotile droplets) and in Fig. 4i, j we have $L_{\text{box}} = 100 \mu\text{m}$, $N_a = N_{na} = 160$, $\phi_0 = 0.05$ and $k_0 = 25 \times 10^3 \text{K} \mu\text{m}^2 \text{s}^{-1}$.

Data availability

All data are available from the corresponding author upon reasonable request.

Code availability

The codes that support the findings of this study are available from the corresponding authors upon reasonable request.

Received: 22 January 2021; Accepted: 27 September 2021;

Published online: 14 October 2021

References

- Nakamura, S. & Minamino, T. Flagella-driven motility of bacteria. *Biomolecules* **9**, 279 (2019).
- Paxton, W. F. et al. Catalytic nanomotors: autonomous movement of striped nanorods. *J. Am. Chem. Soc.* **126**, 13424–13431 (2004).
- Bechinger, C., Di Leonardo, R., Löwen, H., Reichhardt, C., Volpe, G. & Volpe, G. Active particles in complex and crowded environments. *Rev. Mod. Phys.* **88**, 045006 (2016).
- Marchetti, M. C. et al. Hydrodynamics of soft active matter. *Rev. Mod. Phys.* **85**, 1143–1189 (2013).
- Joshi, D. et al. Kinetic control of the coverage of oil droplets by DNA-functionalized colloids. *Sci. Adv.* **2**, e1600881 (2016).
- Shin, Y. & Brangwynne, C. P. Liquid phase condensation in cell physiology and disease. *Science* **357**, eaaf4382 (2017).
- Berry, J., Brangwynne, C. P. & Haataja, M. Physical principles of intracellular organization via active and passive phase transitions. *Rep. Prog. Phys.* **81**, 046601 (2018).
- Moran, J. L. & Posner, J. D. Phoretic self-propulsion. *Annu. Rev. Fluid Mech.* **49**, 511–540 (2017).
- Maass, C. C., Krüger, C., Herminghaus, S. & Bahr, C. Swimming droplets. *Annu. Rev. Condens. Matter Phys.* **7**, 171–193 (2016).
- Li, M., Brinkmann, M., Pagonabarraga, I., Seemann, R. & Fleury, J.-B. Spatiotemporal control of cargo delivery performed by programmable self-propelled Janus droplets. *Commun. Phys.* **1**, 1–8 (2018).
- Hyman, A. A., Weber, C. A. & Jülicher, F. Liquid–liquid phase separation in biology. *Annu. Rev. Cell Dev. Biol.* **30**, 39–58 (2014).
- Duclos, G., Erenkämper, C., Joanny, J.-F. & Silberzan, P. Topological defects in confined populations of spindle-shaped cells. *Nat. Phys.* **13**, 58–62 (2017).
- Palacci, J., Sacanna, S., Steinberg, A. P., Pine, D. J. & Chaikin, P. M. Living crystals of light-activated colloidal surfers. *Science* **339**, 936–940 (2013).
- Soto, R. & Golestanian, R. Self-assembly of catalytically active colloidal molecules: tailoring activity through surface chemistry. *Phys. Rev. Lett.* **112**, 068301 (2014).
- Dey, K. K. et al. Micromotors powered by enzyme catalysis. *Nano Lett.* **15**, 8311–8315 (2015).
- Ginot, F., Theurkauff, I., Detchevyry, F., Ybert, C. & Cottin-Bizonne, C. Aggregation-fragmentation and individual dynamics of active clusters. *Nat. Commun.* **9**, 696 (2018).
- Ebbens, S. J. & Gregory, D. A. Catalytic Janus colloids: controlling trajectories of chemical microswimmers. *Acc. Chem. Res.* **51**, 1931–1939 (2018).
- Heckel, S. et al. Active assembly of spheroidal photocatalytic BiVO₄ microswimmers. *Langmuir* **36**, 12473–12480 (2020).
- Zhang, H. P., Be'er, A., Florin, E.-L. & Swinney, H. L. Collective motion and density fluctuations in bacterial colonies. *Proc. Natl Acad. Sci. USA* **107**, 13626–13630 (2010).
- Schaller, V., Weber, C., Semmrich, C., Frey, E. & Bausch, A. R. Polar patterns of driven filaments. *Nature* **467**, 73–77 (2010).
- Cates, M. E. & Tailleur, J. Motility-induced phase separation. *Annu. Rev. Condens. Matter Phys.* **6**, 219–244 (2015).
- Zwicker, D., Hyman, A. A. & Jülicher, F. Suppression of Ostwald ripening in active emulsions. *Phys. Rev. E* **92**, 012317 (2015).
- Zwicker, D., Seyboldt, R., Weber, C. A., Hyman, A. A. & Jülicher, F. Growth and division of active droplets provides a model for protocells. *Nat. Phys.* **13**, 408–413 (2017).
- Ramos, G., Cordero, M. L. & Soto, R. Bacteria driving droplets. *Soft Matter* **16**, 1359–1365 (2020).
- Rajabi, M., Baza, H., Turiv, T. & Lavrentovich, O. D. Directional self-locomotion of active droplets enabled by nematic environment. *Nat. Phys.* **17**, 260–266 (2021).

ARTICLE

NATURE COMMUNICATIONS | <https://doi.org/10.1038/s41467-021-26319-3>

26. Chakrabarti, B. & Saintillan, D. Hydrodynamic synchronization of spontaneously beating filaments. *Phys. Rev. Lett.* **123**, 208101 (2019).
27. Lavergne, F. A., Wendehenne, H., Bäuerle, T. & Bechinger, C. Group formation and cohesion of active particles with visual perception-dependent motility. *Science* **364**, 70–74 (2019).
28. Gorbonos, D. et al. Long-range acoustic interactions in insect swarms: an adaptive gravity model. *New J. Phys.* **18**, 073042 (2016).
29. Kay, R. R., Langridge, P., Traynor, D. & Hoeller, O. Changing directions in the study of chemotaxis. *Nat. Rev. Mol. Cell Biol.* **9**, 455–463 (2008).
30. Thomas, R. & d'Ari, R. *Biological Feedback* (CRC Press, 1990).
31. Freeman, M. Feedback control of intercellular signalling in development. *Nature* **408**, 313–319 (2000).
32. Grattoni, C. A., Dawe, R. A., Seah, C. Y. & Gray, J. D. Lower critical solution coexistence curve and physical properties (density, viscosity, surface tension, and interfacial tension) of 2,6-lutidine + water. *J. Chem. Eng. Data* **38**, 516 (1993).
33. Varma, A., Montenegro-Johnson, T. D. & Michelin, S. Clustering-induced self-propulsion of isotropic autophoretic particles. *Soft Matter* **14**, 7155–7173 (2018).
34. Bregulla, A. P. & Cichos, F. Flow fields around pinned self-thermophoretic microswimmers under confinement. *J. Chem. Phys.* **151**, 044706 (2019).
35. Chuphal, P., Venugopal, I. & Thakur, S. Formation of self-propelling clusters starting from randomly dispersed Brownian particles. *Bull. Mater. Sci.* **43**, 183 (2020).
36. Schmidt, F., Liebchen, B., Löwen, H. & Volpe, G. Light-controlled assembly of active colloidal molecules. *J. Chem. Phys.* **150**, 094905 (2019).
37. Würger, A. Self-diffusiophoresis of Janus particles in near-critical mixtures. *Phys. Rev. Lett.* **115**, 188304 (2015).
38. Weeks, J. D., Chandler, D. & Andersen, H. C. Role of repulsive forces in determining the equilibrium structure of simple liquids. *J. Chem. Phys.* **54**, 5237–5247 (1971).
39. Cahn, J. W. & Hilliard, J. E. Free energy of a nonuniform system. I. Interfacial free energy. *J. Chem. Phys.* **28**, 258–267 (1958).
40. Voit, A., Krekhov, A., Enge, W., Kramer, L. & Köhler, W. Thermal patterning of a critical polymer blend. *Phys. Rev. Lett.* **94**, 214501 (2005).
41. Vutukuri, H. R. et al. Active particles induce large shape deformations in giant lipid vesicles. *Nature* **586**, 52–56 (2020).
42. Lifshitz, I. & Slyozov, V. The kinetics of precipitation from supersaturated solid solutions. *J. Phys. Chem. Solids* **19**, 35–50 (1961).
43. Bray, A. J. Theory of phase-ordering kinetics. *Adv. Phys.* **51**, 481–587 (2002).
44. Gonnella, G., Marenduzzo, D., Suma, A. & Tiribocchi, A. Motility-induced phase separation and coarsening in active matter. *C. R. Phys.* **16**, 316–331 (2015).
45. Laradji, M. & Sunil Kumar, P. B. Domain growth, budding, and fission in phase-separating self-assembled fluid bilayers. *J. Chem. Phys.* **123**, 224902 (2005).
46. Camley, B. A. & Brown, F. L. H. Dynamic scaling in phase separation kinetics for quasi-two-dimensional membranes. *J. Chem. Phys.* **135**, 225106 (2011).
47. Stanich, C. A. et al. Coarsening dynamics of domains in lipid membranes. *Biophys. J.* **105**, 444–454 (2013).
48. Grauer, J., Löwen, H., Be'er, A. & Liebchen, B. Swarm hunting and cluster ejections in chemically communicating active mixtures. *Sci. Rep.* **10**, 5594 (2020).
49. Cremer, P. & Löwen, H. Scaling of cluster growth for coagulating active particles. *Phys. Rev. E* **89**, 022307 (2014).
50. Schmidt, F. et al. Microscopic engine powered by critical demixing. *Phys. Rev. Lett.* **120**, 068004 (2018).
51. Paladugu, S. et al. Nonadditivity of critical Casimir forces. *Nat. Commun.* **7**, 11403 (2016).
52. Midtvedt, B. et al. Quantitative digital microscopy with deep learning. *Appl. Phys. Rev.* **8**, 011310 (2021).

Acknowledgements

F.S., J.P., B.M., and G.V. acknowledge partial support by the ERC Starting Grant ComplexSwimmers (grant number 677511) and by Vetenskapsrådet (grant number 2016-03523). B.L. acknowledges support by the Deutsche Forschungsgemeinschaft (DFG, German Research Foundation) - Project number 233630050 (TRR-146).

Author contributions

All authors have planned the project, have discussed the results, and have written or edited the manuscript. The experiments have been planned by F.S. and G.V. and the model, and the simulations by J.G., H.L., and B.L. The experiments and the simulations have been performed by F.S. and J.G., respectively. J. P. and B. M. have quantitatively tracked the colloids.

Funding

Open Access funding enabled and organized by Projekt DEAL.

Competing interests

The authors declare no competing interests.

Additional information

Supplementary information The online version contains supplementary material available at <https://doi.org/10.1038/s41467-021-26319-3>.

Correspondence and requests for materials should be addressed to Benno Liebchen.

Peer review information *Nature Communication* thanks the anonymous reviewer(s) for their contribution to the peer review of this work. Peer reviewer reports are available.

Reprints and permission information is available at <http://www.nature.com/reprints>

Publisher's note Springer Nature remains neutral with regard to jurisdictional claims in published maps and institutional affiliations.



Open Access This article is licensed under a Creative Commons Attribution 4.0 International License, which permits use, sharing, adaptation, distribution and reproduction in any medium or format, as long as you give appropriate credit to the original author(s) and the source, provide a link to the Creative Commons license, and indicate if changes were made. The images or other third party material in this article are included in the article's Creative Commons license, unless indicated otherwise in a credit line to the material. If material is not included in the article's Creative Commons license and your intended use is not permitted by statutory regulation or exceeds the permitted use, you will need to obtain permission directly from the copyright holder. To view a copy of this license, visit <http://creativecommons.org/licenses/by/4.0/>.

© The Author(s) 2021

Supplementary Information Active droplids

Jens Grauer,^{1,*} Falko Schmidt,^{2,*} Jesus Pineda,² Benjamin
Midtvedt,² Hartmut Löwen,¹ Giovanni Volpe,² and Benno Liebchen^{3,†}

¹*Institut für Theoretische Physik II: Weiche Materie,*

Heinrich-Heine-Universität Düsseldorf, D-40225 Düsseldorf, Germany

²*Department of Physics, University of Gothenburg, SE-41296 Gothenburg, Sweden*

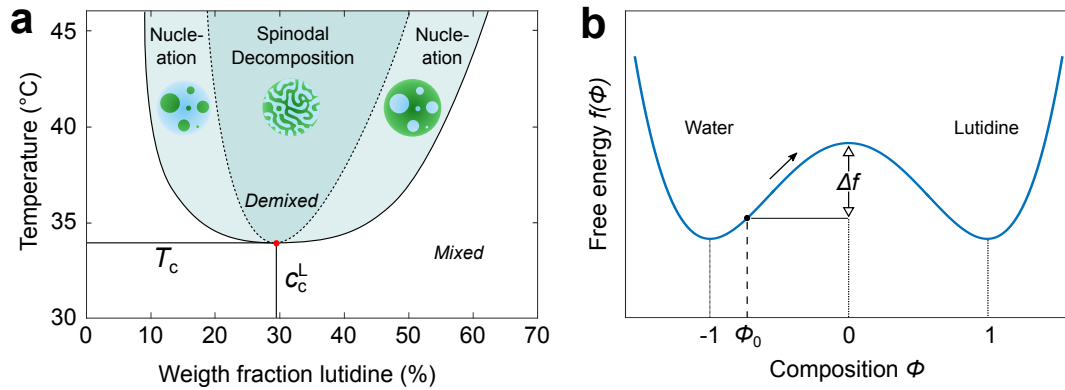
³*Institut für Physik kondensierter Materie, Technische Universität Darmstadt, 64289 Darmstadt, Germany*

Here we provide supplementary information on experimental aspects such as the phase diagram of a water-2,6-lutidine mixture, the experimental setup, the influence of wetting properties on particle behaviour, and the segmentation and tracking of the droplids.

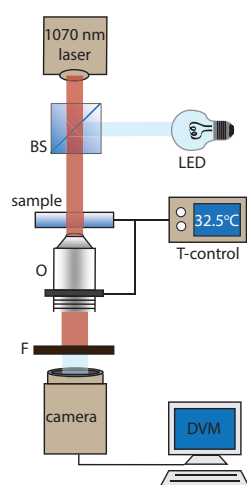
* These authors contributed equally.

† benno.liebchen@pkm.tu-darmstadt.de

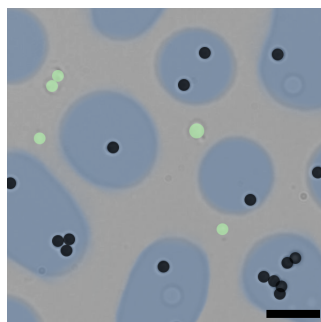
SUPPLEMENTARY FIGURES



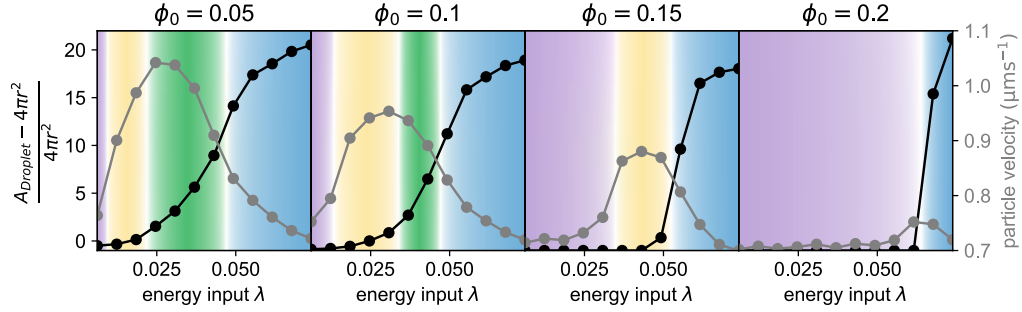
Supplementary Figure 1. **Phase diagram of the water–2,6-lutidine mixture and characteristic free energy.** **a** The water–2,6-lutidine mixture features a lower critical point at $T_c = 34.1^\circ$ and $c_c^L = 28.4\%$, where the binodal (solid line) and the spinodal (dotted line) coincide. Upon heating, two phases with different concentrations occur, which are separated by a pronounced interface (blue: water-rich phase; green: lutidine-rich phase). Between the binodal and the spinodal droplets of the lower concentrated phase grow in the higher concentrated phase, continuously throughout the sample. Above the spinodal line, spinodal decomposition occurs, where both phases form symmetrical structures. **b** Schematic illustration of the free energy profile $f(\phi) = \frac{a}{2}(T - T_c)\phi^2 + \frac{b}{4}\phi^4$ of a binary mixture as a function of the composition ϕ . A free energy barrier of height Δf located at $\phi = 0$ must be crossed during a transition from ϕ_0 (water-rich region) to $\phi > 0$ (lutidine-rich region).



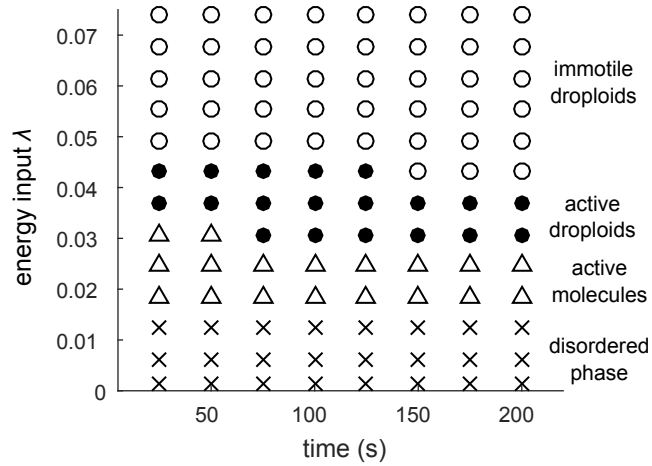
Supplementary Figure 2. **Schematic of the experimental setup.** The setup is a home-made version of an inverted microscope setup. The sample is confined in a quasi-2D space between a coverslip and a microscopic slide and separated by spacer particles ($R = 0.85 \pm 0.02 \mu\text{m}$ microParticles GmbH). A defocused laser ($\lambda = 1070 \text{ nm}$) heats up light-absorbing colloids and causes local demixing of the near-critical mixture. The sample's temperature is fixed close to the critical temperature at $T_0 = 32.5^\circ\text{C}$ using a two-stage controller system consisting of a copper-plate heat exchanger with a water bath (T100, Grant Instruments) and of two Peltier elements attached to the objective (O) in feedback with a temperature controller (TED45, Thorlabs). A background light source (LED) is coupled to the laser beam path using a 50:50 beamsplitter (BS) and illuminates the whole sample area. The scattered light is collected with a 100x oil-immersion objective (O, NA=1.30) and imaged onto a camera where the laser is blocked by a filter (F). Using digital video microscopy (DVM) the particle's motion is being tracked and analyzed.



Supplementary Figure 3. **Influence of wetting properties on particle behaviour.** Whereas hydrophilic absorbing particles (black) are immersed inside water-rich droplets, hydrophobic non-absorbing particles (green) remain outside these regions. Scale bar represents $5 \mu\text{m}$.



Supplementary Figure 4. **Quantitative phase characterization.** To distinguish between the different phases and the colors in Fig. 2a we calculate the area with higher water concentration around the particles (where $\phi < 0$) and use a threshold criterion $A_{\text{Droplet}} > 8\pi r^2$ (or $(A_{\text{Droplet}} - 4\pi r^2)/(4\pi r^2) > 1$) to distinguish phases II and III (active and immotile droplets) from the other ones. This criterion requires that the water-rich area is larger than the area covered by a typical number of 8 colloids within a droplet at the time instance where the snapshots are evaluated. To distinguish phases II and III we calculate the mean particle velocity which indicates whether the appearing structures are active or passive. When the mean velocity clearly exceeds that of passive Brownian particles ($v > 0.8 \mu\text{ms}^{-1}$, for the used sampling rate) we call the resulting structures active droplets (phase II). The data points shown here for different values of ϕ_0 and λ correspond to those from the phase diagram in Fig. 2a.



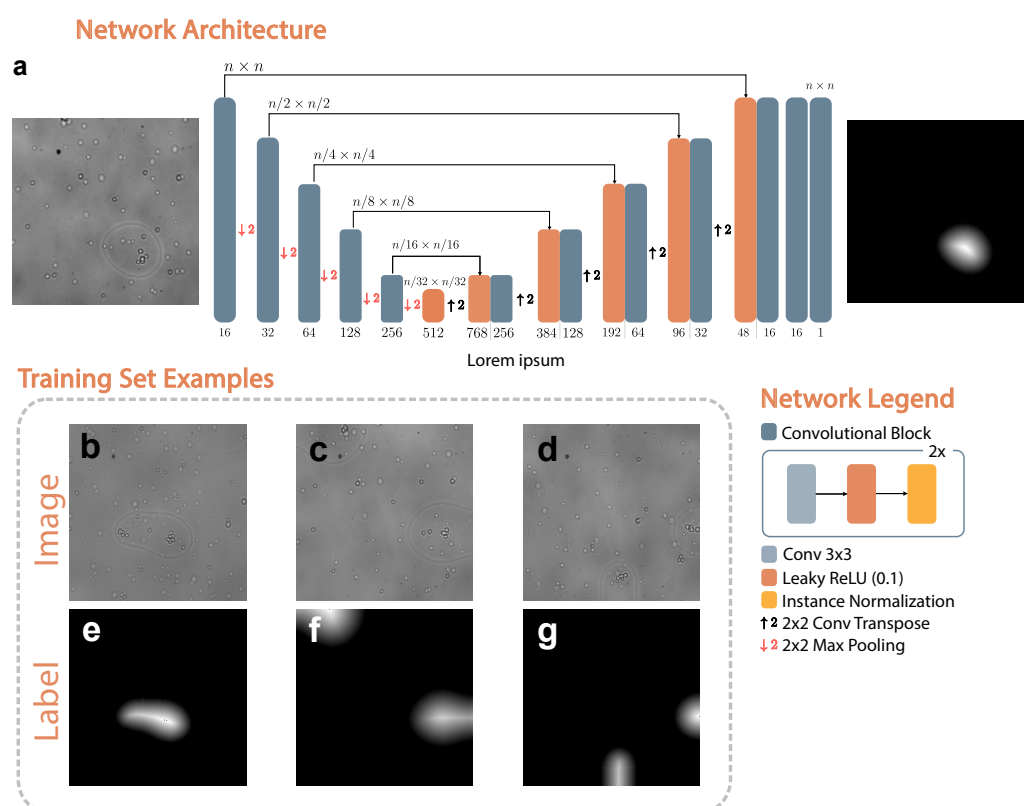
Supplementary Figure 5. **Time-evolution of phase boundaries:** Phases as a function of the net energy input λ and the time for a fixed averaged relative concentration difference from the critical point $\phi_0 = 0.1$. We find the same phases at all times and observe a slight evolution of the phase boundaries over time. The evaluated state points are indicated by crosses (disordered phase), triangles (active molecules), filled circles (active droplets), and empty circles (immotile droplets with particles at the interface). The quantitative criteria for the phases are given in Supplementary Fig. 4.

SUPPLEMENTARY METHODS

Droplet Segmentation

A deep-learning-based approach is used to detect the droplets and follow their morphology over time. Since droplets are never overlapping, the method is built around a binary classification of each pixel in an image into either background or droplet. The network architecture used to perform this task is similar to the U-Net [1], with a down-sampling step and a up-sampling step, and skip-connections there between (Supplementary Fig. 6a). The network was trained using simulated image-label pairs, generated by the deep learning framework DeepTrack 2.0 [2]. Examples are shown in Supplementary Fig. 6b-d.

Notably, the label was not constructed as a binary image directly, but as the distance transform of that binary



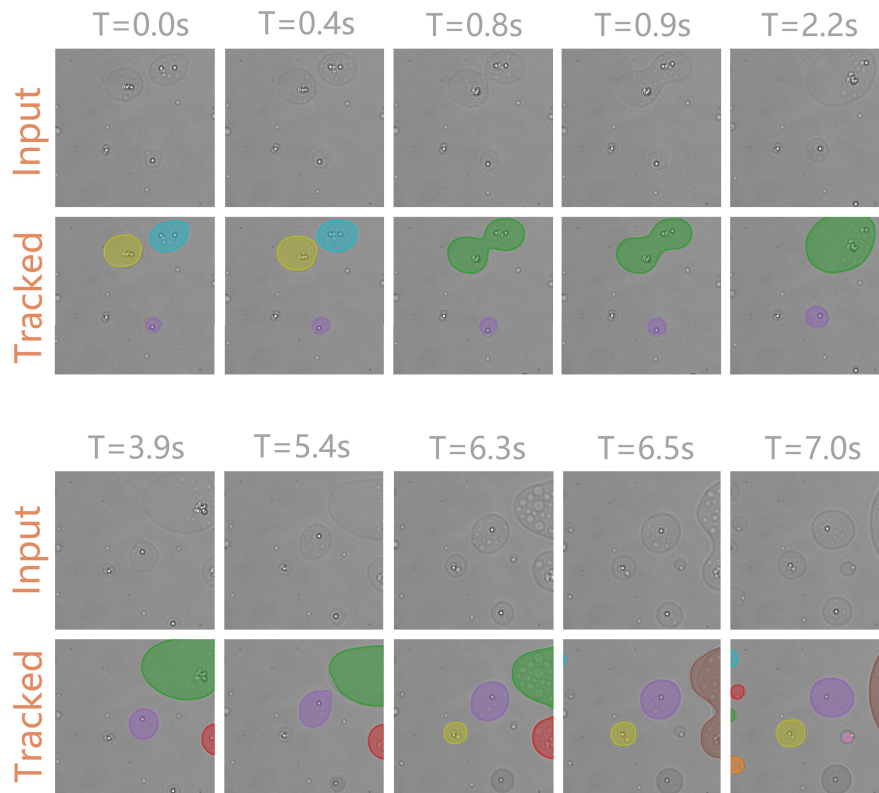
Supplementary Figure 6. **Overview of the deep-learning approach used to track and segment the droplets.** **a** The neural network architecture with an example input and output. The depth of the neural network was chosen as to give it a sufficient receptive field to analyze big droplets. Instance normalization is used to help propagate information deeper into the network. **b-d** Example simulated training images. The images are constructed by merging experimental backgrounds and droplets simulated by approximating the optical transfer function. **e-g** Training labels corresponding to the images in **b-d**. The labels are constructed by taking the distance transform of the binary image where the background is 0 and pixels inside a droplet are 1.

image, as can be seen in Supplementary Fig. 6e-g. In the experimental images, the inside of a droplet is essentially indistinguishable from the outside, and its classification can only be inferred from the surrounding droplet edges. As such, classifying the center of droplets becomes more difficult the larger the droplet is, because the information is further away in the image. We found that using the distance transform instead of the binary image helped the network learn to correctly detect the center of larger droplets, presumably because mistakes are punished more harshly in the training process.

Since the network is now trained on a regression problem, we use mean absolute error as loss function. Moreover, we used the Adam optimizer, with a learning rate of 0.0001. The network was trained for 100 epochs, each of which consisted of 1024 unique training samples split into batches of 8. Note that new training data was continuously generated during training.

A binary classification can be restored by thresholding the network output, from which individual droplets are detected using by finding connected regions of positive classification. Since the droplets are large and well separated, they are easily traced over time by their centroid.

Supplementary Figure 7 demonstrates the tracking of the network by showing input images next to the same image with the segmentation of each droplet overlaid, for a series of images taken from an experimental video. The images were chosen to demonstrate the correctness of the method in a few common scenarios, such as the merging of two droplets, the emergence of new droplets as well as densely populated images. The full tracked video is available as



Supplementary Figure 7. **Example tracked droplets.** A few tracked frames from an experimental video, demonstrating the tracking using the deep learning approach. The top row shows raw images fed to the tracking algorithm, while the bottom row shows the same images with the binary segmentation overlaid. The colors represent individual droplets and are consistent over time to show that the cells are correctly traced.

supplementary material (see Supplementary Movie 7).

SUPPLEMENTARY REFERENCES

- [1] O. Ronneberger, P. Fischer, and T. Brox, U-net: Convolutional networks for biomedical image segmentation, in *Medical Image Computing and Computer-Assisted Intervention – MICCAI 2015*, edited by N. Navab, J. Hornegger, W. M. Wells, and A. F. Frangi (Springer International Publishing, Cham, 2015) pp. 234–241.
- [2] B. Midtvedt, S. Helgadottir, A. Argun, J. Pineda, D. Midtvedt, and G. Volpe, Quantitative digital microscopy with deep learning, *Appl. Phys. Rev.* **8**, 011310 (2021).

8.4 Paper IV: Communicating active agents find food using machine learning

Manuscript in preparation

J. Grauer, H. Löwen, B. Liebchen, & F. J. Schwarzendahl
Communicating active agents find food using machine learning

Statement of contribution

All authors planned the project. I implemented the reinforcement learning algorithm, performed the simulations, analyzed the numerical results and prepared the figures. All authors discussed the results. F.J.S and I wrote the manuscript. H.L. and B.L. edited it.

Communicating active agents find food using machine learning

Jens Grauer,¹ Hartmut Löwen,¹ Benno Liebchen,^{2,*} and Fabian Jan Schwarzendahl^{1,†}

¹*Institut für Theoretische Physik II: Weiche Materie,
Heinrich-Heine-Universität Düsseldorf, D-40225 Düsseldorf, Germany*

²*Institut für Physik der kondensierten Materie, Technische Universität Darmstadt, 64289 Darmstadt, Germany*

Many biological and synthetic self-propelled swimmers perform chemotaxis to move towards and stay at high nutrient concentrations. Similarly, the mutual communication, called quorum sensing, is an important process that regulates their behaviour in response to the density of neighboring particles. Here, we use smart active agents equipped with a machine learning algorithm to find the optimal navigation strategy. We study a system of communicating active particles whose task is to consume a nutrient field as efficiently as possible. Depending on the particle density and the consumption rate we find three optimal strategies that can be classified as: a "uniting strategy", where all agents cooperatively accumulate together; a "spreading strategy", where particles stay separated from each other; and an "adaptive strategy", where particles adaptively decide whether to follow or stay away from others. Our work demonstrates the potential of active systems equipped with artificial intelligence for future applications.

Living organisms ranging from bacteria at the microscale to schools of fish at the macroscale swarm and cooperate in order to efficiently find nutrients. Animals with territories have designated grounds for finding nutrients, in which they are alone and tend to avoid each other. These two collective strategies for the search for nutrition can be classified as: (i) uniting, where all organisms swarm together (Fig. 1 a); and (ii) spreading, where organisms stay well separated (Fig. 1 b). Interpolating between these two strategies we can imagine an adaptive strategy (iii), where organisms group into loose swarm while individuals stay locally separated (Fig. 1 c). Animals developed these strategies cooperatively through communication and evolutionary pressure. Inspired by that, here we apply a machine learning algorithm where active agents communicate in order to efficiently find and consume nutrients and thereby employ the strategies (i)-(iii).

Active particles have been studied extensively, and recently also machine learning algorithms have been applied to active particles [1]. Examples are microswimmers that learn a complex flow field [2–7], gliders navigating in turbulent flow [8, 9], learning to swim at low Reynolds number [10], learning chemotaxis [11, 12], learning flocking of a collection of agents [13] or learning optimal paths in flow [14–17] or force fields [18–20]. Experimentally, there are a number of active particle systems [21] which recently have been equipped artificial visual perception [22] and reinforcement learning [23]. These active particles give a motivation to applications such as targeted drug delivery, minimal invasive surgery [24–27] or decontamination of polluted water [28]. Related to the latter, there have been a number of studies of microswimmers in chemical fields. Whether synthetic or biological, these can sense the concentration of a chemical and move along

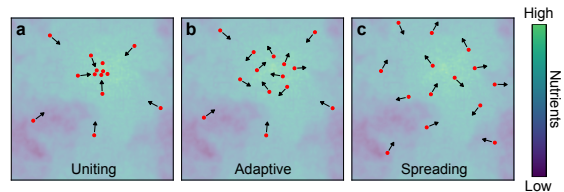


FIG. 1. Collective strategies for the search of nutrients. **a** uniting strategy: all agents behave cooperatively and swarm together. **b** adaptive strategy: the agents either follow others or avoid them depending on the environment. **c** spreading strategy: the agents behave aversely and stay well separated.

its gradient [29, 30]. Signaling microswimmers use this ability and produce certain chemicals to communicate based on quorum sensing mechanism [31–35].

In this letter we equip active agents with a deep reinforcement learning algorithm, where agent's goal is to consume a nutrient field as efficiently as possible. Thereby, the agents communicate through a quorum sensing field. Depending on the density of agents and their consumption rate of the nutrient field, they employ the strategies (i)-(iii). Moreover, they also adapt dynamically to new situations switching between (i)-(iii) depending on changes in the nutrient field.

We consider an ensemble of N (artificial or biological) overdamped colloids located in a Gaussian random nutrient field $c(\mathbf{r}, t)$. Independent starting configurations are produced by placing all agents randomly in the simulation box and generating a Gaussian random field using the power spectrum realization method [36–38]. The particles move with constant speed v_0 along their orientations $\mathbf{p}_i = (\cos \theta_i, \sin \theta_i)$ in a two-dimensional simulation box of size $L \times L$ with periodic boundary conditions. The main task of the particles is to consume nutrients as efficiently as possible by reducing the nutrient field at rate $k_d c(\mathbf{r}_i, t)$ at their position $\mathbf{r}_i(t)$. Here, the consumption rate is proportional to the local concentration of the nu-

* benno.liebchen@pkm.tu-darmstadt.de

† Fabian.Schwarzendahl@hhu.de

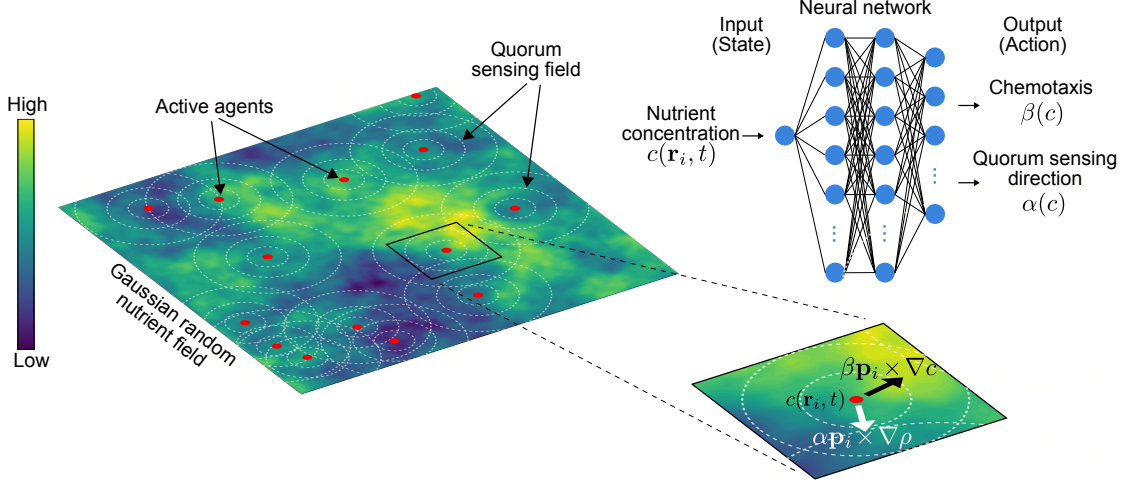


FIG. 2. Schematic of the Quorum sensing strategy model. The consuming particles (red dots) move in a nutrient concentration (colorcoded field) and communicate with each other by producing a Quorum sensing field (illustrated by white circles around the particles). Each particle feeds its local concentration into a neural network. The network will predict two values for α and β that determine the alignment of the agent along $\nabla\rho$ and ∇c .

trients, which allows particles to consume larger amounts when they are at locations of higher concentration. The dynamics of the nutrient concentration field follows a diffusion equation (with diffusion coefficient D_c), with additional sink terms describing the consumption of the particles

$$\dot{c}(\mathbf{r}, t) = D_c \Delta c(\mathbf{r}, t) - k_d \sum_{i=1}^N c(\mathbf{r}_i, t) \delta(\mathbf{r} - \mathbf{r}_i). \quad (1)$$

The particles can orient on the basis of two quantities. On the one hand, via the nutrient concentration field itself, by responding to it via chemotaxis and swimming up the concentration gradient. On the other hand, we assume that the particles can communicate with each other by producing signaling molecules to which the others respond by quorum sensing mechanisms. Similar to Eq. (1), this can be described by another diffusion equation with additional point sources, which take into account the production of signaling molecules by the particles. Also, we consider a sink term that models possible degradation of the molecules by chemical processes or other reactions

$$\dot{\rho}(\mathbf{r}, t) = D_\rho \Delta \rho(\mathbf{r}, t) + \lambda \sum_{i=1}^N \delta(\mathbf{r} - \mathbf{r}_i) - \mu \rho(\mathbf{r}, t). \quad (2)$$

Here, D_ρ is the diffusion coefficient of the quorum sensing field, the particles produce signaling molecules with rate λ , which evaporate with rate μ . Assuming the dynamics of the signaling molecules ρ is fast, i.e. $\dot{\rho} = 0$, the steady

state profile in two dimensions is

$$\rho = \frac{\lambda}{D_\rho} K_0(\kappa r) \quad (3)$$

where $K_0(x)$ is the modified Bessel function of second kind and $\kappa = \sqrt{\frac{\mu}{D_\rho}}$.

The following equations describing the dynamics of the particles thus depend on the nutrient concentration field $c(\mathbf{r}, t)$ as well as the field of quorum sensing molecules $\rho(\mathbf{r}, t)$

$$\dot{\mathbf{r}}_i(t) = v_0 \mathbf{p}_i, \quad (4)$$

$$\dot{\theta}_i(t) = \alpha(c) \mathbf{p}_i \times \nabla \rho + \beta(c) \mathbf{p}_i \times \nabla c, \quad (5)$$

where $\mathbf{a} \times \mathbf{b} = a_1 b_2 - a_2 b_1$ and $\mathbf{r}_i(t)$ is the i 's particles position. The particles steer towards high particle density locations with a strength $\alpha(c) > 0$. The opposite happens for $\alpha(c) < 0$, with particles moving away from locations with high concentrations of signaling molecules. This faces the second term, with which particles swim up the nutrient concentration field with strength $\beta(c) > 0$.

We measure time in units of $t_0 = \frac{1}{10^3 \mu}$ and length in units of $l_0 = \frac{D_\rho}{100 v_0}$. The simulation parameters are: $\frac{D_\rho}{l_0^2/t_0} = 10$, $\lambda l_0 t_0 = 1$, $\frac{D_c}{l_0^2/t_0} = 0.0001$, and $\frac{v_0}{l_0/t_0} = 0.1$

Here we use Q-learning [39], a variant of reinforcement learning (RL), to find the optimal quorum sensing strategy for $\alpha(c)$ and $\beta(c)$. The RL agents interact with their environment by determining their states s_t and performing actions a_t to maximize their expected rewards. The discounted future reward is $R_t = \sum_{t'=t}^T \gamma^{t'-t} r_{t'}$

$r_t + \gamma R_{t+1}$, where T is the last time step, r_t is the reward when moving from state s_t to state s_{t+1} and the discount factor γ ($\gamma=0.9$ in our model) weights the importance of future rewards compared to immediate ones. For each agent we define the state s_t as the local concentration of the nutrient field at its position $c(\mathbf{r}_t, t)$. After each time interval $\Delta t/t_0 = 100$, an agent arrives at the next state s_{t+1} and chooses a new action a_{t+1} , that is, new values for α and β . These control the direction in which they move with α deciding on a movement towards (or away from) neighboring particles and β enforcing alignment along higher concentrations of $c(\mathbf{r}, t)$. To this end, different actions are chosen during training with $\alpha t_0/l_0^3 \in [-5, 5]$ and $\beta t_0/l_0^3 \in [0, 5]$, in steps of 1 and 0.5, respectively. Within each of 5000 episodes with simulation time $t_{max}/t_0 = 2000$, a new Gaussian random nutrient field is generated and the agents are placed randomly in the simulation box. We let the agents train to estimate values for state-action pairs $Q^\pi(s, a)$ that indicate the expected sum of discounted future rewards when starting in state $s_t = s$, performing action $a_t = a$ and following policy π :

$$Q^\pi(s, a) = \sum_{s', r} P(s', r|s, a) \sum_{a'} \pi(a'|s') [r + \gamma Q^\pi(s', a')]. \quad (6)$$

Given the dynamics of the environment, $P(s', r|s, a)$ denotes the transition probability into each possible pair of next state s' with reward r when performing action a in state s . An agent is rewarded the more it consumes: $r = C/(k_d \Delta t) - 1$, where C is the total amount of consumed nutrients of an agent during time Δt . The policy $\pi(a|s)$ maps the state-action pair to the probability of taking action a in state s . In Q -learning, the optimal policy consists in always taking the action a with the largest Q -value $\max_a Q(s, a)$. During training, the agents follow an ϵ -greedy policy to ensure a sufficient exploration of the environment. This means that a random action is chosen with probability ϵ , while the action with the highest Q -value is chosen with probability $1 - \epsilon$. Over the episodes, ϵ is decreased linearly starting from 1 down to 0.01.

Since in simple Q -learning the size of the state-action space is limited and we need to handle the large number of possible states (i.e. nutrient concentrations $c(\mathbf{r}, t)$), we approximate the Q -values by an artificial neural network $Q(s, a; \theta)$ (called deep Q -network (DQN)) [40]. Here θ describes the parameters of the neural network (weights and biases) that are adjusted during training to minimize the difference of the DQN's output and the right-hand side Eq. (6). This is achieved by storing all transitions $\{s_t, a_t, s_{t+1}, r_t\}$ during an episode and using experience replay to train the neural network. We use the mean squared error as a loss function, i.e. the mean value of the difference $(r_t + \gamma \max_a Q(s_{t+1}, a; \theta) - Q(s_t, a_t; \theta))^2$ is calculated over all transitions of an episode. An Adam optimizer [41] with a learning rate of 0.01 and a learning rate decay of 0.05 is applied to update the network parameters. The DQN has an input layer with a single neuron and two hidden layers, each with 256 neurons, using a ReLU activation function [42]. The output layer

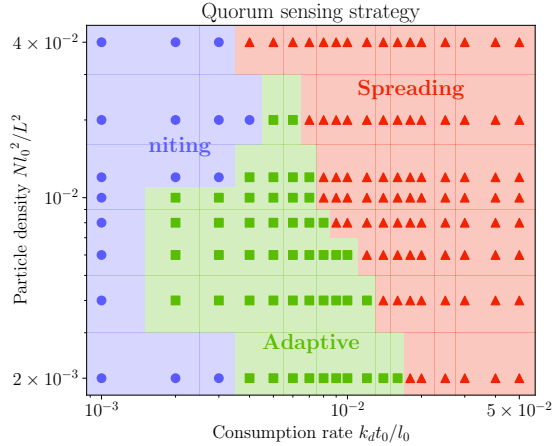


FIG. 3. State diagram of learned quorum sensing strategies. The active agents employ different strategies depending on the agent density N/L^2 and their consumption rate k_0 . Uniting strategy (blue dots): the agents behave cooperatively and congregate, with $\alpha > 0$ for all nutrient concentrations; adaptive strategy (green dots): depending on the local nutrient concentration, the agents either follow others or avoid them; spreading strategy (red dots): the agents behave aversely and avoid each other, with $\alpha < 0$ for all nutrient concentrations.

consists of one output neuron for every action with a linear activation function. In our RL algorithm we trained the neural network with the help of TensorFlow [43].

The RL algorithm can be successfully applied, allowing the agents to maximize the consumed amount of nutrients. To obtain a systematic overview of the possible strategies that the particles employ, we determine the full state diagram as a function of the consumption rate k_d and particle density N/L^2 . We identify the three different strategies (i)-(iii) that differ at the level of alignment along the nutrient field and the quorum sensing field (see also Fig. 1 and Supplementary Movie). For low consumption rates we find a "uniting strategy" (blue dots in Fig. 3), where the particles always follow the self-produced quorum sensing field and try to aggregate. This means that the particles always align their orientation towards higher particle concentration (see blue curves corresponding to $k_d t_0/l_0 = 0.001$ with $\alpha(c) > 0$ for all concentrations in Fig. 4). This effect is especially dominant at low concentrations, since in this case it is profitable for a particle to change local position as quickly as possible and follow the signal of high particle accumulations, which have found areas with high concentrations. In addition, the particle uses the nutrient field itself to navigate. However, as can be seen in Fig. 4, the influence by $\beta(c)$ is small at low concentrations, guaranteeing that particles do not get stuck in local maxima. Once particles reach areas of high nutrient concentration, this behavior changes. The particle orientation is now deter-

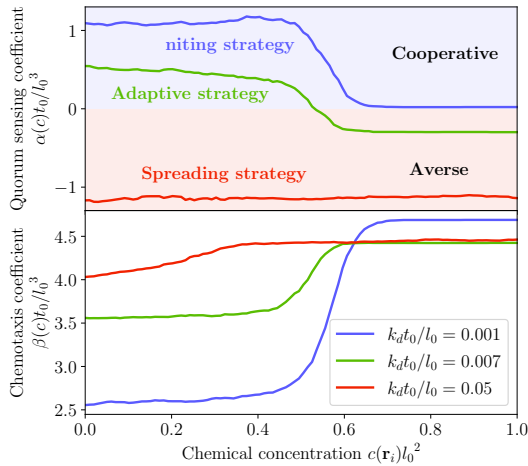


FIG. 4. Active agent orientation. The agents adapt their orientation along the quorum sensing field $\rho(\mathbf{r}, t)$ and the nutrient field $c(\mathbf{r}, t)$ with strength $\alpha(c)$ (top panel) and $\beta(c)$ (bottom panel), respectively. For small consumption rates k_d , the orientation of agents at low nutrient concentrations is mainly determined by communication with surrounding others (blue - uniting). As soon as the agents find places with high nutrient concentration, this behavior changes and they follow local gradients of the nutrient field. As the consumption rate increases, this behavior can also switch completely, with agents moving away from each other at high nutrient concentrations (green - adaptive). For large consumption rates, this strategy is replaced by an overall averse behavior in which the agents attempt to avoid accumulation but simultaneously move along the gradient of the nutrient field (red - spreading).

mined by the local gradients of the nutrient field, as can be seen from the increase in $\beta(c)$ in Fig. 4. Once particles have reached the global maximum, they no longer need guidance from other particles and the influence of the quorum sensing molecules decreases.

For very large consumption rates and with increasing particle density, the exact opposite occurs with a "spreading strategy" by which the particles avoid each other (red dots in Fig. 3). As can be seen in Fig. 4, the particles permanently choose $\alpha < 0$, which causes

them to stay away from each other. Nevertheless, they are still able to follow increasing nutrient concentrations. Since the consumption rate of the particles is high, they also do not easily get lost in local maxima anymore (because these are directly annihilated) and β is increased even for small concentrations c (compared to the uniting strategy).

Between these two strategies, another strategy in the state diagram in Fig. 3 can be observed, which turns out to be a mixture of the previous two in the form of an "adaptive strategy". Here, the local nutrient concentration at the position of the particles decides whether they move towards each other or try to avoid each other. At small nutrient concentrations, the particles orient along the gradient of the quorum sensing field ρ , similar to the uniting strategy. However, this effect is smaller in the adaptive strategy, where an excessive accumulation of particles leads to an immediate degradation of c at exclusively a single location. If the particles are at locations of high nutrient concentration, they adapt their behavior and try to keep distance to neighboring particles (see change of sign in α for $k_d t_0 / l_0 = 0.007$). In this region for moderate consumption rates (green dots in Fig. 3), the particles decide, depending on the local concentration $c(\mathbf{r}, t)$, whether to move towards neighboring particles or to avoid them.

In conclusion active particles were equipped with a machine learning algorithm that enables them to cooperatively consume a nutrient field. Thereby, they learn three different strategies ("uniting", "spreading", "adaptive") depending on their density and their ability to consume nutrients. These results could be applied to help microrobots in finding efficient strategies to decontaminate polluted water [28].

In the future, it would be interesting to realize this in an experimental setting. As a first step, one could use externally controlled microswimmers such as in [33] or macroscopic robots [44], where the nutrient and quorum sensing field are simulated. In the approach used here, the particles sense only the local concentration of the nutrient field, which is a minimal amount of information about their environment. Extending the information that particles receive to include also the orientations of other particles, could give rise to additional strategies such as flocking [13] and might increase the nutrient consumption efficiency. A different path to improving the efficiency of nutrient consumption is to control the quorum sensing depending on the state of the particles or the amount of consumed nutrient.

- [1] F. Cichos, K. Gustavsson, B. Mehlig, and G. Volpe, Machine learning for active matter, *Nature Machine Intelligence* **2**, 94 (2020).
 [2] S. Colabrese, K. Gustavsson, A. Celani, and L. Biferale, Flow navigation by smart microswimmers via reinforcement learning, *Phys. Rev. Lett.* **118**, 158004 (2017).

- [3] S. Colabrese, K. Gustavsson, A. Celani, and L. Biferale, Smart inertial particles, *Phys. Rev. Fluids* **3**, 084301 (2018).
 [4] K. Gustavsson, L. Biferale, A. Celani, and S. Colabrese, Finding efficient swimming strategies in a three-dimensional chaotic flow by reinforcement learning, *Eur.*

- Phys. J. E **40**, 110 (2017).
- [5] J. K. Alageshan, A. K. Verma, J. Bec, and R. Pandit, Machine learning strategies for path-planning microswimmers in turbulent flows, *Phys. Rev. E* **101**, 043110 (2020).
 - [6] J. Qiu, W. Huang, C. Xu, and L. Zhao, Swimming strategy of settling elongated micro-swimmers by reinforcement learning, *Sci. China Phys. Mech. Astron.* **63**, 284711 (2020).
 - [7] L. Biferale, F. Bonaccorso, M. Bazzicotti, P. Clark Di Leoni, and K. Gustavsson, Zermelo's problem: Optimal point-to-point navigation in 2d turbulent flows using reinforcement learning, *Chaos* **29**, 103138 (2019).
 - [8] G. Reddy, A. Celani, T. J. Sejnowski, and M. Vergassola, Learning to soar in turbulent environments, *Proc. Natl. Acad. Sci. USA* **113**, E4877 (2016).
 - [9] G. Reddy, J. Wong-Ng, A. Celani, T. J. Sejnowski, and M. Vergassola, Glider soaring via reinforcement learning in the field, *Nature* **562**, 236 (2018).
 - [10] A. C. H. Tsang, P. W. Tong, S. Nallan, and O. S. Pak, Self-learning how to swim at low Reynolds number, *Phys. Rev. Fluids* **5**, 074101 (2020).
 - [11] B. Hartl, M. Hübl, G. Kahl, and A. Zöttl, Microswimmers learning chemotaxis with genetic algorithms, arXiv:2101.12258 (2021).
 - [12] Y. Dou and K. J. Bishop, Autonomous navigation of shape-shifting microswimmers, *Phys. Rev. Research* **1**, 032030 (2019).
 - [13] M. Durve, F. Peruani, and A. Celani, Learning to flock through reinforcement, *Phys. Rev. E* **102**, 012601 (2020).
 - [14] B. Liebchen and H. Löwen, Optimal navigation strategies for active particles, *EPL* **127**, 34003 (2019).
 - [15] A. Daddi-Moussa-Ider, H. Löwen, and B. Liebchen, Hydrodynamics can determine the optimal route for microswimmer navigation, *Communications Physics* **4**, 1 (2021).
 - [16] L. Zanollo, M. Caraglio, T. Franosch, and P. Faccioli, Target search of active agents crossing high energy barriers, *Phys. Rev. Lett.* **126**, 018001 (2021).
 - [17] M. Nasiri and B. Liebchen, Reinforcement learning of optimal active particle navigation, arXiv preprint arXiv:2202.00812 (2022).
 - [18] E. Schneider and H. Stark, Optimal steering of a smart active particle, *EPL* **127**, 64003 (2019).
 - [19] Y. Yang and M. A. Bevan, Optimal navigation of self-propelled colloids, *ACS Nano* **12**, 10712 (2018).
 - [20] H. M. La, R. Lim, and W. Sheng, Multirobot cooperative learning for predator avoidance, *IEEE Transactions on Control Systems Technology* **23**, 52 (2014).
 - [21] C. Bechinger, R. Di Leonardo, H. Löwen, C. Reichhardt, G. Volpe, and G. Volpe, Active particles in complex and crowded environments, *Reviews of Modern Physics* **88**, 045006 (2016).
 - [22] F. A. Lavergne, H. Wendehenne, T. Bäuerle, and C. Bechinger, Group formation and cohesion of active particles with visual perception-dependent motility, *Science* **364**, 70 (2019).
 - [23] S. Muñios-Landin, A. Fischer, V. Holubec, and F. Cichos, Reinforcement learning with artificial microswimmers, *Science Robotics* **6**, eabd9285 (2021).
 - [24] L. K. Abdelmohsen, F. Peng, Y. Tu, and D. A. Wilson, Micro- and nano-motors for biomedical applications, *J. Mater. Chem. B* **2**, 2395 (2014).
 - [25] D. Patra, S. Sengupta, W. Duan, H. Zhang, R. Pavlick, and A. Sen, Intelligent, self-powered, drug delivery systems, *Nanoscale* **5**, 1273 (2013).
 - [26] B. J. Nelson, I. K. Kaliakatsos, and J. J. Abbott, Microrobots for minimally invasive medicine, *Annu. Rev. Biomed. Eng.* **12**, 55 (2010).
 - [27] M. You, C. Chen, L. Xu, F. Mou, and J. Guan, Intelligent micro/nanomotors with taxis, *Acc. Chem. Res.* **51**, 3006 (2018).
 - [28] W. Gao and J. Wang, The environmental impact of micro/nanomachines: a review, *ACS Nano* **8**, 3170 (2014).
 - [29] G. H. Wadhams and J. P. Armitage, Making sense of it all: bacterial chemotaxis, *Nature Reviews Molecular Cell Biology* **5**, 1024 (2004).
 - [30] Y. Hong, N. M. K. Blackman, N. D. Kopp, A. Sen, and D. Velegol, Chemotaxis of nonbiological colloidal rods, *Phys. Rev. Lett.* **99**, 178103 (2007).
 - [31] M. B. Miller and B. L. Bassler, Quorum sensing in bacteria, *Annual Review of Microbiology* **55**, 165 (2001), PMID: 11544353, <https://doi.org/10.1146/annurev.micro.55.1.165>.
 - [32] M. Rein, N. Heimß, F. Schmid, and T. Speck, Collective behavior of quorum-sensing run-and-tumble particles under confinement, *Phys. Rev. Lett.* **116**, 058102 (2016).
 - [33] T. Bäuerle, A. Fischer, T. Speck, and C. Bechinger, Self-organization of active particles by quorum sensing rules, *Nature Communications* **9**, 3232 (2018).
 - [34] J. Grauer, H. Löwen, A. Be'er, and B. Liebchen, Swarm hunting and cluster ejections in chemically communicating active mixtures, *Scientific Reports* **10**, 5594 (2020).
 - [35] A. Ziepke, I. Maryshev, I. Aronson, and E. Frey, Multi-scale organization in communicating active matter, PREPRINT (Version 1) available at Research Square (2022).
 - [36] U.-L. Pen, Generating cosmological Gaussian random fields, *The Astrophysical Journal* **490**, L127 (1997).
 - [37] E. Bertschinger, Multiscale Gaussian random fields and their application to cosmological simulations, *The astrophysical journal supplement series* **137**, 1 (2001).
 - [38] G. Goon, Gaussian fields (2021), <https://garrettgoon.com/gaussian-fields/>.
 - [39] R. S. Sutton and A. G. Barto, *Reinforcement learning: An introduction* (MIT press, 2018).
 - [40] V. Mnih, K. Kavukcuoglu, D. Silver, A. A. Rusu, J. Veness, M. G. Bellemare, A. Graves, M. Riedmiller, A. K. Fidjeland, G. Ostrovski, *et al.*, Human-level control through deep reinforcement learning, *nature* **518**, 529 (2015).
 - [41] D. P. Kingma and J. Ba, Adam: A method for stochastic optimization 10.48550/arxiv.1412.6980 (2014).
 - [42] V. Nair and G. E. Hinton, Rectified linear units improve restricted Boltzmann machines, in *Proceedings of the 27th International Conference on International Conference on Machine Learning, ICML'10* (Omnipress, Madison, WI, USA, 2010) p. 807–814.
 - [43] M. Abadi, A. Agarwal, P. Barham, E. Brevdo, Z. Chen, C. Citro, G. S. Corrado, A. Davis, J. Dean, *et al.*, TensorFlow: Large-scale machine learning on heterogeneous systems (2015), software available from tensorflow.org.
 - [44] M. Mijalkov, A. McDaniel, J. Wehr, and G. Volpe, Engineering sensorial delay to control phototaxis and emergent collective behaviors, *Physical Review X* **6**, 011008 (2016).

8.5 Paper V: Strategic spatiotemporal vaccine distribution increases the survival rate in an infectious disease like Covid-19

Reproduced from

J. Grauer, H. Löwen, & B. Liebchen
*Strategic spatiotemporal vaccine distribution increases
the survival rate in an infectious disease like Covid-19*
Sci. Rep. 10, 21594 (2020)

Digital Object Identifier (DOI): <https://doi.org/10.1038/s41598-020-78447-3>

See also the related article published in Physik Journal 20 (2021) Nr.2 18-19 by Gerhard Gompper.

Statement of contribution

H.L. and B.L. planned and designed the project. I performed the simulations. All authors analyzed and discussed the results. B.L. wrote the manuscript. H.L. and I edited it.

Copyright and license notice

This article is licensed under a Creative Commons Attribution 4.0 International License, which permits use, sharing, adaptation, distribution and reproduction in any medium or format, as long as you give appropriate credit to the original author(s) and the source, provide a link to the Creative Commons license, and indicate if changes were made. To view a copy of this license, visit <http://creativecommons.org/licenses/by/4.0/>



OPEN Strategic spatiotemporal vaccine distribution increases the survival rate in an infectious disease like Covid-19

Jens Grauer¹, Hartmut Löwen¹ & Benno Liebchen²✉

Present hopes to conquer the Covid-19 epidemic are largely based on the expectation of a rapid availability of vaccines. However, once vaccine production starts, it will probably take time before there is enough vaccine for everyone, evoking the question how to distribute it best. While present vaccination guidelines largely focus on individual-based factors, i.e. on the question to whom vaccines should be provided first, e.g. to risk groups or to individuals with a strong social-mixing tendency, here we ask if a strategic spatiotemporal distribution of vaccines, e.g. to prioritize certain cities, can help to increase the overall survival rate of a population subject to an epidemic disease. To this end, we propose a strategy for the distribution of vaccines in time and space, which sequentially prioritizes regions with the most new cases of infection during a certain time frame and compare it with the standard practice of distributing vaccines demographically. Using a simple statistical model we find that, for a locally well-mixed population, the proposed strategy strongly reduces the number of deaths (by about a factor of two for basic reproduction numbers of $R_0 \sim 1.5 - 4$ and by about 35% for $R_0 \sim 1$). The proposed vaccine distribution strategy establishes the idea that prioritizing individuals not only regarding individual factors, such as their risk of spreading the disease, but also according to the region in which they live can help saving lives. The suggested vaccine distribution strategy can be tested in more detailed models in the future and might inspire discussions regarding the importance of spatiotemporal distribution rules for vaccination guidelines.

The Covid-19 pandemic 2019/2020¹⁻⁵ has led to more than 40 million infections and 1 million deaths worldwide (October 2020)^{6,7} and an unprecedented social and economic cost which comprises a sudden rise of the number of unemployments by more than 20 million in the USA alone, and a damage of trillions of dollars at the stock market and in the worldwide real economy⁸. This situation challenges politicians to decide on suitable measures and researchers to explore their efficiency, based on models allowing to forecast and compare the evolution of infectious diseases (like Covid-19) when taking one or the other action.

Available measures to efficiently deal with epidemic outbreaks at low infection numbers include a rigorous contact-tracing (e.g. based on “Corona-Apps”⁹) and -testing combined with quarantine of infected individuals¹⁰⁻¹³. Strict travel restrictions preventing an infectious disease from entering disease-free regions (or to die out locally¹⁴) present an alternative measure^{15,16}, whereas travel reductions by less than $\sim 99\%$ ¹⁷ slow down the spreading of the disease only slightly¹⁷⁻¹⁹.

At higher infection numbers, the only way to avoid an explosion of contagions is to reduce the contact rate through measures that largely influence the everyday life of the population, such as social distancing^{11,13,20-23} and lock-down^{13,24}. If a population does not persistently reduce the contact rate to the point where infection rates decrease (this requires a contact reduction of $> 60\%$ for a basic reproduction number of $R_0 = 2.5$ ²²), the majority of its members must endure the disease—until it finally reaches herd immunity²⁵.

The main hope which remains at such stages rests on the rapid discovery and admission of vaccine^{26,27} (or antibodies²⁸) to accelerate reaching herd immunity. However, while every day where an infectious disease like Covid-19 is active may cause thousands of additional deaths, even after admission, it may take months until sufficient vaccine is available to overcome an infectious disease. Therefore it is important to strategically distribute the available vaccines such that the number of deaths remains as small as possible. Surprisingly, both official

¹Institut für Theoretische Physik II: Weiche Materie, Heinrich-Heine-Universität Düsseldorf, 40225 Düsseldorf, Germany. ²Institut für Festkörperphysik, Technische Universität Darmstadt, 64289 Darmstadt, Germany. ✉email: liebchen@fkp.tu-darmstadt.de

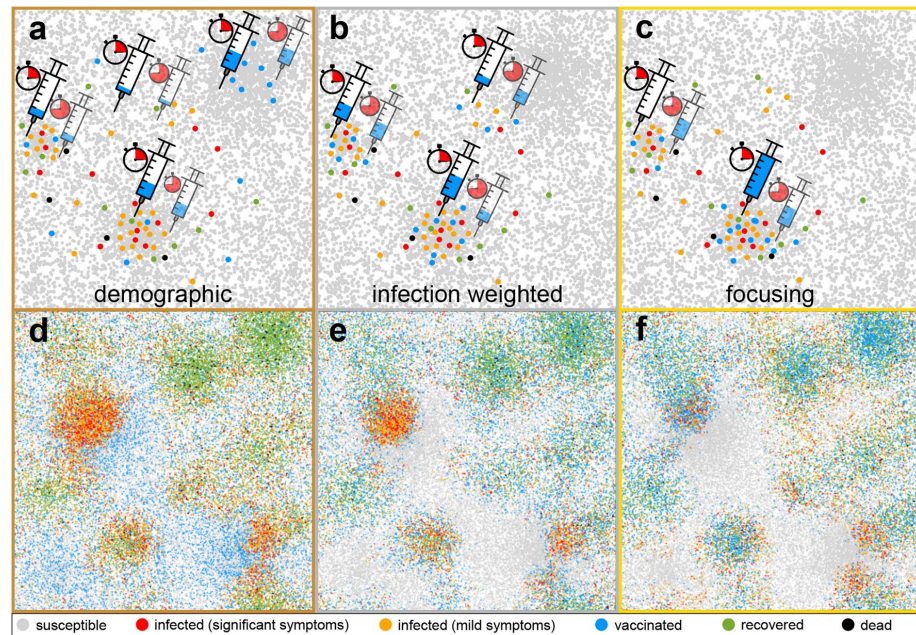


Figure 1. Schematic illustration of the proposed spatiotemporal vaccine distribution strategies and of the simulation model. (a) shows the standard “demographic strategy”, where vaccines (dosage needles) are continuously distributed among all regions (e.g. cities) proportionally to their population density (dots represent groups of individuals). (b) shows the “infection weighted” strategy, where vaccines are distributed proportionally to the local bi-linear incidence rates (red and orange dots) and (c) shows the “focusing strategy” where at early times (clocks; transparent syringes show the vaccine distribution at later times) only the region with the largest bi-linear incidence rate receives vaccines, until the rate of a second region catches up and also receives vaccines. (d)–(f) show typical simulation snapshots for an inhomogeneously distributed population with a “city size distribution” following Zipf’s law, taken 56 days after the onset of vaccination when following the demographic strategy, the infection weighted strategy or the focusing strategy, respectively. The legend below shows the states in our model.

vaccination guidelines, e.g. for pandemic influenza^{29,30}, and previous works on vaccine distribution^{31–33}, focus on the question to whom vaccine should be mainly provided, e.g. to prioritize individuals by age or disease risk, and leave the quest for a suitable spatial and temporal vaccine distribution aside. (Other works like³⁴ ask for the optimal vaccine production rate.) This results in the common practice of simply distributing vaccines proportionally to the population density³⁵.

In the present work we propose alternative strategies for the spatiotemporal distribution of gradually produced vaccines, which hinge on the idea that the number of deaths due to a spreading infectious disease is controlled by the bi-linear incidence rate βSI^{36} , which increases linearly in the number of susceptibles S and infections I , with β being the transmission coefficient, not by population density. With the “infection weighted strategy” (see Fig. 1b,e), the available vaccine is distributed proportionally to the calculated bi-linear incidence rate. This strategy can be further improved by sequentially prioritizing the regions (cities) with the highest bi-linear incidence rate, and correspondingly the highest number of new infections in a certain time frame (see Fig. 1c,f and the Supplementary Movie); that is by exclusively providing, or “focusing”, all available vaccines to those regions (“focusing strategy”). To compare the infection weighted and focusing strategy with the “demographic” vaccine distribution practice, we develop a simple statistical model describing the time-evolution of an epidemic outbreak (such as Covid-19) and its response to vaccination. As our central result, we find that the number of deaths resulting from infections occurring after the onset of vaccine production is *generally* lower, i.e. for the all considered initial reproduction numbers ($R_0 \sim 1 - 4$) and vaccine production rates as well as in the absence and in the presence of additional social distancing rules, when following the focusing strategy rather than the demographic distribution practice. In fact, for sufficiently inhomogeneous infection patterns, the focusing strategy reduces the number of deaths by more than a factor of two, for a large range of basic reproduction numbers R_0 and vaccine production rates. The difference is largest for $R_0 \sim 2 - 3$, i.e. it features a peak in this range, as might be typical for Covid-19 if no additional measures are in action, but even for $R_0 \sim 1$ the focusing strategy significantly increases the survival probability.

Model

To explore the impact of the spatiotemporal vaccine distribution on the disease-evolution in detail, we now introduce a computational model, which is based on Brownian agents and allows deriving a (nonuniform) statistical mean-field model as we will discuss below. Both models are expected to apply to situations where the population is *locally* well-mixed. The model describes the dynamics of N agents moving randomly in continuous space in a box of size $L \times L$ with periodic boundary conditions. The agents represent groups of individuals and have an internal state variable, which is inspired by the SIR model^{37–39} and its variants^{40–44}. We use colors (see legend in Fig. 1) to represent the possible states in our simulations, which refer to individuals which are “susceptible” (grey), “infected with weak symptoms” (orange), “infected with significant symptoms” (red), “recovered” (green) and “vaccinated” (blue). Infected agents (orange and red) have an inner clock; they remain symptom free for a latency time t_L and then show mild (orange) or significant (red) symptoms for a duration $t_D - t_L$. After an overall disease duration of t_D they either recover with a survival probability $s_{o,r}$ (green) or die with probability $1 - s_{o,r}$ (black), where the indices refer to agents with mild (orange) and significant symptoms (red), respectively. To model the infection dynamics we describe the spatial motion of an agent with position $\mathbf{r}_i(t)$ using Brownian dynamics $\dot{\mathbf{r}}_i(t) = \sqrt{2D}\boldsymbol{\eta}_i(t)$, where D is the diffusion coefficient controlling how fast agents move and $\boldsymbol{\eta}_i(t)$ represents Gaussian white noise with zero mean and unit variance. We assume that all infected agents (orange and red) are infectious, both in the latent phase and afterwards (as for Covid-19) and infect a fraction of $\beta_o + \beta_r$ of those susceptible agents (grey) which are closer than a distance R_c ; here, indices refer to mild (orange) and significant (red) symptoms. Agents showing significant symptoms (red) do not move but can infect “visitors” if actively approaching them.

To connect the suggested model with standard mean-field descriptions for infectious diseases, we now deduce a continuum model from the Langevin equations describing the agent dynamics. The resulting model can be viewed as a generalization of standard mean-field models such as the SIR and the SEIR model to inhomogeneous situations and cases where mild and strong infections coexist (as for Covid-19). Let us now consider continuous variables (fields) representing the local mean number density of susceptible agents $S(\mathbf{r}, t)$, exposed agents $E(\mathbf{r}, t)$ (infected but not yet diseased), infected agents which are free of symptoms (or have mild symptoms) $F(\mathbf{r}, t)$, infected agents with symptoms $I(\mathbf{r}, t)$, recovered (immune) agents $R(\mathbf{r}, t)$ and victims $V(\mathbf{r}, t)$. In the absence of social forces (pair attractions, social distancing), the following equations follow by translating Langevin equations to Smoluchowski equations⁴⁵ and coupling them via suitable reaction terms:

$$\begin{aligned}\dot{S}(\mathbf{r}, t) &= -\beta'(E + F + I)S/\rho_0 + D\nabla^2 S - \nabla \cdot (S\mathbf{f}) - v' \\ \dot{E}(\mathbf{r}, t) &= \beta'(E + F + I)S/\rho_0 - \alpha E + D\nabla^2 E - \nabla \cdot (E\mathbf{f}) \\ \dot{F}(\mathbf{r}, t) &= \alpha r E - \delta F + D\nabla^2 F - \nabla \cdot (F\mathbf{f}) \\ \dot{I}(\mathbf{r}, t) &= \alpha(1 - r)E - \delta I - \nabla \cdot (I\mathbf{f}) \\ \dot{R}(\mathbf{r}, t) &= \delta(s_o F + s_r I) + D\nabla^2 R - \nabla \cdot (R\mathbf{f}) + v' \\ \dot{V}(\mathbf{r}, t) &= \delta(1 - s_r)I + \delta(1 - s_o)F\end{aligned}$$

Note here that the exposed state explicitly shows up as a dynamical variable at the continuum level, but only implicitly in our agent-based simulations where infected agents have an inner clock and are in the latent phase before showing (mild) symptoms. In the above equations, β' is the effective contact rate, i.e. $1/\beta'$ is the mean time between infectious contacts; $\alpha = 1/t_L$ is the rate to switch from the exposed (latent) state to the infected state, $\delta = 1/(t_D - t_L)$ is the recovery rate and $v'(\mathbf{r}, t)$ is the spatiotemporal vaccination rate which is linked to the constant total vaccination rate in the agent-based model via $v = \int d\mathbf{r} v'(\mathbf{r}, t)$. The number r is the ratio of infections proceeding symptom free (or with mild symptoms) and $\rho_0 = N/L^2$ is the mean agent density. Finally, D is the diffusion coefficient and $\mathbf{f}(\mathbf{r}) = -\nabla_r U/\gamma$ is the reduced force due to the external potential which we use to create a density profile mimicking a typical city size distribution. The overall density converges to a Boltzmann distribution $S + E + F + I + R + V = N \exp[-U(\mathbf{r})/(kT)] / \int \exp[-U(\mathbf{r})/(kT)] d\mathbf{r}$, yielding the conservation law $\int (S + E + F + I + R + V) d\mathbf{r} = N$ which can be viewed as an expression of the conservation of the overall number density (or the number of agents) in the course of the dynamics.

Numerically solving this model by using finite difference simulations now allows us to further test the spatiotemporal vaccination strategies. In our simulations we start with the initial state $E = F = R = V = 0$ and $S = 1 - \epsilon$, $I = \epsilon$ where $\epsilon(\mathbf{r}, t)$ represents a small perturbation of the unstable steady state (e.g. $E = F = I = R = V = 0, S = 1$ for $U = 0$), which represents the population before the emergence of the disease. The results of these simulations confirm that the spatiotemporal distribution of continuously distributed vaccines plays an important role; also here, the infection-weighted strategy and the focusing strategy strongly increase the number of survivors as compared to the demographic distribution.

Results

We now perform numerical simulations of both the proposed agent based model and the statistical mean-field model which both lead to consistent results. For the agent based model we perform Brownian dynamics simulations^{46–51} starting with $2 \times 10^{-3}N$ randomly distributed initial infections and an initial reproduction number $R_0 = 2.5$ such that infection numbers exponentially increase over time. Let us assume that vaccine production starts after some initial transient and then allows to transfer v individuals per day from the susceptible to the immune state. (Note that the duration of the initial transient is unimportant in our simulations, if vaccination starts long before herd immunity is reached.) Now considering the time-evolution of the percentage of infected, dead and recovered individuals of a given population, and distributing the available vaccines proportionally to

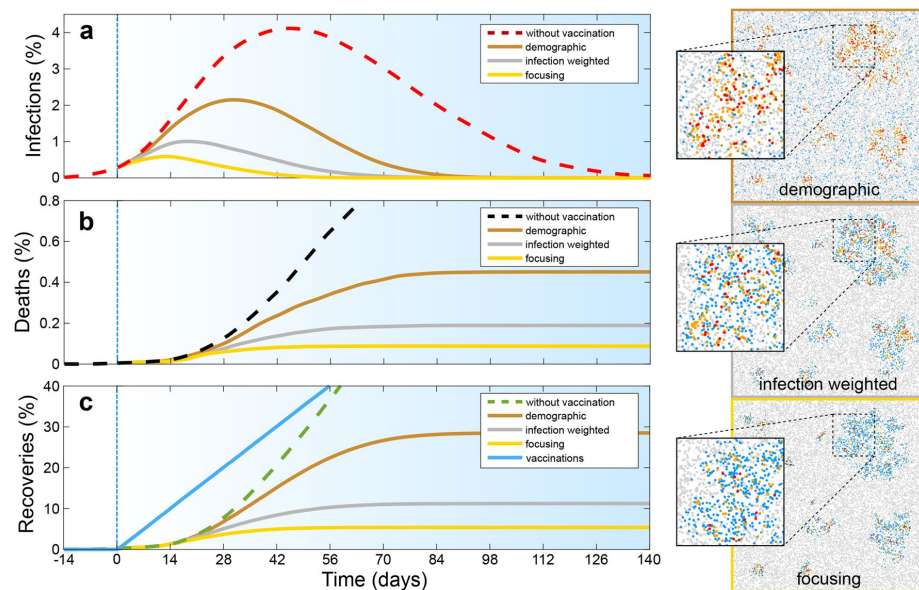


Figure 2. Competition of spatiotemporal vaccine distribution strategies regarding the time evolution of the fraction of infected individuals (a), the fraction of deaths (b), and of recoveries and vaccinations (c). Dashed red lines show simulation results without vaccination and bronze, silver (or grey) and gold show results for the demographic vaccine distribution strategy, the infection weighted strategy and the focusing strategy respectively. The blue line in panel (c) shows the vaccinated fraction of the population and vertical blue lines mark the onset of vaccination; the specific time of which is unimportant (see text). Panels on the right show simulation snapshots taken 14 days after the onset of vaccine production; insets magnify extracts of these snapshots. Parameters: Disease duration $t_D = 14$ days; latency time $t_L = t_D/3$, survival probability $s_r = 0.965$, $s_o = 0.99$, total vaccination rate $v = 0.1N/t_D$ and initial reproduction number $R_0 = 2.5$. (The latter is based on $D = 10^2 R_0^2/t_D$, $\beta_o = 0.3$, $\beta_r = 0.1$; see “Methods”); $L = 500R_0$; curves are averaged over 100 random initial ensembles with $N = 6000$.

the population density (bronze curves in Fig. 2), we observe an infection maximum (panel a) about 30 days (two infection cycles) after the onset of vaccine production, i.e. when about 22% of the population have received vaccines and 2% of the population is infected. When distributing the available vaccines proportionally to the local bi-linear incidence rate βSI instead, which according to $\dot{I} \propto \beta SI$ refers to the number of new infected cases in a given time frame (“infection weighted strategy”), notably, the infection maximum occurs an entire infection cycle earlier (silver curve in panel a). Here the infection number peaks when only 11% of the population has received vaccines and only 1% is infected. However, the infection weighted strategy is not optimal but can be further improved by exclusively providing all available vaccines to the region (e.g. a city) with the highest incidence rate (“focusing strategy”). This means that initially only a single region receives vaccines until the number of new infected individuals in a second region catches up and both regions simultaneously receive vaccines, until a third region catches up and so on. Following this “focusing strategy” the infection peak further shifts to earlier times (golden curve in panel a) and occurs when only 0.6% of the population is infected. Importantly, the resulting fraction of deaths reduces by more than a factor of two when following the infection weighted strategy (silver) rather than the demographic strategy (bronze). It almost halves again when following the focusing strategy instead (gold). This shows that the precise spatial and temporal order of vaccine donation controls the number of survivors from an infectious disease.

We now complement these results by numerical solutions of the statistical mean-field model equations by finite-difference simulations. As in our particle based simulations we find that the focusing strategy is generally better than the infection-weighted strategy and the demographic vaccine distribution strategy. The results of the agent-based simulations and the continuum simulations show a close quantitative agreement (not shown for the uniform system; see Fig. 4 for an exemplaric quantitative comparison in the presence of “cities”).

To systematically explore the robustness of these findings we now repeat our simulations for different vaccine production rates and initial reproduction numbers. Figure 3 shows that the resulting fraction of deaths, counted once the disease is gone, is generally highest for the demographic strategy (bronze) and lowest for the focusing strategy (gold). Mathematically, this is because vaccination is most efficient at locations where it maximally inhibits the development of new cases of infections, which holds true independently of the specific parameter regime. The differences among the individual strategies is comparatively large if vaccine is produced fast enough

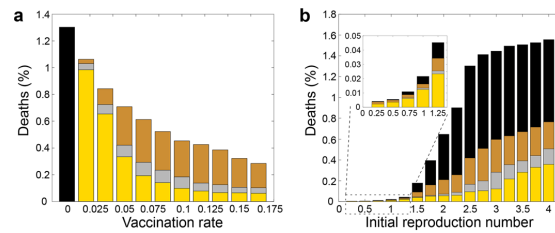


Figure 3. Fraction of deaths as a function of the vaccine production rate (left) and the initial basic reproduction number (right) for the demographic strategy (bronze), the infection-weighted strategy (silver) and the focusing strategy (gold). Results without vaccination (black) are shown for comparison. The results are based on the agent-based model; the statistical mean-field equations lead to very similar graphs. Parameters are shown in the key; remaining ones are as in Fig. 2.

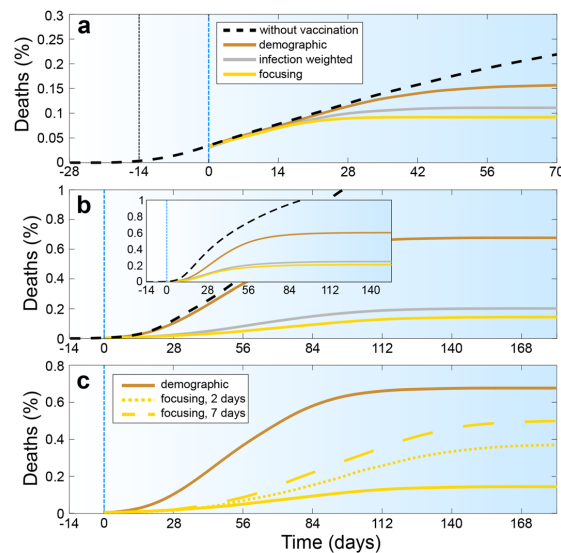


Figure 4. Competition of spatiotemporal vaccination strategies (a) in the presence of social distancing which is activated after 14 days (black vertical line) and reduces the reproduction number to $R \approx 1$ (b) for a population density distribution following Zipf's law. Colors and parameters are as in Fig. 2 but we have $N = 12000$, $L = 700$, $R_0 = 2.7$ (which is based on $D = 10^3 R_c^2 / t_D$ and $\beta_o = 0.05$, $\beta_r = 0.017$) and $v = 0.05N/t_D$. Inset: Analogous results for the mean-field model using same parameters as in the agent-based model and a 140×140 -grid with each grid point corresponding to a spatial area of $5R_c \times 5R_c$ (c) assuming a delay of 2 (dotted golden curve) and 7 (dashed golden curve) days in the registration of the cases of infection. Parameters are as in Fig. 4b.

to allow vaccinating at least about 1% of the population per day and at reproduction rates around $R_0 \sim 2 - 3$. The latter value might be sensible for Covid-19. However, even for slower vaccine production or for $R_0 \sim 1 - 2$ (as typical for influenza), several percent of deaths can be avoided in our simulations by strategically distributing the available vaccines in space and time.

To further explore the applicability-regime of the focusing strategy, we now combine it with social distancing rules, which reduce the effective reproduction number to $R_t \sim 1$. We implement the latter as a phenomenological repulsive three-body interaction among the agents (see “Methods” for details) which prevents them from aggregating in groups of more than two individuals. Also here, the resulting deaths fraction (Fig. 4a) saturates significantly earlier when following the focusing strategy (gold) rather than the demographic strategy (bronze). The difference in deaths numbers among the three different vaccination strategies is almost identical to our corresponding results at $R_0 \sim 1$ but without social distancing (Fig. 3b).

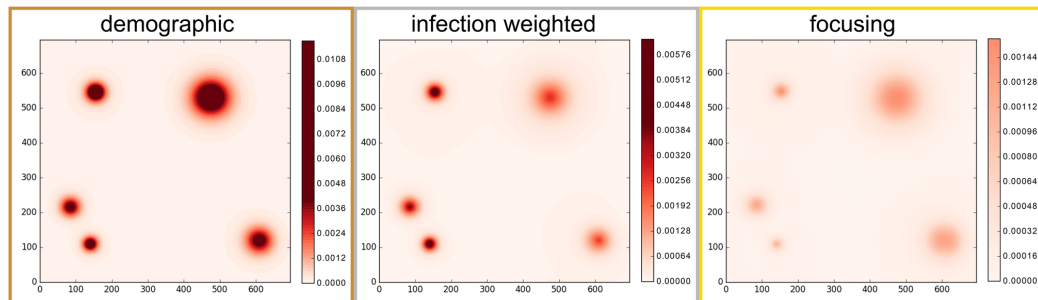


Figure 5. Snapshots of the infection patterns 56 days after the onset of vaccination, based on the statistical mean-field model. Colors show the density of exposed agents $E(\mathbf{r}, t)$. Parameters are as in Fig. 4b.

Finally, we explore a possible impact of a nonuniform population distribution (city structure) on the proposed vaccination strategies. We create a population with a spatial density distribution following Zipf's law which closely describes the city size distribution in most countries⁵² as $\tilde{P}_c(s > S) \propto 1/S$, where $\tilde{P}_c(s)$ is the probability that a city is larger than S . To generate a population featuring a corresponding population distribution, we add an external potential U to the equation of motion of the agents (see “Methods” for details). Following statistical mechanics, the resulting population density follows Boltzmann's law $P(\mathbf{r}) \propto \exp[-U(\mathbf{r})/(kT)]$ where $P(\mathbf{r})$ is the probability that an agent is at position \mathbf{r} and $kT = \gamma D$ is the effective thermal energy of the agents, controlling how often agents leave a “city” (minimum of U). Now matching Boltzmann's distribution with Zipf's law yields a construction rule for U (see “Methods”) to create a population pattern featuring a characteristic city-size distribution. Our resulting simulations, shown in Fig. 4b, and in the Supplementary Movie (for $N = 55,000$ agents), demonstrate that the focusing strategy and the infection weighted-strategy again halve the number of deaths compared to the demographic strategy. Here, the former two strategies are comparatively close to each other regarding the number of resulting deaths, which indicates that in strongly inhomogeneous populations a suitable spatial vaccine distribution rule might be even more important than the precise temporal sequence of vaccine donation. While in the previous simulations we assumed an immediate registration of infected persons, we have tested the strategies when the time scale for registration of infections is delayed by up to seven days (dashed and dotted golden curves in Fig. 4c). Even in the presence of such a delay, we obtain a reduced number of deaths when following the focusing strategy.

To further test the robustness of these findings, we have performed continuum simulations of our statistical mean-field model, which leads to close quantitative agreement with the particle based simulations (Fig. 4b). Typical snapshots of the infection pattern 56 days after the onset of vaccination are shown in Fig. 5. These figures show a clear reduction of the infection number in all infection hotspots for the focusing strategy (panel c) as compared to the infection weighted strategy (b) and in particular compared to the demographic vaccine distribution practice (a).

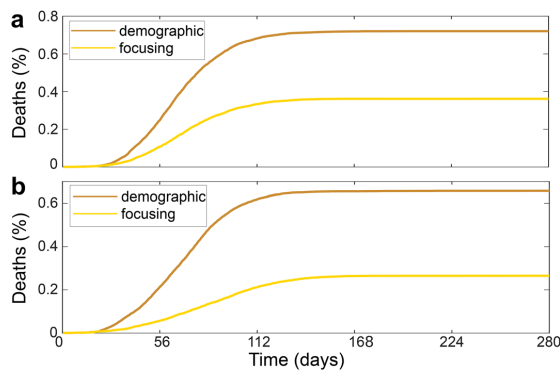
Discussion

Our findings establish the idea that the optimal vaccine distribution depends not only on individual-based factors (who first) but also on the spatiotemporal distribution (e.g. where to provide vaccines first). In particular, our results have shown that by sequentially prioritizing spatial regions (cities) with the highest local bi-linear incidence rates, the proposed “focusing strategy” significantly reduces the number of deaths compared to the standard practice of distributing vaccines demographically. Specifically for locally well-mixed populations, initial reproduction numbers $R_0 \sim 1.5 - 4$ and a sufficiently inhomogeneous infection pattern, and if vaccine production starts long before the population reaches herd immunity, our simulations reveal that the focusing strategy can reduce the number of deaths by more than a factor of two (and for $R_0 \sim 1$ by up to about 35%). These findings should be further tested in detailed models in the future e.g. to explore the impact of the proposed strategy also in situations where the population is not locally well-mixed and to combine the suggested spatiotemporal distribution strategy with individual-based factors such as the prioritization of risk groups, individuals with a strong social mixing tendency or with jobs of systemic relevance. Finally, it should be noted that its applicability hinges on a reasonably detailed knowledge e.g. of the actual local infection numbers and the relevant delay times in the communication of tests.

Methods

Simulation details. To calculate the spatial dynamics of the agents in our model, we solve Langevin equations $\dot{\mathbf{r}}_i(t) = \sqrt{2D}\eta_i(t)$ with $i = 1, \dots, N$ using Brownian dynamics simulations involving a forward Euler time-stepping algorithm and a time-step of $dt = 0.0028$ days which amounts to about 4 minutes. After each timestep we check for each infected agent (red or orange) which susceptible agents (grey) are closer than R_c . We then change the state of the latter agents to an infected state with a transmission rate of $\beta_o = 3\beta_r = 0.0075/dt$ (Figs. 2, 3, 4a), corresponding to infections with mild symptoms (orange) and significant symptoms (red), respectively.

Disease duration t_D	14 days
Latency time t_L	$t_D/3$
Vaccination rate ν	$0.1N/t_D$
Initial reproduction number R_0	2.5–3
Survival probability s_r	96.5%
Survival probability s_o	99%
Effective contact rate β'	R_0/t_D
Diffusion coefficient D	$10^2\text{--}10^3 R_c^2/t_D$
Number of agents N	6,000–55,000
Simulation box length L	500–700 R_c
Strength of "city" potential a	$D\gamma/2$
"City radius" R_{min}, R_{max}	20, 80 R_c

Table 1. Typical simulation parameters.**Figure 6.** Fraction of deaths over time for (a) active particles with inertia and self-propulsion and (b) particles with different mobilities.

These rates yield $\beta_o = 3\beta_r = 0.3$ for the corresponding fractions of contacts which lead to infections. See Table 1 for a list of the simulation parameters which we use in the present work.

Additional simulations. In order to demonstrate that the obtained results do not depend on the details of our simulations, but are rather to be understood as a generic outcome, we have performed additional simulations based on a different particle based model. In particular, we have investigated active underdamped particles, which feature inertia, unlike the Brownian agents considered in our model, and move in a box of size $L \times L$ with periodic boundary conditions. We have also tested this with hard-wall boundary conditions and find similar results (not shown here). In these simulations each particle has an internal drive, represented by an effective self-propulsion force $\mathbf{F}_{SP,i} = \gamma_l v_0 \mathbf{u}(\theta_i)$, where $\mathbf{u}(\theta_i) = (\cos(\theta_i), \sin(\theta_i))$ is the direction of self-propulsion. The behavior of the particles with masses m and moments of inertia I is now substantially different and the underlying equations for the velocities \mathbf{v}_i and orientations θ_i are

$$m \frac{d\mathbf{v}_i(t)}{dt} = -\gamma_l \mathbf{v}_i - \nabla_{\mathbf{r}_i} U + \mathbf{F}_{SP,i} + \sqrt{2D} \gamma_l \boldsymbol{\eta}_i, \quad (1)$$

$$I \frac{d^2\theta_i(t)}{dt^2} = -\gamma_r \frac{d\theta_i}{dt} + \sqrt{2D} \gamma_r \xi_i, \quad (2)$$

where $\boldsymbol{\eta}_i(t), \xi_i(t)$ represent Gaussian white noise of zero-mean unit variance and γ_l, γ_r are translational and rotational drag coefficients. In the simulations we again obtain a significantly reduced number of deaths when applying the focusing strategy as shown in Fig. 6a (with $m/\gamma_l = I/\gamma_r = 10^3/t_D, v_0 = 50R_c/t_D$).

In addition, we carried out further simulations in which we tested the strategies in a structured population in which individuals differ from each other. For this purpose we assigned different mobilities to the agents and modeled two groups of individuals within the population, one with very low mobility ($D = 5 \times 10^2 R_c^2/t_D$) and

the other with very high mobility ($D = 2 \times 10^3 R_c^2/t_D$). The number of deaths is shown in Fig. 6b, where it can be clearly seen how this number is significantly reduced when the focusing strategy is applied.

City size structure. To generate a population density distribution with a structure which is typical for cities, we add an external potential landscape $U(\mathbf{r})$ to the Langevin equations describing the dynamics of the agents, i.e. $\dot{\mathbf{r}}_i(t) = \sqrt{2D}\eta_i(t) - \nabla_{\mathbf{r}_i}U(\mathbf{r}_i)/\gamma$. Here γ is an effective “drag” coefficient determining the strength of the response of the agents to U . We now create U as a superposition of Gaussians, $U(\mathbf{r}) = \sum_j a e^{-\frac{(\mathbf{r}-\mathbf{r}_j)^2}{2\sigma_j^2}}$, each of which leads to a population density maximum around \mathbf{r}_j , which represents the center of city j . Here a is the strength (amplitude) of the reduced potential which we choose as $a = D\gamma/2 = kT/2$ and σ_j defines the radius of city j , which we choose randomly from a distribution $P(\sigma) = \frac{1}{\sigma} \frac{1}{\ln(R_{\max}/R_{\min})}$ where $R_{\min} = 20R_c$ and $R_{\max} = 80R_c$ are the minimal and the maximal possible “city radius” in the simulations underlying Fig. 4b. We randomly distribute the city centers \mathbf{r}_j within the simulation box.

Social distancing. To effectively model social distancing in a simple way, we phenomenologically add repulsive excluded volume interactions among the agents which prevent that groups of more than two agents form. That is, we choose $U = \frac{1}{2} \sum_{k,l \neq k} V_{kl} v_{kl}$ where the sums run over all agents and where V_{kl} represents the Weeks-Chandler-Anderson interaction potential among agents k, l , i.e. $V_{kl} = 4\epsilon \left[\left(\frac{d}{r_{kl}}\right)^{12} - \left(\frac{d}{r_{kl}}\right)^6 \right] + \epsilon$ if $r_{kl} \leq 2^{1/6}d$ and $V_{kl} = 0$ otherwise. Here r_{kl} denotes the distance between agents k and l and $r_{cut} = 2^{1/6}d$ represents a cutoff radius beyond which the interaction potential is zero; ϵ controls the strength of the potential and is chosen such that $\epsilon/\gamma = D$. In our simulations at each timestep we choose $v_{kl} = 1$ if at least one of the agent k and l has a “neighbor” at a distance closer than $d = 3R_c$ and otherwise we choose $v_{kl} = 0$. In addition, we add a weak pair attraction of strength $D/10$ and range $d = 3R_c$ to our simulations to support the formation of pairs. That way, agents can form pairs but there is a significantly reduced probability that they form triplets or larger groups.

Relation of reproduction number to simulation parameters. Here we relate the effective reproduction number $R_e(t)$, which is the average number of infections caused by an infected agent at time t , with the microscopic parameters in our simulation. For this purpose, let us first consider the area $A(t)$ covered by a Brownian agent with radius R_c and diffusion coefficient D over a time t . This area is known as the Wiener sausage⁵³ and reads

$$A(t) = \pi R_c^2 + \frac{8R_c^2}{\pi} \int_0^\infty \frac{1 - e^{-\frac{2Dy^2t}{2R_c^2}}}{y^3(J_0^2(y) + Y_0^2(y))} dy, \quad (3)$$

where $J_0(y)$ and $Y_0(y)$ are the 0-th Bessel functions of the first and second kind. Now denoting the agent density of susceptible agents with ρ_S , the average number of (possibly infectious) contacts during a time τ is $A(\tau)\rho_S$. Thus, if agents are infectious over an overall time of t_D and the fraction of contacts which lead to infections with significant (mild) symptoms is β_r (β_o), we obtain the following expression for the (spatially averaged) effective reproduction number R_e :

$$R_e(t) = A(t_D)\rho_S t(\beta_o + \beta_r), \quad (4)$$

where $R_e(t=0) = R_0$. This expression links the reproduction number with the microscopic simulation parameters and reveals that the reproduction number at time t is proportional to the average density of susceptible agents at time t .

Supplementary movie. The movie shows the time-evolution of the modeled infection pattern for $N = 55,000$ agents and its response to the proposed spatiotemporal vaccine distribution strategies. Parameters are as in Fig. 4b and the population distribution in the movie follows a typical city size structure (Zipf’s law).

Code availability

The source code of the model has been deposited in a recognized public source code repository (Zenodo, <http://doi.org/10.5281/zenodo.4122012>).

Received: 6 July 2020; Accepted: 25 November 2020

Published online: 09 December 2020

References

1. Zhou, P. *et al.* A pneumonia outbreak associated with a new coronavirus of probable bat origin. *Nature* **579**, 270 (2020).
2. Wu, F. *et al.* A new coronavirus associated with human respiratory disease in China. *Nature* **579**, 265 (2020).
3. Li, Q. *et al.* Early transmission dynamics in Wuhan, China, of novel coronavirus-infected pneumonia. *N. Engl. J. Med.* **382**, 1199 (2020).
4. Wang, Y., Hu, M., Li, Q., Zhang, X.-P., Zhai, G., & Yao, N. [arXiv:2002.05534](https://arxiv.org/abs/2002.05534) (2020).
5. Gorbalenya, A. The species Severe acute respiratory syndrome-related coronavirus: Classifying 2019-nCoV and naming it SARS-CoV-2. *Nat. Microbiol.* **5**, 536 (2020).
6. Covid-19 map of the coronavirus resource center of the Johns Hopkins university. <https://coronavirus.jhu.edu/map.html>.

7. Dong, E., Du, H. & Gardner, L. An interactive web-based dashboard to track COVID-19 in real time. *Lancet Infect. Dis.* **20**, 533 (2020).
8. N. Fernandes. *Economic effects of coronavirus outbreak (covid-19) on the world economy* (2020). <https://doi.org/10.2139/ssrn.3557504>.
9. Ferretti, L. *et al.* Quantifying SARS-CoV-2 transmission suggests epidemic control with digital contact tracing. *Science* **368** (2020).
10. Lee, V. J., Chiew, C. J. & Khong, W. X. Interrupting transmission of COVID-19: Lessons from containment efforts in Singapore. *J. Travel. Med.* **27**, taaa039 (2020).
11. Wilder-Smith, A. & Freedman, D. Isolation, quarantine, social distancing and community containment: Pivotal role for old-style public health measures in the novel coronavirus (2019-nCoV) outbreak. *J. Travel. Med.* **27**, 1 (2020).
12. Mizumoto, K., Kagaya, K., Zarebski, A. & Chowell, G. Estimating the asymptomatic proportion of coronavirus disease 2019 (COVID-19) cases on board the Diamond Princess cruise ship, Yokohama, Japan, 2020. *Eurosurveillance* **25**, 2000180 (2020).
13. Maier, B. F. & Brockmann, D. Effective containment explains subexponential growth in recent confirmed COVID-19 cases in China. *Science* **368**, 742 (2020).
14. Bittihn, P. & Golestanian, R. [arXiv:2003.08784](https://arxiv.org/abs/2003.08784) (2020).
15. Kraemer, M. U. *et al.* The effect of human mobility and control measures on the COVID-19 epidemic in China. *Science* **368**, 493 (2020).
16. Tian, H. *et al.* An investigation of transmission control measures during the first 50 days of the COVID-19 epidemic in China. *Science* **368**, 638 (2020).
17. Ferguson, N. M. *et al.* Strategies for mitigating an influenza pandemic. *Nature* **442**, 448 (2006).
18. Chinazzi, M. *et al.* The effect of travel restrictions on the spread of the 2019 novel coronavirus (COVID-19) outbreak. *Science* **368**, 395 (2020).
19. Anzai, A. *et al.* Assessing the impact of reduced travel on exportation dynamics of novel coronavirus infection (COVID-19). *J. Clin. Med.* **9**, 601 (2020).
20. Glass, R. J., Glass, L. M., Beyeler, W. E. & Min, H. J. Targeted social distancing designs for pandemic influenza. *Emerg. Infect. Dis.* **12**, 1671 (2006).
21. Stein, R. A. COVID-19 and rationally layered social distancing. *Int. J. Clin. Pract.* **74**, e13501 (2020).
22. Anderson, R. M., Heesterbeek, H., Klinkenberg, D. & Hollingsworth, T. D. How will country-based mitigation measures influence the course of the COVID-19 epidemic? *Lancet* **395**, 931 (2020).
23. te Vrugt, M., Bickmann, J. & Wittkowski, R. Effects of social distancing and isolation on epidemic spreading modeled via dynamical density functional theory. *Nat. Commun.* **11**, 5576 (2020).
24. Lau, H. *et al.* The positive impact of lockdown in Wuhan on containing the COVID-19 outbreak in China. *J. Travel. Med.* **27**, taaa037 (2020).
25. Fine, P., Eames, K. & Heymann, D. L. "Herd immunity": A rough guide. *Clin. Infect. Dis.* **52**, 911 (2011).
26. Lurie, N., Saville, M., Hatchett, R. & Halton, J. Developing Covid-19 vaccines at pandemic speed. *N. Engl. J. Med.* **382**, 1969 (2020).
27. Graham, B. S. Rapid COVID-19 vaccine development. *Science* **368**, 945 (2020).
28. Cohen, J. The race is on for antibodies that stop the new coronavirus. *Science* **368**, 564 (2020).
29. *U.S. department of health and human services, guidance on allocating and targeting pandemic influenza vaccine.* <https://www.cdc.gov/flu/pandemic-resources/pdf/2018-Influenza-Guidance.pdf>.
30. *Who guidelines on the use of vaccines and antivirals during influenza pandemics* (2004). https://www.who.int/csr/resources/publications/influenza/11_29_01_A.pdf.
31. Sah, P., Medlock, J., Fitzpatrick, M. C., Singer, B. H. & Galvani, A. P. Optimizing the impact of low-efficacy influenza vaccines. *Proc. Natl. Acad. Sci.* **115**, 5151 (2018).
32. Medlock, J. & Galvani, A. P. Optimizing influenza vaccine distribution. *Science* **325**, 1705 (2009).
33. Tuite, A. R., Fisman, D. N., Kwong, J. C. & Greer, A. L. Optimal pandemic influenza vaccine allocation strategies for the Canadian population. *PLoS One* **5**, e10520 (2010).
34. Hethcote, H. W. & Waltman, P. Optimal vaccination schedules in a deterministic epidemic model. *Math. Biosci.* **18**, 365 (1973).
35. Venkatramanan, S. *et al.* Optimizing spatial allocation of seasonal influenza vaccine under temporal constraints. *PLoS Comput. Biol.* **15**, e1007111 (2019).
36. Li, M. & Liu, X. *Abstr. Appl. Anal.* **2014**, 131257. <https://doi.org/10.1155/2014/131257> (2014) (ISSN 1085-3375).
37. Kermack, W. O. & McKendrick, A. G. A contribution to the mathematical theory of epidemics. *Proc. R. Soc. Lond.* **115**, 700 (1927).
38. Hethcote, H. W. The mathematics of infectious diseases. *SIAM Rev.* **42**, 599 (2000).
39. Marathe, M. & Vullikanti, A. K. S. Computational epidemiology. *Commun. ACM* **56**, 88 (2013).
40. Pastor-Satorras, R., Castellano, C., Van Mieghem, P. & Vespignani, A. Epidemic processes in complex networks. *Rev. Mod. Phys.* **87**, 925 (2015).
41. Li, M. Y. & Muldowney, J. S. Global stability for the SEIR model in epidemiology. *Math. Biosci.* **125**, 155 (1995).
42. Liu, W.-M., Hethcote, H. W. & Levin, S. A. Dynamical behavior of epidemiological models with nonlinear incidence rates. *J. Math. Biol.* **25**, 359 (1987).
43. De Falco, U. S. I., Della Cioppa, A. & Tarantino, E. [arXiv:2004.00553v2](https://arxiv.org/abs/2004.00553v2) (2020).
44. Adhikari, R., Bolitho, A., Caballero, F., Cates, M., Dolezal, E. J., Ekeh, T., Guieth, J., Jack, R. L., Kappler, J., Kikuchi, L., *et al.* [arXiv:2005.09625](https://arxiv.org/abs/2005.09625) (2020).
45. Risken, H. *The Fokker-Planck Equation* (Springer, New York, 1996).
46. Erban, R. From molecular dynamics to Brownian dynamics. *Proc. R. Soc. A* **470**, 20140036 (2014).
47. Romanczuk, P., Bär, M., Ebeling, W., Lindner, B. & Schimansky-Geier, L. Active Brownian particles. *Eur. Phys. J. Spec. Top.* **202**, 1 (2012).
48. Volpe, G. & Volpe, G. Simulation of a Brownian particle in an optical trap. *Am. J. Phys.* **81**, 224 (2013).
49. Stenhammar, J., Tiribocchi, A., Allen, R. J., Marenduzzo, D. & Cates, M. E. Continuum theory of phase separation kinetics for active Brownian particles. *Phys. Rev. Lett.* **111**, 145702 (2013).
50. Winkler, R. G., Wysocki, A. & Gompper, G. Virial pressure in systems of spherical active Brownian particles. *Soft Matter* **11**, 6680 (2015).
51. Martín-Gómez, A., Levis, D., Díaz-Guilera, A. & Pagonabarraga, I. Collective motion of active Brownian particles with polar alignment. *Soft Matter* **14**, 2610 (2018).
52. Gabaix, X. Zipf's law for cities: An explanation. *Q. J. Econ.* **114**, 739 (1999).
53. Rataj, J., Schmidt, V. & Spodarev, E. On the expected surface area of the Wiener sausage. *Math. Nachr.* **282**, 591 (2009).

Acknowledgements

We thank Michael E. Cates for helpful comments.

Author contributions

H.L. and B.L. have planned and designed the project. J.G. has performed the simulations. All authors have discussed the results. B.L. has written the manuscript with input from J.G. and H.L.

www.nature.com/scientificreports/

Funding

Open Access funding enabled and organized by Projekt DEAL.

Competing interests

The authors declare no competing interests.

Additional information

Supplementary information is available for this paper at <https://doi.org/10.1038/s41598-020-78447-3>.

Correspondence and requests for materials should be addressed to B.L.

Reprints and permissions information is available at www.nature.com/reprints.

Publisher's note Springer Nature remains neutral with regard to jurisdictional claims in published maps and institutional affiliations.



Open Access This article is licensed under a Creative Commons Attribution 4.0 International License, which permits use, sharing, adaptation, distribution and reproduction in any medium or format, as long as you give appropriate credit to the original author(s) and the source, provide a link to the Creative Commons licence, and indicate if changes were made. The images or other third party material in this article are included in the article's Creative Commons licence, unless indicated otherwise in a credit line to the material. If material is not included in the article's Creative Commons licence and your intended use is not permitted by statutory regulation or exceeds the permitted use, you will need to obtain permission directly from the copyright holder. To view a copy of this licence, visit <http://creativecommons.org/licenses/by/4.0/>.

© The Author(s) 2020

8.6 Paper VI: Mutation induced infection waves in diseases like COVID-19

Reproduced from

F. J. Schwarzendahl, J. Grauer, B. Liebchen, & H. Löwen
Mutation induced infection waves in diseases like COVID-19
Sci. Rep. **12**, 9641 (2022)

Digital Object Identifier (DOI): <https://doi.org/10.1038/s41598-022-13137-w>

Statement of contribution

H.L. and B.L. designed the research project. I contributed to this publication by performing the simulations together with input from F.J.S. F.J.S did the analytical calculations and the simulation data analysis. All authors discussed the results and wrote or edited the manuscript.

Copyright and license notice

This article is licensed under a Creative Commons Attribution 4.0 International License, which permits use, sharing, adaptation, distribution and reproduction in any medium or format, as long as you give appropriate credit to the original author(s) and the source, provide a link to the Creative Commons license, and indicate if changes were made. To view a copy of this license, visit <http://creativecommons.org/licenses/by/4.0/>



OPEN Mutation induced infection waves in diseases like COVID-19

Fabian Jan Schwarzendahl¹, Jens Grauer¹, Benno Liebchen² & Hartmut Löwen¹

After more than 6 million deaths worldwide, the ongoing vaccination to conquer the COVID-19 disease is now competing with the emergence of increasingly contagious mutations, repeatedly supplanting earlier strains. Following the near-absence of historical examples of the long-time evolution of infectious diseases under similar circumstances, models are crucial to exemplify possible scenarios. Accordingly, in the present work we systematically generalize the popular susceptible-infected-recovered model to account for mutations leading to repeatedly occurring new strains, which we coarse grain based on tools from statistical mechanics to derive a model predicting the most likely outcomes. The model predicts that mutations can induce a super-exponential growth of infection numbers at early times, which self-amplify to giant infection waves which are caused by a positive feedback loop between infection numbers and mutations and lead to a simultaneous infection of the majority of the population. At later stages—if vaccination progresses too slowly—mutations can interrupt an ongoing decrease of infection numbers and can cause infection revivals which occur as single waves or even as whole wave trains featuring alternative periods of decreasing and increasing infection numbers. This panorama of possible mutation-induced scenarios should be tested in more detailed models to explore their concrete significance for specific infectious diseases. Further, our results might be useful for discussions regarding the importance of a release of vaccine-patents to reduce the risk of mutation-induced infection revivals but also to coordinate the release of measures following a downwards trend of infection numbers.

The COVID-19 pandemic^{1,2} has led to more than 500 million infected³ and more than 6 million death³ worldwide until the beginning of May 2022. During the course of the pandemic the SARS-CoV-2 virus has mutated into various different strains^{4,5}, some of which have led to an increased infection rate^{6–8} as compared to the original strain² (Wuhan 2019). Examples are the variants B.1.1.7 and B.1.351, which have driven a strong rise of infection numbers in the United Kingdom and South Africa^{9,10} in late 2020^{11,12} and the P.1 mutation which has induced an infection wave in Brazil¹³ in early 2021.

The availability and ongoing vaccine production gives hope to slowly gain control of the disease^{14–16}. However, before herd immunity (if at all achievable) is finally reached worldwide it will take many month or even years, which the virus will exploit to mutate into a range of new strains. Thus, at the timescale of months or years a race is looming ahead between the occurrence of new mutations and the adaption and mass-production of existing vaccines to get these mutations under control. In particular, this makes it questionable if the present (and future) vaccination programs are sufficiently effective to ultimately get diseases like COVID-19 under control. It is therefore important to understand possible mutation-induced long-time disease-evolution scenarios e.g. in view of the ongoing discussions regarding the release of patents to accelerate worldwide vaccination but also regarding requirement of measures like social distancing once the infection numbers show a downwards trend.

Notably, historical examples to assess possible long-time consequences of mutation cascades are scarce, since particularly severe mutations have traditionally led to a rapid death of infected individuals eliminating these mutations. Thanks to modern medical treatment based e.g. on extracorporeal membrane oxygenation support or artificial aspiration, however, such a self-elimination of severe mutations is largely absent. Notably, besides the positive effect of immediately saving many lives, these treatments also have the side effect of inducing a potentially disastrous self-amplification of mutations and infection-rates. Here we are interested in particular in the effects of mutations on the spreading of an infectious disease in phases where (i) mutations can serve as seeds for further mutations some of which are even more infectious than the strain from which they have emerged and (ii) mutation rates are either constant or higher when infection numbers are high. Both factors together can generally lead to a positive feedback loop between infection numbers and mutations suggesting severe long-time

¹Institut für Theoretische Physik II: Weiche Materie, Heinrich-Heine-Universität Düsseldorf, 40225 Düsseldorf, Germany. ²Institute of Condensed Matter Physics, Technische Universität Darmstadt, Darmstadt, Germany. ✉email: Fabian.Schwarzendahl@hhu.de

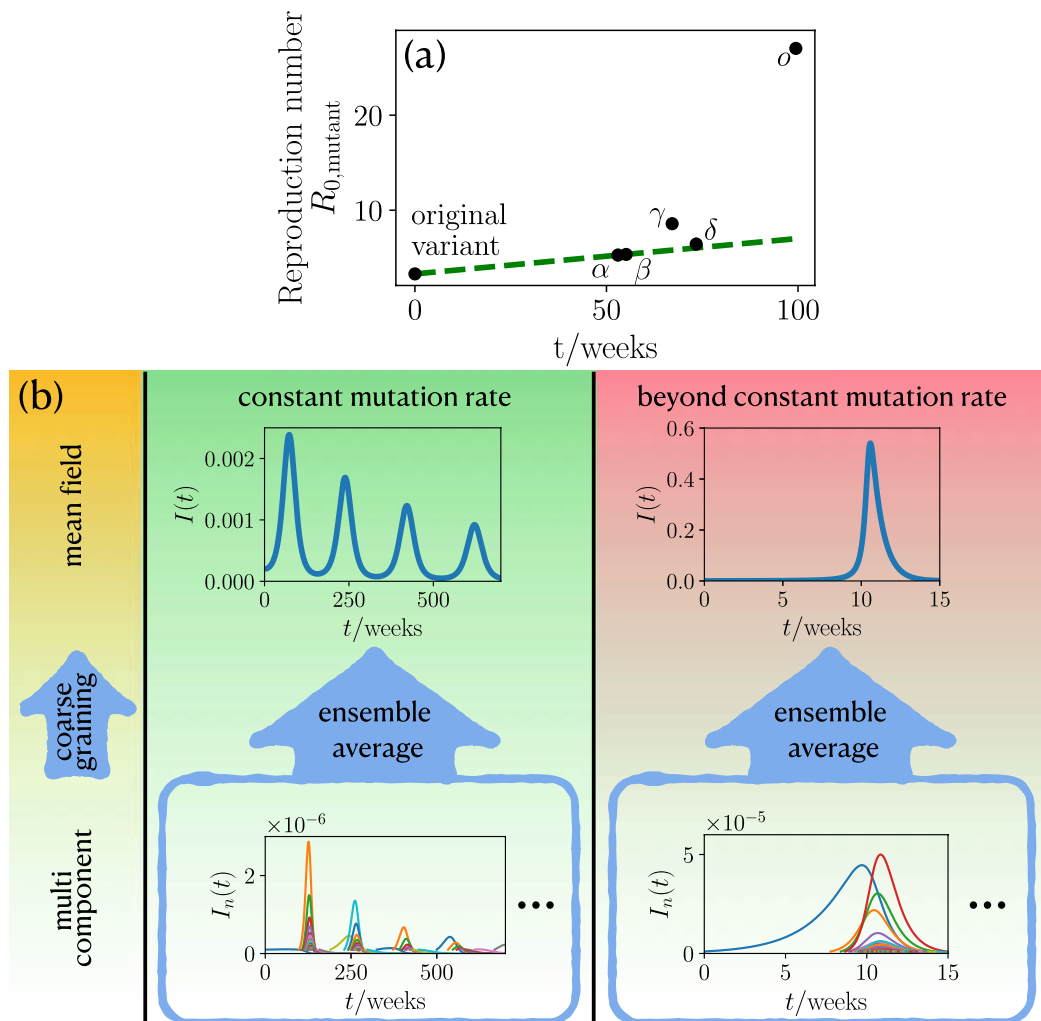


Figure 1. The statistics of mutation formation and its impact on the course of an epidemic. (a) Reproduction number for different COVID-19 mutations as a function of their emergence time (for details see “Methods”). Green dashed line shows a linear fit to initial constant growth. (b) For a constant mutation rate (middle panel, green background) an ensemble average of the multi component description with many infection strains $I_n(t)$ leads to multiple infection waves of the global infection number $I(t)$. Beyond the constant mutation rate, if the mutation rate is coupled to the infection number (right panel, red background), the ensemble average produces a hidden singularity, as manifested by the giant infection wave. Only one representative realization of the multi component description is shown in the blue frames. The left panel (yellow background) indicates the different levels of description starting from multi components leading to an effective mean field by coarse graining.

mutation-induced effects for the disease evolution. Actual data for COVID-19 mutations show, in fact, early signatures supporting such a possible self-amplification scenario during some phases of the disease: They reveal an initial constant and a subsequent nonlinear growth of the relevant infection rate (Fig. 1a). For future pandemics, it would be highly important to understand the possible long-time consequences of such a self-amplification mechanism and how fast vaccination has to progress worldwide in order to suppress the most dramatic ones. However, following the scarcity of useful historical examples illustrating the possible consequences, we have to rely on models to explore the possible impact of mutations on the long-time evolution of the disease dynamics, in particular also in the presence of vaccination and other actions counteracting the self-amplification mechanism. To provide a concrete starting point for such an exploration, in the present work, we develop a statistical

minimal model to predict possible mutation-induced effects for the long-time evolution of infectious diseases like COVID-19. We first develop a stochastic multi-strain generalization of the popular susceptible-infected-recovered (SIR) model to account for the random occurrence of mutations and then use the coarse-graining concept of statistical physics to derive an effective mean-field model enabling general predictions of the most likely scenarios for a given scenario (characterized by parameters such as the mutation and the vaccination rate). See Fig. 1b for a schematic illustration of our approach.

One generic prediction of our model is that mutations induce an *explosive super-exponential growth* of the infection numbers rather than the ordinary and much discussed normal exponential growth, in phases where the population is far away from herd immunity. At later phases, when a population comes close enough to herd-immunity that the reproduction number drops below one ($R < 1$) and infection numbers subsequently decrease to a very low level, mutations can raise the reproduction number to $R > 1$ inducing a new infection wave, which is followed by a whole train of further waves. This scenario occurs even for a constant mutation rate (Fig. 1b). If the mutation rate increases with the number of infections, as generally expected and discussed above, their effect is even more dramatic: then, mutations occur at a self-accelerating pace and continuously prevent the population from reaching herd-immunity by persistently enhancing the effective reproduction number of the disease. As a result the infection dynamics approaches a hidden singularity and displays signatures of a critical dynamics. That is, infection numbers grow extremely fast, giving a giant infection wave, such that the majority of the population is infected at the same time (see the values on the vertical axis in Fig. 1b), which would massively overstrain any existing medical system. Finally, in phases where vaccination of the population takes place and is sufficiently effective to suppress the hidden singularity and hence the explosive self-acceleration of infection numbers, our model predicts the possibility of mutation-induced infection wave trains, as in the case of constant vaccination, illustrating once more the possible dramatic consequences following from the fact that herd-immunity is not necessarily a permanent state in the presence of mutations. To see how these predictions come about, let us now discuss our general modelling approach in detail. Based on this approach we will then discuss our results for a constant mutation rate model and a model that goes beyond a constant mutation rate.

Model

To describe the impact of mutations on the infection dynamics within a simple statistical framework, we first generalize the popular susceptible-infected-recovered (SIR) model^{17–37}, which has been intensively explored in the context of the COVID-19 pandemic^{38–49}. While some recent works have generalized this model to account for two different infectious strains^{50,51}, here we allow for the continuous emergence of new strains with a rate ν , which in general depends on the present infection number. Denoting the fraction of susceptible and recovered individuals with S and R respectively and the fraction of individuals which is infected with strain n as I_n , this leads us to the following dynamical equations:

$$\dot{S} = - \sum_n \beta_n S I_n, \quad (1)$$

$$\dot{I}_n = \beta_n S I_n - \gamma I_n, \quad (2)$$

$$\dot{R} = \sum_n \gamma I_n. \quad (3)$$

Here, γ is the inverse of the average disease duration, i.e. the recovery/death rate and β_n is the infection rate of strain n , which we randomly choose from a certain characteristic distribution. As an initial state, we assume that initially (time $t = 0$) we have only a single infectious strain with a low positive infection number such that only $I_0 \gtrsim 0$ whereas $I_{n \neq 0} = 0$ for $n = 1, 2, \dots$

To allow predicting the average (or most likely) result of the infection dynamics we now coarse grain this model, essentially by averaging over many strains and disease-realizations (see “Methods” section for technical details), which leads to the following effective model:

$$\dot{S} = -\beta(t, I) S I, \quad (4)$$

$$\dot{I} = \beta(t, I) S I - \gamma I, \quad (5)$$

$$\dot{R} = \gamma I, \quad (6)$$

Here, I is the overall infection number (all strains together) and $\beta(t, I)$ is the average infection rate, which can depend on the overall infection number, depending on the underlying mutation statistics (see “Methods”).

Results

Let us now explore the impact of mutations on the disease evolution by comparing numerical simulations of the multi-component model with analytical predictions based on the mean-field model (Fig. 1b). To allow distinguishing between direct effects of mutations from the prevailing (and most infectious) strain and indirect effects due to the self-accelerating mutation cascade which we have described in the introduction and which may or may not become effective in reality, depending on the actual mutation rate and other parameters, we will

sequentially follow on the cases of (i) a constant mutation rate μ leading to the emergence of new strains in our simulations with a constant rate and (ii) a mutation rate which depends on the present infection number $\mu(I)$.

Constant mutation rate. *Mutation-driven infection dynamics.* Let us assume that the infection rate β_n of a newly occurring virus-strain is randomly selected from a normal distribution p with standard deviation σ centered around the infection rate of the presently prevailing strain:

$$p(\beta_n) = \frac{1}{\sqrt{2\pi}\sigma} \text{Exp}\left(-\frac{(\beta_n - \beta_{\max,n-1})^2}{2\sigma^2}\right), \quad (7)$$

Here $\beta_{\max,n-1}$ denotes the largest infection rate of all currently existing strains. This distribution, the average of which moves towards higher values in the course of a disease, is motivated by the fact that newly occurring mutations typically become visible only if they have a higher (or at least not much lower) infection rate than the currently prevailing ones. Coarse graining this mutation statistic (see “Methods”: “Details on model beyond constant mutation rate”) yields an the following average infection rate for our mean-field model

$$\beta = \beta_0 + \mu t \quad (8)$$

where μ is the constant mutation rate and β_0 is the initial infection rate. That is, coarse graining the distribution (7) leads to a constant increase of the infection rate with time.

Let us first explore the disease evolution at early times when the majority of the population is susceptible, such that $S(t) \approx 1$. Then Eq. (5) reduces to

$$\dot{I} = \beta(I, t)I - \gamma I. \quad (9)$$

Now using Eq. (8) we find

$$I(t) = I_0 \exp\left[\frac{1}{2}t(2\beta_0 - 2\gamma + t\mu)\right]. \quad (10)$$

Thus, the fraction of infected individuals does not grow exponentially as in the standard SIR model but even faster. Following Eq. (10) if the mutation rate is high enough that $t\mu \gg 2(\beta_0 - \gamma)$ long before herd-immunity is reached, the infection dynamics generically converges towards $I(t) \propto e^{\mu t/2}$, which is completely mutation-driven. To test this prediction, we now numerically solve the full multi-component model and show the overall $I(t) = \sum_n I_n(t)$ in Fig. 2a. Notably, the result is close to the analytical prediction of the mean-field model and shows an even slightly larger growth.

Clearly, the predicted (super)exponential growth of the infection numbers can not continue forever but has to saturate once the population reaches herd-immunity either by collectively going through the infection or through vaccination. Once herd-immunity is reached, the infection numbers are normally expected to monotonously decrease, as predicted by the standard SIR model. However, numerical solutions of our mean-field model show that after a phase where the population recovers and infection numbers decay to a very low level, they can rapidly grow again (Fig. 2b). This sequence of decreasing and increasing infection numbers can even repeat for many times, leading to an infection wave-train. The maxima of the wave-trains follow a scaling law of $I_{\max} \sim 1/(\beta_0 + \mu t_{\max})^2$ (see SI for derivation), which is shown in Fig. 2c. The prediction of wave trains is also confirmed by numerical solutions of the multi-component model, but somewhat weakened, because the individual strains can show waves occurring at individual “frequencies.” Let us now ask about the mechanism leading to these infection waves. They are induced by the nonlinear coupling of the infected and susceptible. First, the number of infected people grows, when the term βS in Eq. (5) is large enough. At a certain point, the number of susceptible is too small and the saturation effect from the recovery rate γ in Eq. (5) takes over such that the number of infected decreases. However, the infection rate β continues growing with time, such that βS can become large enough to induce a second wave. This feedback continues on multiple times giving rise to the oscillatory behavior shown in Fig. 2b. On a more intuitive level, these considerations show that in the presence of mutations herd-immunity is not necessarily a persistent state of a population and that strongly decreasing infection numbers are not an overall reliable sign that the population has overcome the disease. From a socio-political viewpoint each growth phase within such wave trains might evoke (nonpharmaceutical) interventions, creating an immense mental burden on the population.

Phase diagram. To see how strong measures have to be taken to prevent such an infection wave train (or a super-exponential growth) in the first place, we now systematically vary the parameters in the model to create a state diagram providing a systematic overview on the possible scenarios. It turns out that there are three dimensionless control parameters in our system (see SI), one of which is the initial infection number and the other two ones are the effective reproduction number $S_0\beta_0/\gamma$ and a dimensionless mutation rate μ/β_0^2 . Varying both parameters systematically and solving the mean-field mutation susceptible-infected-recovered (MSIR) model for each parameter combination we obtain the phase diagram shown in Fig. 2e, which shows four qualitatively different epidemic courses: a lethargic phase, which is characterized by an exponential decay, multiple waves, super exponential wave, and a rebound, with an initial local minimum and a proceeding super exponential increase. The occurrence of these states in parameter space is summarized in Fig. 2d. At large reproduction number the dynamics is “super exponential” (green domain) for any positive mutation rate. When decreasing the reproduction number, depending on the mutation rate, one reaches the regime of “multiple waves” which we have previously discussed (pink) or a “rebound” phase (blue) where infection numbers initially decrease, pass

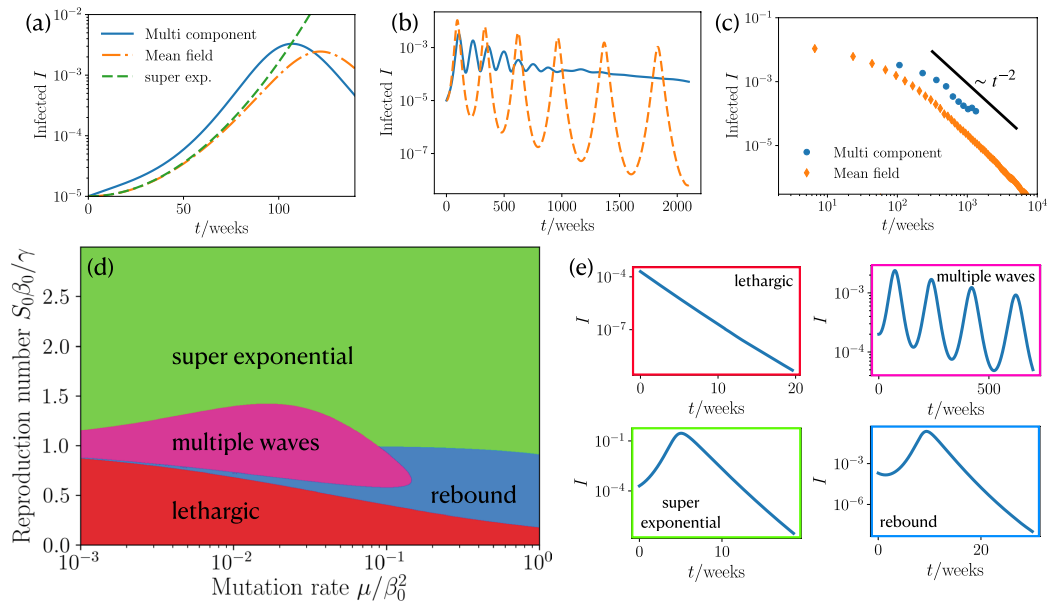


Figure 2. Power law dependence of infection dynamics, phase diagram and state classification for constant mutation rate. (a) Fraction of infected people I at short times t for the coarse grained MSIR, multi component MSIR and the early time approximation Eq. (10). ($I_0 = 10^{-5}$, $R_0 = 1$, $\mu/\beta_0^2 = 0.05$). (b) Long time wave pattern of fraction of infected people for coarse grained MSIR and multi component MSIR approach. ($I_0 = 10^{-5}$, $R_0 = 1$, $\mu/\beta_0^2 = 0.2$). (c) Scaling of maxima of infections for coarse grained MSIR and multi component MSIR approach. ($I_0 = 10^{-5}$, $R_0 = 1$, $\mu/\beta_0^2 = 0.2$). (d) Phase diagram for our coarse grained infection dynamics showing the occurrence of four different courses of the pandemic for varying mutation rate and reproduction number ($I_0 = 2 \times 10^{-4}$). (e) Different courses of infections during an epidemic: lethargic, multiple waves, super exponential, and rebound.

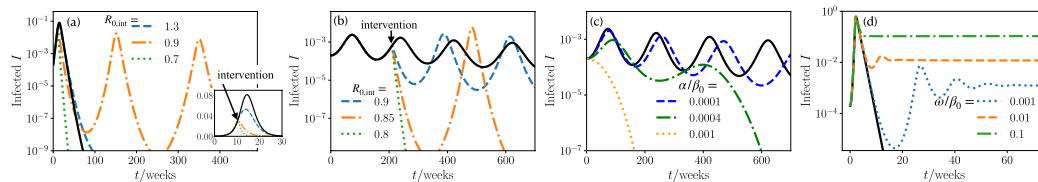


Figure 3. Nonpharmaceutical interventions, vaccinating, and immune escape. (a) Infections as function of time for a super exponential wave. Measures are taken by reducing the reproduction number to $R_{0,int}$ at time t_{int} . Inset: zoom in to the early time regime (black line has no interventions, $R_0 = 1.5$, $\mu/\beta_0^2 = 0.004$, $t_{int} = 10.5$ weeks). (b) Infections as function of time for a wave like pandemic course. Measures are taken by reducing the reproduction number to $R_{0,int}$ at time t_{int} (black line has no interventions, $R_0 = 1$, $\mu/\beta_0^2 = 10^{-3}$, $t_{int} = 210$ weeks). (c) Infections as function of time of different vaccination rates α (black line has no vaccination, $R_0 = 1$, $\mu/\beta_0^2 = 10^{-3}$, $I_0 = 2 \times 10^{-4}$). (d) Infections as function of time of different immune escape rates ω (black line has no immune escape, $R_0 = 1.2$, $\mu/\beta_0^2 = 2$, $I_0 = 2 \times 10^{-4}$).

a minimum and then increase to reach a single maximum before finally decreasing (Fig. 2e). For even lower mutation rates, the population is in the “lethargic” regime, where the infection numbers monotonously decrease.

Nonpharmaceutical interventions, vaccination, and immune escape. In practice the goal is of course be to apply appropriate measures to safely reach the lethargic regime in Fig. 2d and not to end up in the multiple wave or rebound regime where the evolution of infection numbers show a promising initial trend but a severe evolution at later times. To understand the impact of nonpharmaceutical interventions, we reduce the reproduction number^{38–40,42,52,53}, from R_0 to a reduced reproduction number including measures $R_{0,int}$ at a time t_{int} in our simulations and numerical solutions of the MSIR model. Starting in the super exponential wave regime ($R_0 = 1.5$) we apply interventions during the rise of a first wave (see Fig. 3a). By including weak measures ($R_{0,int} = 1.3$),

the maximum of infections decreases as intended, however, the wave needs a longer time to decay, implying a longer period of restrictions for the public. Lowering the reproduction number to $R_{0,int} = 0.9$, results in the appearance of a second and third intervention-mutation induced wave. These waves are enabled by the increased infection rate and the fact that due to the interventions there are more susceptible at a later point in time, where they can facilitate the growth of infections. Here, the situation would be particularly confounding to the public, since it was subjected to measures to decrease the number of infections in the first place; however, this results in more waves and a likely extension of the period of interventions. On the other hand, a strong reduction of the reproduction number ($R_{0,int} = 0.7$) gives a fast decay of infections, as intended. Of course the situation changes when we start from an infection dynamics with multiple waves ($R_0 = 1$) and apply measures during the rise of the second wave (see Fig. 3b). As expected, strong measures ($R_{0,int} = 0.8$) have the intended effect of eliminating the epidemic. On the other hand, if the measures are slightly weaker ($R_{0,int} = 0.85$), the infections first decrease, but then lead to a second intervention-mutation induced delayed wave, which is stronger in magnitude than the first wave. Again, this wave is induced by the growing infection rate and the enhanced number of susceptible individuals due to interventions. To decision makers and the public this type of wave could likely appear as unexpected. However, note that at least the overall number of recovered people at the end of our the epidemic is decreasing with stronger interventions, meaning that if only the cumulative number of infections is considered every reduction of R_0 is useful.

Specifically for COVID-19 vaccines have become available and their continuous production gives hope to get the disease under control. However, one and half a years after vaccines have first become available only about 67% of the worldwide population has been fully vaccinated (early Mai 2022), leaving much time for the emergence of highly infectious mutations. Vaccinations effectively reduce the number of susceptible in the SIR model¹⁴, such that we modify Eq. (4) as

$$\dot{S} = -\beta(I, t)SI - \alpha, \quad (11)$$

with a vaccination rate α . Note that a more realistic model for vaccination would also account for a time dependent roll out. We investigate the effect of vaccination on the infection dynamics for a situation leading to multiple waves (see Fig. 3c). Following Fig. 3c vaccinations have a clear effect; they have to be applied fast enough to significantly reduce the number of infections and temper the train of waves. This further shows the importance of manufacturing and distributing vaccinations as fast as possible.

When newly mutated strains arise the possibility of an immune escape increases, where a recovered individual does not stay immune against the new strain. Let us therefore now include a term which accounts for an effective immune escape in our model in the form of a transition from recovered to susceptible. Explicitly we modify Eqs. (4)–(6) to read

$$\dot{S} = -\beta(t, I)SI + \omega R, \quad (12)$$

$$\dot{I} = \beta(t, I)SI - \gamma I, \quad (13)$$

$$\dot{R} = \gamma I - \omega R, \quad (14)$$

where ω is the immune escape rate. The transition rate between susceptible and recovered introduces two new effects. First, this term leads to a positive feedback loop between the number of susceptible and recovered individuals which induces infection waves (see Fig. 3d), which can also be seen from a linear stability analysis (see SI) of Eqs. (12)–(14). Second, the infected population fraction saturates to a nonzero steady state, due to a replenishment of susceptibles (see also SI).

Beyond constant mutation rate. As a second possible scenario, let us now assume that the mutation rate is coupled to the infection number, such that mutations are more likely in phases where the infection numbers are large. To account for this effect in our model, we assume that new (relevant) mutations occur with a probability of $p_0 I_{n-1}$ from the most infectious strain where p_0 is constant and also that the infection rates of new strains follow from a random walk with a mutation-induced bias as $\beta_n = \beta_{n-1} + \Delta\beta$ (see “Methods” for details). Coarse graining the biased random walk yields a mean field infection rate which evolves as

$$\beta(t) = \int_0^t \lambda I(t') dt', \quad (15)$$

with a mutation rate λ . Intuitively, this means that new mutations occur in our mean-field model with a rate which is proportional to the present infection number.

Mutation-induced dynamics. At early times, where $S \approx 1$ we obtain again Eq. (9), which yields together with Eq. (15)

$$I(t) = -\frac{\delta_1}{\lambda [1 + \cosh(2 \ln \delta_2 + t \sqrt{\delta_1})]}, \quad (16)$$

where δ_1 and δ_2 are constants that are given in the SI. Importantly, the infections in Eq. (16) do not grow exponentially, but there is an explosive super exponential growth, which asymptotically has a scaling behavior following $I_{sc}(t) \sim 1/|t - t_c|^2$ with a critical time t_c (see SI for explicit expression). Crucially, this giant infection

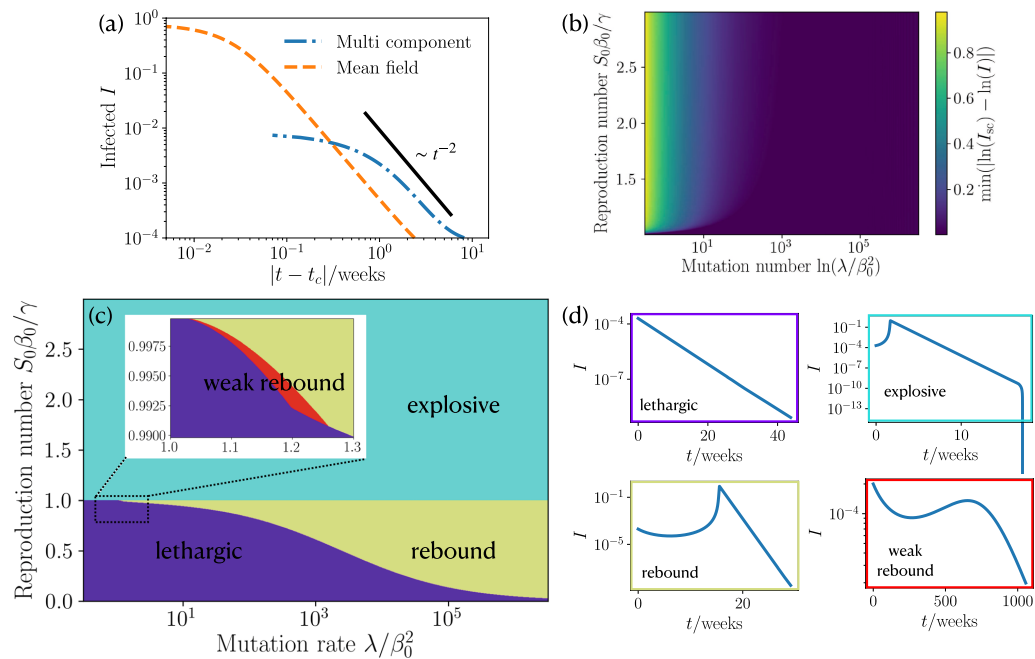


Figure 4. Scaling law of short time infection dynamics, Phase diagram and state classification of approach beyond constant mutation rate. (a) Infections as function of reduced time $|t - t_c|$ where t_c is the critical time at which the infections diverge (see SI for details). We show the scaling law, coarse grained MSIR and our multi component MSIR approach. ($R_0 = 2, \lambda/\beta_0^2 = 2 \times 10^4, I_0 = 10^{-4}$). (b) Deviation of the fraction of infections at short times from our coarse grained MSIR approach to the $a/|t - t_c|^2$ scaling by using $\min(\ln(I_{sc}) - \ln(I))$. Mutation rate and reproduction number are varied ($I_0 = 2 \times 10^{-4}$). (c) Phase diagram of our coarse grained MSIR approach showing the occurrence of four different courses of the pandemic for varying mutation rate and reproduction number ($I_0 = 2 \times 10^{-4}$). (d) Example plots of the infections as function of time for four different courses of the pandemic: lethargic, super exponential wave; rebound, and weak rebound.

wave qualitatively differs from the comparatively mild super-exponential behaviour which we have encountered for the case of a constant mutation rate in that it leads to a much more extreme self-acceleration of the infection numbers. As a result, the infection numbers peak only at extremely high values where a large fraction of the population is infected at the same time (see Figs. 1b and 4a). Clearly, such an explosive growth would be interrupted at some point as the population approaches herd immunity. To quantify to which extend the predicted explosive growth would occur before herd-immunity causes significant deviations, we consider the expression $\min(\ln(I_{sc}) - \ln(I))$, which quantifies how closely the fraction of infections approaches the underlying (idealized) power law dependence in the presence of saturation effects. We find that for large mutation rates the power-law dependence is strong for any reproduction number (Fig. 4b) and weakens for lower mutation rates. Remarkably, the explosive growth depends only weakly on the reproduction which is the parameter that is controllable due to interventions. After the initial super-exponential increase of infections the saturation effects from people recovering induce a maximum and a succeeding decrease in infection numbers.

Phase diagram. Depending on the basic reproduction number and the mutation rate the MSIR model predicts four distinct courses summarized in the phase diagram Fig. 4c, which has been obtained analytically (see SI). We find a lethargic regime characterized by an exponential decay (purple regime, Fig. 4d); an explosive regime (cyan regime); a rebound regime (dark yellow) where we have a minimum followed by a mutant induced super exponential increase; and weak rebound (red) leading to an infection maximum which is smaller than the initial fraction of infected individuals. Generally, the explosive (or super exponential) regime occurs for reproduction numbers $R_0 > 1$ and any positive mutation rate, whereas the other three regimes occur for $R_0 < 1$. For low mutation rate and $R_0 < 1$ the epidemic is in the desired lethargic regime, increasing the mutation rate leads to a small region of weak rebound which then transitions to a rebound dynamics.

Nonpharmaceutical interventions, vaccination, and immune escape. To explore the efficiency of measures which effectively reduce the reproduction number, we again change the reproduction number R_0 to a value of $R_{0,int}$ at time t_{int} . Now starting from the explosive (super exponential) regime ($R_0 = 1.2$) we decrease the reproduction

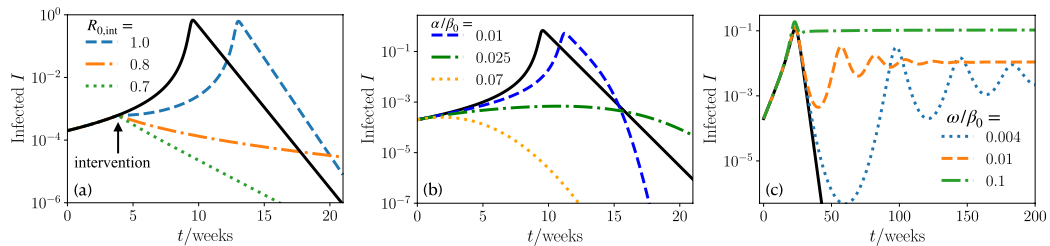


Figure 5. Nonpharmaceutical interventions, vaccinating, and immune escape. **(a)** Infections as function of time for a super exponential wave. Measures are taken by reducing the reproduction number to $R_{0,int}$ at time t_{int} (black line has no intervention. $R_0 = 1.2$, $\lambda/\beta_0^2 = 50$, $I_0 = 2 \times 10^{-4}$, $t_{int} = 3.85$ weeks). **(b)** Infections as function of time of different vaccination rates α (black line has no vaccination. $R_0 = 1.2$, $\lambda/\beta_0^2 = 50$, $I_0 = 2 \times 10^{-4}$). **(c)** Infections as function of time of different immune escape rates ω (black line has no immune escape. $R_0 = 1.2$, $\lambda/\beta_0^2 = 2$, $I_0 = 2 \times 10^{-4}$).

number during the rise of the wave (Fig. 5). Strong measures yielding $R_{0,int} = 0.7$ or $R_{0,int} = 0.8$ induce an immediate decay of the infection numbers as desired. However, weak measures, leading to $R_{0,int} = 1$ only delay the occurrence of the infection maximum but hardly change the value of I at the peak. Hence, it is clear that measures need to be strong enough to have a significant effect, while weak measures only delay the infection number explosion.

We finally ask how fast vaccination would have to progress in order to suppress a mutation-induced explosion of infection numbers or a mutation-induced rebound at initial reproduction numbers smaller than 1. Vaccinations effectively reduce the number of susceptibles by a vaccination rate α (see also Eq. 11). If we start in the explosive (super exponential) regime, a high vaccination rate is needed to interrupt the rapid growth of the infection numbers (Fig. 5b): while small vaccination rates ($\alpha/\beta_0 = 0.01$) merely shift the infection maximum to a later time, while having little change in the number of infections, larger vaccination rates ($\alpha/\beta_0 = 0.025$) effectively suppress the explosion of infection numbers. Therefore, to prevent possible mutation-induced long-time consequences it is imperative to maximize vaccine production worldwide. Enhancing vaccine production is particularly important in countries with a weak healthcare system, which face the threat of being overloaded by COVID-19 cases^{54–59}.

Newly mutated strains allow for an immune escape of the virus, effectively representing a transition of recovered individuals to susceptible ones with an immune escape rate ω (see also Eqs. (12)–(14)). This leads to a continued recovery of the number of susceptibles and drives the population away from herd immunity, which in turn can cause new infection waves (see Fig. 5c), that can also be predicted using a linear stability analysis (see SI). Further, we find that the number of infected saturates to a nonzero steady state (see also SI).

Discussion

Inspired by the ongoing COVID-19 disease and the continued emergence of new mutations supplanting preceding ones, in the present work we have developed a stochastic multistrain generalization of the popular SIR model. Combining this model with coarse graining concepts from statistical physics has allowed us to predict a panorama of possible scenarios for the mutation-controlled evolution of infectious diseases.

In particular, our approach suggests that mutations can induce a super-exponential growth of infection numbers in populations which are highly susceptible to the disease (e.g. because they are far from reaching herd immunity). As compared to the standard exponential growth, interrupting such an super-exponential growth is much more difficult and requires stronger and stronger measures as the disease evolves. In practice, such a super-exponential growth may occur e.g. if measures are applied too late, or if vaccines suddenly become ineffective against mutations.

One particularly severe form of such an super-exponential growth can occur if the mutation rate of a virus is proportional to the current number of infections. For this case our model predicts a giant infection wave, which is based on a positive feedback loop between the mutation-rate and the infection number causing a massive self-acceleration of the latter resulting in a state where the majority of the population gets infected at the same time. Clearly, such a situation would not only massively overstress any existing health system but once in action it would hardly be interruptable through vaccination.

At later stages of an infectious disease, where the population approaches herd immunity and the infection numbers decrease, an obvious political reaction would be to release measures. However, our simulations suggest that mutations can drive new infection waves even after a longer downwards trend. Such waves can even self-repeat and lead to a pattern of repeated phases of strongly decaying and increasing infection numbers provoking an endless sequence of renewed non-pharmaceutical interventions.

Since our work is on a conceptual basis we did not include explicit data to model COVID-19. However, the panorama of mutation induced phenomena which we have identified might inspire detailed modeling works to test them for specific infectious diseases such as COVID-19. Further, our results could be applied to diseases in the animal world such as the avian influenza⁶⁰. These results might also be useful for discussions regarding

the importance of a release of vaccine-patents to reduce the risk of mutation-induced infection revivals and to coordinate the release of measures following a downwards trend of infection numbers.

Methods

Basic reproduction number of COVID-19 mutants. The basic reproduction numbers were extracted from: original variant⁶¹, B.1.1.7 (α)¹¹, B.1.351 (β)⁶², P.1 (γ)¹³, B.1.617.2 (δ)⁶³, and B.1.1.529 (ρ)⁶⁴. The time point at which a variant has reached 5% in the sequenced genomes reported in* (<https://nextstrain.org/ncov/global>) is used as the emergence time.

Details on constant mutation rate. We assume that the new infection rates β_n are drawn from a Gaussian distribution, whose mean is the largest current infection rate. Explicitly we have

$$p(\beta_n) = \frac{1}{\sqrt{2\pi}\sigma} \text{Exp}\left(-\frac{(\beta_n - \beta_{\max,n-1})^2}{2\sigma^2}\right), \quad (17)$$

where $\beta_{\max,n-1}$ denotes the maximal infection rate of the current strains, β_n is the infection rate of the newly mutated strain, σ is the standard deviation of the distribution, and new strains are produced at a rate m (in our multi component simulations we use $\beta_0/\gamma = 1$, $\sigma = 2 \times 10^{-4}$, $m/\gamma = 2$, and the new strain obtains an initial $I_n(0) = 10^{-7}$).

To coarse grain this mutation model, we assume that the infections immediately assume the maximal infection rate of the newly mutated strain $\beta_{\max,n}$. It follows that the mean infection rate is dominated by $\beta_{\max,n}$, since all other infections grow exponentially slower. This reduces our multicomponent model to an effective one component model with the infection rate $\beta_{\max,n}$. To determine $\beta_{\max,n}$ we compute

$$\int_{\max_n \beta_n}^{\infty} p(\beta_n) d\beta_n = \frac{\gamma}{m}, \quad (18)$$

where m is the number of times drawn from the distribution Eq. (17). Explicitly, Eq. (18) yields

$$\beta_{\max,n} = \beta_{\max,n-1} - \sqrt{2}\sigma \text{erf}^{-1}\left(-1 + \frac{2\gamma}{m}\right), \quad (19)$$

where $\text{erf}^{-1}(\ast)$ is the inverse error function and can here be approximated by a negative constant $-C_1$. We now write the standard deviation as $\sigma = \mu^* \tau$, with a mutation rate μ^* and mutation timescale τ , giving

$$\frac{\beta_{\max,n} - \beta_{\max,n-1}}{\tau} = C_1 \sqrt{2} \mu^*, \quad (20)$$

which is a discretized version of $\dot{\beta} = \mu$, and equivalent to our coarse grained constant mutation rate model.

Details on model beyond constant mutation rate. For the model beyond constant mutation rate the infection rates perform a biased random walk. Given an infection rate β_n it will mutate with a probability p_0 and not mutate with probability $1 - p_0$. Furthermore, this strain has I_n infections, which are all able to mutate, giving a total mutation probability of $1 - (1 - p_0)^{I_n} = p_0 I_n + \mathcal{O}(p_0^2)$. A mutation gives a new strain I_n with an increased $\beta_n = \beta_{n-1} + \Delta\beta$ (in our multi component simulations we use $\beta_0 = 0.1$, $\gamma = 0.1$, $\Delta\beta = 0.03$, $p_0 = 2 \times 10^{-4}$, and the new strain obtains an initial $I_n(0) = 10^{-6}$).

To coarse grain, we assume that the expectation value of the infection rate $\langle \beta_n \rangle$ is proportional to the mutation probability. Then a new mutation has the expectation value $\langle \beta_{n+1} \rangle = p_0 I_n$ and the old strain has $\langle \beta_n \rangle = 1 - p_0 I_n$. Computing the difference gives

$$\langle \beta_{n+1} \rangle - \langle \beta_n \rangle = 2p_0 I_n - 1, \quad (21)$$

which is a discretization of $\dot{\beta} = \lambda I$, which is our coarse grained model beyond a constant mutation rate.

Received: 5 October 2021; Accepted: 20 May 2022

Published online: 10 June 2022

References

- Zhou, P. *et al.* A pneumonia outbreak associated with a new coronavirus of probable bat origin. *Nature* **579**, 270–273 (2020).
- Wu, F. *et al.* A new coronavirus associated with human respiratory disease in China. *Nature* **579**, 265–269 (2020).
- Dong, E., Du, H. & Gardner, L. An interactive web-based dashboard to track COVID-19 in real time. *Lancet Infect. Dis.* **20**, 533–534. [https://doi.org/10.1016/S1473-3099\(20\)30120-1](https://doi.org/10.1016/S1473-3099(20)30120-1) (2020).
- Hadfield, J. *et al.* Nextstrain: Real-time tracking of pathogen evolution. *Bioinformatics* **34**, 4121–4123 (2018).
- Rambaut, A. *et al.* A dynamic nomenclature proposal for SARS-CoV-2 lineages to assist genomic epidemiology. *Nat. Microbiol.* **5**, 1403–1407 (2020).
- Yao, H. *et al.* Patient-derived SARS-CoV-2 mutations impact viral replication dynamics and infectivity in vitro and with clinical implications in vivo. *Cell Discov.* **6**, 76 (2020).
- Korber, B. *et al.* Tracking changes in SARS-CoV-2 spike: Evidence that D614G increases infectivity of the COVID-19 virus. *Cell* **182**, 812–827 (2020).
- Grubaugh, N. D., Hanage, W. P. & Rasmussen, A. L. Making sense of mutation: What D614G means for the COVID-19 pandemic remains unclear. *Cell* **182**, 794–795 (2020).

9. Tegally, H. *et al.* Emergence and rapid spread of a new severe acute respiratory syndrome-related coronavirus 2 (SARS-CoV-2) lineage with multiple spike mutations in South Africa. *medRxiv* (2020).
10. Priesemann, V. *et al.* An action plan for pan-European defence against new SARS-CoV-2 variants. *Lancet* **397**, 469–470 (2021).
11. Volz, E. *et al.* Assessing transmissibility of SARS-CoV-2 lineage B. 1.1. 7 in England. *Nature* **593**, 266–269 (2021).
12. Davies, N. G. *et al.* Estimated transmissibility and impact of SARS-CoV-2 lineage B. 1.1. 7 in England. *Science* **372**, eabg3055 (2021).
13. Coutinho, R. M. *et al.* Model-based evaluation of transmissibility and reinfection for the p. 1 variant of the SARS-CoV-2. *medRxiv* (2021).
14. Grauer, J., Löwen, H. & Liebchen, B. Strategic spatiotemporal vaccine distribution increases the survival rate in an infectious disease like COVID-19. *Sci. Rep.* **10**, 21594 (2020).
15. Zhou, S., Zhou, S., Zheng, Z. & Lu, J. Optimizing spatial allocation of COVID-19 vaccine by agent-based spatiotemporal simulations. *GeoHealth* e2021GH000427.
16. Molla, J. *et al.* Adaptive and optimized COVID-19 vaccination strategies across geographical regions and age group. *arXiv preprint arXiv:2105.11562* (2021).
17. Kermack, W. O. & McKendrick, A. G. A contribution to the mathematical theory of epidemics. *Proc. R. Soc. Lond. A* **115**, 700–721 (1927).
18. Hethcote, H. W. The mathematics of infectious diseases. *SIAM Rev.* **42**, 599–653 (2000).
19. Andersson, H. & Britton, T. *Stochastic Epidemic Models and their Statistical Analysis* Vol. 151 (Springer Science & Business Media, 2012).
20. Grassly, N. C. & Fraser, C. Mathematical models of infectious disease transmission. *Nat. Rev. Microbiol.* **6**, 477–487 (2008).
21. Gog, J. R. & Grenfell, B. T. Dynamics and selection of many-strain pathogens. *Proc. Natl. Acad. Sci. USA* **99**, 17209–17214. <https://doi.org/10.1073/pnas.252512799> (2002).
22. Harko, T., Lobo, F. S. & Mak, M. Exact analytical solutions of the susceptible-infected-recovered (SIR) epidemic model and of the SIR model with equal death and birth rates. *Appl. Math. Comput.* **236**, 184–194 (2014).
23. Kröger, M. & Schlickeiser, R. Analytical solution of the SIR-model for the temporal evolution of epidemics. Part A: Time-independent reproduction factor. *J. Phys. A Math. Theor.* **53**, 505601 (2020).
24. Schlickeiser, R. & Kröger, M. Analytical solution of the sir-model for the temporal evolution of epidemics: Part b. Semi-time case. *J. Phys. A Math. Theor.* **54**, 175601 (2021).
25. Bittihn, P. & Golestanian, R. Stochastic effects on the dynamics of an epidemic due to population subdivision. *Chaos* **30**, 101102 (2020).
26. Das, S. K. A scaling investigation of pattern in the spread of COVID-19: Universality in real data and a predictive analytical description. *Proc. R. Soc. A* **477**, 20200689 (2021).
27. Yaari, R., Katriel, G., Huppert, A., Axelsen, J. & Stone, L. Modelling seasonal influenza: The role of weather and punctuated antigenic drift. *J. R. Soc. Interface* **10**, 20130298 (2013).
28. Zhao, Y., Huepe, C. & Romanczuk, P. Contagion dynamics in self-organized systems of self-propelled agents. *arXiv preprint arXiv:2103.12618* (2021).
29. Norambuena, A., Valencia, F. J. & Guzmán-Lastra, F. Understanding contagion dynamics through microscopic processes in active Brownian particles. *Sci. Rep.* **10**, 20845 (2020).
30. Day, T. & Gandon, S. Insights from price's equation into evolutionary epidemiology. *Dis. Evol. Models Concepts Data Anal.* **71**, 23–44 (2006).
31. Day, T. & Gandon, S. Applying population-genetic models in theoretical evolutionary epidemiology. *Ecol. Lett.* **10**, 876–888 (2007).
32. Day, T. & Proulx, S. R. A general theory for the evolutionary dynamics of virulence. *Am. Nat.* **163**, E40–E63 (2004).
33. Koelle, K., Ratmann, O., Rasmussen, D. A., Pasour, V. & Mattingly, J. A dimensionless number for understanding the evolutionary dynamics of antigenically variable RNA viruses. *Proc. R. Soc. B Biol. Sci.* **278**, 3723–3730 (2011).
34. Koelle, K., Khatri, P., Kamradt, M. & Kepler, T. B. A two-tiered model for simulating the ecological and evolutionary dynamics of rapidly evolving viruses, with an application to influenza. *J. R. Soc. Interface* **7**, 1257–1274 (2010).
35. He, D., Dushoff, J., Day, T., Ma, J. & Earn, D. J. Inferring the causes of the three waves of the 1918 influenza pandemic in England and Wales. *Proc. R. Soc. B Biol. Sci.* **280**, 20131345 (2013).
36. Boni, M. F., Gog, J. R., Andreasen, V. & Christiansen, F. B. Influenza drift and epidemic size: The race between generating and escaping immunity. *Theor. Popul. Biol.* **65**, 179–191 (2004).
37. Levin, S. & Pimentel, D. Selection of intermediate rates of increase in parasite-host systems. *Am. Nat.* **117**, 308–315 (1981).
38. Maier, B. F. & Brockmann, D. Effective containment explains subexponential growth in recent confirmed COVID-19 cases in China. *Science* **368**, 742–746 (2020).
39. Dehning, J. *et al.* Inferring change points in the spread of COVID-19 reveals the effectiveness of interventions. *Science* **369**, eabb9789 (2020).
40. Te Vrugt, M., Bickmann, J. & Wittkowski, R. Effects of social distancing and isolation on epidemic spreading modeled via dynamical density functional theory. *Nat. Commun.* **11**, 5576 (2020).
41. Duran-Olivencia, M. A. & Kalliadasis, S. More than a year after the onset of the COVID-19 pandemic in the UK: Lessons learned from a minimalistic model capturing essential features including social awareness and policy making. *medRxiv* (2021).
42. te Vrugt, M., Bickmann, J. & Wittkowski, R. Containing a pandemic: Nonpharmaceutical interventions and the “second wave”. *J. Phys. Commun.* **5**, 055008 (2021).
43. Lasser, J. *et al.* Assessing the impact of sars-cov-2 prevention measures in schools by means of agent-based simulations calibrated to cluster tracing data. *medRxiv* (2021).
44. Desvars-Larrive, A. *et al.* A structured open dataset of government interventions in response to COVID-19. *Sci. Data* **7**, 285 (2020).
45. Bittihn, P., Hupe, L., Isensee, J. & Golestanian, R. Local measures enable COVID-19 containment with fewer restrictions due to cooperative effects. *EclinicalMedicine* **32**, 100718 (2021).
46. Zhang, X. *et al.* Epidemic spreading under pathogen evolution. *arXiv preprint arXiv:2102.11066* (2021).
47. Contreras, S. *et al.* The challenges of containing SARS-CoV-2 via test-trace-and-isolate. *Nat. Commun.* **12**, 1–13 (2021).
48. Estrada, E. COVID-19 and SARS-CoV-2. Modeling the present, looking at the future. *Phys. Rep.* **869**, 1–51 (2020).
49. Yang, C. & Wang, J. A mathematical model for the novel coronavirus epidemic in Wuhan, China. *Math. Biosci. Eng.* **17**, 2708 (2020).
50. Gonzalez-Parra, G., Martínez-Rodríguez, D. & Villanueva-Micó, R. J. Impact of a new SARS-CoV-2 variant on the population: A mathematical modeling approach. *Math. Comput. Appl.* **26**, 25 (2021).
51. Fudolig, M. & Howard, R. The local stability of a modified multi-strain sir model for emerging viral strains. *PLoS ONE* **15**, e0243408 (2020).
52. Tian, L. *et al.* Harnessing peak transmission around symptom onset for non-pharmaceutical intervention and containment of the COVID-19 pandemic. *Nat. Commun.* **12**, 1–12 (2021).
53. Meidan, D. *et al.* Alternating quarantine for sustainable epidemic mitigation. *Nat. Commun.* **12**, 1–12 (2021).
54. Hasan, M. M. *et al.* Emergence of highly infectious SARS-CoV-2 variants in Bangladesh: The need for systematic genetic surveillance as a public health strategy. *Trop. Med. Health* **49**, 1–3 (2021).
55. Essar, M. Y. *et al.* COVID-19 and multiple crises in Afghanistan: An urgent battle. *Conflict Health* **15**, 1–3 (2021).
56. Islam, Z. *et al.* Food security, conflict, and COVID-19: Perspective from Afghanistan. *Am. J. Trop. Med. Hyg.* **106**, 21 (2022).

57. Aborode, A. T. *et al.* Impact of poor disease surveillance system on COVID-19 response in Africa: Time to rethink and rebuild. *Clin. Epidemiol. Glob. Health* **12**, 100841 (2021).
58. Aborode, A. T. *et al.* Dengue and coronavirus disease (COVID-19) syndemic: Double threat to an overburdened healthcare system in Africa. *Int. J. Health Plan. Manag.* (2021).
59. Rackimuthu, S., Hasan, M. M., Bardhan, M. & Essar, M. Y. COVID-19 vaccination strategies and policies in India: The need for further re-evaluation is a pressing priority. *Int. J. Health Plan. Manag.* (2021).
60. O'Regan, S. M. *et al.* Chaos in a seasonally perturbed SIR model: Avian influenza in a seabird colony as a paradigm. *J. Math. Biol.* **67**, 293–327 (2013).
61. Liu, Y., Gayle, A. A., Wilder-Smith, A. & Rocklöv, J. The reproductive number of COVID-19 is higher compared to SARS coronavirus. *J. Travel Med.* <https://doi.org/10.1093/jtm/taaa021> (2020).
62. Assessment, R. R. Risk related to the spread of new SARS-CoV-2 variants of concern in the EU/EEA—first update. *European Centre for Disease Prevention and Control An agency of the European Union* (2021).
63. Campbell, F. *et al.* Increased transmissibility and global spread of SARS-CoV-2 variants of concern as at June 2021. *Eurosurveillance* **26**, 2100509 (2021).
64. Nishiura, H. *et al.* Relative reproduction number of SARS-CoV-2 omicron (b. 1.1. 529) compared with delta variant in South Africa (2021).

Author contributions

H.L. and B.L. designed the research. J.G. and F.J.S. performed the simulations. F.J.S. did the analytical calculations and the simulation data analysis. All authors discussed and wrote the manuscript.

Funding

Open Access funding enabled and organized by Projekt DEAL.

Competing interests

The authors declare no competing interests.

Additional information

Supplementary Information The online version contains supplementary material available at <https://doi.org/10.1038/s41598-022-13137-w>.

Correspondence and requests for materials should be addressed to F.J.S.

Reprints and permissions information is available at www.nature.com/reprints.

Publisher's note Springer Nature remains neutral with regard to jurisdictional claims in published maps and institutional affiliations.



Open Access This article is licensed under a Creative Commons Attribution 4.0 International License, which permits use, sharing, adaptation, distribution and reproduction in any medium or format, as long as you give appropriate credit to the original author(s) and the source, provide a link to the Creative Commons licence, and indicate if changes were made. The images or other third party material in this article are included in the article's Creative Commons licence, unless indicated otherwise in a credit line to the material. If material is not included in the article's Creative Commons licence and your intended use is not permitted by statutory regulation or exceeds the permitted use, you will need to obtain permission directly from the copyright holder. To view a copy of this licence, visit <http://creativecommons.org/licenses/by/4.0/>.

© The Author(s) 2022

Supplementary information: Mutation induced infection waves in diseases like COVID-19

Fabian Jan Schwarzendahl,¹ Jens Grauer,¹ Benno Liebchen,² and Hartmut Löwen¹

¹*Institut für Theoretische Physik II: Weiche Materie,
Heinrich-Heine-Universität Düsseldorf, 40225 Düsseldorf, Germany*

²*Institute of Condensed Matter Physics, Technische Universität Darmstadt, Darmstadt, Germany*
(Dated: May 9, 2022)

I. MAXIMUM OF WAVES IN THE CONSTANT MUTATION RATE MODEL

To obtain some analytical an understanding of the scaling of the maxima in the constant mutation model, we start by considering the equations of susceptible and infections which read

$$\dot{S} = -(\beta_0 + \mu t)SI, \quad (\text{S1})$$

$$\dot{I} = (\beta_0 + \mu t)SI - \gamma I, \quad (\text{S2})$$

where the recovered R follow from $S + I + R = 1$. Redefining the time variable $t' = (\beta_0 + \mu t)$ yields

$$\mu \dot{S} = -t' SI, \quad (\text{S3})$$

$$\mu \dot{I} = t' SI - \gamma I, \quad (\text{S4})$$

$$(\text{S5})$$

where the dot now denotes derivatives with respect to t' . Maxima can be found using $\dot{I} = 0$, which is explicitly

$$S^* t'^* = \gamma \quad (\text{S6})$$

where S^* are the susceptible at the maximum and t'^* is the time at which the maximum appears. Taking a derivate of S^* with respect to t'^* gives

$$\dot{S}^* = -\frac{\gamma}{(t'^*)^2}, \quad (\text{S7})$$

which is only valid between maxima. Since the susceptible decay monotonically in time, we assume that the S^* also decays monotonically with

$$\dot{S}^* \sim -S^* t'^* I^*, \quad (\text{S8})$$

where I^* are the infected at the maximum. Using Eq. (S7) and Eq (S8) then yields the scaling

$$I^* \sim \frac{\mu}{(\beta + \mu t'^*)^2}. \quad (\text{S9})$$

II. MATHEMATICAL ANALYSIS OF PHASE DIAGRAM IN BEYOND CONSTANT MUTATION RATE APPROACH

The dynamical equations of our model which goes beyond a constant mutation rate are given by

$$\dot{S} = -\beta SI, \quad (\text{S10})$$

$$\dot{I} = \beta SI - \gamma I, \quad (\text{S11})$$

$$\dot{\beta} = \lambda I, \quad (\text{S12})$$

$$(\text{S13})$$

where R follows from $S + I + R = 1$. Dividing Eq. (S10)-(S11) by Eq. (S12) gives

$$\frac{dS}{d\beta} = -\frac{\beta S}{\lambda}, \quad (\text{S14})$$

$$\frac{dI}{d\beta} = \frac{\beta S}{\lambda} - \frac{\gamma}{\lambda}, \quad (\text{S15})$$

where β reparameterises time. Equation (S14) is solved by

$$S = S_0 e^{\frac{\beta_0^2 - \beta^2}{2\lambda}}, \quad (\text{S16})$$

with initial susceptible S_0 and initial infection rate β_0 . Equation (S15) can be rewritten as

$$dI = \frac{\beta S}{\lambda} d\beta - \frac{\gamma}{\lambda} d\beta \quad (\text{S17})$$

$$= -dS - \frac{\gamma}{\lambda} d\beta, \quad (\text{S18})$$

where we used Eq. (S14). Integrating then yields

$$I - I_0 = S_0 - S - \frac{\gamma}{\lambda} (\beta - \beta_0) \quad (\text{S19})$$

To obtain the phase diagram shown in the main text, we need to look for the extrema of the infections. Extrema of I are given by the condition $\dot{I} = 0$ which explicitly read

$$S^* \beta^* - \gamma = 0, \quad (\text{S20})$$

where S^* are the susceptible at the extremum and β^* is the infection rate at the extremum. Using Eq. (S16) gives

$$\frac{\gamma}{\beta^*} = S_0 e^{\frac{\beta_0^2 - (\beta^*)^2}{2\lambda}}, \quad (\text{S21})$$

which is solved by

$$\beta^* = -i\sqrt{\lambda} \left(W \left(-\frac{\gamma^2}{\lambda S_0^2} e^{-\frac{\beta_0^2}{\lambda}} \right) \right)^{1/2} \quad (\text{S22})$$

where $W(*)$ is the Lambert function. The argument in the Lambert function of Eq (S22) is smaller than zero. This gives rise to two solutions, implying two extrema of the infections. Explicitly the extrema I^* can be found by using

$$I^* = I_0 + S_0 - \frac{\gamma}{\beta^*} - \frac{\gamma}{\lambda} (\beta^* - \beta_0), \quad (\text{S23})$$

together with Eq (S22). Furthermore, to determine maxima and minima we can use

$$\ddot{I}|_{S^* \beta^* = \gamma} = (I^*)^2 S^* (\lambda - (\beta^*)^2) \quad (\text{S24})$$

such that the sign of $(\lambda - (\beta^*)^2)$ decides between minimum and maximum.

III. CRITICAL SHORT TIME BEHAVIOR IN BEYOND CONSTANT MUTATION RATE APPROACH

At small times we can approximate the number of susceptible people by $S \approx 1$, which gives the set of equations

$$\dot{I} = \beta[I]I - \gamma I, \quad (\text{S25})$$

$$\dot{\beta} = \lambda I, \quad (\text{S26})$$

with the initial condition $\beta(0) = \beta_0$. By changing the initial condition of Eq.(S26) to $\beta(0) = \beta_0 - \gamma$ we can rewrite Eq.(S25) as

$$\frac{d \ln I}{dt} = S_0 \beta[I]. \quad (\text{S27})$$

We now use the transformation $\omega = \ln I$, giving

$$\frac{d\omega}{dt} = S_0\beta [e^\omega] \quad (\text{S28})$$

$$\dot{\beta} = \lambda e^\omega. \quad (\text{S29})$$

Taking a derivative of Eq.(S28), gives

$$\frac{d^2\omega}{dt^2} = S_0\dot{\beta} = S_0\lambda e^\omega, \quad (\text{S30})$$

which has initial conditions $\omega(0) = \ln(I(0))$ and $\dot{\omega}(0) = \beta - \gamma$ and can be solved explicitly. Putting back the transformation, we arrived at the following expression for the number of infected people

$$I(t) = -\frac{\delta_1}{\lambda [1 + \cosh(2 \ln \delta_2 + t\sqrt{\delta_1})]}, \quad (\text{S31})$$

with $\delta_1 = -2I_0\lambda + (\gamma - S_0\beta_0)^2$ and $\delta_2 = -\frac{\sqrt{\gamma - S_0\beta_0 + \sqrt{\delta_1}}}{\sqrt{-\gamma + S_0\beta_0 + \sqrt{\delta_1}}}$. Equation (S31) has poles at

$$t_c = \frac{-2 \log(\delta_2) + i\pi(2k-1)}{\sqrt{\delta_1}}, \quad (\text{S32})$$

where k is an integer and the physically relevant critical time t_c is given by k yielding the smallest positive t_c . Expanding Eq. (S31) around the critical time t_c gives

$$I(t) = \frac{2}{\lambda} \frac{1}{(t - t_c)^2}. \quad (\text{S33})$$

IV. INDEPENDENT PARAMETERS OF COARSE GRAINED MSIR MODEL

The equations of our constant mutation rate coarse grained model are

$$\dot{S} = -\beta SI, \quad (\text{S34})$$

$$\dot{I} = \beta SI - \gamma I, \quad (\text{S35})$$

$$\dot{\beta} = \mu. \quad (\text{S36})$$

From the condition $S + I + R = 1$ it then follows that $R(t=0) = 1 - I_0 - S_0$, such that we have three parameters I_0 , S_0 and β_0 for the initial condition. Additionally, we have the parameters μ and γ , making our parameter space five dimensional.

We continue considering the units of each parameter and variable which are $[S] = 1$, $[I] = 1$, $[\beta] = 1/\text{time}$, $[\beta_0] = 1/\text{time}$, $[\gamma] = 1/\text{time}$ and $[\mu] = 1/\text{time}^2$. By nondimensionalizing Eq.(S34)-(S36) we find

$$\dot{S} = -\beta S \mathcal{I}, \quad (\text{S37})$$

$$\dot{\mathcal{I}} = \beta S \mathcal{I} - \mathcal{I}, \quad (\text{S38})$$

$$\dot{\beta} = \mu/\beta_0^2. \quad (\text{S39})$$

with $S = S\beta_0/\gamma$, and $\mathcal{I} = I\beta_0/\gamma$. The parameter space then reduces to three dimensions where the nondimensional parameters are the initial infected I_0 , the basic reproduction number $S_0\beta_0/\gamma$ and the mutation rate μ/β_0^2 . The calculation for our model that goes beyond a constant mutation rate is analogous, with the resulting nondimensional mutation rate λ/β_0^2 .

V. ESCAPE OF IMMUNITY

A. Steady state

In the steady state the equations including immune escape read

$$0 = -\beta(t, I)SI + \omega R, \quad (\text{S40})$$

$$0 = \beta(t, I)SI - \gamma I, \quad (\text{S41})$$

$$0 = \gamma I - \omega R. \quad (\text{S42})$$

Solving Eqs.(S40)-(S42) together with $S + I + R = 1$, yields

$$S = \frac{\gamma}{\beta}, \quad (\text{S43})$$

$$I = \frac{1 - \frac{\gamma}{\beta}}{1 + \frac{\gamma}{\omega}}, \quad (\text{S44})$$

$$R = \frac{\gamma}{\omega} \frac{1 - \frac{\gamma}{\beta}}{1 + \frac{\gamma}{\omega}}. \quad (\text{S45})$$

$$(\text{S46})$$

In the long time limit β becomes very large for both mutation models, such that γ/β is effectively zero and we find

$$S_\infty = 0, \quad (\text{S47})$$

$$I_\infty = \frac{1}{1 + \frac{\gamma}{\omega}}, \quad (\text{S48})$$

$$R_\infty = \frac{1}{1 + \frac{\omega}{\gamma}}, \quad (\text{S49})$$

$$(\text{S50})$$

which shows a nonzero steady state solution for the infected.

B. Infection waves from linear stability

We start by considering our coarse grained beyond constant mutation rate model with immune escape, which reads

$$\dot{S} = -\beta SI + \omega R, \quad (\text{S51})$$

$$\dot{I} = \beta SI - \gamma I, \quad (\text{S52})$$

$$\dot{R} = \gamma I - \omega R, \quad (\text{S53})$$

$$\dot{\beta} = \lambda I. \quad (\text{S54})$$

We now linearize the system of equations (S51)-(S54) around the state $S = S_0 + \delta S$, $I = I_0 + \delta I$, $R = R_0 + \delta R$ and $\beta = \beta_0 + \delta\beta$, where we neglect term of δ^2 . This results in the following system of equations

$$\frac{d}{dt} \begin{pmatrix} \delta S \\ \delta I \\ \delta R \\ \delta\beta \end{pmatrix} = \underbrace{\begin{pmatrix} -\beta_0 I_0 & -\beta_0 S_0 & \omega & -S_0 I_0 \\ \beta_0 I_0 & \beta_0 S_0 & 0 & S_0 I_0 \\ 0 & \gamma & \omega & 0 \\ \lambda & 0 & 0 & 0 \end{pmatrix}}_{=\mathcal{M}} \begin{pmatrix} \delta S \\ \delta I \\ \delta R \\ \delta\beta \end{pmatrix}, \quad (\text{S55})$$

where we defined the stability matrix \mathcal{M} . In Fig. S1 we show the imaginary part of the four eigenvalues of \mathcal{M} as a function of the rate of immunity escape ω , which are nonzero. Therefore, we expect the system to show oscillations, which are the infection waves shown in Fig. 5(c) (main text). Note that the oscillations are induced by the escape of immunity and are also present with a constant β or a constant mutation rate.

VI. VACCINATION WITH NON-CONSTANT ROLLOUT

Vaccinations are typically not distributed in the public with a constant rate, as assumed in our main text. The vaccination rate is for example influenced by the rate of production and the willingness of the public to get vaccinated. To see what effect a non constant rollout has, we assume the following dynamic infection rate

$$\alpha_{eff} = \frac{\alpha_0}{\sqrt{2\pi}} e^{-(t-t_{max})^2/(2w^2)}, \quad (\text{S56})$$

where we chose the time of maximal vaccination $t_{max} = 5$ weeks, the width of the distribution to be $w = 2$ weeks and α_0 is the bare vaccination rate.

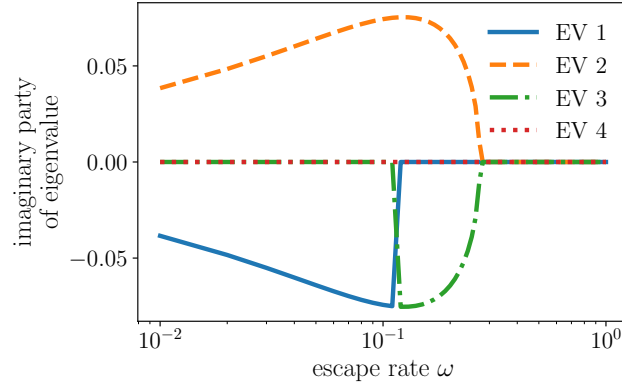


FIG. S1. Imaginary part of the four eigenvalues obtained the stability matrix \mathcal{M} . (here $R_0 = 1.2$, $\mu/\beta_0^2 = 2$, $I_0 = 2 \times 10^{-4}$)

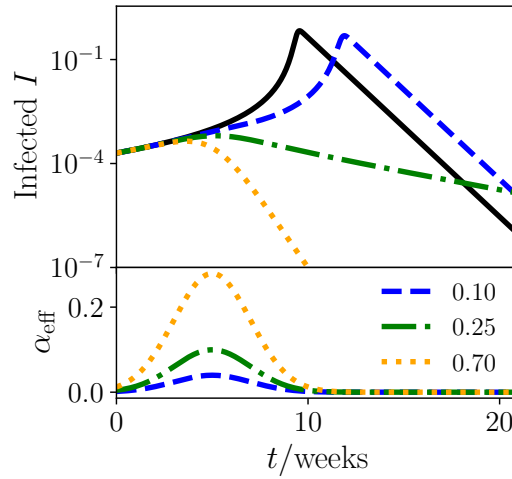


FIG. S2. (Top) Infections as function of time of different α_0 . (Black line has no vaccination. $R_0 = 1.2$, $\lambda/\beta_0^2 = 50$, $I_0 = 2 \times 10^{-4}$). (Bottom) Effective infection rate as function of time for different α_0 .

In Fig. S2(Top) we show the infected as a function of time with the vaccination rollout specified in Eq.(S56) (see Fig. S2(Bottom)) for our beyond constant mutation rate model. The resulting infected show a behavior that is very similar to the constant vaccination rate model shown in our main text Fig. 5(b). Hence we conclude that the vaccination rollout Eq. (S56) does not induce qualitative changes.

VII. DYNAMICS OF THE INFECTION RATE

A. Constant mutation rate

In our multi component model we constantly draw a new infection rates β_n , which evolve according to the distribution Eq. 7 (main text). In Fig. S3 we show the evolution of the infection rate with time, which shows a linear increase

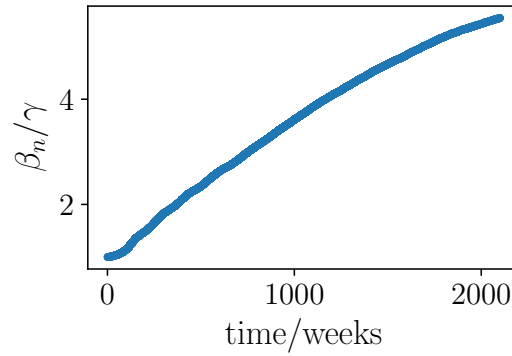


FIG. S3. Infection rates β_n as function of time for our multi component constant mutation rate model.

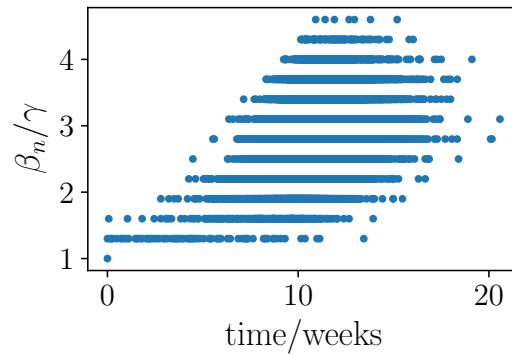


FIG. S4. Infection rates β_n as function of time for our multi component model beyond a constant mutation rate.

of the mean infection rate. This behavior is consistent with the linear increase of our coarse grained infection rate.

B. Beyond constant mutation rate

For our multi component model that goes beyond a constant mutation rate, the infection rates β_n evolve according to a biased random walk (see also Methods). Figure S4 shows the infections rate β_n as a function of time. We find a very broad distribution, whose mean increases with time.

We also study the coarse grained infection rate $\beta(t) = \int_0^t \lambda I(t') dt'$ of our beyond constant mutation rate model. In Fig. S5 we show the infection rate together with the infected for the four different phases that we find in the pandemic. A lethargic (Fig. S5(a)) behavior shows an almost constant mutation rate. The explosive (Fig. S5(b)) and rebound (Fig. S5(c)) phases show a strong sudden increase of the infection rate that coincides with the strong increase in infections. Finally the weak rebound (Fig. S5(d)) has a small constant increase of the infection rate.

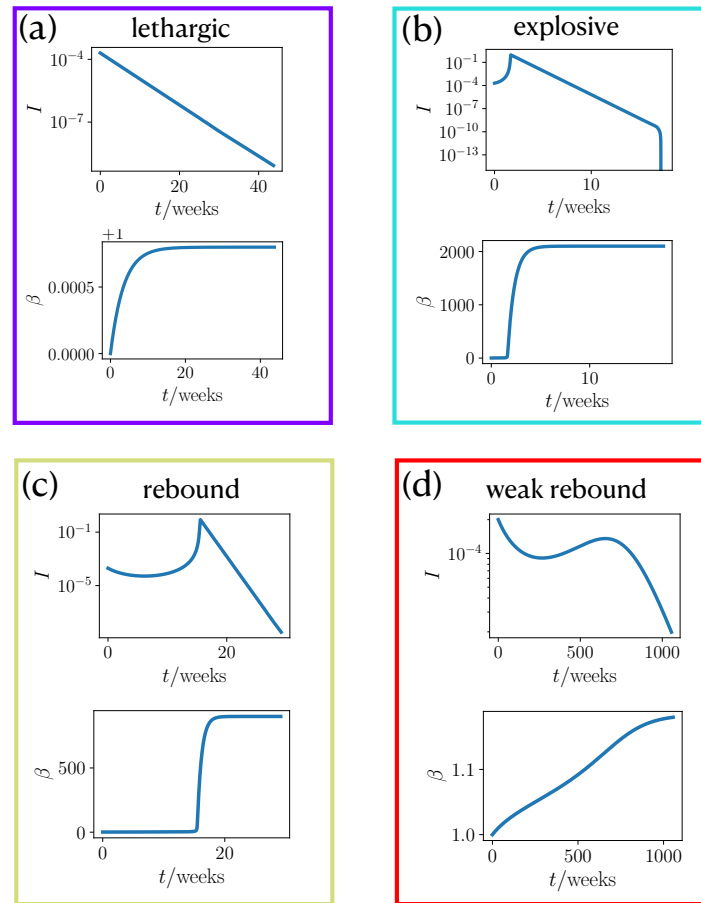


FIG. S5. Coarse grained infection rate (bottom) and infected (top) as a function time for the four different phases: (a)lethargic, (b) explosive, (c) rebound and (d) weak rebound.

9 Summary

In this thesis I have used agent-based models to study collective effects in various systems of active matter. First, inspired by the diversity of multi-species chemotaxis among microorganisms, a generic model in which each species produces its own chemical concentration field was studied in **Paper I**. This species selective production leads to interesting collective behavior as it is not known from the one-species limit. Using a particle-based description and a continuous model, the different phases were analyzed, which include a “hunting-swarm” phase and several complex cluster phases. In principle, it should be possible to realize and observe such a behavior with artificial particle mixtures, if they interact through a combination of non-reciprocal attractive and repulsive forces, e.g., via thermophoresis or diffusiophoresis.

Subsequently, the autophoretic behavior of spheroidal photocatalytic microswimmers was investigated in **Paper II**. Bismuth vanadat (BiVO_4) can be used to overcome the conventional asymmetrization step in order to provide colloidal particles with self-propulsion. With the help of a simulation model and analytical calculations, the velocities and particle trajectories of the formed assemblies can be understood. In the future, it would be interesting to extend the simulations to high particle densities in order to study the collective behavior on larger scales. Similarly, the simple fabrication method may allow the microswimmers to be coated with additional functional materials, giving them further capabilities beyond the self-propulsion mechanism.

In **Paper III**, a two-way coupling between light-activated colloidal particles and a near-critical environment was studied. The mutual feedback results in novel structures comprising a colloidal engine enclosed by a liquid droplet. We name them “active droploids”, a portmanteau of droplet and colloids. Size and motility of these active structures can be controlled by light intensity. This two-way coupling between droplets and colloids could provide valuable insights into the role of feedback in future active matter research.

In a further work described in Chapter 4, an easy to apply method was studied to anneal interfacial colloidal crystals. Using a conventional loudspeaker, standing waves are generated that provide more surface area for the colloidal particles and enable accelerated grain growth. Simulations can be used to track the particle motions and unveil the annealing process. Due to the simple but efficient method, this work could be interesting not only for the study of crystallization phenomena but also for the field of surface pattern production.

In **Paper IV**, active agents were equipped with artificial intelligence. We intentionally kept the information flow simple and only allowed the particles to know the local concentration at which they are located. Using a deep Q -learning algorithm, the particles learn to consume a nutrient field as efficiently as possible. Depending on agent density, consumption rate but also local concentration of the nutrient field, the agents apply different strategies in which they either unite and move towards each other or stay separated. This link between active particles and machine learning could open up new possibilities in this rapidly developing field of research. Furthermore, these results could be used for microrobots in finding efficient strategies to decontaminate polluted water.

In the last two papers, methods from statistical mechanics were used to mathematically model infectious diseases. In **Paper V**, we encouraged the idea of an optimal vaccine distribution strategy during a pandemic which is based not only on individual factors (who should be vaccinated first), but also on a distribution dependent on time and space (where and when should be vaccinated first). Sequentially prioritizing the locations with the highest bilinear incidence rate significantly reduces the number of deaths compared to the common practice of distributing vaccines demographically. As a further step, it would be useful to validate these results in more detailed models and examine impeding factors, such as inaccurate knowledge of current infection numbers or delays in communicating test results.

By generalizing the classical SIR model, the influence of the repeated occurrence of new strains in a pandemic was investigated in **Paper VI**. The developed multistrain SIR model allows the evaluation of different scenarios in which the contagion dynamics is controlled by mutations. A notable finding was the mutation-driven occurrence of super-exponential growth in infection numbers, different from the usual exponential growth in the classical SIR model. This is particularly severe when assuming that the mutation rate is proportional to infection numbers. Also, the simulations predicted that mutations can lead to recurrent waves of infection even when infection numbers have long been on a downward trend. These findings should be tested in more detailed models, possibly including data specific to Covid-19.

References

- [1] de Gennes, P.-G. Soft matter. *Science* **256**, 495–497 (1992).
- [2] Chaikin, P. M. & Lubensky, T. C. *Principles of Condensed Matter Physics* (Cambridge University Press, 1995).
- [3] Kleman, M. & Lavrentovich, O. D. *Soft matter physics: an introduction* (Springer, 2003).
- [4] Barrat, J.-L. & Hansen, J.-P. *Basic Concepts for Simple and Complex Liquids* (Cambridge University Press, 2003).
- [5] Doi, M., Edwards, S. F. & Edwards, S. F. *The theory of polymer dynamics*, vol. 73 (Oxford University Press, 1988).
- [6] de Gennes, P.-G. & Prost, J. *The physics of liquid crystals*. 83 (Oxford University Press, 1993).
- [7] Janssen, L. M. C. Mode-coupling theory of the glass transition: A primer. *Front. Phys.* **6**, 97 (2018).
- [8] Janssen, L. M. C. Active glasses. *J. Phys.: Condens. Matter* **31**, 503002 (2019).
- [9] Berg, H. C. *E. coli in Motion* (Springer, 2004).
- [10] Nakamura, S. & Minamino, T. Flagella-driven motility of bacteria. *Biomolecules* **9** (2019).
- [11] Löwen, H. Colloidal soft matter under external control. *J. Phys.: Condens. Matter* **13**, R415–R432 (2001).
- [12] Dzubiella, J., Hoffmann, G. P. & Löwen, H. Lane formation in colloidal mixtures driven by an external field. *Phys. Rev. E* **65**, 021402 (2002).
- [13] Royall, C. P., Dzubiella, J., Schmidt, M. & van Blaaderen, A. Nonequilibrium sedimentation of colloids on the particle scale. *Phys. Rev. Lett.* **98**, 188304 (2007).
- [14] Moncho-Jordá, A. & Dzubiella, J. Controlling the microstructure and phase behavior of confined soft colloids by active interaction switching. *Phys. Rev. Lett.* **125**, 078001 (2020).
- [15] Jäger, S. & Klapp, S. H. L. Pattern formation of dipolar colloids in rotating fields: layering and synchronization. *Soft Matter* **7**, 6606–6616 (2011).

- [16] Hansen, J.-P. & McDonald, I. R. *Theory of simple liquids: with applications to soft matter* (Academic Press, 2013).
- [17] Klapp, S. H. Collective dynamics of dipolar and multipolar colloids: From passive to active systems. *Curr. Opin. Colloid Interface Sci.* **21**, 76–85 (2016).
- [18] Brown, R. XXVII. A brief account of microscopical observations made in the months of june, july and august 1827, on the particles contained in the pollen of plants; and on the general existence of active molecules in organic and inorganic bodies. *Philos. Mag.* **4**, 161–173 (1828).
- [19] Einstein, A. Über die von der molekularkinetischen Theorie der Wärme geforderte Bewegung von in ruhenden Flüssigkeiten suspendierten Teilchen. *Ann. Phys.* **322**, 549–560 (1905).
- [20] von Smoluchowski, M. Zur kinetischen Theorie der Brownschen Molekularbewegung und der Suspensionen. *Ann. Phys.* **326**, 756–780 (1906).
- [21] Be’er, A. & Ariel, G. A statistical physics view of swarming bacteria. *Mov. Ecol.* **7**, 9–9 (2019).
- [22] A “tornado” of schooling barracudas (large, predatory fishes). Photo taken by Robin Hughes. CC BY-SA 2.0. <https://www.flickr.com/photos/robinhughes/> (2007).
- [23] Pedestrian scramble at Shibuya Crossing in Tokyo. Photo taken by Sei F. CC BY-SA 2.0. <https://www.flickr.com/people/125983633@N03> (2020).
- [24] Aubret, A., Martinet, Q. & Palacci, J. Metamachines of pluripotent colloids. *Nat. Commun.* **12**, 6398 (2021).
- [25] Berg, H. C. The rotary motor of bacterial flagella. *Annu. Rev. Biochem.* **72**, 19–54 (2003).
- [26] Ramaswamy, S. The mechanics and statistics of active matter. *Annu. Rev. Condens. Matter Phys.* **1**, 323–345 (2010).
- [27] Bechinger, C. *et al.* Active particles in complex and crowded environments. *Rev. Mod. Phys.* **88**, 045006 (2016).
- [28] Vicsek, T., Czirók, A., Ben-Jacob, E., Cohen, I. & Shochet, O. Novel type of phase transition in a system of self-driven particles. *Phys. Rev. Lett.* **75**, 1226–1229 (1995).
- [29] Katz, Y., Tunstrøm, K., Ioannou, C. C., Huepe, C. & Couzin, I. D. Inferring the structure and dynamics of interactions in schooling fish. *Proc. Natl. Acad. Sci. U.S.A.* **108**, 18720–18725 (2011).
- [30] Bialek, W. *et al.* Statistical mechanics for natural flocks of birds. *Proc. Natl. Acad. Sci. U.S.A.* **109**, 4786–4791 (2012).

- [31] Buhl, J. *et al.* From disorder to order in marching locusts. *Science* **312**, 1402–1406 (2006).
- [32] Riedel, I. H., Kruse, K. & Howard, J. A self-organized vortex array of hydrodynamically entrained sperm cells. *Science* **309**, 300–303 (2005).
- [33] Helbing, D., Farkas, I. & Vicsek, T. Simulating dynamical features of escape panic. *Nature* **407**, 487–490 (2000).
- [34] Silverberg, J. L., Bierbaum, M., Sethna, J. P. & Cohen, I. Collective motion of humans in mosh and circle pits at heavy metal concerts. *Phys. Rev. Lett.* **110**, 228701 (2013).
- [35] Adler, J. Chemotaxis in bacteria. *Science* **153**, 708–716 (1966).
- [36] Eisenbach, M. *Chemotaxis* (Imperial College Press: London, U.K., 2004).
- [37] Wadhams, G. H. & Armitage, J. P. Making sense of it all: bacterial chemotaxis. *Nat. Rev. Mol. Cell Biol.* **5**, 1024–1037 (2004).
- [38] Adler, J. Chemoreceptors in bacteria. *Science* **166**, 1588–1597 (1969).
- [39] Macnab, R. M. & Koshland, D. E. The gradient-sensing mechanism in bacterial chemotaxis. *Proc. Natl. Acad. Sci. U.S.A.* **69**, 2509–2512 (1972).
- [40] Mori, I. & Ohshima, Y. Neural regulation of thermotaxis in *Caenorhabditis elegans*. *Nature* **376**, 344–348 (1995).
- [41] Bahat, A. *et al.* Thermotaxis of mammalian sperm cells: A potential navigation mechanism in the female genital tract. *Nat. Med.* **9**, 149–150 (2003).
- [42] Witman, G. B. *Chlamydomonas* phototaxis. *Trends Cell Biol.* **3**, 403–408 (1993).
- [43] Jékely, G. Evolution of phototaxis. *Philos. Trans. R. Soc. Lond., B, Biol. Sci.* **364**, 2795–2808 (2009).
- [44] Lozano, C., ten Hagen, B., Löwen, H. & Bechinger, C. Phototaxis of synthetic microswimmers in optical landscapes. *Nat. Commun.* **7**, 12828 (2016).
- [45] ten Hagen, B. *et al.* Gravitaxis of asymmetric self-propelled colloidal particles. *Nat. Commun.* **5**, 4829 (2014).
- [46] Campbell, A. I., Wittkowski, R., ten Hagen, B., Löwen, H. & Ebbens, S. J. Helical paths, gravitaxis, and separation phenomena for mass-anisotropic self-propelling colloids: Experiment versus theory. *J. Chem. Phys.* **147**, 084905 (2017).
- [47] Liebchen, B., Monderkamp, P., ten Hagen, B. & Löwen, H. Viscotaxis: Microswimmer navigation in viscosity gradients. *Phys. Rev. Lett.* **120**, 208002 (2018).

-
- [48] Zampetaki, A. V., Liebchen, B., Ivlev, A. V. & Löwen, H. Collective self-optimization of communicating active particles. *Proc. Natl. Acad. Sci. U.S.A.* **118**, e2111142118 (2021).
- [49] Eidi, Z., Mohammad-Rafiee, F., Khorrami, M. & Gholami, A. Modelling of dictyostelium discoideum movement in a linear gradient of chemoattractant. *Soft Matter* **13**, 8209–8222 (2017).
- [50] Laganenka, L., Colin, R. & Sourjik, V. Chemotaxis towards autoinducer 2 mediates autoaggregation in escherichia coli. *Nat. Commun.* **7**, 12984 (2016).
- [51] Colin, R., Drescher, K. & Sourjik, V. Chemotactic behaviour of escherichia coli at high cell density. *Nat. Commun.* **10**, 5329 (2019).
- [52] Berg, H. C. & Brown, D. A. Chemotaxis in escherichia coli analysed by three-dimensional tracking. *Nature* **239**, 500–504 (1972).
- [53] Tailleur, J. & Cates, M. E. Statistical mechanics of interacting run-and-tumble bacteria. *Phys. Rev. Lett.* **100**, 218103 (2008).
- [54] Solon, A. P., Cates, M. E. & Tailleur, J. Active brownian particles and run-and-tumble particles: A comparative study. *Eur. Phys. J.: Spec. Top.* **224**, 1231–1262 (2015).
- [55] Dreyfus, R. *et al.* Microscopic artificial swimmers. *Nature* **437**, 862–865 (2005).
- [56] Liebchen, B. & Löwen, H. Synthetic chemotaxis and collective behavior in active matter. *Acc. Chem. Res.* **51**, 2982–2990 (2018).
- [57] Kaiser, A., Wensink, H. H. & Löwen, H. How to capture active particles. *Phys. Rev. Lett.* **108**, 268307 (2012).
- [58] Romanczuk, P., Bär, M., Ebeling, W., Lindner, B. & Schimansky-Geier, L. Active Brownian particles. *Eur. Phys. J.: Spec. Top.* **202**, 1–162 (2012).
- [59] Walther, A. & Müller, A. H. E. Janus particles. *Soft Matter* **4**, 663–668 (2008).
- [60] Buttinoni, I., Volpe, G., Kümmel, F., Volpe, G. & Bechinger, C. Active Brownian motion tunable by light. *J. Phys.: Condens. Matter* **24**, 284129 (2012).
- [61] Liebchen, B. & Löwen, H. Which interactions dominate in active colloids? *J. Chem. Phys.* **150**, 061102 (2019).
- [62] Theurkauff, I., Cottin-Bizonne, C., Palacci, J., Ybert, C. & Bocquet, L. Dynamic clustering in active colloidal suspensions with chemical signaling. *Phys. Rev. Lett.* **108**, 268303 (2012).
- [63] Palacci, J., Sacanna, S., Steinberg, A. P., Pine, D. J. & Chaikin, P. M. Living crystals of light-activated colloidal surfers. *Science* **339**, 936–940 (2013).

- [64] Pohl, O. & Stark, H. Dynamic clustering and chemotactic collapse of self-phoretic active particles. *Phys. Rev. Lett.* **112**, 238303 (2014).
- [65] Stark, H. Artificial chemotaxis of self-phoretic active colloids: Collective behavior. *Acc. Chem. Res.* **51**, 2681–2688 (2018).
- [66] Grauer, J., Löwen, H., Be'er, A. & Liebchen, B. Swarm hunting and cluster ejections in chemically communicating active mixtures. *Sci. Rep.* **10**, 5594 (2020).
- [67] Saragosti, J. *et al.* Directional persistence of chemotactic bacteria in a traveling concentration wave. *Proc. Natl. Acad. Sci. U.S.A.* **108**, 16235–16240 (2011).
- [68] Liebchen, B., Marenduzzo, D., Pagonabarraga, I. & Cates, M. E. Clustering and pattern formation in chemorepulsive active colloids. *Phys. Rev. Lett.* **115**, 258301 (2015).
- [69] Liebchen, B., Marenduzzo, D. & Cates, M. E. Phoretic interactions generically induce dynamic clusters and wave patterns in active colloids. *Phys. Rev. Lett.* **118**, 268001 (2017).
- [70] Keller, E. F. & Segel, L. A. Model for chemotaxis. *J. Theor. Biol.* **30**, 225–234 (1971).
- [71] Hillen, T. & Painter, K. J. A user's guide to pde models for chemotaxis. *J. Math. Biol.* **58**, 183 (2008).
- [72] Liebchen, B. & Löwen, H. Modeling chemotaxis of microswimmers: From individual to collective behavior. In *Chemical Kinetics: Beyond the Textbook*, 493–516 (World Scientific, 2020).
- [73] Painter, K. J. Mathematical models for chemotaxis and their applications in self-organisation phenomena. *J. Theor. Biol.* **481**, 162–182 (2019).
- [74] Liebchen, B. & Mukhopadhyay, A. K. Interactions in active colloids. *J. Phys.: Condens. Matter* **34**, 083002 (2021).
- [75] Buttinoni, I. *et al.* Dynamical clustering and phase separation in suspensions of self-propelled colloidal particles. *Phys. Rev. Lett.* **110**, 238301 (2013).
- [76] Stenhammar, J., Tiribocchi, A., Allen, R. J., Marenduzzo, D. & Cates, M. E. Continuum theory of phase separation kinetics for active Brownian particles. *Phys. Rev. Lett.* **111**, 145702 (2013).
- [77] Cates, M. E. & Tailleur, J. Motility-induced phase separation. *Annu. Rev. Condens. Matter Phys.* **6**, 219–244 (2015).
- [78] Caprini, L., Marini Bettolo Marconi, U. & Puglisi, A. Spontaneous velocity alignment in motility-induced phase separation. *Phys. Rev. Lett.* **124**, 078001 (2020).

-
- [79] Sesé-Sansa, E., Liao, G.-J., Levis, D., Pagonabarraga, I. & Klapp, S. H. L. Impact of dipole–dipole interactions on motility-induced phase separation. *Soft Matter* (2022).
- [80] Elgeti, J., Winkler, R. G. & Gompper, G. Physics of microswimmers—single particle motion and collective behavior: a review. *Rep. Prog. Phys.* **78**, 056601 (2015).
- [81] Zöttl, A. & Stark, H. Emergent behavior in active colloids. *J. Phys.: Condens. Matter* **28**, 253001 (2016).
- [82] Drescher, K., Goldstein, R. E., Michel, N., Polin, M. & Tuval, I. Direct measurement of the flow field around swimming microorganisms. *Phys. Rev. Lett.* **105**, 168101 (2010).
- [83] Guasto, J. S., Johnson, K. A. & Gollub, J. P. Oscillatory flows induced by microorganisms swimming in two dimensions. *Phys. Rev. Lett.* **105**, 168102 (2010).
- [84] Löwen, H. Inertial effects of self-propelled particles: From active Brownian to active langevin motion. *J. Chem. Phys.* **152**, 040901 (2020).
- [85] Risken, H. *Fokker-Planck Equation*, 63–95 (Springer Berlin Heidelberg, Berlin, Heidelberg, 1996).
- [86] Smoluchowski, M. V. Über Brownsche Molekularbewegung unter Einwirkung äußerer Kräfte und deren Zusammenhang mit der verallgemeinerten Diffusionsgleichung. *Ann. Phys.* **353**, 1103–1112 (1916).
- [87] Keller, E. F. & Segel, L. A. Initiation of slime mold aggregation viewed as an instability. *J. Theor. Biol.* **26**, 399–415 (1970).
- [88] Knútsdóttir, H., Pálsson, E. & Edelstein-Keshet, L. Mathematical model of macrophage-facilitated breast cancer cells invasion. *J. Theor. Biol.* **357**, 184–199 (2014).
- [89] Singh, D. P., Choudhury, U., Fischer, P. & Mark, A. G. Non-equilibrium assembly of light-activated colloidal mixtures. *Adv. Mater.* **29**, 1701328 (2017).
- [90] Stürmer, J., Seyrich, M. & Stark, H. Chemotaxis in a binary mixture of active and passive particles. *J. Chem. Phys.* **150**, 214901 (2019).
- [91] Agudo-Canalejo, J. & Golestanian, R. Active phase separation in mixtures of chemically interacting particles. *Phys. Rev. Lett.* **123**, 018101 (2019).
- [92] Safdar, M., Khan, S. U. & Jänis, J. Progress toward catalytic micro- and nanomotors for biomedical and environmental applications. *Adv. Mater.* **30**, 1703660 (2018).
- [93] Howse, J. R. *et al.* Self-motile colloidal particles: From directed propulsion to random walk. *Phys. Rev. Lett.* **99**, 048102 (2007).

-
- [94] Piazza, R. & Parola, A. Thermophoresis in colloidal suspensions. *J. Phys.: Condens. Matter* **20**, 153102 (2008).
- [95] Paxton, W. F. *et al.* Catalytic nanomotors: autonomous movement of striped nanorods. *J. Am. Chem. Soc.* **126**, 13424–13431 (2004).
- [96] Paxton, W. F. *et al.* Catalytically induced electrokinetics for motors and micropumps. *J. Am. Chem. Soc.* **128**, 14881–14888 (2006).
- [97] Ke, H., Ye, S., Carroll, R. L. & Showalter, K. Motion analysis of self-propelled pt–silica particles in hydrogen peroxide solutions. *J. Phys. Chem. A* **114**, 5462–5467 (2010).
- [98] Jiang, H.-R., Yoshinaga, N. & Sano, M. Active motion of a janus particle by self-thermophoresis in a defocused laser beam. *Phys. Rev. Lett.* **105**, 268302 (2010).
- [99] Dong, R., Zhang, Q., Gao, W., Pei, A. & Ren, B. Highly efficient light-driven TiO₂–Au janus micromotors. *ACS Nano* **10**, 839–844 (2016).
- [100] Heckel, S. *et al.* Active assembly of spheroidal photocatalytic BiVO₄ microswimmers. *Langmuir* **36**, 12473–12480 (2020).
- [101] Heckel, S. & Simmchen, J. Photocatalytic bivo4 microswimmers with bimodal swimming strategies. *Adv. Intell. Syst.* **1**, 1900093 (2019).
- [102] Villa, K. *et al.* Visible-light-driven single-component bivo4 micromotors with the autonomous ability for capturing microorganisms. *ACS Nano* **13**, 8135–8145 (2019).
- [103] Li, R. *et al.* Spatial separation of photogenerated electrons and holes among {010} and {110} crystal facets of bivo4. *Nat. Commun.* **4**, 1432 (2013).
- [104] Moran, J. L. & Posner, J. D. Phoretic self-propulsion. *Annu. Rev. Fluid Mech.* **49**, 511–540 (2017).
- [105] Zwicker, D., Hyman, A. A. & Jülicher, F. Suppression of ostwald ripening in active emulsions. *Phys. Rev. E* **92**, 012317 (2015).
- [106] Maass, C. C., Krüger, C., Herminghaus, S. & Bahr, C. Swimming droplets. *Annu. Rev. Condens. Matter Phys.* **7**, 171–193 (2016).
- [107] Zwicker, D., Seyboldt, R., Weber, C. A., Hyman, A. A. & Jülicher, F. Growth and division of active droplets provides a model for protocells. *Nat. Phys.* **13**, 408–413 (2017).
- [108] Li, M., Brinkmann, M., Pagonabarraga, I., Seemann, R. & Fleury, J.-B. Spatiotemporal control of cargo delivery performed by programmable self-propelled janus droplets. *Commun. Phys.* **1**, 1–8 (2018).
- [109] Ramos, G., Cordero, M. L. & Soto, R. Bacteria driving droplets. *Soft Matter* **16**, 1359–1365 (2020).

- [110] Rajabi, M., Baza, H., Turiv, T. & Lavrentovich, O. D. Directional self-locomotion of active droplets enabled by nematic environment. *Nat. Phys.* (2020).
- [111] Keating, C. D. Aqueous phase separation as a possible route to compartmentalization of biological molecules. *Acc. Chem. Res.* **45**, 2114–2124 (2012).
- [112] Hyman, A. A., Weber, C. A. & Jülicher, F. Liquid-liquid phase separation in biology. *Annu. Rev. Cell Dev. Biol.* **30**, 39–58 (2014).
- [113] Berry, J., Brangwynne, C. P. & Haataja, M. Physical principles of intracellular organization via active and passive phase transitions. *Rep. Prog. Phys.* **81**, 046601 (2018).
- [114] Weber, C. A., Zwicker, D., Jülicher, F. & Lee, C. F. Physics of active emulsions. *Rep. Prog. Phys.* **82**, 064601 (2019).
- [115] Thomas, R. & d’Ari, R. *Biological feedback* (CRC press, 1990).
- [116] Freeman, M. Feedback control of intercellular signalling in development. *Nature* **408**, 313–319 (2000).
- [117] Binder, K. Theory of first-order phase transitions. *Rep. Prog. Phys.* **50**, 783–859 (1987).
- [118] Grattoni, C. A., Dawe, R. A., Seah, C. Y. & Gray, J. D. Lower critical solution coexistence curve and physical properties (density, viscosity, surface tension, and interfacial tension) of 2,6-lutidine + water. *J. Chem. Eng. Data* **38**, 516 (1993).
- [119] Grauer, J. *et al.* Active droplets. *Nat. Commun.* **12**, 6005 (2021).
- [120] Cahn, J. W. On spinodal decomposition. *Acta Metallurgica* **9**, 795–801 (1961).
- [121] Cahn, J. W. & Hilliard, J. E. Free energy of a nonuniform system. III. Nucleation in a two-component incompressible fluid. *J. Chem. Phys.* **31**, 688–699 (1959).
- [122] Lifshitz, I. & Slyozov, V. The kinetics of precipitation from supersaturated solid solutions. *J. Phys. Chem. Solids* **19**, 35–50 (1961).
- [123] Wagner, C. Theorie der Alterung von Niederschlägen durch Umlösen (Ostwald-Reifung). *Z. Elektrochem., Ber. Bunsenges. Phys. Chem.* **65**, 581–591 (1961).
- [124] Huse, D. A. Corrections to late-stage behavior in spinodal decomposition: Lifshitz-slyozov scaling and monte carlo simulations. *Phys. Rev. B* **34**, 7845–7850 (1986).
- [125] Landau, L. D. On the theory of phase transitions. *Zh. Eksp. Teor. Fiz.* **7**, 19–32 (1937).
- [126] Wittkowski, R. *et al.* Scalar ϕ^4 field theory for active-particle phase separation. *Nat. Commun.* **5**, 4351 (2014).

-
- [127] Cahn, J. W. & Hilliard, J. E. Free energy of a nonuniform system. I. Interfacial free energy. *J. Chem. Phys.* **28**, 258–267 (1958).
- [128] Landau, L. D. & Ginzburg, V. L. On the theory of superconductivity. *Zh. Eksp. Teor. Fiz.* **20**, 1064 (1950).
- [129] Hohenberg, P. C. & Halperin, B. I. Theory of dynamic critical phenomena. *Rev. Mod. Phys.* **49**, 435–479 (1977).
- [130] Cahn, J. W. Phase separation by spinodal decomposition in isotropic systems. *J. Chem. Phys.* **42**, 93–99 (1965).
- [131] Schmidt, F., Liebchen, B., Löwen, H. & Volpe, G. Light-controlled assembly of active colloidal molecules. *J. Chem. Phys.* **150**, 094905 (2019).
- [132] Pieranski, P. Two-dimensional interfacial colloidal crystals. *Phys. Rev. Lett.* **45**, 569–572 (1980).
- [133] Dinsmore, A. D., Crocker, J. C. & Yodh, A. G. Self-assembly of colloidal crystals. *Curr. Opin. Colloid Interface Sci.* **3**, 5–11 (1998).
- [134] Retsch, M. *et al.* Fabrication of large-area, transferable colloidal monolayers utilizing self-assembly at the air/water interface. *Macromolecular Chemistry and Physics* **210**, 230–241 (2009).
- [135] Vogel, N., Weiss, C. K. & Landfester, K. From soft to hard: the generation of functional and complex colloidal monolayers for nanolithography. *Soft Matter* **8**, 4044–4061 (2012).
- [136] Lotito, V. & Zambelli, T. Approaches to self-assembly of colloidal monolayers: A guide for nanotechnologists. *Adv. Colloid Interface Sci.* **246**, 217–274 (2017).
- [137] Lavergne, F. A., Curran, A., Aarts, D. G. A. L. & Dullens, R. P. A. Dislocation-controlled formation and kinetics of grain boundary loops in two-dimensional crystals. *Proc. Natl. Acad. Sci. U.S.A.* **115**, 6922–6927 (2018).
- [138] Kolle, M. *et al.* Mimicking the colourful wing scale structure of the papilio blumei butterfly. *Nat. Nanotechnol.* **5**, 511–515 (2010).
- [139] Boechler, N. *et al.* Interaction of a contact resonance of microspheres with surface acoustic waves. *Phys. Rev. Lett.* **111**, 036103 (2013).
- [140] Graczykowski, B., Vogel, N., Bley, K., Butt, H.-J. & Fytas, G. Multiband hypersound filtering in two-dimensional colloidal crystals: Adhesion, resonances, and periodicity. *Nano Lett.* **20**, 1883–1889 (2020).
- [141] Retsch, M. *et al.* Parallel preparation of densely packed arrays of 150-nm gold-nanocrescent resonators in three dimensions. *Small* **5**, 2105–2110 (2009).

-
- [142] Nemiroski, A. *et al.* Engineering shadows to fabricate optical metasurfaces. *ACS Nano* **8**, 11061–11070 (2014).
- [143] Wei, Q.-H., Cupid, D. M. & Wu, X. L. Controlled assembly of two-dimensional colloidal crystals. *Appl. Phys. Lett.* **77**, 1641–1643 (2000).
- [144] Das, S., Duraia, E. M., Velev, O. D., Gatabi, J. R. & Beall, G. W. Reduction of defects in self-assembling colloidal monolayer via surface modifiers and periodic mechanical vibration. *Surf. Coat. Technol.* **319**, 353–358 (2017).
- [145] Geng, C. *et al.* Thermal annealing of colloidal monolayer at the air/water interface: a facile approach to transferrable colloidal masks with tunable interstice size for nanosphere lithography. *J. Mater. Chem.* **22**, 22678–22685 (2012).
- [146] Ramanarivo, S., Ducrot, E. & Palacci, J. Activity-controlled annealing of colloidal monolayers. *Nat. Commun.* **10**, 3380 (2019).
- [147] Kao, P.-K., VanSaders, B. J., Glotzer, S. C. & Solomon, M. J. Accelerated annealing of colloidal crystal monolayers by means of cyclically applied electric fields. *Sci. Rep.* **11**, 11042 (2021).
- [148] Allen, M. P. & Tildesley, D. J. *Computer simulation of liquids* (Oxford University Press, 2017).
- [149] Cichos, F., Gustavsson, K., Mehlig, B. & Volpe, G. Machine learning for active matter. *Nat. Mach. Intell.* **2**, 94–103 (2020).
- [150] Muiños-Landin, S., Fischer, A., Holubec, V. & Cichos, F. Reinforcement learning with artificial microswimmers. *Sci. Robot.* **6**, eabd9285 (2021).
- [151] Midtvedt, B. *et al.* Quantitative digital microscopy with deep learning. *Appl. Phys. Rev.* **8**, 011310 (2021).
- [152] Scholz, C. & Scholz, S. Exploring complex pattern formation with convolutional neural networks. *Am. J. Phys.* **90**, 141–151 (2022).
- [153] Verma, S., Novati, G. & Koumoutsakos, P. Efficient collective swimming by harnessing vortices through deep reinforcement learning. *Proc. Natl. Acad. Sci. U.S.A.* **115**, 5849–5854 (2018).
- [154] Durve, M., Peruani, F. & Celani, A. Learning to flock through reinforcement. *Phys. Rev. E* **102**, 012601 (2020).
- [155] Colabrese, S., Gustavsson, K., Celani, A. & Biferale, L. Flow navigation by smart microswimmers via reinforcement learning. *Phys. Rev. Lett.* **118**, 158004 (2017).
- [156] Schneider, E. & Stark, H. Optimal steering of a smart active particle. *EPL* **127**, 64003 (2019).

- [157] Yang, Y., Bevan, M. A. & Li, B. Efficient navigation of colloidal robots in an unknown environment via deep reinforcement learning. *Adv. Intell. Syst.* **2**, 1900106 (2020).
- [158] Hartl, B., Hübl, M., Kahl, G. & Zöttl, A. Microswimmers learning chemotaxis with genetic algorithms. *Proc. Natl. Acad. Sci. U.S.A.* **118**, e2019683118 (2021).
- [159] Nasiri, M. & Liebchen, B. Reinforcement learning of optimal active particle navigation. *arXiv preprint arXiv:2202.00812* (2022).
- [160] Li, J., de Ávila, B. E.-F., Gao, W., Zhang, L. & Wang, J. Micro/nanorobots for biomedicine: Delivery, surgery, sensing, and detoxification. *Sci. Robot.* **2**, eaam6431 (2017).
- [161] Li, S. *et al.* A DNA nanorobot functions as a cancer therapeutic in response to a molecular trigger in vivo. *Nat. Biotechnol.* **36**, 258–264 (2018).
- [162] Soler, L., Magdanz, V., Fomin, V. M., Sanchez, S. & Schmidt, O. G. Self-propelled micromotors for cleaning polluted water. *ACS Nano* **7**, 9611–9620 (2013).
- [163] Goodfellow, I., Bengio, Y. & Courville, A. *Deep Learning* (MIT Press, 2016).
- [164] Rumelhart, D. E., Hinton, G. E. & Williams, R. J. Learning representations by back-propagating errors. *Nature* **323**, 533–536 (1986).
- [165] Kaelbling, L. P., Littman, M. L. & Moore, A. W. Reinforcement learning: A survey. *J. Artif. Int. Res.* **4**, 237–285 (1996).
- [166] Sutton, R. S. & Barto, A. G. *Reinforcement Learning: An Introduction* (The MIT Press, 2018), second edn.
- [167] Littman, M. L. Reinforcement learning improves behaviour from evaluative feedback. *Nature* **521**, 445–451 (2015).
- [168] Williams, R. J. Simple statistical gradient-following algorithms for connectionist reinforcement learning. *Mach. Learn.* **8**, 229–256 (1992).
- [169] Arulkumaran, K., Deisenroth, M. P., Brundage, M. & Bharath, A. A. Deep reinforcement learning: A brief survey. *IEEE Signal Process. Mag.* **34**, 26–38 (2017).
- [170] Watkins, C. J. C. H. & Dayan, P. Q-learning. *Mach. Learn.* **8**, 279–292 (1992).
- [171] van Hasselt, H., Guez, A. & Silver, D. Deep reinforcement learning with double q-learning. *Proc. Conf. AAAI Artif. Intell.* **30** (2016).
- [172] Wang, Z. *et al.* Dueling network architectures for deep reinforcement learning. In *International conference on machine learning*, 1995–2003 (PMLR, 2016).
- [173] Schaul, T., Quan, J., Antonoglou, I. & Silver, D. Prioritized experience replay. *arXiv preprint arXiv:1511.05952* (2015).

- [174] Cui, J., Li, F. & Shi, Z.-L. Origin and evolution of pathogenic coronaviruses. *Nat. Rev. Microbiol.* **17**, 181–192 (2019).
- [175] Wu, F. *et al.* A new coronavirus associated with human respiratory disease in china. *Nature* **579**, 265–269 (2020).
- [176] Zhou, P. *et al.* A pneumonia outbreak associated with a new coronavirus of probable bat origin. *Nature* **579**, 270–273 (2020).
- [177] NOBLE, J. V. Geographic and temporal development of plagues. *Nature* **250**, 726–729 (1974).
- [178] Kermack, W. O., McKendrick, A. G. & Walker, G. T. A contribution to the mathematical theory of epidemics. *Proc. R. Soc. Lond. A* **115**, 700–721 (1927).
- [179] Hethcote, H. W. The mathematics of infectious diseases. *SIAM Rev.* **42**, 599–653 (2000).
- [180] Grassly, N. C. & Fraser, C. Mathematical models of infectious disease transmission. *Nat. Rev. Microbiol.* **6**, 477–487 (2008).
- [181] Andersson, H. & Britton, T. *Stochastic epidemic models and their statistical analysis*, vol. 151 (Springer Science & Business Media, 2012).
- [182] Norambuena, A., Valencia, F. J. & Guzmán-Lastra, F. Understanding contagion dynamics through microscopic processes in active Brownian particles. *Sci. Rep.* **10**, 20845 (2020).
- [183] Kerr, C. C. *et al.* Covasim: An agent-based model of COVID-19 dynamics and interventions. *PLoS Comput. Biol.* **17**, 1–32 (2021).
- [184] Lasser, J. *et al.* Agent-based simulations for protecting nursing homes with prevention and vaccination strategies. *J. R. Soc. Interface* **18**, 20210608 (2021).
- [185] Lasser, J. *et al.* Assessing the impact of SARS-CoV-2 prevention measures in austrian schools using agent-based simulations and cluster tracing data. *Nat. Commun.* **13**, 554 (2022).
- [186] Dehning, J. *et al.* Inferring change points in the spread of COVID-19 reveals the effectiveness of interventions. *Science* **369**, eabb9789 (2020).
- [187] Bauer, S. *et al.* Relaxing restrictions at the pace of vaccination increases freedom and guards against further COVID-19 waves. *PLoS Comput. Biol.* **17**, 1–37 (2021).
- [188] Marconi, U. M. B. & Tarazona, P. Dynamic density functional theory of fluids. *J. Chem. Phys.* **110**, 8032–8044 (1999).
- [189] Archer, A. J. & Evans, R. Dynamical density functional theory and its application to spinodal decomposition. *J. Chem. Phys.* **121**, 4246–4254 (2004).

-
- [190] te Vrugt, M., Bickmann, J. & Wittkowski, R. Effects of social distancing and isolation on epidemic spreading modeled via dynamical density functional theory. *Nat. Commun.* **11**, 5576 (2020).
- [191] Li, M. Y. & Muldowney, J. S. Global stability for the seir model in epidemiology. *Math. Biosci.* **125**, 155–164 (1995).
- [192] Fernández-Villaverde, J. & Jones, C. I. Estimating and simulating a SIRD model of COVID-19 for many countries, states, and cities. *J. Econ. Dyn. Control* 104318 (2022).
- [193] Gray, A., Greenhalgh, D., Hu, L., Mao, X. & Pan, J. A stochastic differential equation sis epidemic model. *SIAM. J. Appl. Math.* **71**, 876–902 (2011).
- [194] Korobeinikov, A. & Maini, P. K. A lyapunov function and global properties for *SIR* and *SEIR* epidemiological models with nonlinear incidence. *Math. Biosci. Eng.* **1**, 57–60 (2004).
- [195] Randolph, H. E. & Barreiro, L. B. Herd immunity: Understanding COVID-19. *Immunity* **52**, 737–741 (2020).
- [196] Ferretti, L. *et al.* Quantifying SARS-CoV-2 transmission suggests epidemic control with digital contact tracing. *Science* **368**, eabb6936 (2020).
- [197] Ferguson, N. M. *et al.* Strategies for mitigating an influenza pandemic. *Nature* **442**, 448–452 (2006).
- [198] Kraemer, M. U. G. *et al.* The effect of human mobility and control measures on the COVID-19 epidemic in china. *Science* **368**, 493–497 (2020).
- [199] Maier, B. F. & Brockmann, D. Effective containment explains subexponential growth in recent confirmed COVID-19 cases in china. *Science* **368**, 742–746 (2020).
- [200] Mercer, T. R. & Salit, M. Testing at scale during the COVID-19 pandemic. *Nat. Rev. Genet.* **22**, 415–426 (2021).
- [201] Grauer, J., Löwen, H. & Liebchen, B. Strategic spatiotemporal vaccine distribution increases the survival rate in an infectious disease like COVID-19. *Sci. Rep.* **10**, 21594 (2020).
- [202] Venkatramanan, S. *et al.* Optimizing spatial allocation of seasonal influenza vaccine under temporal constraints. *PLoS Comput. Biol.* **15**, 1–17 (2019).
- [203] Drake, J. W. Rates of spontaneous mutation among RNA viruses. *Proc. Natl. Acad. Sci. U.S.A.* **90**, 4171–4175 (1993).
- [204] Drake, J. W. & Holland, J. J. Mutation rates among RNA viruses. *Proc. Natl. Acad. Sci. U.S.A.* **96**, 13910–13913 (1999).

-
- [205] Sanjuán, R., Nebot, M. R., Chirico, N., Mansky, L. M. & Belshaw, R. Viral mutation rates. *J. Virol.* **84**, 9733–9748 (2010).
- [206] Harvey, W. T. *et al.* SARS-CoV-2 variants, spike mutations and immune escape. *Nat. Rev. Microbiol.* **19**, 409–424 (2021).
- [207] Thakur, V. *et al.* Waves and variants of SARS-CoV-2: understanding the causes and effect of the COVID-19 catastrophe. *Infection* **50**, 309–325 (2022).
- [208] Schwarzendahl, F. J., Grauer, J., Liebchen, B. & Löwen, H. Mutation induced infection waves in diseases like COVID-19. *Sci. Rep.* **12**, 9641 (2022).
- [209] Robbins, M. O., Kremer, K. & Grest, G. S. Phase diagram and dynamics of yukawa systems. *J. Chem. Phys.* **88**, 3286–3312 (1988).
- [210] Weeks, J. D., Chandler, D. & Andersen, H. C. Role of repulsive forces in determining the equilibrium structure of simple liquids. *J. Chem. Phys.* **54**, 5237–5247 (1971).
- [211] Øksendal, B. *Stochastic Differential Equations: An Introduction with Applications* (Springer Berlin Heidelberg, 2003).
- [212] Holden, H., Øksendal, B., Ubøe, J. & Zhang, T. *Stochastic Partial Differential Equations: A Modeling, White Noise Functional Approach* (Springer New York, 2010).
- [213] Maruyama, G. Continuous markov processes and stochastic equations. *Rendiconti del Circolo Mat. di Palermo* **4**, 48 (1955).
- [214] Kloeden, P. E. & Platen, E. *Numerical Solution of Stochastic Differential Equations* (Springer Berlin Heidelberg, 1992).
- [215] Press, W. H., Teukolsky, S. A., Vetterling, W. T. & Flannery, B. P. *Numerical recipes 3rd edition: The art of scientific computing* (Cambridge University Press, 2007).
- [216] Courant, R., Friedrichs, K. & Lewy, H. Über die partiellen Differenzengleichungen der mathematischen Physik. *Math. Ann.* **100**, 32–74 (1928).

Eidesstattliche Versicherung

Ich versichere an Eides Statt, dass die Dissertation von mir selbständig und ohne unzulässige fremde Hilfe unter Beachtung der „Grundsätze zur Sicherung guter wissenschaftlicher Praxis an der Heinrich-Heine-Universität Düsseldorf“ erstellt worden ist.

Düsseldorf, _____